# A STUDY ON HIGH-SPEED MAGNETIC INDUCTION TOMOGRAPHY INSTRUMENTATION AIMING AT LOW CONDUCTIVITY APPLICATIONS

GEORGIOS PANAGI

A submission presented in partial fulfilment of the requirements of the University of South Wales/Prifysgol De Cymru for the degree of Doctor of Philosophy

2014

# Abstract

Magnetic Induction Tomography is a contactless imaging technique which uses a coil array to induce eddy currents to a conductive object and detects the secondary magnetic field containing the conductivity information. Magnetic Induction Tomography instrumentation for low conductivity applications ($\sigma<30$ S/m) is very demanding due to the low amplitude signals. Depending on the application a high data acquisition rate might be required.

The aim of this study was to investigate and develop practical and inexpensive high speed Magnetic Induction Tomography instrumentation to provide a solution to low conductivity applications requiring high data acquisition rate. Specifically the multiphase flow in oil pipes and the detection of the cardiac activity and the lung activity were targeted.

A thorough investigation for the specifications, the design and the development of the required MIT instrumentation was performed. Two low cost MIT systems operating at 10 MHz based on the zero crossing phase measurement technique were developed and implemented.

The eight channel Cardiff Mk2c aimed at the multiphase flow in oil pipes. The Cardiff Mk2c achieved a frame rate of 12.5 frames per second making it the fastest 10 MHz multichannel MIT system until this thesis was submitted. Its precision was down to 15 millidegrees. The Cardiff Mk2c detected the flow of 250 ml volume of 3 S/m saline through an inclined water pipe. The detected signal had a duration of 200 ms and the system's observed maximum peak SNR was 38.75 dB.

The single channel Cardiff Mk2d aimed at the detection of the cardiac activity and the lung activity making it the first zero crossing system used for these applications. The Cardiff Mk2d used a recording rate of 20 Hz and achieved a phase precision down to 4 millidegrees. Measurement with four human volunteers were taken in which the Cardiff Mk2d detected successfully the heart rate and the respiration rate concurrently.

# Acknowledgements

This thesis would not have been possible without the help and support of so many wonderful people whom I wish to thank in the following lines.

First of all I want to express my gratitude to my Director of Studies Prof. Dr. Ralf Patz who was a superb teacher and a great supervisor. Prof. Patz stood by me all the way counselling me on my work and transferring knowledge to me that I have not come across before. Prof. Patz never refused to discuss even the silliest idea I came up with – and I had quite a few. He was always the hardest critic of my work but it was Prof. Patzs' wise critique that guided me through this work. I only hope to prove worthy of his trust and his time.

I extend my gratitude to Dr. Stuart Watson who aided me during this work. Dr. Watson never refused to discuss my work and ideas and provided constructive and helpful critique that shed new light on the work I performed. Dr. Watson taught me many things but above all with his actions he taught me the value of helping without expecting anything in return.

I would like to thank Prof. Robert Williams and Prof. Soteris Kalogerou for opening this door to me and for pushing me into this magnificent journey. Indeed if it was not for Prof. Williams and Prof. Kalogerou I do not think I would ever had the chance or the strength to embark on such life shaping experience.

I take this opportunity to thank Mrs. Nathalie Patz and Mrs. Rose Watson for showing me so much kindness the magnitude of which words cannot express. Indeed I consider my self very fortunate that I have met these two wonderful and respected ladies.

I want to thank my mother Athena, my sisters Panayiota, Paraskevi and Andri and my brother Sotos for their love and support through the course of this work. Each with their own unique way made me feel that I was not standing alone. And I want to thank Panayiota's kids Nikolas, Athena and Chrysoulis for their smile and innocence that was so comforting at troubled times.

I also want to thank Prof. Sotos Voskarides PhD, Mr. Elias Elia, Mrs. Vasiliki Savva, Mrs. Maria Foka RN, Mr. Constantinos Ioannou, Mr. Christos Efthyvoulou, Dr. Theodoros Kyprianou MD PhD, Dr. Andreas Kouyialis MD PhD and Prof. Efthyvoulos Kyriakou PhD. Each of them helped me in his or her own unique way.

Finally with all my heart and soul I want to thank my daughter Athena who quietly waited her daddy to finish his work in order to spend some time with her. And I want to especially thank Athena for the love and the happiness that brings in my life from the day she was born.

ὅτι ἐν πλήθει σοφίας πλῆθος γνώσεως, καὶ ὁ προστιθεὶς γνῶσιν προσθήσει ἄλγημα

Εκκλησιαστής 1:18

(For in much wisdom is much knowledge, and he who increases his knowledge increases his pain)

Ecclesiastes 1:18

Nos esse quasi nanos, gigantium humeris insidentes

(We are like dwarfs mounted on the shoulders of giants)

Bernard of Chartres

# Contents

1. Introduction.....1

1.1 Background of study.....1
1.2 Objectives of the project.....5
1.3 Thesis structure.....6

2. Review of literature.....8

2.1 Physical aspects of Magnetic Induction Tomography.....8
2.1.1 Principle of operation.....9
2.1.2 The composition of the detected signal and its measurement.....11
2.1.3 Skin depth and frequency dependence.....15
2.2 The MIT system.....17
2.2.1 Architecture and characteristics.....17
2.2.2 Architectural components.....17
2.2.3 Noise and the MIT system.....20
2.3 Phase measurements in MIT.....24
2.3.1 Characteristics of the sinusoidal signal.....24
2.3.2 The phase precision and the phase drift.....26
2.4 Phase measurement techniques in MIT and some implementations.....28
2.4.1 The zero crossing technique.....28
2.4.2 Vector-voltmeter technique.....33
2.4.3 Direct digitisation technique.....36
2.4.4 The downconverted direct digitisation technique.....42
2.5 Possible low conductivity industrial application for a fast MIT system.....44
2.5.1 Multiphase flow measurements in oil pipes.....45
2.5.2 MIT system for multiphase flow measurements in oil pipes.....48
2.6 Possible low conductivity biomedical applications for a fast MIT system.....49
2.6.1 The electrical properties of the living tissue.....50
2.6.2 Frequency dependency of the living tissue.....53
2.6.3 Dielectric properties of the thorax main tissues from 10 Hz to 100 MHz.....56
2.6.4 Physical aspects of the heart and lungs and their monitoring.....59
2.6.5 MIT systems for detecting the cardiac activity and lung function.....63
2.7 Summary and identified areas of further research work.....72

3. The zero crossing phase measurement subsystem.....75

3.1 Background and requirements.....75
3.2 Design.....77
3.2.1 General architecture.....77
3.2.2 Implementation details for the analogue processing stage.....78
3.2.3 Implementation details for the measurement stage.....80
3.3 Theoretical aspects of the subsystem's operation.....84

3.3.1 The equation for calculating the phase difference....85
3.3.2 The measurement stage standard deviation....86
3.3.3 The measurement stage recording time....87
3.3.4 The resolution of the phase measurement subsystem....88
3.3.5 The subsystem phase precision and phase drift equations....89
3.4 Implementation of the zero crossing phase measurement subsystem....90
3.4.1 The analogue processing stage....91
3.4.2 The measurement stage....98
3.5 Characterisation....113
3.5.1 Measurement stage characterisation....113
3.5.2 Phase measurement subsystem characterisation....116
3.6 Summary....123

4. The Cardiff Mk2c MIT system....126

4.1 Requirements and specifications....126
4.2 Theoretical aspects....128
4.2.1 The MIT system architecture....128
4.2.2 Factors affecting the MIT system frame rate....129
4.3 Design of the Cardiff Mk2c system....134
4.3.1 System architecture....134
4.3.2 System components and implementation details....135
4.4 Implementation of the coil array subsystem....139
4.4.1 The coil array body....139
4.4.2 The excitation signal circuit....143
4.4.3 The detection signal circuit....147
4.4.4 The reference signal circuit....148
4.4.5 The power supply....149
4.5 Implementation of the multichannel SPMU....149
4.5.1 Architecture and implementation considerations....149
4.5.2 The analogue stage of SPMU....150
4.5.3 The measurement stage of SPMU....152
4.6 The Cardiff Mk2c as a complete system....159
4.6.1 The hardware part of the system....159
4.6.2 Calculation of the frame rate of the hardware part....162
4.7 Characterisation of the multichannel SPMU....163
4.7.1 Test set-up....163
4.7.2 Phase precision....164
4.7.3 Phase drift....165
4.7.4 Recording rate....166
4.8 Characterisation of the Cardiff Mk2d system....166
4.8.1 Performance of the coil array....166
4.8.2 Frame rate....168
4.8.2 Phase precision....169
4.8.2 Phase drift....170
4.9 Water pipe phantom flow measurements....171
4.9.1 Test set-up....171
4.9.2 Experiment for detecting fast moving saline volume through the pipe....172
4.9.3 Experiment for detecting free flow of saline through the pipe....177
4.10 Summary....183

5. The Cardiff Mk2d MIT system.....187

5.1 Background and requirements.....187
5.2 Design and implementation.....189
5.2.1 Design.....189
5.2.2 Implementation.....189
5.3 Characterisation.....193
5.3.1 Performance of the coil array.....193
5.3.2 Phase precision.....195
5.3.3 Phase drift.....196
5.3.4 Recording rate.....197
5.4 Measurement of the cardiac activity and the lung function.....197
5.4.1 Measurement set-up.....197
5.4.2 Measurements methodology.....200
5.4.3 Measurements analysis.....202
5.4.4 Measurement results at detection coil position 1.....204
5.4.5 Measurement results at detection coil position 2.....211
5.4.6 Measurement results at detection coil position 3.....220
5.5 Summary.....225

6. Discussion.....227

6.1 Theoretical aspects regarding the MIT system.....228
6.1.1 The MIT architecture.....228
6.1.2 The MIT system frame rate.....230
6.1.3 Terminology used for the MIT system.....230
6.2 The Cardiff Mk2c system.....232
6.4 The Cardiff Mk2d system.....236

7. Conclusions and further work.....239

7.1 Conclusions.....239
7.2 Further work arising from the project.....240

Appendix 1.....242

A1.1 The heterodyne technique of frequency shifting.....242

Appendix 2.....243

A2.1 Electrical Capacitance Tomography.....243
A2.2 Electrical Resistance Tomography.....244
A2.3 Electrical Impedance Tomography.....245

Appendix 3.....247

A3.1 Data of the dielectric properties of some thorax tissues in the frequency range from 10 Hz to 100 MHz.....247

Appendix 4.....250

A4.1 The LABWINDOWS/CVI computer application software code.....250

Appendix 5.....255

A5.1 Air circular coil inductance calculation.....255

A5.2 Air circular coil self resonance frequency calculation.....255
A5.3 Air rectangular coil inductance calculation.....255

Appendix 6.....256

A6.1 The MATLAB code.....256
A6.1.1 Function for loading the files.....256
A6.1.2 Function for heart signal extraction from MIT signal.....257
A6.1.3 Function for breathing signal extraction from MIT signal.....258
A6.1.4 Function for FFT.....259
A6.1.5 Function for STFT.....261

# List of Figures

Figure 2.1: MIT principle of operation....9
Figure 2.2: The phasor diagram of the received signal (not to scale) (from [7])....12
Figure 2.3: The model used in [12] to propose the quasi-static approximation....13
Figure 2.4: The equivalent circuit input of a magnetic induction coil array (from [8])....14
Figure 2.5: Types of MIT coil arrays - (a) an annular coil array and (b) an application specific coil array....18
Figure 2.6: General representation of noise....20
Figure 2.7: Sine wave characteristics: (a) voltage V changes with time t and (b) amplitude changes with phase angle φ (from [47])....24
Figure 2.8: The phase difference between two sinusoidal signals....26
Figure 2.9: Time interval between the zero crossing points of two sinusoidal waves....28
Figure 2.10: Linear interpolation to find the zero-crossing points using sampling....30
Figure 2.11: Block diagram of the zero crossing MIT system implemented in [32]....31
Figure 2.12: Block diagram of the single channel zero crossing phase measurement system using an XOR gate as the phase detector proposed in [21]....32
Figure 2.13: Block diagram of a typical lock-in amplifier....33
Figure 2.14: The mechanical coil alignment (a) and the electrical set up (b) of the multichannel planar array system described in [42]....35
Figure 2.15: The phase measurement circuit for each detection coil used in [42]....36
Figure 2.16: The direct digitisation technique as used in MIT (from [30])....37
Figure 2.17: The Cardiff Mk2a system....39
Figure 2.18: The block diagram of the MIT system implemented in [61]....40
Figure 2.19: The MIT system configuration as given in [14]....41
Figure 2.20: The MIT system presented in [64]. On the left is the FPGA subsystem and on the right the coil array....42
Figure 2.21: Block diagram of the Musimitos system (from [68])....43
Figure 2.22: Stratified three phase flow in a horizontal oil pipe (from [72])....45
Figure 2.23: The conventional approach for multiphase flow metering (from [73])....46
Figure 2.24: A multiphase meter for multiphase flow measurements (from [76])....46
Figure 2.25: Tomographic MPF measurement (from [71])....48
Figure 2.26: The MIT system described in [11,29] simulating the MPF measurements....49
Figure 2.27: Equivalent electrical circuit for the plasma membrane (adapted from [84])…52
Figure 2.28: An idealised perception of the living tissue permittivity variation in the three major dispersions (from [84])....54
Figure 2.29: High frequency and low frequency current path in tissue. The solid line is low frequency and the dashed line is the high frequency. (from [83])....55
Figure 2.30: Conductivity distribution of the thorax tissues from 10 Hz to 100 MHz....56
Figure 2.31: Permittivity distribution of the thorax tissues from 10 Hz to 100 MHz....57
Figure 2.32: Permittivity distribution of the thorax tissues from 1 kHz to 100 MHz....57
Figure 2.33: The cardiac cycle (from [10])....60
Figure 2.34: Lung capacity and lung volume relationship (from [109])....62
Figure 2.35: The coil configuration of the single channel system described in [121]....64
Figure 2.36: Conductivity changes recorded when the subject was breathing normally as recorded in [121] (In the centre of the graph the subject hold its breath)....65

Figure 2.37: Alternative coil configurations for conductivity changes recording at the torso area as proposed in [121] (EXC is the excitation coil, PU is the detection coils).....66
Figure 2.38: Conductivity changes in comparison with the ECG of the subject as recorded in [20].....67
Figure 2.39: The comparison of airflow and magnetic induction performed in [24].....68
Figure 2.40: An overview of the signals measured simultaneously in [68].....68
Figure 2.41: The block diagram of the portable impedance measurement system developed in [123].....70
Figure 2.42: Shallow, normal and deep breathing of a subject captured by the system developed in [123].....71
Figure 3.1: The concept diagram of the phase measurement subsystem configuration.....77
Figure 3.2: Block diagram of the hardware required for the multichannel version.....78
Figure 3.3: Sinewave to square wave conversion using high gain saturated amplifiers.....79
Figure 3.4: The two sinusoidal signals having 45 degrees phase difference and their respective zero crossings.....80
Figure 3.5: The ideal phase detector (from [124]).....81
Figure 3.6: The XOR phase detector (from [124]).....81
Figure 3.7: The input/output characteristic of the XOR phase detector with (a) single-ended output and (b) differential output (from [124]).....82
Figure 3.8: Time interval measurement (from [126]).....83
Figure 3.9: The ±1 count error.....84
Figure 3.10: The XOR pulses and the input signal.....87
Figure 3.11: The AD835 functional block diagram (from [132]).....92
Figure 3.12: Implementation circuit of the AD835 multiplier.....93
Figure 3.13: The AD8056 functional block diagram (from [133]).....94
Figure 3.14: The implementation of the gain section.....95
Figure 3.15: The output of the analogue processing stage.....96
Figure 3.16: The LT1016 functional block diagram (from [135]).....96
Figure 3.17: The implementation of the LT1016 comparator.....97
Figure 3.18: 74LVC245 pin configuration(a) and connection diagram (b) (from [137])….98
Figure 3.19: The level translation by the 74LVH245 – LT1016 input (yellow trace) and 74LVH245 output (purple trace).....98
Figure 3.20: Block diagram of the measurement stage.....100
Figure 3.21: The functional block diagram of the component channel.....101
Figure 3.22: The channel's state machine flow diagram.....102
Figure 3.23: The metastability phenomenon recorded during the preliminary tests of the measurement section.....103
Figure 3.24: The synchroniser stage in detail.....104
Figure 3.25: The UART component as implemented in the FPGA.....105
Figure 3.26: The complete measurement stage implementation in the FPGA.....107
Figure 3.27: The main state machine (MSM) flow diagram.....109
Figure 3.28: The UART state machine (UART SM) flow diagram.....110
Figure 3.29: The application software GUI.....112
Figure 3.30: The test set-up for the measurement stage phase precision characterisation.113
Figure 3.31: Measurement stage phase precision Vs delay line.....114
Figure 3.32: The phase precision characterisation test set-up for the subsystem without downconversion.....116
Figure 3.33: The subsystem without downconversion phase precision at 10 kHz.....117
Figure 3.34: The phase precision characterisation test set-up for the subsystem with the downconversion.....118
Figure 3.35: The complete subsystem phase precision at 1 MHz operation frequency.....119
Figure 3.36: The complete subsystem phase precision at 10 MHz operation frequency…120

Figure 3.37: The complete subsystem phase precision at 20 MHz operation frequency…120
Figure 3.38: The complete subsystem phase drift characterisation test set-up.....122
Figure 3.39: The subsystem phase drift over 5 hours showing the maximum drift (a) and the average drift (b).....123
Figure 4.1: The proposed architecture for a practical MIT system.....128
Figure 4.2: The excitation signal chain time delays.....130
Figure 4.3: The parallel MIT system detection signal chain time delays.....130
Figure 4.4: The multiplexed MIT system detection signal chain time delays.....131
Figure 4.5: The coil formation used in Cardiff Mk2 (from [11]).....136
Figure 4.6: Conceptual block diagram of the designed signal route in the Cardiff Mk2c system.....139
Figure 4.7: The coil array of the Cardiff Mk2c MIT system.....140
Figure 4.8: The dimensions of the outer screen.....141
Figure 4.9: A coil former on the left and it dimensions on the right.....141
Figure 4.10: The coil formers' rings dimensions and placement on the outer shield (viewed from the side and from above).....142
Figure 4.11: The coil former configuration in the coil array.....142
Figure 4.12: The daisy chain distribution of the excitation signal (a) block diagram (b) photo of the realisation.....144
Figure 4.13: The input pulse (purple trace), the output of the transistor connector (yellow trace) and the relay output (blue trace) when (a) uncompensated and (b) compensated with 1N4004 diode with BZX79-C24 zener diode.....146
Figure 4.14: The RF relay circuit diagram (a) and the implementation (b).....147
Figure 4.15: The low noise preamplifier used in the Cardiff Mk2c (from [11]).....148
Figure 4.16: The reference signal coil used in the Cardiff Mk2c.....148
Figure 4.17: Block diagram of the SPMU general architecture.....150
Figure 4.18: The implemented analogue processing stage of the multichannel SPMU.....151
Figure 4.19: The component channel presented as a black box.....152
Figure 4.20: Block diagram of the measurement section as implemented in the SPMU measurement stage.....154
Figure 4.21: Block diagram of the communication section implementation.....155
Figure 4.22: The communication section state machine.....156
Figure 4.23: The transition counter.....157
Figure 4.24: The circuit for activating and deactivating the RF relays.....157
Figure 4.25: The measurement stage state machine.....158
Figure 4.26: The Cardiff Mk2c system.....160
Figure 4.27: Block diagram of the CardiffMk2c as a working unit.....161
Figure 4.28: The test set-up for the 8 channel SPMU characterisation.....163
Figure 4.29: SPMU phase precision Vs input amplifier graph.....164
Figure 4.30: The test set-up for the measurement stage phase precision characterisation.165
Figure 4.31: The reference signal from excitation coil 3 (yellow trace) and the detection signal from the detection coil 3 (blue signal).....167
Figure 4.32: The reference signal from excitation coil 7 (yellow trace) and the detection signal from the detection coil 3 (blue signal).....168
Figure 4.33: Average phase precision Vs RF amplifier output.....169
Figure 4.34: The test set-up for the water pipe phantom measurements.....171
Figure 4.35: The saline sealed bottle in the water pipe (a) and the saline bottle used (b). 172
Figure 4.36: Saline bottle experiment – Excitation coils Tx1 and Tx2 results.....173
Figure 4.37: Saline bottle experiment – Excitation coils Tx3 and Tx4 results.....174
Figure 4.38: Saline bottle experiment – Excitation coils Tx5 and Tx6 results.....175
Figure 4.39: Saline bottle experiment – Excitation coils Tx7 and Tx8 results.....176
Figure 4.40: The saline free flow through the water pipe.....178

Figure 4.41: Saline flow experiment – Excitation coils Tx1 and Tx2 results.....179
Figure 4.42: Saline flow experiment – Excitation coils Tx3 and Tx4 results.....180
Figure 4.43: Saline flow experiment – Excitation coils Tx5 and Tx6 results.....181
Figure 4.44: Saline flow experiment – Excitation coils Tx7 and Tx8 results.....182
Figure 5.1: The Cardiff Mk2d system architecture.....189
Figure 5.2: The Cardiff Mk2d coil array.....190
Figure 5.3: The excitation coil and the reference coil used in Cardiff Mk2d.....191
Figure 5.4: The ADA4899-1 functional block diagram (from [153]).....192
Figure 5.5: Implementation of the preamplifier circuit.....192
Figure 5.6: The reference signal (a) and the detected signal from the preamplifier (b).....194
Figure 5.7: The orthogonal configuration of the coil array.....194
Figure 5.8: Phase precision Vs RF amplitude output.....195
Figure 5.9: Position 1 coil array configuration (a) and the detection coil position (b).....197
Figure 5.10: Position 2 coil array configuration (a) and the detection coil position (b).....198
Figure 5.11: A volunteer in the coil array of detection coil position 2.....198
Figure 5.12: Position 3 orthogonal coil array configuration.....199
Figure 5.13: A volunteer in the coil array of detection coil position 3.....199
Figure 5.14: Lung capacities and lung volumes relationship (from [109]).....200
Figure 5.15: The Dyna Vision device used for ECG recording.....201
Figure 5.16: MIT normal breathing signal of a volunteer for 1 minute at position 1.....204
Figure 5.17: ECG signal of volunteer in normal breathing at position 1.....205
Figure 5.18: FFT spectrum of the MIT normal breathing signal and the ECG signal at position 1. From top to bottom: the MIT-breath signal FFT, the MIT-heart FFT and the ECG FFT.....205
Figure 5.19: Heart rate spectrogram generated by the MIT normal breathing signal at position 1.....206
Figure 5.20: No breathing MIT signal of a male volunteer at position 1.....207
Figure 5.21: ECG signal when the volunteer did not breath (no breathing) at position 1. 207
Figure 5.22: FFT spectrum of the no breathing MIT signal at position 1. From top to bottom: the MIT-breath signal FFT, the MIT-heart FFT and the ECG FFT.....208
Figure 5.23: MIT signal of a volunteer after exercise at position 1.....209
Figure 5.24: ECG signal of volunteer after exercise at position 1. From top to bottom: at beginning of measurement, at end of measurement.....209
Figure 5.25: FFT spectrum of the MIT signal and the ECG signal after exercise at position 1. From top to bottom: the MIT-breath signal FFT, the MIT-heart FFT and the ECG FFT. .....210
Figure 5.26: Heart rate spectrogram after exercise at position 1.....210
Figure 5.27: The MIT signal during normal breathing of a volunteer at position 2.....212
Figure 5.28: ECG signal of volunteer during normal breathing exercise at position 2.....212
Figure 5.29: FFT spectrum of the MIT normal breathing signal and the ECG signal at position 2. From top to bottom: the MIT-breath signal FFT, the MIT-heart FFT and the ECG FFT.....213
Figure 5.30: Heart rate spectrogram of the MIT signal during normal breathing at position 2.....213
Figure 5.31: The MIT signal recorded after the exercise at position 2.....215
Figure 5.32: The MIT signal captured after the exercise at different time periods. From top to bottom: Measurement beginning, middle and end.....215
Figure 5.33: ECG signal of volunteer after exercise at position 2. From top to bottom: at the beginning of the measurement and in the middle.....216
Figure 5.34: FFT spectrum of the MIT signal and the ECG signal after the exercise at position 2. From top to bottom: the MIT-breath signal FFT, the MIT-heart FFT and the ECG FFT.....217

Figure 5.35: Heart rate spectrogram of the MIT signal after exercise at position 2.....217
Figure 5.36: MIT signal of the breathing pattern at position 2.....219
Figure 5.37: FFT spectrum of the MIT signal and the ECG signal of the breathing pattern at position 2.....219
Figure 5.38: Heart rate spectrogram of the breathing pattern MIT signal at position 2.....220
Figure 5.39: Normal breathing MIT signal at position 3.....221
Figure 5.40: ECG signal of volunteer during normal breathing exercise at position 2.....221
Figure 5.41: FFT of the MIT signal and the ECG signal during normal breathing at position 3.....222
Figure 5.42: Heart rate spectrogram of the MIT signal during normal breathing at position 3.....222
Figure 5.43: MIT signal of the breath pattern at position 3.....223
Figure 5.44: FFT spectrum of the MIT signal and the ECG signal during the breathing pattern at position 3.....224
Figure 5.45: Heart rate spectrogram of the MIT signal during the breathing pattern at position 3.....224
Figure 6.1: The proposed architecture for the MIT system.....229
Figure A2.1: An 8-electrode ECT coil array (from [71]).....243
Figure A2.2: The ECT measurement principle (from [78]).....244
Figure A2.3: The ERT measurement principle (from [78]).....245

# List of Tables

Table 3.1: Calculation of the zero crossings of the sinusoidal signals of figure 3.4.....80
Table 3.2: The theoretical standard deviation of the measurement stage for averaged measurement.....87
Table 3.3: The actual bit rate values passed to the UART component and the bit rate error percentage.....106
Table 3.4: Measurement stage time for various values of N and fDC.....111
Table 3.5: Synthesis results of the phase measurement subsystem.....111
Table 4.1: The excitation signal chain time delays.....130
Table 4.2: The parallel MIT system detection signal chain time delays.....130
Table 4.3: The multiplexed MIT system detection signal chain time delays.....131
Table 4.4: Time delays for the data transfer and the image processing.....131
Table 4.5: Results from the compensation used on the ARE134 mechanical relay.....146
Table 4.6: The decoder truth table.....158
Table 4.7: Saline bottle experiment maximum phase and SNR for the excitation coils....177
Table 4.8: Saline flow experiment maximum phase and SNR for the excitation coils.....183
Table 6.1: Comparison of single channel phase subsystems with time constant 20 ms or below.....233
Table 6.2: Comparison of multichannel MIT systems that used at least 10 MHz excitation frequency.....235
Table A2.1: Some EIT measurement methods (summarized from [114]).....246
Table A3.1: Conductivity of thorax tissues and components from 10 Hz to 100 MHz.....247
Table A3.2: Permittivity of thorax tissues and components from 10 Hz to 100 MHz.....248

# 1. Introduction

## 1.1 Background of study

“Tomography” is derived from the Greek words “tomos” meaning “slice, section” and “graphy”[1]. “Grafy” is a noun which in combining form means “writing or representation in a (specified) manner or by a (specified) means or of a (specified) object” [2]. The combination of the two literally bears the meaning of the representation of a section.

On a more technological basis however the Compact Oxford English Dictionary defines tomography as the “technique for displaying a cross section through a human body or other solid object using X-rays or ultrasound” [3]. This definition however can be broadened in such a way as to include any technique capable to produce a tomographic image of the human body or a solid object.

Tomography is typologically divided in the hard field and the soft field tomography. In the hard field type of tomography the energy waves from the power source are constant regardless of the type or substance of material or medium. In the soft field type of tomography electric current is introduced into the sample and the distribution of the electric field is imaged depending on the physical electrical properties of the sample. The soft field tomography is much more complex than the hard field tomography and requires considerably more computer analysis and algorithms to reconstruct the image. [4]

A number of tomographic modalities are available for either biomedical and industrial imaging applications. These include infra-red, optical, X-ray tomography, Computed Tomography (CT), Gamma-ray tomography, Positron Emission Tomography (PET), Magnetic Resonance Imaging (MRI) and sonic or ultrasonic tomography. Each of these techniques provides information on the distributions of different physical parameters and therefore are suited for different applications. [5, 6]

New tomographic techniques are constantly being developed aiming to provide a better

and/or a more cost efficient method for biomedical and industrial applications. One of these techniques is the Magnetic Induction Tomography (MIT) which applies an alternating electromagnetic field for imaging the object under study. [7, 8]

The operation of the MIT is based on the physical phenomenon of mutual induction which can be defined as the production of an electromotive force in a circuit by a change in the current in an adjacent circuit which is linked to the first by the flux lines of a magnetic field. [9]

In MIT a sinusoidal current passes through an excitation coil which produces an AC primary magnetic field. When a conductive object is placed in the primary magnetic field, eddy currents are induced within the object which in turn produce a secondary magnetic field. Both, the primary and the secondary magnetic fields, are detected by a detection coil and each contribute to the received induced signal. The signal is measured and the measurements are used for the construction of an image of the internal distribution of the passive electrical properties of the object. [7]

MIT has a number of advantages which make it very attractive for industrial and biomedical imaging applications. One advantage for biomedical imaging applications is that it does not use ionizing radiation [7] and therefore is safer compared to techniques such as the X-ray and the CT which can be teratogenic and should be minimized or avoided during pregnancy [10].

Another advantage is the non-contact nature of MIT with coils used for the excitation and the detection of the signal. For biomedical applications this allows quick and ease of use of an MIT system within the clinical environment without the need for laborious application of an array of surface electrodes as required by the Electrical Impedance Tomography (EIT). [11]

Industrial environments on the other hand are frequently hostile to any employed sensor and the non-contact nature of MIT allows the sensors to be well protected. In comparison to alternative impedance imaging methods such as the EIT and Electrical Capacitance Tomography (ECT) a further advantage of MIT is the fact that it is in principle sensitive to all three passive electromagnetic properties namely the conductivity, the permittivity and the permeability. Furthermore it shares with EIT and ECT the fact that the hardware is relatively inexpensive and that the data may be collected quickly allowing potential frames rates of tens per second. [8, 12]

However a major drawback of the MIT is the technologically demanding instrumentation required to produce usable conductivity images. As in all imaging techniques the image quality depends on the precision of the measurements performed. [7]

In the MIT if the primary magnetic field is applied to a conductive object then the produced secondary magnetic field will be in-quadrature to the primary field. The measurement of the secondary field which contains the information about the conductivity distribution of the object therefore requires a phase sensitive approach. Thus a continuous and very precise measurement of the secondary signal's phase in comparison with the phase of the primary signal which serves as the reference should be performed by a phase measurement system. [8, 12]

The measurement itself has inherent difficulties due to the principle of the MIT. The secondary magnetic field is measured in the presence of the primary magnetic field which is typically far greater in magnitude than the secondary magnetic field. The expected phase changes introduced by the secondary magnetic fields will therefore be small of the order of a few degrees. It has been suggested that for practical biomedical MIT a phase precision in the millidegree range will be required. [13]

MIT has been suggested for a number of industrial and biomedical applications that could benefit by the measurement of the electromagnetic properties of the sample volume. [7]

The majority of the proposed industrial applications for MIT concern the detection of metal or ferromagnetic objects with high conductivity or permeability in low conductivity surroundings. The proposed applications include the tracking of ferrite powder in a separation process [7], the detection of defects in metal objects [7], the monitoring of the flow regime in the pouring nozzle during the continuous casting of steel [14, 15] and the positioning and integrity of steel reinforcing bars embedded in concrete [15].

Another application for which MIT has been proposed is the determination of interface levels in separation tanks in petrochemical industry [16] as well as the monitoring of bulk ionised water in pipelines for the petrochemical industry based on the conductivity difference between the crude oil and salt water [7].

For the high conductivity industrial applications the excitation frequency range is up to 500 kHz because the conductivity characteristics of the sample volumes imaged are enough to give the required signal magnitude at such low excitation frequencies. However for low

conductivity applications such as the monitoring of bulk ionised water in pipelines the excitation frequency range can well extend to 10 MHz. It is expected that a high frame acquisition rate will be required for many industrial applications especially when the acquired data will be used for process control. [7]

The MIT has been proposed for a number of biomedical applications as well. These applications include the early detection of brain oedema [17, 18] and haemorrhage [19], the measurement of thoracic conductivity changes for monitoring the cardiac output of the heart [20] and the recording of the cardiac activity and lung function [7].

An obstacle that MIT faces for practical use in biomedical applications is the fact that the conductivity of biological tissues is much lower than those of metals and thus they produce smaller signals. Therefore the excitation frequency of the proposed biomedical systems is usually much higher than the excitation frequency of industrial systems. [7]

Some studies have indicated that excitation frequencies from 3 MHz to 30 MHz offer advantages for systems intended for biomedical use in comparison to lower or medium frequencies [21]. However it was noted that changes in the hydration status of tissue would be better recorded using multi-frequency measurements (spectroscopy) rather than single frequency measurements [22].

The suggested typical frequency range for these measurements would be between 50 kHz – 10 MHz which are in the region of the b-dispersion of the observed tissues [23]. Multi-frequency systems operating at such frame rates would be technically very demanding and the use of single or multi-frequency measurements depends solely on the application intended. Furthermore for some biomedical applications like the heart rate monitoring a high data acquisition rate higher than 12 Hz is required [24].

As a conclusion Magnetic Induction Tomography poses a number of advantages which are:

- It is sensitive to conductivity and permittivity
- It uses non ionising radiation
- Non invasive
- The construction of the coils and the instrumentation allow MIT systems to be implemented and survive in harsh industrial environments (as was shown in [15])
- Can be a cheaper but still reliable alternative solution for certain applications than some of the solutions employed or proposed.

However it must be stated that Magnetic Induction Tomography is at a very early stage of development and has not been routinely applied for any of the applications mentioned above.

If MIT is to reach routine industrial or biomedical application then the practical issues related to both the MIT system measurement precision and the speed of data acquisition must be addressed.

Therefore the main purpose of this project was to investigate and develop practical and inexpensive high speed Magnetic Induction Tomography (MIT) instrumentation to provide a solution to low conductivity applications requiring high data acquisition rate.

## 1.2 Objectives of the project

This study is aimed at developing MIT phase measurement systems for industrial and biomedical applications requiring high data acquisition rates, i.e. of the order of tens of measurements per second.

For this purpose an investigation leading to the development, implementation and characterisation of a multichannel MIT system will be performed. This system will be capable of achieving phase measurement precision of the order suitable for low conductivity industrial applications requiring high data acquisition rates.

Another investigation leading to the development, implementation and characterisation of a single channel MIT system will be conducted. This system will be capable of achieving phase measurement precision of the order suitable for low conductivity biomedical applications requiring high data acquisition rates.

More specifically the objectives of the research work include:

- Critical review of existing phase measurement techniques and MIT instrumentation able to achieve high data acquisition rates and high precision. The review will cover possible industrial and biomedical low conductivity applications suited for precise high acquisition rate MIT system. The review will aim to identify the areas of further research work that this work can address.
- Investigation for the design, implementation and characterisation of a high acquisition rate, high-precision low cost single channel phase measurement subsystem. The investigation will include the evaluation of the performance and the characterisation of the developed single channel phase measurement subsystem.

The aim will be the construction and the characterisation of the single channel phase measurement subsystem.

- Investigation for the design, implementation and characterisation of a multichannel channel MIT system with high acquisition rate comprising the results of the previous work for specific low conductivity industrial applications. During this stage a multichannel measurement subsystem based on the findings of the single channel measurement subsystem will be implemented. The first aim will be the construction and the characterisation of the multichannel phase measurement subsystem. The second aim will be the construction and the characterisation of the multichannel MIT system. The third aim will be the experimental use of the multichannel MIT system in a low conductivity industrial application.
- Investigation for the design, implementation and characterisation of a single channel MIT system with high acquisition rate comprising the results of the previous work for specific low conductivity biomedical applications. The first aim will be the construction and the characterisation of the single channel MIT system. The second aim will be the experimental use of the single channel MIT system in two low conductivity biomedical applications.

## 1.3 Thesis structure

This thesis presents the work performed in the context of this project and follows the work progress through to the completion of the project. In more detail each chapter addresses the following work.

Chapter 2 presents the review of the literature. The review first examines the physical aspects and the principle of operation of the MIT and continues with an examination of the architecture, the components and the noise of the MIT system. A review on the phase measurements in MIT is contacted followed by an examination of the phase measurement techniques used in MIT and their implementations. A review on a potential low conductivity industrial application for a fast MIT system and the examination of the proposed MIT system is conducted. A similar review for two potential biomedical applications and an examination on some of the proposed MIT systems is performed. A summary of the review findings and the identification of the further research work regarding the subject of this study is finally presented.

Chapter 3 presents the work performed for the design, development and characterisation of a low cost single channel phase measurement subsystem based on the zero crossing

technique. It analyses the theoretical and practical aspects for the design of the subsystem and provides the required technical details and information regarding the implementation of the system. The characterisation results of the subsystem in terms of phase precision, phase drift and recording rate are provided.

Chapter 4 presents the work performed for the design, the development and the characterisation of an eight channel parallel Magnetic Induction Tomography system operating at 10 MHz for low conductivity industrial applications requiring a high data acquisition rate. The analysis of the theoretical aspects and the practical details for the design and the implementation of the system are given. The results of two experiments conducted to prove the suitability of the system for low conductivity industrial applications are given.

Chapter 5 presents the work performed for the design, the development and the characterisation of a single channel Magnetic Induction Tomography system employing the zero crossing phase measurement subsystem for contactless detection of the cardiac activity and the lung function. Measurements on human volunteers have been performed to prove the operation of the system and the results are presented.

Chapter 6 discusses critically the results of the investigations conducted during this study for the development of the MIT systems and compares them to results published in the literature.

Chapter 7 presents the conclusions from the work performed in the context of this study and points out further work arising from it.

# 2. Review of literature

The aim of this project was to investigate and develop practical and inexpensive high speed Magnetic Induction Tomography (MIT) instrumentation to provide a solution to low conductivity applications requiring high data acquisition rate. A literature review has been conducted and it is presented in this chapter to critically examine the prior knowledge and to identify the research work required relevant to the subject of this thesis.

The literature review begins with the examination of the physical aspects and the principle of operation of the MIT which is presented in section 2.1. A critical examination focusing on the architecture, the characteristics, the components and the subject of noise of the practical MIT system is performed in section 2.2. A critical review on the phase measurements in MIT is contacted in section 2.3. In section 2.4 a critical examination of the phase measurement techniques that have been used in MIT and their implementations either in standalone MIT phase measurement subsystems or in MIT systems is presented.

A review on a potential industrial application that a fast MIT system could be considered and a critical examination on the proposed MIT system is performed in section 2.5. A similar review for two potential biomedical applications and an examination on some of the proposed MIT systems is performed in section 2.6. A summary of the review findings and the identification of the further research work regarding the subject of this thesis is presented in section 2.7.

## 2.1 Physical aspects of Magnetic Induction Tomography

Magnetic Induction Tomography (MIT) is a contact-less imaging technique which offers the possibility to visualize the distribution of the conductivity, the permeability and the permittivity in an inhomogeneous medium [8]. In this section the physical aspects of MIT are examined.

### 2.1.1 Principle of operation

The principle of operation can be expressed in mathematical form starting from first principles. The MIT principle of operation is shown in figure 2.1.

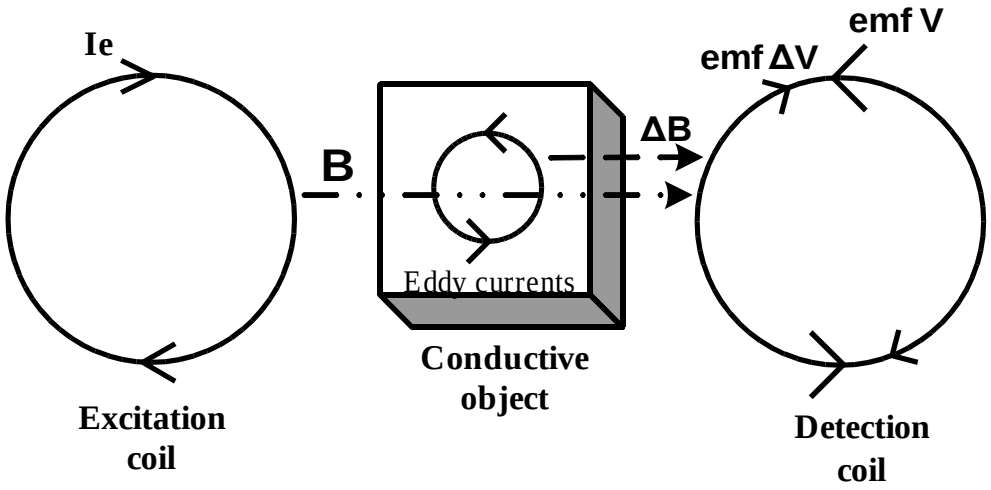


**Figure 2.1**: MIT principle of operation

When an alternating voltage V of angular frequency ω drives a current $I_e$ through an excitation coil an alternating magnetic field **B** is produced. To calculate the magnetic field **B** produced by the excitation coil at a point P the Biot-Savart equation is used (in SI units)

$$\boldsymbol{B} = \frac{\mu_0 I_e}{4\pi} \oint \frac{\boldsymbol{dl} \times r_0}{r^2} \qquad (2.1)$$

where $\mu_0$ is the magnetic permeability of free space, $I_e$ is the current flowing within the coil, dl are the coil elements, r is the distance from a line element to the point P and $r_0$ is the unit vector from the coil element to the point P.

From equation (2.1) it can be seen that the magnitude of **B** is proportional to the current $I_e$, independent of the frequency and depends on the geometry of the excitation coil and the relative displacement from it. Furthermore the Gauss's law of magnetism states that the magnetic field B is a solenoid vector field thus

$$\vec{\nabla} \cdot \vec{\boldsymbol{B}} = 0 \qquad (2.2)$$

where $\nabla\cdot$ is the divergence.

When a conductive object is placed in the primary magnetic field **B** an electric field **E** will be induced in the object described by the Maxwell-Faraday equation

$$\vec{\nabla} \times \vec{\boldsymbol{E}} = -\frac{\partial \vec{\boldsymbol{B}}}{\partial t} \qquad (2.3)$$

where $\nabla\times$ is the curl.

The electric field **E** will in turn generate eddy currents of current density **J** in the object described by the Maxwell-Ampère equation

$$\vec{\nabla} \times \vec{\boldsymbol{H}} = \vec{\boldsymbol{J}} + \frac{\partial \vec{\boldsymbol{D}}}{\partial t} \qquad (2.4)$$

where **H** is the magnetic intensity, **J** is the current density and t denotes time

and the Gauss's flux theorem

$$\vec{\nabla} \cdot \vec{\boldsymbol{D}} = \rho \qquad (2.5)$$

where **D** is the electric displacement field, and ρ is the volume charge density.

From vector calculus it is known that the divergence of the curl of any vector field is equal to 0. Therefore taking the divergence of equation (2.4) results in

$$\nabla \cdot (\nabla \times \boldsymbol{H}) = \nabla \cdot (\boldsymbol{J} + \frac{\partial \boldsymbol{D}}{\partial t}) = 0 \qquad (2.6)$$

The field quantities in a linear isotropic medium can be described with the following supplementary equations

$$\boldsymbol{D} = \varepsilon \boldsymbol{E} \qquad (2.7)$$

$$\boldsymbol{B} = \mu \boldsymbol{H} \qquad (2.8)$$

$$\boldsymbol{J} = \sigma \boldsymbol{E} \qquad (2.9)$$

where ε is the permittivity, μ is the permeability and σ is the electrical conductivity.

Substituting equations (2.7) and (2.9) into equation (2.6) gives

$$\nabla \cdot (\sigma \mathrm{E} + \frac{\partial \varepsilon \mathrm{E}}{\partial t}) = 0 \qquad (2.10)$$

Considering that MIT is using sinusoidal excitation signals the governing equations can be expressed in time harmonic form. Thus replacing the time derivatives by jω (the time harmonic dependence) in equation (2.10) gives

$$\nabla \cdot (\sigma + j\omega\varepsilon)\boldsymbol{E} = 0 \quad \text{or} \quad \nabla \cdot \boldsymbol{J}_e = 0 \qquad (2.11)$$

where $\mathbf{J_e}$ is the induced eddy current.

The induced eddy current $\mathbf{J_e}$ is composed from the conduction current $\mathbf{J_c}$ and the displacement current $\mathbf{J_d}$ such as

$$\boldsymbol{J}_e = (\sigma + j\omega\varepsilon)\boldsymbol{E} = \boldsymbol{J}_c + \boldsymbol{J}_d \qquad (2.12)$$

The permittivity ε is given by

$$\varepsilon = \varepsilon_r \varepsilon_0 \qquad (2.13)$$

where $\varepsilon_r$ is the relative permittivity and $\varepsilon_0$ is the permittivity of the vacuum.

Thus equation (2.12) can be written as

$$\boldsymbol{J_e} = (\sigma + j\omega\varepsilon_r\varepsilon_0)\boldsymbol{E} = \boldsymbol{J_c} + \boldsymbol{J_d} \qquad (2.14)$$

The conduction current $\mathbf{J_c}$ is given by

$$\boldsymbol{J_c} = \sigma \boldsymbol{E} \qquad (2.15)$$

and the induced displacement current $\mathbf{J_d}$ is given by

$$\boldsymbol{J_d} = j\omega\varepsilon_r\varepsilon_0\boldsymbol{E} = \frac{\partial \varepsilon_r \varepsilon_0 \boldsymbol{E}}{\partial t} \qquad (2.16)$$

Equations (2.3) to (2.9) show that the induced electric field **E** and hence the induced eddy current $\mathbf{J_e}$ will be in-quadrature to the primary field **B** (since d**B**/dt) and proportional to the frequency ω. Furthermore equation (2.14) shows that the induced eddy current $\mathbf{J_e}$ is composed from two components which are the conduction current $\mathbf{J_c}$ and the displacement current $\mathbf{J_d}$.

Equation (2.15) shows that the conduction current $\mathbf{J_c}$ is in-phase to the induced **E** field with a magnitude that is proportional to the conductivity of the object. Equation (2.16) shows that the displacement current $\mathbf{J_d}$ is in-quadrature to the induced **E** field with a magnitude that is proportional to the permittivity and the frequency ω of the applied magnetic field.

The induced current $\mathbf{J_e}$ will produce a secondary magnetic field **ΔB** with a magnitude proportional to $\mathbf{J_e}$ and dependent of the frequency ω. The secondary magnetic field **ΔB** is considered to have two components – one due to $\mathbf{J_c}$ and one due to $\mathbf{J_d}$. Thus the induced eddy currents will have a real component and an imaginary component depending on the objects' electrical properties of permittivity ε and conductivity σ respectively. This indicates that MIT is suitable for detecting the passive electrical properties of a conductive object.

### 2.1.2 The composition of the detected signal and its measurement

The primary magnetic field B produces the primary signal **V** which induces the eddy currents in the object which in turn create the smaller secondary magnetic field **ΔB** that produces the secondary signal **ΔV**. The magnitudes of **V** and **ΔV** are both given by

equation (2.3). The signal **V** and the secondary signal **ΔV** compose the signal **V+ΔV** which is detected by the detection coil and which lags the primary signal **V** by an angle φ. The composition of the detected signal can be graphically illustrated using the phasor diagram in figure 2.2.

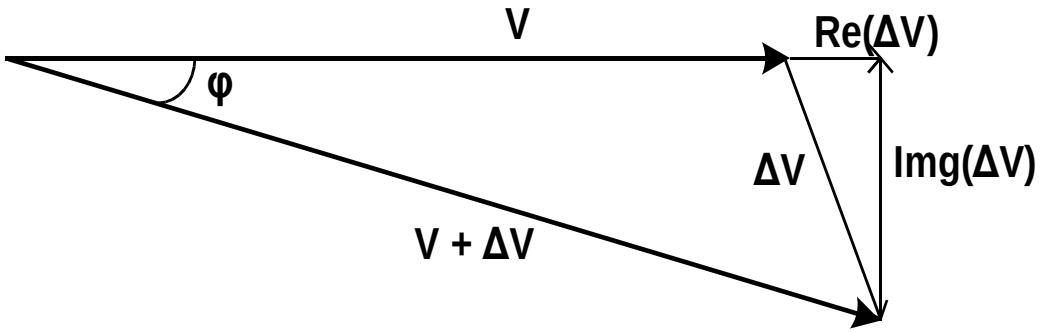


**Figure 2.2**: The phasor diagram of the received signal (not to scale) (from [7])

The displacement current $\mathbf{J_d}$ produces the real part **Re(ΔV)** which is the in-phase component and represents the permittivity of the object. The conduction current $\mathbf{J_c}$ produces the imaginary part **Img(ΔV)** which is the quadrature component and represents the conductivity of the object.

When a two port system with ports A and B is fed by a current I a general expression for the secondary signal ΔV is given by [25]

$$\Delta V = \frac{1}{I}[\Delta_\kappa \int_\Omega (\nabla \Phi + j\omega A_\Phi)\cdot(\nabla \Psi + j\omega A_\Psi)\, d\Omega + j\omega \Delta_\mu \int_\Omega H_\varphi \cdot H_\psi \, d\Omega] \qquad (2.17)$$

where $\Phi$ and $A_\Phi$ are the electrical scalar potential and magnetic vector potential when feeding the system from port A, $\Psi$ and $A_\Psi$ are the electrical scalar potential and magnetic vector potential when feeding the system from port B and $H_\Phi$ and $H_\Psi$ are the corresponding magnetic field intensity vectors.

The general solution of equation (2.17) requires complicated numerical methods however for simple geometries a simplified closed solution to calculate **B** and **ΔB** using the quasi-static approximation was proposed in [12]. In this approach a dielectric circular disc (radius R and thickness t) is placed halfway between two coils (one being the excitation coil and the other the detection coil). The model is shown in figure 2.3.

Without the disk present the magnetic field at the detection coil is denoted by **B** which produces the primary signal **V** however when the disc is placed between the coils it causes a perturbation **ΔB** which produces the secondary signal **ΔV**.

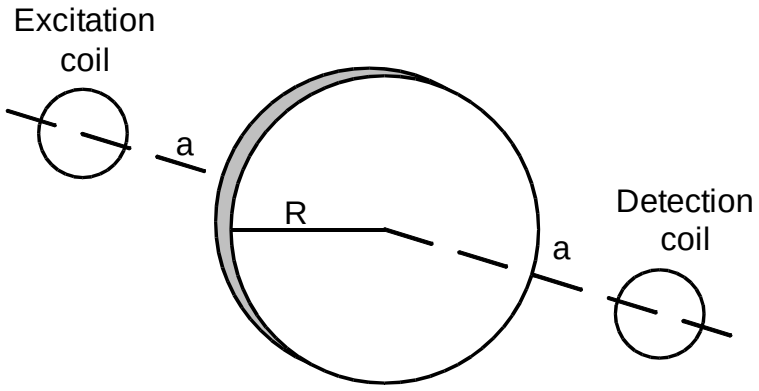


**Figure 2.3**: The model used in [12] to propose the quasi-static approximation

Using the quasi-static approximation (which is also known as signal to noise carrier ratio or SCR) the ratio of ΔB/B and subsequently ΔV/V is given by

$$\frac{\Delta V}{V}=\frac{\Delta \boldsymbol{B}}{\boldsymbol{B}}=P\left(\omega^2\mu_0\varepsilon_0\varepsilon_r-j\omega\sigma\mu_0\right)+Q\left(\mu_r-1\right) \qquad (2.18)$$

where P and Q are geometrical constants that refer to the disk and the coils and $\mu_0$ is the permeability of free space.

The approximation of this approach is that **B** is considered to be the applied magnetic field without any contributions from the induced currents in order to solve equation (2.3) and **ΔB** is computed from the solution. [11]

Three distinct characteristics of the detected signal can be seen from equation (2.18).

1. The conduction current $\mathbf{J_c}$ produce a signal component ($j\omega\sigma\mu_0$) proportional to the conductivity and the frequency which lags the primary signal by 90°.
2. The displacement current $\mathbf{J_d}$ produce a signal component ($\omega^2\mu_0\varepsilon_0\varepsilon_r$) proportional to the permittivity and to the square of the frequency and is in-phase with the primary signal.
3. A non-unity relative permeability results in a signal component ($\mu_r$-1) which is not frequency dependant and is in-phase with the primary signal.

In [8] the equivalent circuit of figure 2.4 was used to examine the relationship between the circuits interacting in a magnetic induction coil array. Three inductive circuit elements were considered to primarily interact which were the excitation coil $L_e$ connected to a voltage source, the detection coil $L_d$ and a conducting object $L_o$ placed between them.

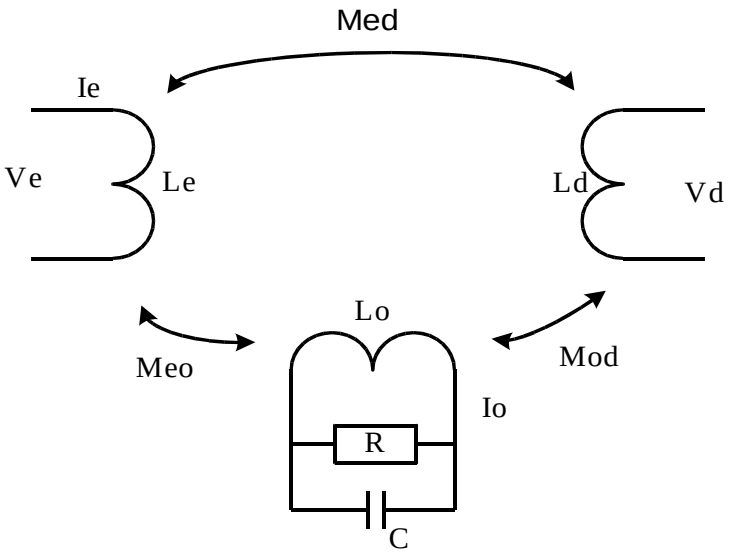


**Figure 2.4**: The equivalent circuit input of a magnetic induction coil array (from [8])

The model of the object was a transformer winding with a parallel resistance $R >> \omega L_o$ and a parallel capacitance $C \leq 1/\omega R$ (the displacement current in the object is equal or less than the conduction current). By using Kirchhoff's laws and neglecting the terms higher than first order the authors stated that the relation between the excitation current $I_e$ and the detection voltage $V_d$ is given by [8]

$$V_d = [\omega M_{eo} M_{od} (\frac{1}{R} + j\omega C) + jM_{ed}] \omega I_e \qquad (2.19)$$

and the relation between the excitation voltage $V_e$ and the detection voltage $V_d$ is given by

$$V_d = [M_{eo} - j\omega M_{eo} M_{od} (1 - \frac{M_{ed} M_{eo}}{M_{do} L_e})(\frac{1}{R} + j\omega C)] \frac{V_e}{L_e} \qquad (2.20)$$

where $\omega$ is the excitation frequency, $I_e$ is the excitation current, $M_{eo}$ is the mutual coupling between the excitation coil and the object, $M_{od}$ is the mutual coupling between the object and the detection coil, $M_{ed}$ is the mutual coupling between the excitation coil and the detection coil.

From equations (2.19) and (2.20) it was stated in [8] that:

1. The amplitude of the detected signal is independent of the conductivity but depends on the permittivity of the object and thus the measurement of the phase difference which can be done readily and to a high degree of accuracy is preferable over the measurement of the signal amplitudes which is effort consuming and involve inaccurate voltage-code conversions.
2. It was advisable to observe the phase difference of the detected signal relative to the current of the excitation coil and not the voltage as this would provide a more

accurate measurement.

Returning to figure 2.2 in page 12 it is observed that the perturbed voltage **ΔV** is given by

$$\Delta V = Re(\Delta V) + j\, Img(\Delta V) \qquad (2.21)$$

and the phase angle φ is given by

$$\varphi = \tan^{-1}\left(\frac{Img(\Delta V)}{V + Re(\Delta V)}\right) \qquad (2.22)$$

Dividing by the primary signal **V** gives

$$\varphi = \tan^{-1}\left(\frac{Img\left(\frac{\Delta V}{V}\right)}{1 + Re\left(\frac{\Delta V}{V}\right)}\right) \qquad (2.23)$$

Assuming that the real part **Re(ΔV)** is much smaller than V and hence that **Re(ΔV/V)** is much smaller than 1 then the angle φ is very small and it is given by

$$\varphi \approx Img\left(\frac{\Delta V}{V}\right) \qquad (2.24)$$

Equation (2.24) emphasizes what was stated in [8] and [11]. To determine the conductivity of the object a phase sensitive measurement can be used to measure the angle φ between the primary signal **V** and the total detected signal **V+ΔV**. This measurement of the phase angle is only an approximation and it becomes more accurate as the permittivity of the object becomes smaller as it is the case in tissues. However it remains that to measure the permittivity of the object the measurement of the signals amplitudes is required.

### 2.1.3 Skin depth and frequency dependence

In section 2.1.1 it was shown that MIT is suitable for detecting the passive electrical properties of a conductive object. In section 2.1.2 it was shown that the quasi-static approximation can be used to calculate the primary signal V and the secondary signal ΔV and thus to measure the passive electrical properties of a conductive object. However from the quasi-static approximation it is deducted that to have access to the complete reconstruction information of the passive electrical properties the skin depth of the electromagnetic field should be greater than the thickness of the object.

The skin depth can be defined as the depth below the surface of a conducting object at which the current density has fallen to 1/e of its value at the surface (approximately 0.37 of its value at the surface). A good approximation of the skin depth in normal cases is given

by [26]

$$\delta = \sqrt{\frac{2}{\omega \mu_0 \mu_r \sigma}} \qquad (2.25)$$

where $\mu_r$ is the ratio of the permeability of the object to the permeability of free space and $\sigma$ is the bulk conductivity (reciprocal to bulk resistivity).

Equation (2.25) shows that the skin depth is inversely related to the excitation frequency and the conductivity of the object which indicates that there is a limitation on the excitation frequency that can be used in MIT systems. This frequency limitation is due to the attenuation of the electromagnetic field, the geometry of the system and the geometry and substance of the object. [11]

Frequency not only imposes a limitation to the MIT system and the use of the quasi-static approximation but also influences heavily the total detected signal $\mathbf{V+\Delta V}$ which carries the conductivity distribution. Equation (2.14) states that for a sinusoidal excitation the magnitude of the induced currents $\mathbf{J_e}$ is proportional to the frequency $\omega$. Thus the secondary magnetic field $\mathbf{\Delta B}$ produced by the eddy currents is proportional to $\omega$ and therefore the detected signal $\mathbf{V+\Delta V}$ due to the eddy currents is proportional to $\omega^2$.

It becomes obvious that as the frequency of the primary signal $\mathbf{V}$ is reduced the amplitude of $\mathbf{\Delta V}$ decreases also resulting into an increased difficulty in measuring accurately the $\mathbf{\Delta V}$. This frequency dependency complicates the design of MIT systems because they have to operate in a restricted frequency range which will will depend on the object.

For low conductivity materials such as biological tissues the secondary field $\Delta B$ will be significantly smaller in magnitude than B and conductivity will dominate hence

$$\varphi \approx \frac{\boldsymbol{\Delta B}}{\boldsymbol{B}} \propto \omega \sigma \qquad (2.26)$$

This shows that MIT systems will have to operate at frequencies of the order of MHz to compensate for the low values of conductivity and thus of $\mathbf{\Delta V}$. This complication however can be partially overcome if the MIT systems are constructed aiming at specific applications rather than covering a general spectrum of applications.

For materials which have high conductivity and almost negligible permittivity such as metals the MIT systems operating frequency can be of the order of few kHz as the high values of conductivity will cause a large value of $\mathbf{\Delta V}$. In [27] it was stated that for a

biological tissue the detected signal at 10 MHz is 1% of the excitation signal.

## 2.2 The MIT system

This section provides a review on the architecture, the characteristics, the components and the subject of noise of a MIT system.

### 2.2.1 Architecture and characteristics

The first attempt to address the MIT system from the point of architecture was given in [28] it was stated that an MIT system consists of three main sub-systems defined as the sensor array (coil array), the conditioning electronics and the host computer. In [19] it was suggested that an MIT system consists of only one component which is the coil array (coil array).

In [11] four sub-systems were mentioned which were identified as the coil array, the signal conditioning electronics, the phase measurement system and the processing unit. This architecture description was repeated in [29]. The block diagrams of the architectures described in [11] and [28] is given in figure 2.5.

In [30] the Cardiff Mk2a MIT system was used as basis and an architecture was proposed comprising nine components which were the signal source, the source distribution network, the sensor and chassis, the signal and reference distribution circuit, the signal measurement, the measurement control routine, the multicore PC and GPU workstation, the digital signal processing and the forward mode and reconstruction software.

An examination on the characteristics of a multichannel MIT system was performed in [19]. It was stated that generally a multichannel MIT system is characterised by the spatial resolution of the tomographic image produced, the measurement precision and the noise. It was further stated that the spatial resolution depends on the image processing technique used and the ratio of the coil arrays' excitation and detection coils. It was further stated that the measurement precision relies heavily on the coil array and the phase detection technique used.

### 2.2.2 Architectural components

In [11] and [29] four components of the MIT system were identified. These are the coil array, the signal conditioning electronics, the measurement system and the processing unit. The latter deals with the image reconstruction process and will not be examined further as

this thesis focuses only on the measurement hardware components of the MIT system.

The MIT coil array can be defined as the device that generates the alternate primary magnetic field and detects the secondary magnetic field generated by the object with the use of coil configurations without any physical contact with the object. It can be classified as a single channel coil array comprising an excitation coil and a detection coil or as a multichannel coil array comprising many excitation and detection coils.

The coil array can be further classified in one of the three geometrical types according to its coil arrangement which are the annular coil array [31, 32], the planar array coil array [33, 34] and the application specific coil array [35]. The latter is a coil array that is specifically designed for use at a certain region of interest such as the human head in biomedical imaging. In figure 2.5 the annular coil array and the application specific coil array are shown.

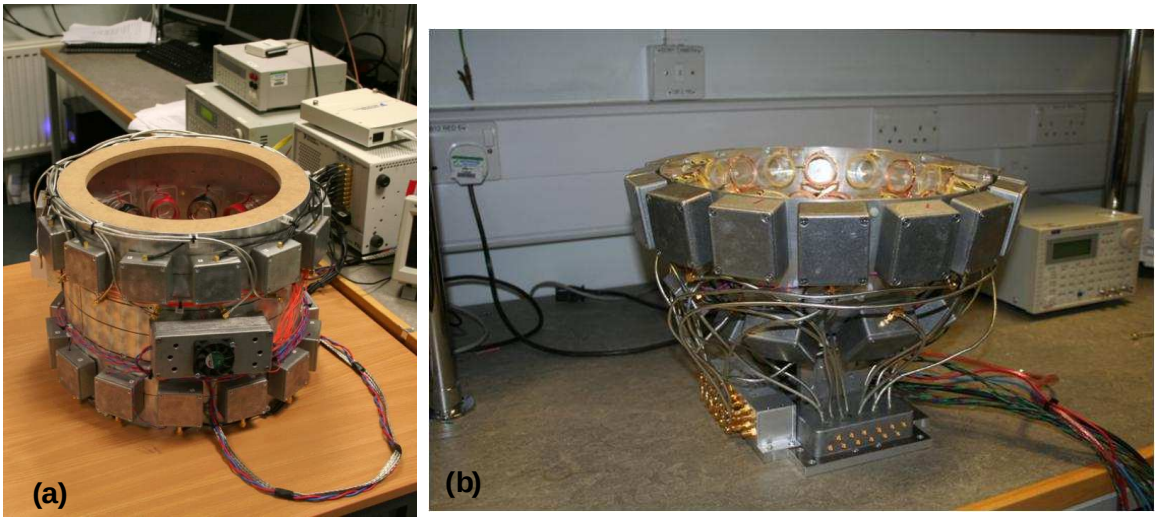


**Figure 2.5**: Types of MIT coil arrays - (a) an annular coil array and (b) an application specific coil array

The MIT coil arrays share some common characteristics which are the outer shield, the coils and the signal generation electronics. However it is noted here that coil array implementations that did not use the outer shield have appeared in the literature although this is scarce.

The outer shield is used to confine the magnetic field in the boundaries of the coil array, to prevent interference from external conductive or magnetic objects, to improve the susceptibility to interference from electrical devices and as a ground plane for the electric fields generated by the coils. [36]

The effect of the outer conductive shield on the performance of the annular array was examined in [36]. It was concluded that the only effect the shield had on the coil array was

an alteration of the dynamic range of the signal between the excitation and the detection coils. It was further determined that the dynamic range was increasing as the shields' diameter was decreased and its height was increased. The study did not examine the other two geometric types of MIT coil arrays.

The MIT coil array uses the excitation coils to produce the alternate magnetic field and the detection coils to detect its perturbation. For the acquisition of tomographic images the coils are combined as a matrix m x n where m is the number of the excitation coils and n is the number of the detection coils [11]. A complete set of measurement process all the channel combinations of the m x n multiplication.

The number of the excitation and detection coils used therefore has a direct impact on the speed of a practical MIT system. Furthermore the number of the excitation and the detection coils used directly affects the spatial resolution of the coil array [11, 19]. A demand for high spatial resolution requires the use of more excitation and detection coils which in turn results into an increased measurement time.

The alternate magnetic field is generated with the use of an excitation signal chain which comprise a frequency source for generating the sinusoidal signal at the frequency required and an RF power amplifier to amplify the signal to the required amplitude for the coils excitation. As pointed out in section 2.1 the frequency is selected depending on the physical substance of the object under study.

The signal conditioning electronics process the sinusoidal signals produced by the primary and the secondary magnetic fields. They are connected to the detection coils of the coil array through pre-amplifiers and directly to the reference coils situated near the excitation coils.

The signal conditioning electronics may process the detected signals by multiplexing them or by processing them in parallel. The multiplexing uses a multiplexer to select the detected channel to process. The parallel processing measures all the detected signals concurrently thus decreasing the processing time and hence increasing the speed of the system. Both processing ways have been used in the MIT field. [11, 13, 31, 32, 37]

The purpose of the phase measurement subsystem is to measure the phase difference between the excitation signals and the detected signals. To do that it applies a phase measurement technique. The requirements for a phase measurement technique are to

provide continuous phase measurements and depending on the application satisfactory millidegree precision, millidegree resolution, millidegree accuracy and a high measurements rate.

The phase measurement subsystem connects to a coil array through the signal conditioning electronics and can be classified into a single channel or a multichannel subsystem. The single channel measures the phase difference between the excitation signal and one detection signal at the same time as does a multiplexed multichannel subsystem. In contrast to that the parallel multichannel subsystem measures the phase difference of all detection signals against the excitation signal at the same time thus decreasing the measurement time.

### 2.2.3 Noise and the MIT system

In electronics the noise can be defined as a random fluctuation in an electrical signal [39]. The noise sources in a circuit can be divided into device noise and interference. The device noise[1] include the thermal noise, the shot noise and the flicker noise and the interference the substrate and supply noise [38]. At lower frequencies the main component of the noise is the flicker noise and as the frequency increases the thermal noise and the shot noise are becoming the main constituents of noise. The general representation of noise against frequency is given in figure 2.6.

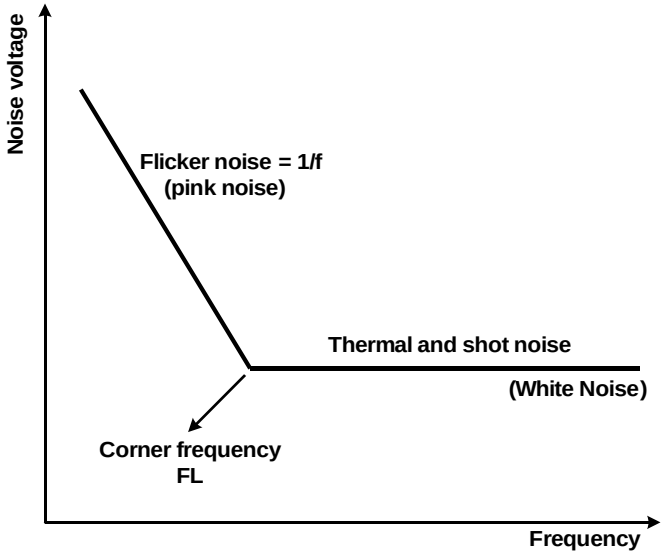


**Figure 2.6**: General representation of noise

The flicker noise (1/f or pink noise) occurs almost in all electronic devices in low frequencies, it is device specific and decreases as frequency increases. The flicker noise is

[1] There are also the burst noise and the avalanche noise but they are not addressed here as they are not main contributors to noise

characterised by the corner frequency $f_{CL}$ between the region dominated by the low-frequency flicker noise and the higher frequency white noise (thermal and shot noise).

The thermal noise is generated by the random thermal motion of electrons inside an electrical conductor and depends on the temperature of the electronic conductor. The thermal noise is given by [39]

$$V_n = \sqrt{4k_B TR\Delta f} \qquad (2.27)$$

where $k_B$ is the Boltzmann's constant, T is the conductor's absolute temperature in Kelvin, $\Delta f$ is the bandwidth in which the noise is observed and R is the resistance of the electric conductor.

The shot noise is generated by current flowing across a PN junction and is a function of the bias current and the electron charge. It is given by [39]

$$I_n = \sqrt{2qI_{DC}\Delta f} \qquad (2.28)$$

where q is the electron charge and $I_{DC}$ is the bias current.

The total input noise $V_{ip}$ is given by

$$V_{ip} = \sqrt{V_{ns}^2 + V_n^2 + I_n^2 R_s^2} \qquad (2.29)$$

where $R_s$ is the source resistance.

The noise bandwidth is a Gaussian representation of an ideal power/frequency bandpass which has the same height as the maximum value of the actual signal-to-power/frequency response of the actual system and which passes the same noise power. [39]

The total noise of a device or a system is described by the noise factor F given by

$$F = \frac{SNR_{ip}}{SNR_{op}} \approx \frac{V_{ip}^2}{V_{ns}^2} \qquad (2.30)$$

where $SNR_{ip}$ and $SNR_{op}$ are the signal to noise ratios of the input and the output signals.

From equations (2.27), (2.29) and (2.30) it results that the noise factor F is given by

$$F = 1 + \frac{V_n^2 + I_n^2 R_s^2}{4kTR_s} \qquad (2.31)$$

The noise figure NF is a way to describe the noise factor in dB and it is given by

$$NF = 10\log\frac{SNR_{ip}}{SNR_{op}} = 10\log(F) \qquad (2.32)$$

The signal to noise ratios are given by

$$SNR_{ip} = \frac{Received\ signal\ power}{Received\ noise\ power} = \frac{V_{sig}^2}{V_{ns}^2} \tag{2.33}$$

$$SNR_{op} = \frac{Output\ signal\ power}{Output\ noise\ power} = \frac{V_{sig}^2}{V_{ip}^2} \tag{2.34}$$

The noise figure NF is also given by [40]

$$NF = 1 + \frac{T_e}{T_0} \tag{2.35}$$

where $T_e$ is the effective noise temperature of the device and $T_0$ is equal to 290 K.

The noise factor of a signal chain of cascaded devices or subsystems is described by the Friis formula [40]

$$F = F_{s1} + \frac{F_{s2} - 1}{G_1} + \frac{F_{s3} - 1}{G_1 G_2} + \cdots \tag{2.36}$$

where $F_{s1}$, $F_{s2}$ and $F_{s3}$ are the noise figures of the first, second and third stage respectively and $G_1$ and $G_2$ are the gain of the first and the second stage.

The Friis formula shows that in a signal chain of cascaded devices or subsystems the main contributor to the noise figure of the system is the first device or subsystem. This is particularly important in a signal processing chain such as those employed in an MIT system.

Excessive noise in an MIT system will definitely mask the signal or at least part of it and this may result into erroneous phase measurements and thus erroneous imaging. The noise is a significant factor for designing MIT systems especially for the systems aimed for biomedical applications where very small phase changes must be detected in the presence of a much higher signal [12].

In [19] it was stated that the noise of a practical MIT system depends on the hardware components used and more specifically on the construction of the coil array, the signal conditioning electronics[2] and the phase measurement subsystem. These three components form the signal processing chain of an MIT system.

As was mentioned in section 2.2.2 the coil array comprises the outer shield, the coils

[2] In [19] the phase measurement subsystem was included in the term signal conditioning electronics

(excitation and detection) and the signal generation electronics. The generation of the excitation signal in reported MIT systems was achieved with the use of signal generators [29], digital generation using multifunction boards [41] and Direct Digital Synthesis (DDS) sources [11, 30, 42].

The presence of noise in a signal generator undermines its frequency stability and it introduces phase noise to the generated signal. To minimize the introduction of noise in the MIT signal chain it is required therefore to use low noise signal generation devices in MIT. The development of a precise phase source based on the DDS for use in MIT was the subject of investigation by the author of this thesis and was presented in [43] and [44].

The coil array connects to the signal conditioning electronics through a preamplifier. According to the Friis formula (2.36) the main contributor to the noise figure of a signal processing chain is the first device. The preamplifier is the first device in the MIT signal processing chain followed by the signal conditioning electronics and the phase measurement subsystem. Hence it is expected that it will contribute heavily to the noise figure of the phase measurement signal chain and special consideration is required in the implementation of the preamplifier.

In [24] it was stated that for an MIT system intended for monitoring the cardiac and the lung activity a preamplifier input noise of 20 nV/√Hz can be considered as a good trade-off between circuit complexity and low-noise design. The use of low noise components in general and of a low noise preamplifier in particular is also supported in [11].

The construction of a novel low noise preamplifier was reported in [11] and [30]. The design of the low noise preamplifier was based on the active compensation concept in which the resistor in the feedback loop of the amplifier is replaced by an amplifier (active component) [45]. The preamplifier provided below 3 nV/√Hz input voltage noise, 4 kΩ input impedance at 10 MHz, a 20 GHz equivalent gain bandwidth product and 20X fixed gain [11]. It was used in the Cardiff Mk2a [11] and the Cardiff Mk2b [30] MIT systems.

The above however does not mean that the only consideration for low noise design of an MIT system is or should be the preamplifier. It merely points out the significance of using a low noise preamplifier in front of the phase measurement signal chain. It is obvious that the overall noise figure of the MIT system should be kept as low as possible to minimize the contamination of the phase measurements by noise. A closer look on the phase measurements in the context of MIT is taken in the following section.

## 2.3 Phase measurements in MIT

In section 2.1.2 was mentioned that the conductivity of the object can be determined by measuring the phase angle φ between the excitation signal **V** and the total detected signal **V+ΔV**. In MIT a sinusoidal signal is used for the source for the excitation signal **V** and the total signal **V+ΔV** is detected in the form of a sinusoidal signal. This focus the interest on phase angle measurements of sinusoidal signals.

### 2.3.1 Characteristics of the sinusoidal signal

The standard form of the ideal sinusoidal wave as a function of time is given by [46]

$$y(t) = A \cdot \sin(\omega t + \varphi) \qquad (2.37)$$

where y(t) is the instantaneous amplitude of the sinusoid, A is the amplitude, ω is the angular frequency given by 2πf and φ is the initial or relative phase confined to the interval $-\pi \leq \varphi \leq \pi$.

The phase is measured from a zero crossing and this can be shown by plotting the phase angle as the radius vector that rotates at a constant angular rate determined by the frequency [47]. The sinewave characteristics are shown in figure 2.7.

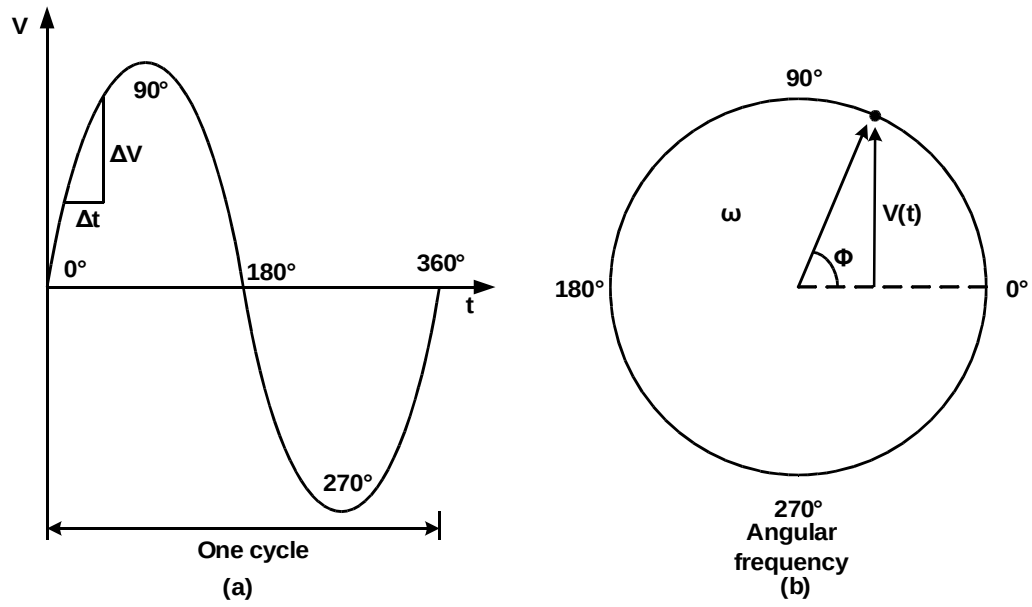


**Figure 2.7**: Sine wave characteristics: (a) voltage V changes with time t and (b) amplitude changes with phase angle φ (from [47])

The relationship of the phase φ with the frequency f and the time interval t is given in radians by [47]

$$\varphi = \omega t \quad \text{or} \quad \varphi = 2\pi f t \qquad (2.38)$$

However in the physical world a periodical sinusoidal signal is not ideal as was described

before but it is perturbed by noise which causes the ΔV and Δt to occur in other frequencies. Hence frequency variations occur in a given instant in the cycle. Thus the standard form of the ideal sinusoidal signal becomes [47]

$$y(t)=(V+A(t))\sin(2\pi f t+\varphi(t)) \qquad (2.39)$$

where V is the nominal amplitude and A(t) and φ(t) are the instantaneous amplitude and phase fluctuations.

The amplitude and phase fluctuations are caused by the frequency variations discussed earlier and they can be termed as amplitude noise and phase noise respectively. For a noisy signal the relationship of the phase with the frequency f and the time interval is given in radians by [47]

$$\varphi(t)=2\pi f t+\varphi_n(t) \qquad (2.40)$$

where $\varphi_n(t)$ is the instantaneous phase fluctuation.

Equation (2.39) can also be expressed as follows [47]

$$y(t)=(V+\delta A(t))\sin(2\pi f t+\delta\varphi(t)+c) \qquad (2.41)$$

where c is a constant, δ is the fluctuations operator and δA(t) and δφ(t) are the fluctuations of amplitude and phase.

Hence the frequency fluctuation δf in respect to phase fluctuation δφ is given in hertz by [47]

$$\delta f=\frac{d\omega}{2\pi}=\frac{1}{2\pi}\frac{d(\delta\varphi)}{dt} \qquad (2.42)$$

and the phase fluctuation δφ is related to the time interval fluctuation δt in radians by [47]

$$\delta\varphi=(2\pi f)\delta t \qquad (2.43)$$

A way to determine the phase of a periodical sinusoidal signal is to measure the phase difference between that signal and a known reference sinusoidal signal as shown in figure 2.8. The phase difference is defined as the difference expressed in electrical degrees or time between two sinusoidal signals having the same frequency and referenced to the same point in time [48].

It becomes obvious that a prerequisite to perform a phase measurement is for both sinusoidal signals to have the same frequency. Any frequency difference or fluctuation between them will introduce errors in the measurement.

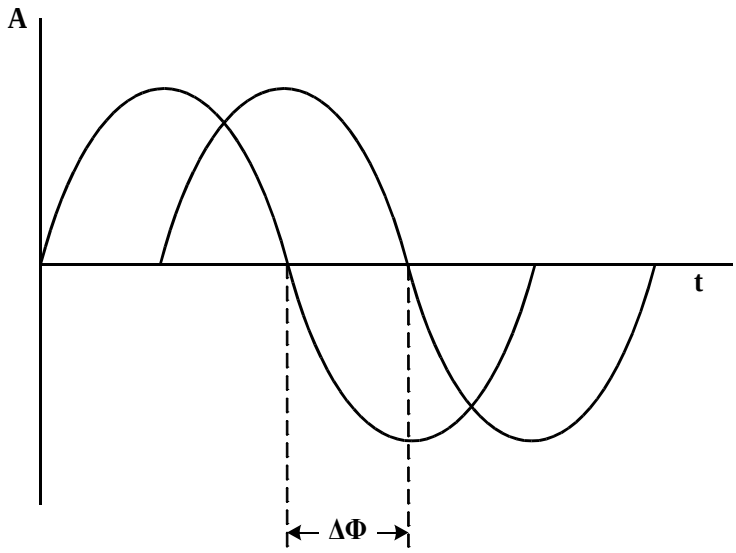


**Figure 2.8**: The phase difference between two sinusoidal signals

### 2.3.2 The phase precision and the phase drift

In [11] the phase precision (or phase noise as was called in [11]) was defined as the short termed standard deviation of a number of phase measurements and it was stated that it can be calculated in radians by

$$\varphi = \tan^{-1}\left(Img\left(\frac{\Delta V}{V}\right)\right)\times\frac{180}{\pi} \qquad (2.44)$$

where **ΔV** is the perturbed signal and **V** is the primary signal.

In [30] the definition above for the phase precision (or phase noise as was called in [30]) was adopted and its calculation was given as

$$Phase\ precision = \sqrt{\left(\frac{1}{n-1}\right)\sum_{i=1}^{n}\left(\varphi_i - \bar{\varphi}\right)^2} \qquad (2.45)$$

where φ is the result of the phase measurement and n is the number of phase measurement used.

The phase precision equation proposed in [30] is actually the general equation for calculating the standard deviation of a population of measurements modified to suit the MIT phase measurements. The phase precision is graphically illustrated against the input amplitude of the detected signal because the phase measurement is affected by the amplitude.

The phase precision is an extremely important figure in the characterization of an MIT system. It denotes the phase measurement precision the MIT system can accomplish and

also the system's capability for the detection of small phase changes. Especially for biomedical applications the phase precision would be required to be in the order of 10 millidegrees or less [13]. Through the years the MIT system research has lead into the development of systems with phase precision of 1 millidegree and below for biomedical applications [37].

Another important factor for an MIT system is the capability to reproduce the phase measurement result for an object of the same conductivity during a long period of operational time or during temperature changes. The term phase drift has been used to point this capability of an MIT system. The phase drift is graphically illustrated against time.

The capability of reproducing the result of the same phase measurement after the MIT system has been in operation for a long period of time assures that the user will not be misinformed. Especially for MIT systems intended for long term monitoring in biomedical applications a low phase drift figure is a necessity since clinical decisions made by physicians in the clinical setting are based on data provided by the biomedical instruments.

In [11] it was stated that the phase drift is the variation of phase over a period of time or temperature and that it encompassed the total noise introduced by phase noise, phase jitter and phase shift caused by the temperature change over a long period of time (>1 hour). It was further stated that the phase drift of an MIT system or subsystem can be calculated by obtaining the maximum and the minimum values over a period of time.

In [30] it was stated that the phase drift is a phase variation caused by the thermal drift of the components and the biological sample. Furthermore it was stated that the phase drift will have a somewhat less effect on the precision of MIT phase measurements but it will greatly affect the measurement accuracy under the assumption that the phase drift within the length of signals acquisition is small. Hence it was proposed that the phase drift can be calculated in degrees per seconds by

$$Phase\ drift = \frac{\theta_{max} - \theta_{min}}{t_{total}} \qquad (2.46)$$

where $t_{total}$ is the period of the measurement range in seconds and $\theta_{max}$ and $\theta_{min}$ are the maximum and the minimum phase measured within the measurement period.

The phase precision and the phase drift are used to characterise MIT systems and phase measurement subsystems. Both are derived from the phase measurements performed by an

MIT system or an MIT phase subsystem. In the following section the phase measurement techniques used in MIT and their implementations will be reviewed.

## 2.4 Phase measurement techniques in MIT and some implementations

This section reviews the phase measurement techniques that have been used in MIT and their implementations either in standalone phase measurement subsystems or in systems (single channel and multichannel). The performance of the implemented MIT systems and phase measurement subsystems is examined in terms of the phase precision, the phase drift, the time constant and the frame rate. The construction and other characteristics of the MIT systems and phase measurement subsystems mentioned in this section are not thoroughly examined.

The term time constant is used in this section to denote the time required by a phase measurement subsystem or an MIT system to acquire a single phase difference value. The term frame rate is used to denote the time required by a multichannel MIT system to perform a complete set of measurement and output a result of all channel combinations (m x n multiplication). [11]

### 2.4.1 The zero crossing technique

The zero crossing technique is based on the realisation that the phase difference between two periodical sinusoidal waves is proportional to the time interval between their zero crossing points as shown in figure 2.12. If the time interval $t_0$ is measured then the phase difference $\Delta\varphi$ between the two signals can be calculated in radians by

$$\Delta \varphi = 2\pi f t_0 \qquad (2.47)$$

where f is the frequency of the sinusoidal signals.

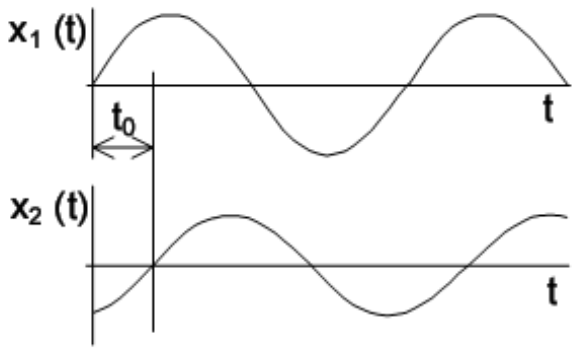


**Figure 2.9**: Time interval between the zero crossing points of two sinusoidal waves

#### 2.4.1.1 Approaches for measuring the zero crossing points

One way to measure the time interval $t_0$ is to convert the periodic sinusoidal signals into square pulses which converts the time interval $t_0$ into a time difference. Hence by measuring the time difference and using equation (2.47) the phase difference can be calculated.

The measurement of the time difference may suffer from measurement uncertainties due to the phase offset and the threshold levels created by frequency changes of the input signals and distortion from harmonic components which may contaminate the calculation of the phase difference. [21, 49-51]

However in [49] it was stated that averaging may compensate the variation in the offsets and the threshold levels if an even number of consecutive pulses is averaged. This was further supported in [21] where it was stated that equation (2.47) holds true if the zero crossing points of one signal always lags the corresponding points of the other and averaging of the rise and fall pulses is used.

In [50] it was proposed to measure the time difference between the pulse centres of the resultant square waves and not the time difference created by the zero crossing points to compensate for the distortion from harmonic components. This approach was further expanded in [51] in which was stated that equation (2.47) cannot always be true due to the harmonic components and a new equation which holds true for all cases was suggested to replace equation (2.47).

The expanded approach of [51] was implemented in [52] with the use of a microprocessor and discrete counters. The authors mentioned that errors in phase could be introduced from the input offset voltage and the offset current of the operational amplifiers and the quantization errors from the counters. They concluded that the phase resolution depended on the clock frequency and the width of the counters. The time constant of the implemented subsystem was not stated.

Another way to measure the phase shift of two periodic sinusoidal signals is to take samples of the signals and use linear interpolation to find the times $t_1$, $t_2$ and $t_3$ of the zero crossing points and then to use equation (2.48) to calculate the phase shift [48]. The technique is shown in figure 2.10.

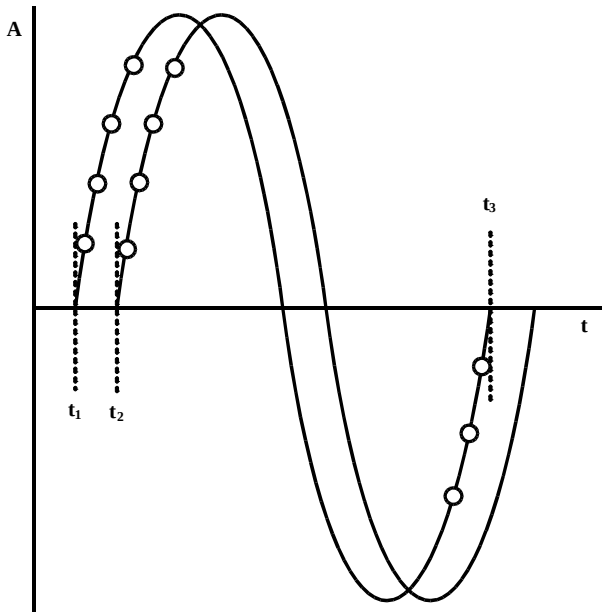


**Figure 2.10**: Linear interpolation to find the zero-crossing points using sampling

$$\Delta\varphi = 2\pi \frac{t_2 - t_1}{t_3 - t_1} \qquad (2.48)$$

The linear interpolation suffers from a number of uncertainties that may introduce errors in the measurement. The sampling rate must be sufficient to detect the timing of the zero crossing points correctly. Furthermore simple linear interpolation gives an approximation between the two points of a given function and the "curvier" a function is the worse the approximation gets.

In [53] adaptive sampling was used which as mentioned it compensates for the errors mentioned above. The periodic sinusoidal signals were sampled and the phase difference $\Delta\varphi$ was calculated using the equations given in the article. An essential condition for the technique to work was that the frequency of the signals had to be known. It was suggested the initial sampling rate of the signals to be equal to 3 samples/cycle. If the phase shift was found to be invalid then the technique "adapted" itself automatically by increasing the sampling rate by 1 sample/cycle until the phase shift was valid or until the sampling rate reached its maximum. An algorithm for implementing the technique was also given.

In [54] a possible microprocessor-based implementation of the adaptive sampling technique described in [53] was proposed but not implemented. Based on the simulation results presented in the article it was claimed that the adaptive sampling technique could be more precise in measuring the phase shift of harmonic distorted sinusoidal signals than the techniques proposed in [49-51] but on the cost of a slower acquisition time. However

figures of the acquisition time required for the phase measurement was not disclosed.

### 2.4.1.2 The Moscow MIT system

In [32] the implementation of a multiplexed multichannel MIT system was reported. The block diagram of the system is shown in figure 2.11.

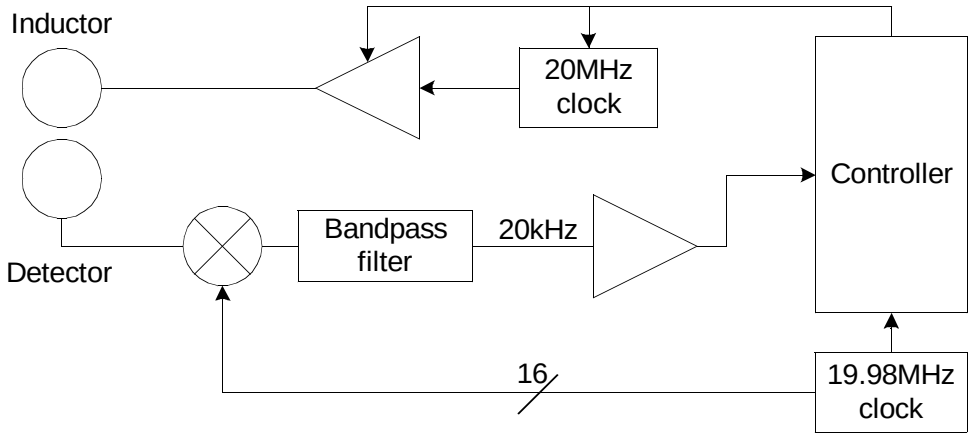


**Figure 2.11**: Block diagram of the zero crossing MIT system implemented in [32]

The MIT system comprised an annular coil array with 16 channels operating at 20 MHz and the phase measurement subsystem. The excitation coils had 5 cm diameter, 2 turns and an inductance of 0.7 H. The amplitude of the excitation current was 60 mA. The detection coils were of the same diameter and had 4 turns. Both coils were placed on the same coil former which was placed on an aluminum outer shield. No screens were placed around the coils.

Each detected signal was fed to a mixer where it was downconverted to 20 kHz using the heterodyne technique and then was amplified and limited to produce the square waves. The reference signal followed the same conditioning procedure as the detected signal. The downconverted square waves were multiplexed and used as input to an Atmel AT90S8515 microcontroller that measured their phase difference.

The time required to complete a set of 240 measurements (16 excitation coils x 15 detection) with averaging over 64 periods was quoted to be about 1 sec (1 frame per second). The system's quoted time constant was 4 ms and the phase precision for the complete system was stated to be 0.005 rad (286 millidegrees).

### 2.4.1.3 Single channel subsystem using an XOR gate for phase detector

In [21] and [55] a single channel implementation of the zero crossing technique in a phase measurement system was proposed. This was further investigated in [13] and [56] and also

presented in [11]. The block diagram of the XOR phase measurement system is shown in figure 2.12.

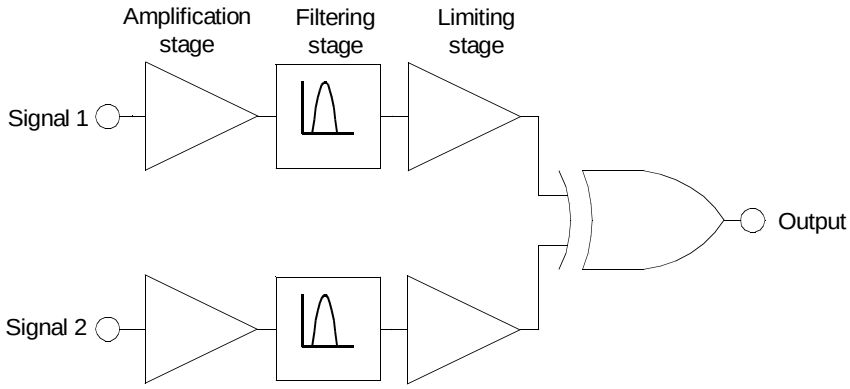


**Figure 2.12**: Block diagram of the single channel zero crossing phase measurement system using an XOR gate as the phase detector proposed in [21]

The frequency of the two test sinusoidal signals used as inputs to the subsystem was 10 MHz. The signals were first downconverted to 10 kHz and then were amplified and limited to produce the square waves which were the inputs to a discrete XOR gate.

The XOR gate output is a logic low ('0') when the inputs have the same logic state and a logic high ('1') when they do not. The XOR output pulse width was equal to the time interval $t_0$ hence by measuring it and using equation (2.47) the phase difference was calculated. The output of the XOR gate was the input to an oscilloscope and a commercial counter which performed the phase measurement.

In [56] it was stated that the subsystem achieved 8 millidegrees phase precision for an input amplitude of -21 dBV (≈250 $mV_{pp}$) and below 22 millidegrees phase precision for an input amplitude of -45 dBV (≈2.8 $mV_{pp}$). The quoted phase drift was 56 millidegrees over 15 minutes. The measurements were taken using a 100 sample average however the time constant was not quoted. In the article it was mentioned that the phase measurement of high frequency biomedical MIT was possible using downconversion if the coils and the pre-amplifiers would not add significant phase noise.

In a later implementation [13] the quoted phase precision was 22 millidegrees at 20 ms time constant when set to achieve a precision of 50 millidegrees or better. The quoted phase drift was 56 millidegrees over 20 minutes.

In [50] it was mentioned that the use of counter for measuring the pulse width makes the clock frequency of the counter an integral part of the phase equation (2.47). The time difference $t_0$ of the zero crossing points is given by

$$t_0 = \frac{M}{f_c} \qquad (2.49)$$

where M is the output of the counter and $f_c$ is the operational clock frequency of the counter.

Substituting equation (2.49) to equation (2.47) gives

$$\Delta\varphi = \frac{2\pi f_s M}{f_c} \qquad (2.50)$$

where $f_s$ is the signal frequency.

Equation (2.50) shows that any sudden and unwanted changes in the clock frequency can affect the phase measurement however this is remedied if the clock frequency is kept constant for the whole set of the phase measurements.

### 2.4.2 Vector-voltmeter technique

The vector-voltmeter technique is an indirect technique for MIT phase measurements. To perform the measurement the signals are first downconverted to a lower frequency and then the phase measurement is performed using a vector-voltmeter based phase detector. The vector-voltmeter technique is employed in lock-in amplifiers. The block diagram of a typical lock-in amplifier is shown in figure 2.13.

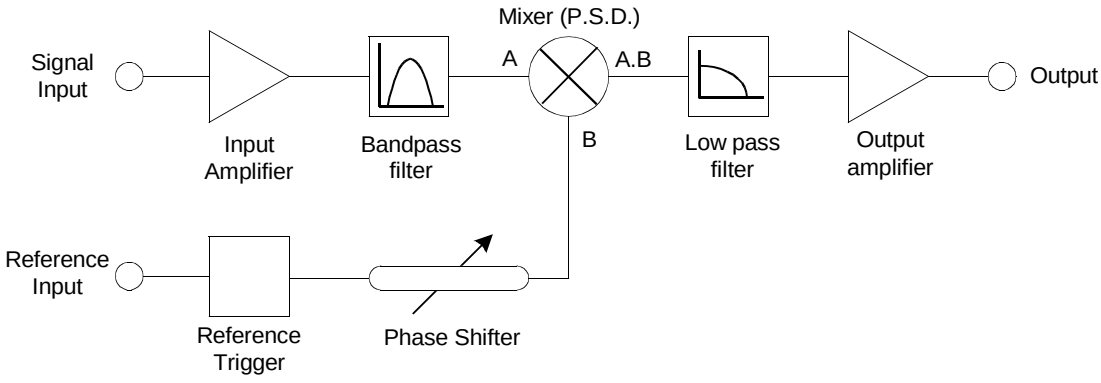


**Figure 2.13**: Block diagram of a typical lock-in amplifier

In the vector-voltmeter technique a phase sensitive detector (PSD) measures the components of the signals at a specific reference frequency and phase [57, 58]. The detector operates by multiplying an input signal of a constant amplitude, frequency and phase with a known reference signal. The outputs of the detector are the constant voltage levels $V_x$ (real part) and $V_y$ (imaginary part). The vector magnitude is dependent on the amplitude of the input signal and is given by

$$Magnitude = \sqrt{(V_x^2 + V_y^2)} \qquad (2.51)$$

and the phase angle between the signals is given by

$$Phase = \arctan \frac{V_y}{V_x} \qquad (2.52)$$

The vector-voltmeter technique has been implemented in MIT with an 'off-the-shelf' lock-in amplifier [13, 29, 31] and self made vector-voltmeter phase detectors [22, 42].

#### 2.4.2.1 The Cardiff Mk1 MIT system

In [13] an MIT multiplexed multichannel system was presented. It comprised a 16 annular coil array and a two channel lock-in amplifier as the phase measurement subsystem. The system operated at 10 MHz. The excitation coils and the detection coils had 4.5 cm diameter and consisted of 2 turns and their self resonance was above 50 MHz. Both coils were placed on the same coil former which was placed on an aluminium outer shield. No screens were placed around the coils. The reference signal from the activated excitation coil and the detection signals were multiplexed and downconverted to 10 kHz prior the phase measurement.

In [13] was mentioned that the Cardiff Mk1 achieved an average phase precision of 27 millidegrees with a maximum phase precision of 88 millidegrees and that it required 135 seconds to acquire 1 frame. Furthermore it was mentioned that the single channel subsystem which used a two channel lock-in amplifier achieved 50 millidegrees phase precision with 166 ms time constant. The subsystem's phase drift was quoted to be 27 millidegrees over 15 minutes.

In a later report [29] by the same authors it was stated that the Cardiff Mk1 system achieved an average phase precision of 17 millidegrees and that it acquired 1 frame every 90 seconds. The quoted average drift figure was 800 millidegrees over 48 minutes and was attributed to the multiplexers used.

#### 2.4.2.2 Single channel system using self developed vector-voltmeter detector

In [22] a single channel system was reported which used a self developed phase detector circuit based on the vector-voltmeter technique. The phase detector had two parts. The one part was used to detect the permittivity (Re(ΔV)) and the other part to detect the conductivity (Img(ΔV)). The subsystem was used in two different configurations. The first employed an excitation coil and a detection coil and the second employed an excitation

coil and a detection gradiometer.

The coil-coil configuration achieved a phase precision of 63 millidegrees and the coil-gradiometer configuration a phase precision of 240 millidegrees. The quoted time constant was 100 ms irrespective of the configuration used. The quoted excitation frequency range was from 20 kHz to 370 kHz however it was stated that it could operate up to 1 MHz.

### 2.4.2.3 Multichannel planar array system

In [42] a 12 channel parallel processing MIT system was presented which was directly influenced by the work performed in [33]. The system used a planar array coil array with 4 excitation coils and 12 detection coils. The quoted excitation frequency used was 10 MHz and was provided by a 4 channel DDS source. The system's block diagram is shown in figure 2.14.

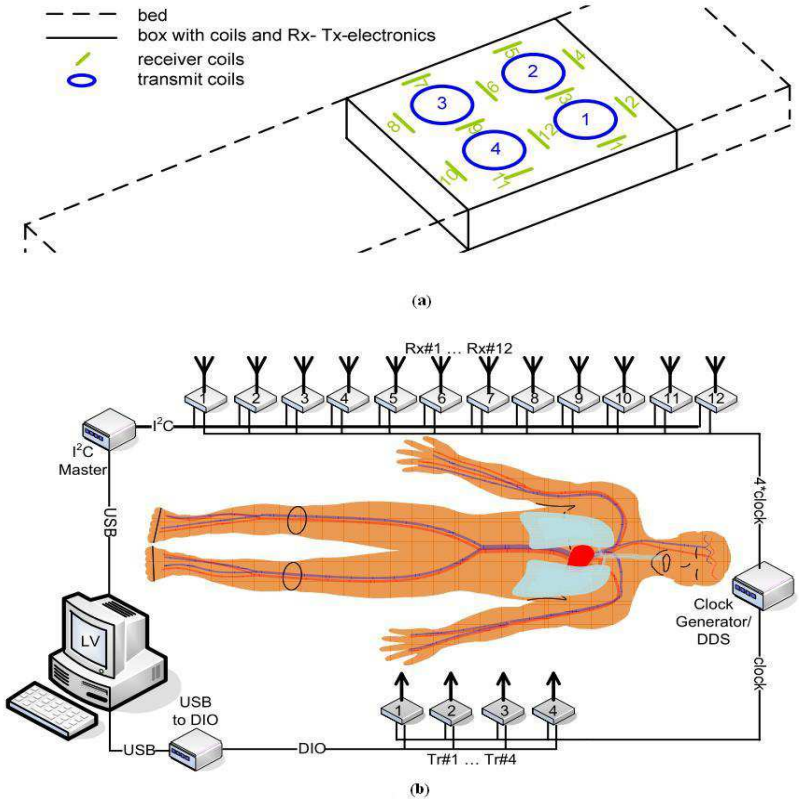


**Figure 2.14**: The mechanical coil alignment (a) and the electrical set up (b) of the multichannel planar array system described in [42]

The excitation coils were controlled by a computer via a digital input output array of switches (DIO). Each detection coil was connected to a dual lock-in phase sensitive detector (PSD) as the processing circuit illustrated in figure 2.15.

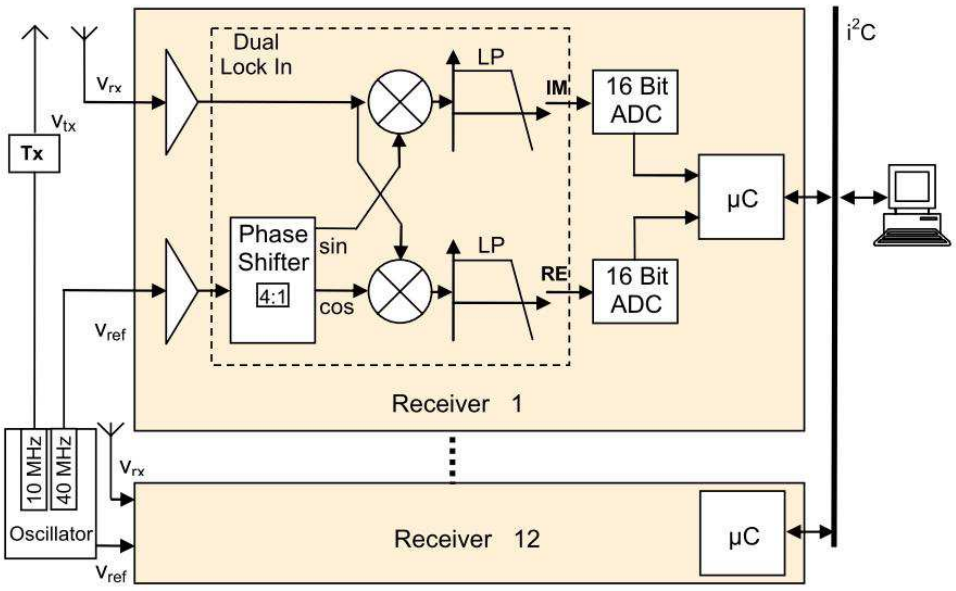


**Figure 2.15**: The phase measurement circuit for each detection coil used in [42]

A phase shifter produced a sine wave and a cosine wave reference signal at 40 MHz. The detected signal was mixed with the sine wave to produce the real part and the cosine wave to produce the imaginary part. An analogue low pass filter with a 2 Hz cut off frequency was used to filter the signals because as mentioned in the article the authors expected that the vital signals occurred below that frequency

After the filtering the signals were sampled by a 16 bit ADC at 1.6 kHz sampling frequency. A total of 32 samples were averaged to produce a measurement and the output of each channel was 2×50 samples per second. The microcontroller stored the sampling information and transmitted it to the computer via the $I^2C$ communication bus.

The quoted spectral noise figure of the system after the analogue filtering was 2.7 µV/√Hz for the real part and 3.7 µV/√H for the imaginary part. The quoted drift of the system was 27 µV for the real part and 25 µV for the imaginary part over 20 minutes. The frame rate of the system was not stated.

### 2.4.3 Direct digitisation technique

The direct digitisation can be defined as the analogue to digital conversion of the high frequency signal without downconversion to a lower frequency [11]. The use of the direct digitisation in MIT is shown in figure 2.16.

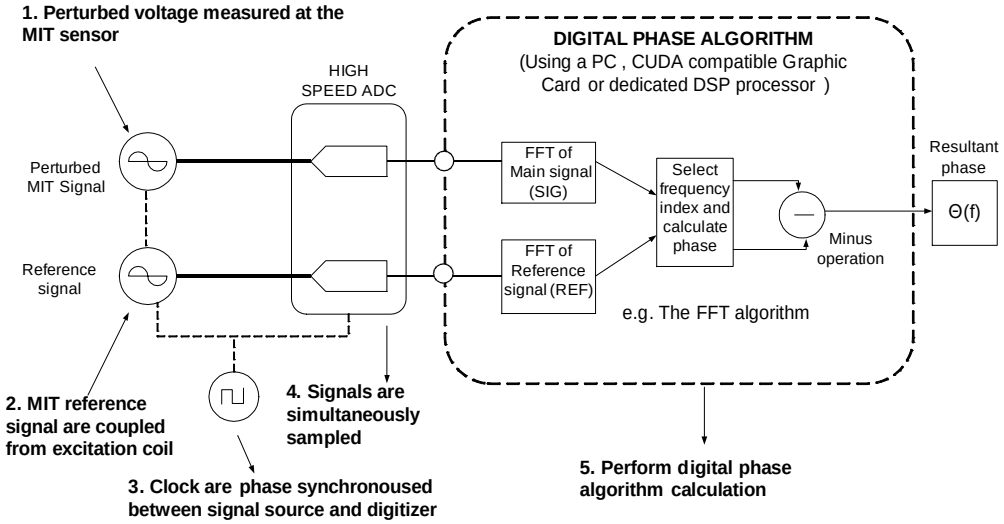


**Figure 2.16**: The direct digitisation technique as used in MIT (from [30])

The excitation signal and the detected signals are processed to remove the noise and then they are digitised with the use of ADC. The digitised signals are then passed to a computer or a standalone processor where the phase calculation is performed with the use of the Fast Fourier Transform (FFT). The FFT can be used to measure the phase of a signal or more signals simultaneously something that drawn interest in MIT as a possible technique for phase measurements.

The amplitude information for each signal is given by

$$|F(j\omega)| = \sqrt{(Real(j\omega)^2 + Img(j\omega)^2)} \qquad (2.53)$$

The respective phase information contained in each signal is given by

$$Phase\ spectrum = \tan^{-1}\left(\frac{Img(j\omega)}{Real(j\omega)}\right) \qquad (2.54)$$

where the arctangent function here returns values of phase between $-\pi$ and $+\pi$. [59]

The direct digitisation technique provides information about the phase and the magnitude of the signals and therefore the conductivity and the permittivity of the object can be measured. This makes the direct digitisation technique suitable for applications in which both electrical properties of an object are required to be measured.

### 2.4.3.1 The Graz Mk2 system

In [23] and [41] a frequency differential multichannel MIT system intended for biomedical applications was described. It used an annular coil array and the quoted excitation frequency range was from 50 kHz to 1.5 MHz.

The coil array had 16 excitation-detection units (TRXU). Eight units were placed at an upper ring and eight units at a lower ring. Each TRXU consisted of a shielded solenoid excitation coil and a detection planar gradiometer. The excitation coil had 8 turns, its diameter was 10 cm and the inductance was 11.2 μH. The gradiometers used 2×40 spiral turns, their inductance was 95 μH and the resonance frequency was 1.56 MHz. The excitation signals were generated by the 16-bit NI PXI-6259 (National Instruments Inc., Texas, USA) multifunction boards.

The coil array had two notable differences from other annular coil arrays used in the MIT field. The first was the absence of an outer shield and the second was a joint on the coil array ring which could be opened to allow a person to enter inside the coil array. According to [11] these construction modifications of the coil array were possible weaknesses of the system.

To perform the phase measurement the reference and the detection signals were first digitised using the 12-bit NI PXI-5105 digitiser board (National Instruments Inc., Texas, USA) with up to 60 MS/s sampling rate. The data were then transferred to a computer where FFT was used for the phase calculation. The quoted spectral noise of the signals was 10 nV/√H however figures for the phase drift and the frame rate of the system were not given. The quoted time constant was 20 ms.

#### 2.4.3.2 The Cardiff Mk2a

In [11] and [30] a multichannel MIT system intended for biomedical applications was presented. It used an annular coil array with two rings of coils. The 14 excitation coils were placed in one ring and the 14 detection coils were placed in the other. The system is shown in figure 2.17.

The excitation coils had 4 turns and the detection coils had 2 turns. All coils had 4.5 cm diameter and were located 4 cm from the outer screen. The quoted excitation frequency was from 500 kHz to 14 MHz. In [11] and [30] it was mentioned that the system was designed to act as a single frequency system or a frequency differential system depending on the required use.

To perform the phase measurement the signals were digitised using the NI PXI-5105 (National Instruments Inc., Texas, USA). The signals were then transferred to a computer where the phase calculation was performed using FFT.

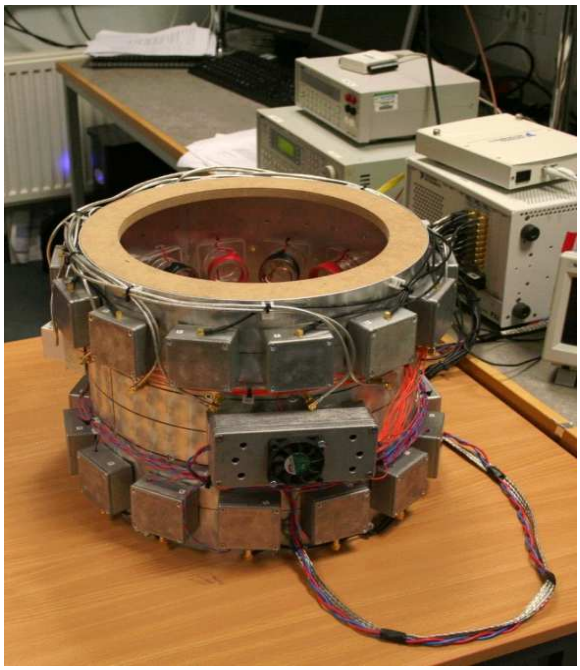

**Figure 2.17**: The Cardiff Mk2a system

The Cardiff Mk2a phase precision was stated below 1 millidegree and the phase drift below 10 millidegrees over 12 hours. The quoted time constant for the measurements was 17 ms and the quoted system frame rate 0.70 fps. The latter was attributed partly to the increased time required for sampling but mainly to the time required to transfer the data from the NI PXI-5105 to the computer.

#### 2.4.3.3 Single channel subsystem

In [60] a single channel phase measurement subsystem was reported aiming to rectify the problem with the increased transfer data time of the Cardiff Mk2a. The subsystem used the dual 120 MS/s 14-bit LTC 2285 (Linear Technology Inc., California, USA) ADC to digitise the reference and the measured signal. The signals were then fed to a Spartan-3 FPGA device (Xilinx Inc., California, USA) in which real-time I/Q demodulation with built-in time-averaging was performed. The data were then transferred to a computer for analysis.

The quoted phase precision was down to 7.5 millidegrees at 40 $mV_{pp}$ for a 6 ms time constant. The quoted phase drift was 119 millidegrees over 5 hours when both input signals were 65 $mV_{RMS}$ ($\approx$ 184 $mV_{pp}$).

#### 2.4.3.4 The Bath system

In [61] a multichannel multiplexed MIT system intended for biomedical applications was presented. It used an annular array coil array with 8 excitation coils and 8 detection coils

placed interchangeably on the same ring. All the coils had 6 turns and their diameter was 4 cm. The resonance frequency of the coils was 45 MHz and the inductance was 1.8 μH. The excitation frequency used was 10 MHz. The system is shown in figure 2.18.

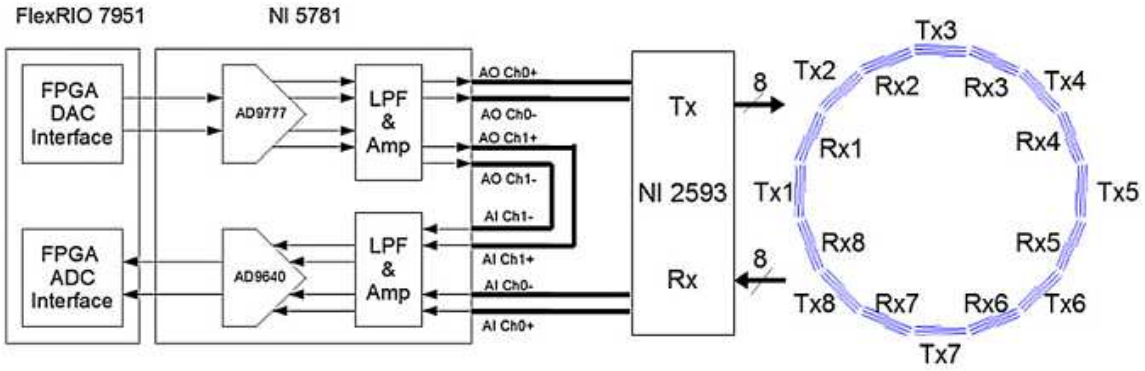


**Figure 2.18:** The block diagram of the MIT system implemented in [61]

The system used a single channel phase measurement subsystem connected to the coil array through the NI 2593 multiplexer (National Instruments Inc., Texas, USA). The phase measurement subsystem used the NI 5781 (National Instruments Inc., Texas, USA) for digitizing the signals and the FlexRIO 7951 (National Instruments Inc., Texas, USA) to perform the phase measurement.

For the single channel phase measurement subsystem the quoted phase precision was 4 millidegrees at 40 $mV_{pp}$ input and the quoted maximum drift figure was 25 millidegrees over 5 hours. The quoted time constant was 6 ms. Figures of the phase precision, the phase drift and the frame rate for the entire system were not quoted.

#### 2.4.3.5 Multichannel MIT system for high contrast metal imaging

In [14] a multichannel MIT system that targeted the monitoring of the high contrast metal process (high conductivity application) was described. The system comprised an annular coil array with 8 coils in a circular ring, the data acquisition switch unit HP 34970A (Agilent Technologies Inc., California, USA) for the phase measurement and a computer for the image reconstruction. The excitation frequency was 5 kHz. The system is shown in figure 2.19.

The coil array employed one of the coils as the excitation coil and the remaining seven as the detection coils sequentially thus 56 measurements were acquired instead of 64 measurements. It was mentioned that for the image reconstruction only 28 measurements out of the 56 measurements were used due to reciprocity an approach adopted from [62].

The data were transferred through GPIB to the computer and were stored for post-

processing. The system was stated to require approximately 1.35 s for the acquisition of 1 frame. The phase precision, the phase drift and the time constant figures were not quoted.

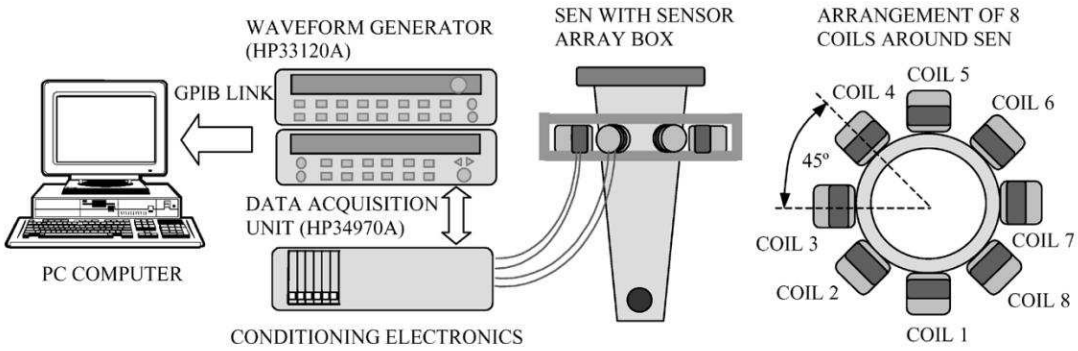


**Figure 2.19**: The MIT system configuration as given in [14]

In [15] the further development of the system was described. The coil array was retained unchanged however the rest of the system was replaced. The DAQ 2205 data acquisition card (ADLINK Technology Inc., Taipei, Taiwan) with a maximum sampling rate of 500 kS/s [63] was used for the phase measurement. The 12-bit DAC LTC 7545 (Linear Technology Inc., California, USA) placed on the DAQ 2205 was used for the excitation signal generation which as reported increased the excitation frequency range up to 100 kHz maximum. The raw data were transmitted to the computer using the PCI communication bus.

The new implementation of the system achieved a maximum frame rate of 10 fps at 5 kHz excitation frequency. It was mentioned that the system could reach up to 100 fps with 50 kHz frequency however this would prohibit the system's use for the high contrast metal process monitoring. The phase precision, the phase drift and the time constant figures of the new implementation were also not quoted.

#### 2.4.3.6 Multichannel MIT system for metallic object imaging

In [64] a multichannel parallel MIT system targeting the metallic object imaging (high conductivity application) was described. The system comprised an annular coil array with 8 coils on a circular ring, the Spartan XC3S400 FPGA (Xilinx Inc., California, USA Inc., California, USA) for the phase measurement subsystem and a computer for the image reconstruction. The excitation sinusoidal signal was generated by a DDS IP core implemented in the XC3S400 FPGA. The system is shown in figure 2.20.

The system was quoted to achieve the reconstruction of real time images at a frame rate of 200 fps with the excitation frequency at 50 kHz thus making it the fastest low frequency

multichannel MIT system reported until this thesis was submitted. The phase precision, the phase drift and the time constant of the system were not quoted.

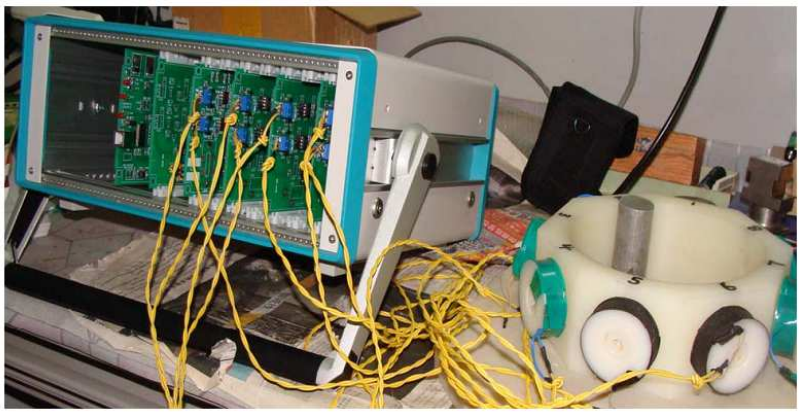

**Figure 2.20**: The MIT system presented in [64]. On the left is the FPGA subsystem and on the right the coil array.

In [65] the further development of the system reported in [64] was presented. The hardware of the system was kept the same however two changes occurred. The first change was reported in the digital demodulation module in the XC3S400 in which half the period of the signal of interest was used to obtain the in-phase and quadrature components. As it was stated this improved the operation speed of the new system in comparison to the old system from 20 ms to 10 ms.

The second change occurred in the image reconstruction. Similar to [15] the authors used only 28 measurements instead of using the whole 56 measurements for a frame. The frame rate, the phase precision and the phase drift figures of the system were not quoted in the article.

### 2.4.4 The downconverted direct digitisation technique

In the downconverted direct digitisation technique the signals are first downconverted to an intermediate frequency using the heterodyne technique (described in Appendix 1) and then sampled using analogue to digital conversion.

#### 2.4.4.1 The Philips MIT system

In [66] and [67] a multichannel parallel MIT system was presented. The system used an annular coil array with 16 excitation channels and 16 detection channels. The coil array had a ring of 16 coil holders and an excitation and a detection coil were mounted at each holder which was secured on the system's aluminium shield. Each of the excitation and the detection coils were made on a PCB with two turns of 50 mm in diameter. One turn was placed on the top layer and the other on the bottom layer of the PCB.

The excitation frequency used was 10 MHz. The system used two external signal generators for the excitation signal and the local oscillator signal. Both were connected to all channels through 1:16 power splitters. Given the set-up the system could in theory be operated in sequential multi-frequency mode.

To perform the phase measurement the excitation and detection signals were downconverted to 10 kHz and then digitised with the use of a 24-bit audio-frequency digitiser which sampled the downconverted signal at a sampling rate of 192 kHz. The downconversion and the digitisation were performed concurrently on all 16 channels.

The quoted phase precision for the channels closest to the active excitation coil was below 10 millidegrees and for the coils farthest over 200 millidegrees. The quoted average phase precision was 80 millidegrees for a 100 ms time constant. The frame rate was not quoted either in [66] or [67]. However in a review of this system in [11] it was mentioned that the frame rate was expected to be in the order of 0.5 fps based on the time constant of 100 ms quoted in [67].

### 2.4.4.2 The MUSIMITOS system

In [24] and [68] the development of a multichannel system aiming to record the cardiac activity and the lung function was described. The system was used in [24] to capture the respiratory activity of a human subject and in [68] to record the cardiac activity and the lung function of a human subject. The block diagram of the system is shown in figure 2.21.

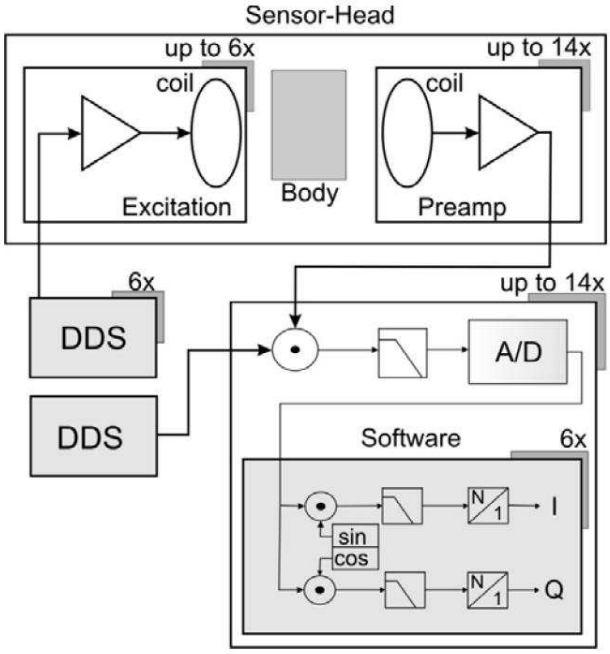


**Figure 2.21**: Block diagram of the Musimitos system (from [68])

In [24] the signal bandwidth acquired from human subjects was defined from 0.1 Hz for flat respiration up to 4 Hz for a heart rate of 250 beats per minute. Thus it was mentioned that to capture the first odd harmonic a sampling frequency of 12 Hz (80 ms time constant) was required.

Furthermore it was stated that to realize the application the system required a total of about 64 channels however it was designed to use 6 excitation and 14 detection coils. A reason for the reduction in the number of the channels was not given. It was also stated that a preamplifier noise value of 20nV/√Hz can be considered as a good trade off between circuit complexity and low-noise design.

In both [24] and [68] the excitation frequency was 10 MHz produced by two 4 channel DDS generators. A super-heterodyne receiver combined with an intermediate frequency digital signal processor (IF-DSP) was used for the phase measurements. The received signals were first downconverted down to a baseband signal from 20 kHz to 100 kHz [68] and then used as input to the DSP for digital processing with the use of FFT and IFFT transforms.

In [24] the spectral noise level of the system for frequencies lower than 2 Hz was quoted below 20 nV/√Hz. The quoted phase noise of the demodulated signal in the time domain was 570 millidegrees and in the frequency domain was 1 millidegree for frequencies above 2 Hz. The frame rate, the time constant and the phase drift figures of the system were not quoted.

## 2.5 Possible low conductivity industrial application for a fast MIT system

The majority of the proposed industrial applications for a fast multichannel MIT system are for high conductivity applications. This is because the requirements in terms of excitation frequency, phase precision and phase drift are more relaxed and can be satisfied without the need for employing high end equipment. These applications include the high contrast metal process monitoring [14, 15], the metallic object imaging [64, 65], the inspection of a two-phase flow GaInSn and argon [69] and the monitoring of liquid metal/gas flow regimes of an industrial steel caster [70].

A low conductivity industrial application which requires a high acquisition rate is the multiphase flow measurement in oil pipes. Although it has attracted attention in the field of

MIT there is only one reference [29] of a multichannel MIT system used for investigating it. In this section the requirements of the application and the performance of the multichannel MIT system proposed for the application are examined.

### 2.5.1 Multiphase flow measurements in oil pipes

Oil wells produce a mixture of gas, oil, water and soil [71, 72] however the required resources are the oil and the gas. The water and the soil are considered contamination and must be removed as they can be become extremely harmful to the processing stage of the oil wells.

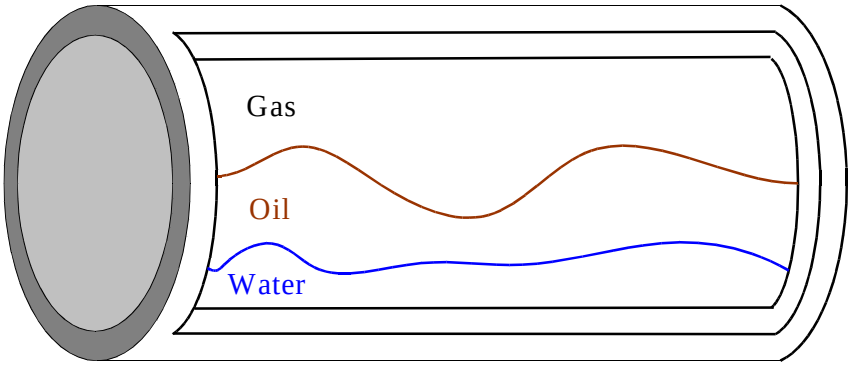


**Figure 2.22**: Stratified three phase flow in a horizontal oil pipe (from [72])

This procedure requires accurate measurements of the mixture for detecting the components prior their removal [73]. Furthermore the measurement of the fluids produced in oil wells is important in the oil industry because it contributes to the efficient exploitation and production of oil [71]. A method that has been found to be efficient and accurate is the flow measurement of the mixture in the pipes. [71]

The presence of components of the three phases of matter[3] (solid, liquid, gas) in the pipes calls for multiphase flow (MPF) measurements. The term multiphase flow measurements as it is applied in the oil/gas industry refers to the measurement of multiple fluid components that appear in a flowing stream. The detection of water in oil pipes is termed as a two-phase flow measurement although water and oil are both liquids and the measurement of water, oil and gas is termed as a multiphase measurement. [74]

The conventional approach to perform an MPF measurement is to separate the mixture into individual components and then to use single-phase meters to measure them as illustrated in figure 2.23. However this approach suffers from the bulkiness and the high cost of the apparatus installation and the high cost of maintenance. [71]

[3] The term phase in regards to matter is used to describe its state. There are four phases or states of matter: solid, liquid, gas and plasma

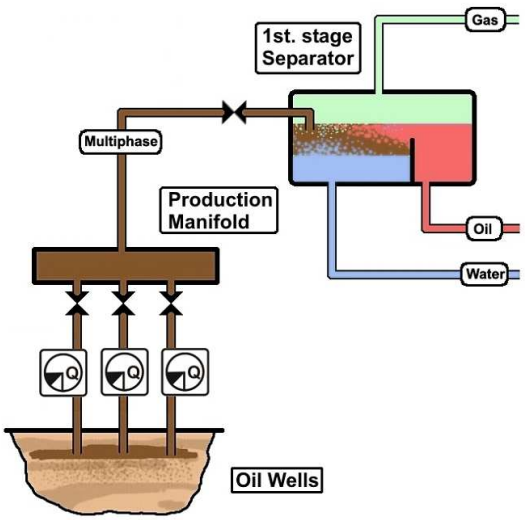


**Figure 2.23**: The conventional approach for multiphase flow metering (from [73])

A different approach to perform the MPF measurements is to use an MPF meter as illustrated in figure 2.24. The use of MPF meters has been demonstrated to be beneficial for the oil industry in terms of the layout of the production facilities, the well testing, the reservoir management, the production allocation, the production monitoring and the capital and operating expenses. This has led to a considerable research towards their development and use in the oil industry. [75]

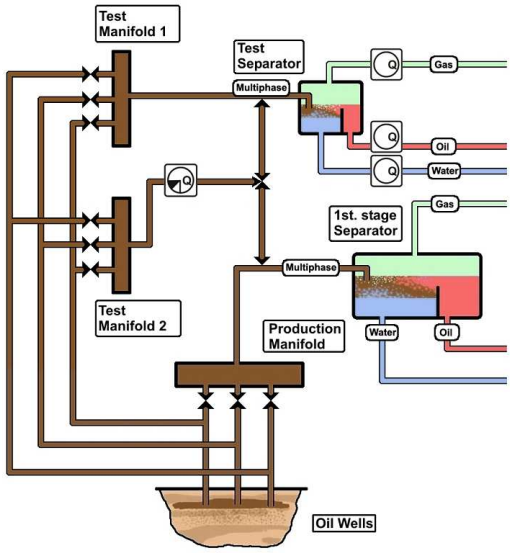


**Figure 2.24**: A multiphase meter for multiphase flow measurements (from [76])

In general the MPF meters can be categorised into two types. The meters that perform the measurement using separation techniques and the meters that can perform on-line measurements [75]. Usually they fall into four technological categories which are the dual-energy gamma densitometry, the impedance and microwave, the differential pressure and the cross-correlation (the correlation between signals obtained at two positions along a

pipe) [75].

Ideally an MPF meter that performs on-line measurement need to satisfy the following requirements [71, 72, 76]:

- distinguish between water, oil and gas
- a typical accuracy of ± 5 % of rate for each phase
- non-intrusive
- flow regime independent
- withstand the harsh environment of the oil wells in sea and sub-sea level

These requirements limit the possible solutions that can be employed as on-line MPF measurements. A possible technological solution that has been proposed for the development of on-line MPF meters is the Industrial Process Tomography (IPT). The term refers to the non-destructive, non-invasive imaging techniques that can be used in a variety of industrial applications for visualizing the internal behaviour of industrial processes. The cross-sectional images produced by these imaging techniques provide valuable information that can be used primarily for visualisation and monitoring. [71, 77]

Apart from the general requirements for MPF meters the use of IPT for MPF measurements requires the development of tomography systems capable of producing images of sufficient accuracy with high frame rates (up to hundreds of frames per second). Furthermore the combination of two techniques that can measure two distinct physical properties may be required to address the requirement for MPF measurements. [71]

There are many types of tomography systems available such as electrical, ultrasonic, radiation, nuclear magnetic resonance (NMR), microwave and optical [71]. Of special interest for this thesis is the research conducted for the development of MPF meters based on the Electrical Capacitance Tomography (ECT) and the Electrical Resistance (or Resistivity) Tomography (ERT) due to their proximity with MIT. A short description of these techniques is given in Appendix 2 however it is noted here that MPF meters based on these techniques have yet to reach use in the oil industry [71, 75].

Proposed ECT systems for use as MPF flow meters include stand alone ECT systems [71, 78] or combined systems which use other tomography techniques like the γ-ray tomography [76]. The advantages of using ECT for MPF measurements are its non invasive nature, the high frame rate and the low production cost [71]. The disadvantages are its low spatial image resolution [71], the fact that it can only be used for oil/water

mixtures that contain water below 60% to 70% [73] and that it cannot be used in non-invasive configuration with pipes constructed from conducting materials [29, 71].

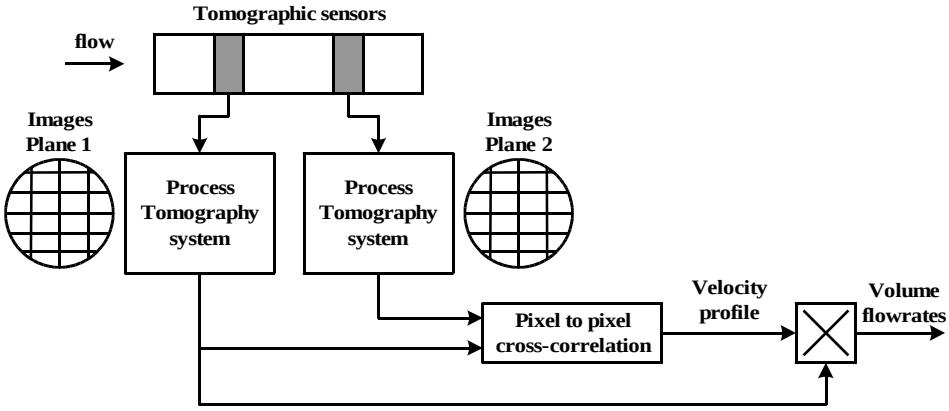


**Figure 2.25**: Tomographic MPF measurement (from [71])

Similar to ECT various configurations of ERT systems have been proposed as MPF meters [78, 79]. The advantages of using ERT for MPF measurements are its high frame rate and the low production cost. The disadvantages of the ERT are its invasive nature [71], the low spatial image resolution [71] and that it can be used only for oil/water mixtures containing water above 60% to 70% e.g. considered as wet mixtures [73, 78].

The concept of using a magnetic induction meter for flow measurements in the oil industry for monitoring the bulk ionised water in pipelines is based on the fact that the conductivity of process water is much higher than the conductivity of the oil [7, 11]. This concept was examined in a single coil configuration published in [80] and in [81]. Both studies concluded that a multichannel magnetic induction tomography system was required for this task.

### 2.5.2 MIT system for multiphase flow measurements in oil pipes

In [29] the results of MPF measurements acquired with the use of the Cardiff Mk1 (reviewed in 2.4.3) were published. It was the first multichannel MIT system used for MPF measurements and the only multichannel system published in the literature until this thesis was submitted. The system is illustrated in figure 2.26.

The system comprised an annular coil array with 16 coils, a digital lock-in amplifier for implementing the vector-voltmeter phase measurement technique and a computer for the image reconstruction. The quoted phase precision of the system was 17 millidegrees and the quoted average drift figure was 800 millidegrees over 48 minutes. As the authors pointed out the latter was a significant source of error for the system which was attributed to the multiplexers used.

**Figure 2.26**: The MIT system described in [11,29] simulating the MPF measurements

To obtain the MPF measurement images a plastic cylindrical pipe with a diameter of 200 mm and length of 500 mm was used as a phantom. It was filled in with different volume fractions of saline solution of 5 S/m conductivity simulating the stratified flow of an oil pipeline. The authors assumed that the air in the phantom represented the oil and the gas in a pipeline because oil is non-conductive and it has a low relative permittivity compared to that of sea water. The system required 240 measurements (16×15) per frame which in turn resulted in obtaining a complete measurement every 90 seconds [29].

The authors acknowledged that the system's frame rate was significantly low for this application and indicated that further work was required for investigating the development of a fast MIT system for MPF measurements. They further stated that a multichannel MIT system employing a fast phase measurement technique such as the zero crossing technique would possibly be required. [29]

## 2.6 Possible low conductivity biomedical applications for a fast MIT system

The contactless nature of MIT is one of the main attractions for use in biomedical applications. The majority of the proposed applications have focused in two main areas of the human body which are the head and the thorax.

At the head area the interest focuses in the early detection of brain oedema [17, 18] and haemorrhage [19]. In the thorax area the interest focuses in the measurement of the thoracic conductivity changes for monitoring the cardiac output of the heart [20] and the

recording of the cardiac activity and the lung function [7]. The thoracic conductivity changes require a high sampling rate and thus a fast MIT system would be needed to record these changes.

This section starts by examining the electrical properties of the living tissues in general, their response to frequency variation and the properties of some tissues at the thorax area in the range from 10 kHz to 100 MHz. It continues with a brief look into the biology of the heart and the lungs and reviews some of the proposed MIT systems for this application.

### 2.6.1 The electrical properties of the living tissue

The electrical properties of a living organism are defined by its constituents. The most simple and functional unit of life are the cells whose activities form the structure and the functions of an organism. In the human body there are about 200 kinds of cells varying in shapes, sizes, and functions. [10]

The major components of the cell are the plasma membrane, the cytoplasm, the cytoskeleton, the organelles, the inclusions, the cytosol and the nucleoplasm. The plasma membrane (cell membrane) is the surface boundary of the cell. Between the plasma membrane and the nucleus is the cytoplasm which contains the cytoskeleton, the organelles and the inclusions [10].

The cytoskeleton is a framework of protein filaments and tubules. The organelles are structures that perform various metabolic tasks for the cell. The inclusions include stored cell products such as lipids and pigments and foreign bodies such as dust and bacteria. The nucleus is the largest organelle of the cell and contains the nucleoplasm in which the chromosomes are contained. [10]

The cytoskeleton, the organelles and the inclusions are embedded in the intracellular fluid (ICF). All body fluids which are not contained in the cells are called the extracellular fluid (ECF). The extracellular fluid located between the cells is also called tissue fluid. Some other extracellular fluids include blood plasma, lymph, and cerebrospinal fluid. [10]

The living biological tissue therefore can be generally defined as an aggregate of similar cells and intercellular products surrounding them that form a specific region of an organ which performs a specific function. [10]

An electrolyte is a mass with ionic DC conductivity. The ICF and the ECF are both

electrolytes. This means that they contain ions and that they can conduct electric current in the presence of an external electrical field. Thus the tissue can be electrically considered as an ionic conductor. The human tissues have finite ionic conductivities related with the nature and the extent of their ionic content and ionic mobility. [82, 83]

In contrast the plasma membrane elemental structure which is formed by a dual layer of lipids is mostly dielectric. However intermixed with the lipid dual layer are the integral proteins which allow substances like ions and water to pass through the plasma membrane and thus electric current in a passive manner. This causes the plasma membrane to have a high capacitance and a low but complicated pattern of conductance. [83]

The structure formed by the ECF, the plasma membrane and the ICF behaves electrically as a capacitor with a capacitance of 1 $\mu F/cm^2$ [84]. As it was noted at the beginning of this section the living tissue exhibits the same dielectric properties as its constituents and thus displays both conductance and capacitance.

A dielectric can be explained with the use of a capacitor in which the passive electrical properties of the dielectric material between the two parallel electrodes are characterised by the electrical conductance G and the capacitance C. Supposing a capacitor with two parallel electrodes of surface A placed at a distance d from each other then if a sample of conductivity $\sigma$ and permittivity $\varepsilon$ is placed between the electrodes the conductance G of the sample is given in Siemens (S) by

$$G = \frac{\sigma A}{d} \qquad (2.55)$$

and the capacitance C in Farads (F) by

$$C = \frac{\varepsilon_0 \varepsilon A}{d} \qquad (2.56)$$

The plasma membrane can therefore be represented with an equivalent electrical circuit of two parallel components which are the conductance and the capacitance as depicted in figure 2.27.

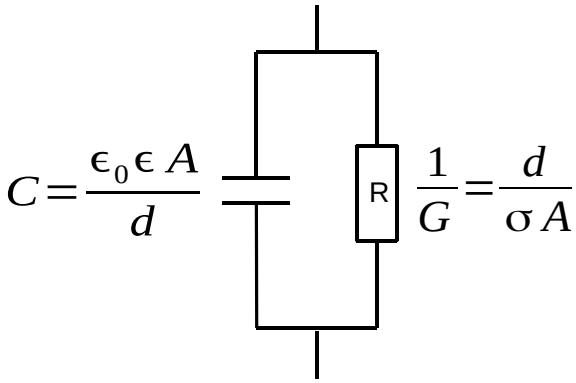


**Figure 2.27**: Equivalent electrical circuit for the plasma membrane (adapted from [84])

If the electrical characteristics of the equivalent circuit are frequency varied with a sinusoidal signal then at a frequency ω the complex admittance $Y_c$ of a living tissue sample can be defined as

$$Y_C = G + j\omega C = \frac{A}{d}(\sigma + j\omega\varepsilon\varepsilon_0) \qquad (2.57)$$

The complex conductivity $\sigma_c$ (also denominated as admittivity or specific admittance [83]) can be defined in Siemens per meters as [84]

$$\sigma_c = \sigma + j\omega\varepsilon\varepsilon_0 \qquad (2.58)$$

Hence the complex capacitance $C_c$ can be defined as

$$C_C = \frac{Y_c}{j\omega} = \frac{A}{d}\left(\frac{-j\sigma}{\omega} + \varepsilon_0\varepsilon\right) \qquad (2.59)$$

The impedance is the inverse of the admittance therefore the complex impedance of the living tissue sample can be defined as

$$Z_c = \frac{1}{Y_C} = \frac{G - j\omega C}{G^2 + (\omega C)^2} \qquad (2.60)$$

and the complex specific impedance $z_c$ (also denominated as impedivity or complex resistivity [83]) in Ohm-meters (Ωm) as

$$z_c = \frac{1}{\sigma_C} = \frac{\sigma - j\omega\varepsilon\varepsilon_0}{\sigma^2 + (\omega\varepsilon\varepsilon_0)^2} = \rho_c \qquad (2.61)$$

The equations (2.60) and (2.61) show that the complex electrical impedance of the living tissue is greatly affected by the cell membranes and that it is sensitive not only to the material composition of the living tissue but also to its cellular structure.

### 2.6.2 Frequency dependency of the living tissue

The complex permittivity and the complex conductivity of the living tissue are functions of the frequency which makes the living tissue a dispersive substance. Following the Debye approach which considers the biomolecules as polar materials [83] the frequency dependency introduced by each polarised subsistence of a tissue into the complex permittivity of the tissue can be described by [84]

$$\hat{\varepsilon}(\omega) = \varepsilon_\infty + \frac{\Delta\varepsilon}{1 + j\omega\tau} = \varepsilon_\infty + \frac{\varepsilon_s - \varepsilon_\infty}{1 + j\omega\tau} \qquad (2.62)$$

where $\varepsilon_\infty$ is the permittivity at the high frequency limit, $\varepsilon_s$ is the static low frequency permittivity and $\tau$ is the polarisation relaxation time.

The corresponding frequency dependent expression for the complex conductivity is described by

$$\hat{\sigma}(\omega) = \sigma_s + \frac{\sigma_\infty - \sigma_s}{1 + j\omega\tau} j\omega\tau \qquad (2.63)$$

where $\sigma_\infty$ is the conductivity at the high frequency limit, $\sigma_s$ is the low frequency conductivity as for $\varepsilon_\infty$ and $\varepsilon_s$.

Equations (2.63) and (2.64) however have a poor fit on experimental data [11]. A modification of the permittivity equation was given in [85] based on empirical basis

$$\hat{\varepsilon}(\omega) = \varepsilon_\infty + \frac{\varepsilon_s - \varepsilon_\infty}{1 + (j\omega\tau)^{1-\alpha}} \qquad (2.65)$$

where $\alpha$ is a variable based on empiric data and $1 \geq \alpha \geq 0$ [83].

The parameter $\alpha$ can be regarded in a number of ways. It can be considered as a measure of the distribution of relaxation times, as a measure of the deviation from an ideal resistor and capacitor in the equivalent circuit, according to energy models or continuous-time random walk charge carrier translocation. [83]

The frequency dependence of the living tissue according to the laws of relaxation also called dispersion shows the permittivity as a function of frequency. It is introduced by various mechanisms and three major steps have been identified namely the $\alpha$-dispersion, the $\beta$-dispersion and the $\gamma$-dispersion [83, 84, 86, 87]. An idealised perception of the  of the living tissue permittivity variation is shown in figure 2.28.

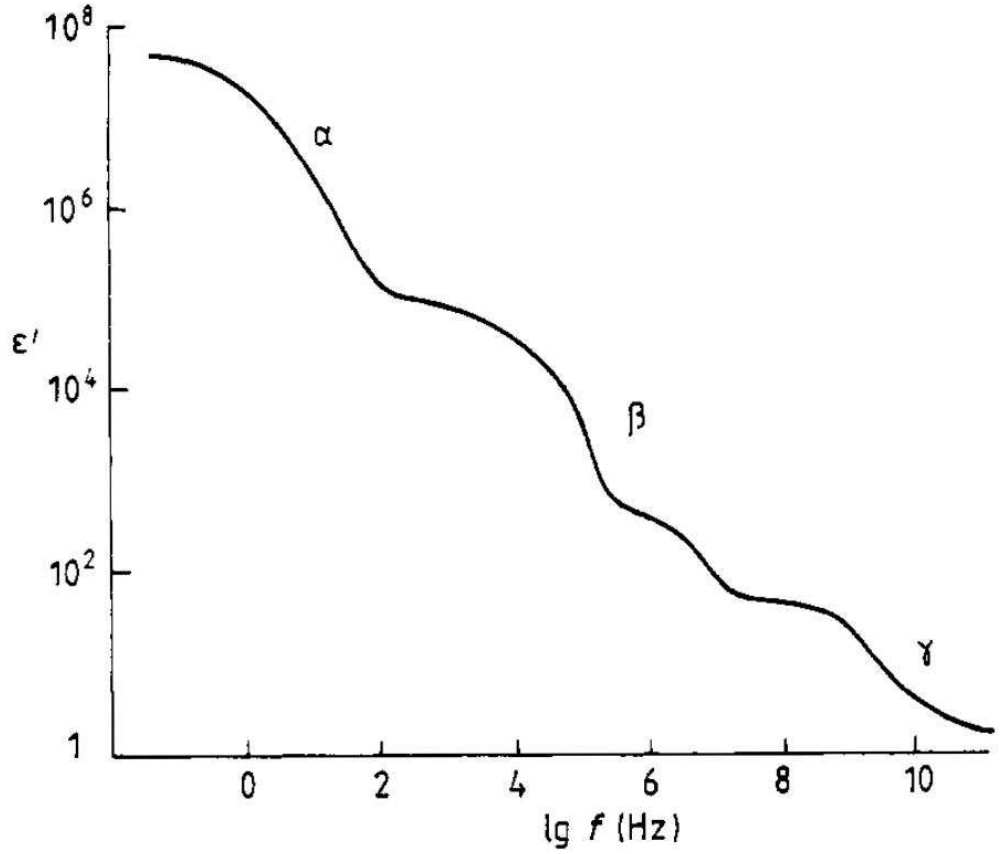


**Figure 2.28**: An idealised perception of the living tissue permittivity variation in the three major dispersions (from [84])

The α-dispersion is in the low frequency region and is associated with the ionic diffusion processes at the cellular membrane. Although its understanding is not yet complete and a number of mechanisms and elements contribute to the tissue dispersion there are three well established mechanisms which are: [88, 89]

- The frequency dependent conductance of the channel proteins in the cell membrane
- The frequency dependence of the surface conductance and the capacitance caused by the counter-ion effect atmosphere effect which exists near charged cell surfaces
- The endoplasmic reticulum effect when exists

The β-dispersion is in the region of hundreds of kilohertz to Megahertz and occurs due to the polarization of the cellular membranes which act as barriers to the flow of ions between the intra and extra cellular media [82]. The membranes require time for charging through the intracellular and extracellular fluids and this time is determined by the plasma membrane capacitance, the cell radius and the fluid conductivities [87]. Other tissue components contribute to the β-dispersion like proteins, amino acid residues and organelles [86].

The γ-dispersion is in the region of gigahertz and is due to the high content of water in cell and tissue and due to the polarization of water molecules in the tissue. The tissue water relaxes at 20 GHz except for the presence of proteins, amino acids etc. [84]

The plasma membranes are considered to have a high capacitance and a low but complicated pattern of conductance. This has the result that at DC and at low frequencies the current flows around the cells because of the high impedance of the cell membranes. At high frequencies the membrane impedance decreases and the current can flow through the cells as well according to the local conductivity [83]. The low frequency and high frequency current paths are shown in figure 2.29.

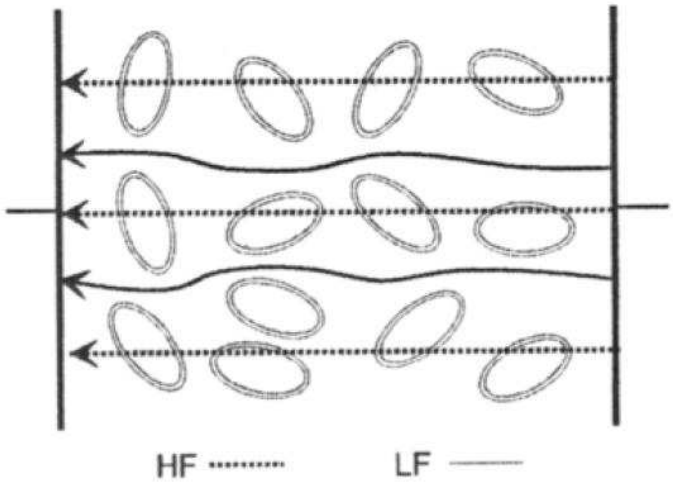


**Figure 2.29**: High frequency and low frequency current path in tissue. The solid line is low frequency and the dashed line is the high frequency. (from [83])

The living tissue cannot be considered as a homogeneous medium in terms of electrical conduction. The tissue conductivity presents large differences between its constituents due to the uneven size of the cells and their different functions and a presumption is that anisotropy seems to be the rule rather than the exception. [83]

A general conclusion is that the permittivity and the conductivity of the living tissue vary with frequency. Permittivity is decreased as the frequency increases while in contrast conductivity increases. However both appear to have an upper frequency limit as equations (2.63) and (2.64) suggest. For different tissues different values of permittivity and conductivity are observed at the same frequency range.

The frequency dependency of the living tissues is extremely important in the development of MIT systems for biomedical applications and a careful selection of the excitation frequency is required to acquire meaningful data from the living tissues. Furthermore a

multi-frequency excitation approach could prove beneficial in certain biomedical applications based on the differences of the dielectric properties of different tissues at different frequencies.

### 2.6.3 Dielectric properties of the thorax main tissues from 10 Hz to 100 MHz

Two possible biomedical applications for a fast MIT system could be the contactless monitoring of the cardiac activity and the lung function. A comparison of the permittivity and the conductivity of the main living tissues found at the thorax area can aid in identifying the excitation frequency required for an MIT system aiming to target these applications. The main thorax tissues considered were the heart, the muscle, the dry skin, the lungs in inflated and deflated state, the blood which is found in high volumes in the thorax area and the breast fat.

To facilitate the comparison the conductivity and the permittivity in the frequency range from 10 Hz to 100 MHz were calculated using an online database [90]. For the calculations the online database uses the parametric model and the parameter values developed by C.Gabriel et al and was published in [82, 91-93]. The tables of the data calculated using the online database are given in Appendix 3. Based on the calculated data the conductivity and the relative permittivity graphs of the tissues were produced. The conductivity graph is shown in figure 2.30 and the relative permittivity graph in figures 2.31 and 2.32.

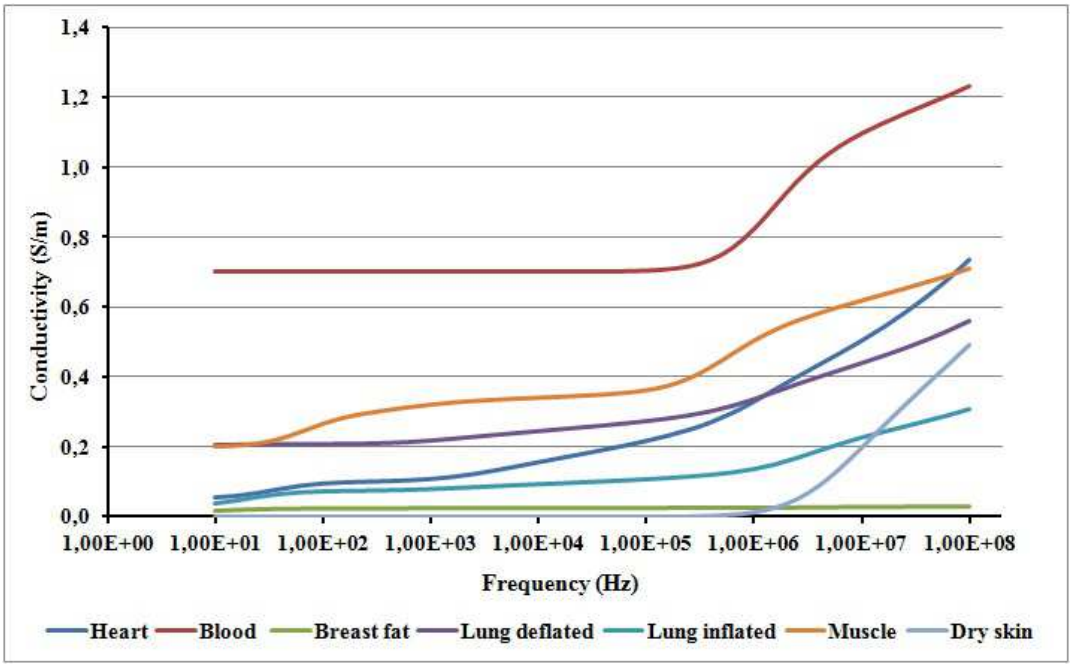


**Figure 2.30**: Conductivity distribution of the thorax tissues from 10 Hz to 100 MHz

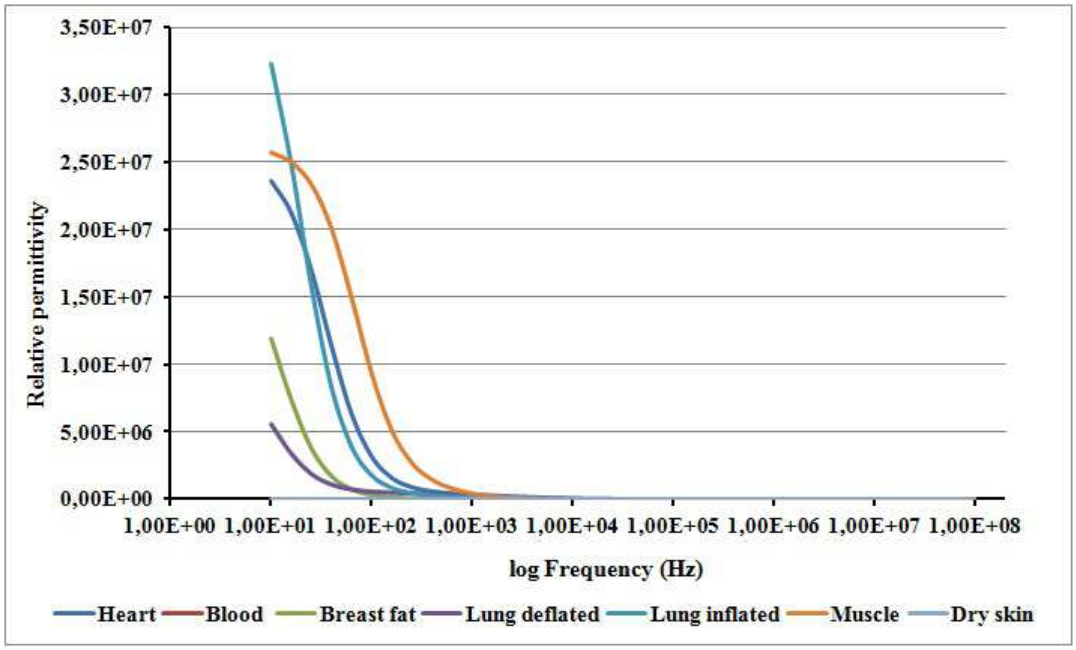


**Figure 2.31**: Permittivity distribution of the thorax tissues from 10 Hz to 100 MHz

It is noted here that in figure 2.31 the relative permittivity of blood falls in the same graph line as the dry skin due to the scale used for the relative permittivity axis. A clearer view of the relative permittivity of the blood and the dry skin is given in figure 2.32 below.

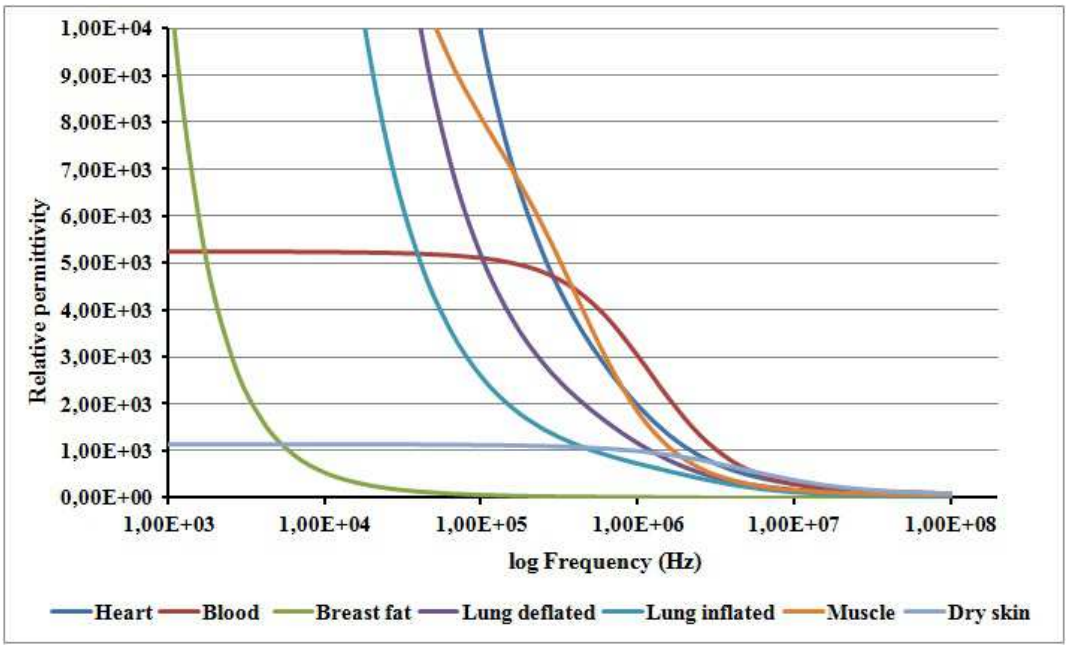


**Figure 2.32**: Permittivity distribution of the thorax tissues from 1 kHz to 100 MHz

A general observation from the graphs is that the different tissues exhibit different dielectric properties as the frequency increases. Specifically the conductivity increases with the increase of frequency and the permittivity is decreased as was shown in section 2.6.2.

In the conductivity and the permittivity graphs (figures 2.30, 2.31, 2.32) there is a

formation of two regions marking similar behaviour of most tissues in regards to the frequency. The regions are from 10 Hz to 100 kHz and from 100 kHz to 100 MHz. These regions correspond to the α-dispersion and the β-dispersion (section 2.6.2).

In the α-dispersion the conductivity of most tissues in the comparison is slowly increasing while in the β-dispersion the conductivity rapidly increases. In contrast the permittivity of the tissues decreases rapidly in the α-dispersion and exhibits a mild decrease in the β-dispersion.

A notable exception however are the blood, the dry skin and the breast fat. The blood and the dry skin exhibit an almost constant conductivity and permittivity in the α-dispersion and a galloping increase in conductivity and decrease in permittivity in the β-dispersion. The breast fat exhibit an almost constant conductivity in the whole spectrum and an almost constant permittivity from 100 kHz to 100 MHz.

From the conductivity graph (figure 2.30) a number of observations can be made. The blood conductivity is much higher than the rest tissues in the whole spectrum region. The muscle conductivity is higher from the rest tissues conductivities apart from the blood in the whole spectrum region. The breast fat conductivity is almost constant from 10 Hz to 100 MHz and is considerably lower than the conductivities of the other tissues.

The dry skin conductivity exhibits an almost constant conductivity up to 1 MHz from which point a rapid increase begins. This increase is lower than the conductivity of the blood, the inflated and deflated lungs up to 10 MHz and higher than the conductivity of the inflated lungs from about 15 MHz to 100 MHz.

The inflated lungs conductivity becomes more and more distant from the heart conductivity as the frequency increases with almost a three times difference at 100 MHz. The deflated lungs conductivity is higher than the hearts' conductivity up to 1 MHz and this is reversed as the frequency increases to 100 MHz. Although from 1 MHz to 100 MHz the conductivities of the heart and the deflated lungs remain close however they are distinctively apart and distinguishable from each other.

From the permittivity graphs (figure 2.31 and 2.32) the following observations can be made. The blood permittivity is almost constant up to 100 kHz from where a steep decrease begins up to 10 MHz and then has a rather constant value. The dry skin has the lowest permittivity from all the tissues up to about 10 kHz and the second lower to the

breast permittivity from that frequency onwards.

The muscle permittivity decreases rapidly in the spectrum from 10 Hz to 1 MHZ and then has a very slow decrease. In the spectrum from 10 kHz up to 1 MHz the permittivity of the inflated lungs, the deflated lungs and the heart are distinctively apart. However above 1 MHz the permittivity of the lungs and the heart comes more and more closer and it is getting more difficult to distinguish between them. This is obvious as the frequency increases past the 10 MHz.

The conductivity graph 2.30 shows that if an MIT system is to record the conductivity changes for detecting the cardiac and the lung activity then it is required to use a high excitation frequency in the order of 10 MHz and above. The permittivity graphs 2.31 and 2.32 show that if an MIT is to record permittivity then the excitation frequency should be set at 1 MHz and below as shown in.

However due to the frequency dependency of the MIT signals and the domination of the conductivity in low conductivity materials such as the biological tissues (section 2.1.3) the recording of permittivity would be more difficult to perform than the recording of conductivity. Therefore an MIT system which records the conductivity would be more suitable for detecting the cardiac and the lung activity at an excitation frequency starting at 10 MHz.

### 2.6.4 Physical aspects of the heart and lungs and their monitoring

#### 2.6.4.1 The heart and its monitoring

The human heart is a muscular organ that maintains a continuous blood circulation in the human body through the cardiac cycle. It is considered to be one of the most vital organs in the human body. The human heart is located in the thoracic cavity between the lungs and below the sternum. [10]

The heart along with the blood and the blood vessels form the circulatory system. The pumping activity or heartbeat is a product of the heart's own pacemaker and electrical conduction system. The electrical conduction system of the heart consists of muscle cells (myocytes) that electrically depolarize by themselves at regular time intervals. [10]

As the myocytes depolarizes and re-polarizes electrical currents are generated that are conducted by electrolytes in the body fluids to the skin surface. The recording of this activity produces the electrocardiogram (ECG) which is a clinical method of evaluating the

heart function. [10]

One complete cycle of contraction and relaxation is called the cardiac cycle and repeats itself typically every 0.8 sec in a resting adult heart thus generating a heart rate of about 75 heartbeats per minute. The heart rate is defined as the number of heartbeats over a time period and usually is expressed in beats per minute (bpm) [10].

The heart rate is used by the physicians as a tool for the diagnosis of life threatening cardiac events like tachycardia, bradycardia and arrhythmias[4] [94-97]. The cardiac cycle is shown in figure 2.33.

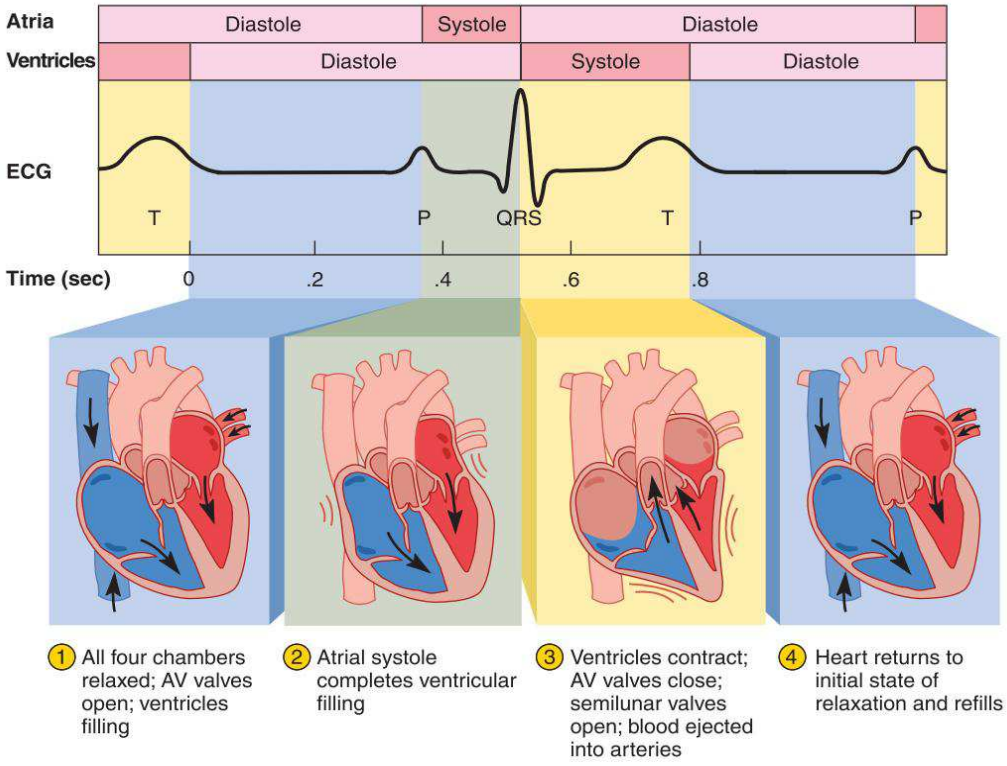


**Figure 2.33**: The cardiac cycle (from [10])

The implemented approaches for contactless ECG include ballistocardiography [98], the use of capacitive (insulated) electrodes over the clothes of the patient [99, 100] and the use of piezo-resistive sensors [101]. These approaches however are not truly contactless in nature as they require physical contact with the body of the subject in spite of being applied for example over the clothes. From the review of literature it was concluded that until the date this thesis was submitted a true contactless approach that does not require physical contact with the patient for recording the ECG does not exist.

On the other hand applications for the recording and monitoring of the heart rate that do

[4] The term arrhythmia defines any variation from the normal rate of regularity of the heartbeat and usually result from irregularities within the conduction system of the heart [98]

not require physical contact with the patient have been implemented. These include the use of contactless LED based cameras for pulse oximetry ($SpO_2$) and hence the pulse rate monitoring [102], the use of fibre Bragg grating (FBG) sensors [103] and the use of electromagnetic radiation [104-106].

#### 2.6.4.2 Lung function and monitoring

The respiratory system is an organ system that is primarily specialised to provide oxygen to the blood and remove the carbon dioxide from it [10]. The upper respiratory tract consists of the nose, the pharynx and the larynx while the lower respiratory tract consists of the trachea and the bronchi, the lungs and the pleurae.

The exchange of gases between an organism and the medium where it lives is called respiration. The exchange of gases between the lungs and the blood is called external respiration and the exchange of gases between the blood and the nearby cells is called internal respiration [107]. Of interest for this thesis is the external respiration only and the measurements associated with it and thus a short review of its physiology follows.

The major component of the lower respiratory tract that participates in the external respiration are the lungs[10]. They consist of two conical organs which are similar with a broad, concave base resting on the diaphragm and a blunt peak called the apex slightly above the clavicle. The left lung although taller is narrower than the right because the heart tilts toward it [108].

On the medial surface the left lung has an indentation called the cardiac impression where the heart presses against it. The right lung has three lobes called the superior, the middle and the inferior. The horizontal fissure separates the superior lobe from the middle lobe and the oblique fissure separates the middle and inferior lobes. The left lung has only a superior and inferior lobe and a single oblique fissure.[10]

In the inside of each lung is a branching system of air passages called the bronchial tree. It extends from one main bronchus to the lobar bronchi, the segmental bronchi, the bronchioles, the terminal bronchioles and respiratory bronchioles. Each lobar bronchus supplies one lobe of the lung and each segmental bronchus supplies one bronchopulmonary segment. The terminal bronchioles are the end of the conducting division. All branches beyond the terminal bronchioles have alveoli and belong to the respiratory division. [10]

The blood that needs oxygen enters the lungs from the pulmonary arteries into the

bronchial tree where it disposes $CO_2$ and receives $O_2$. The oxygenated blood then leaves the lungs through the pulmonary veins. The respiration is distinguished into two phases which are the inspiration phase and the expiration phase. The inspiration phase is caused by the contraction of the diaphragm and the intercostal[5] muscles and the expiration phase by their relaxation. [10, 108]

The state of the lung functioning is given by monitoring the parameters of respiration which include the lung volume, the lung capacity, the airway resistance, the lung compliance and elasticity and intrathoracic pressure. In figure 2.34 the relationship between the lung capacities and the lung volumes is illustrated. [107, 109]

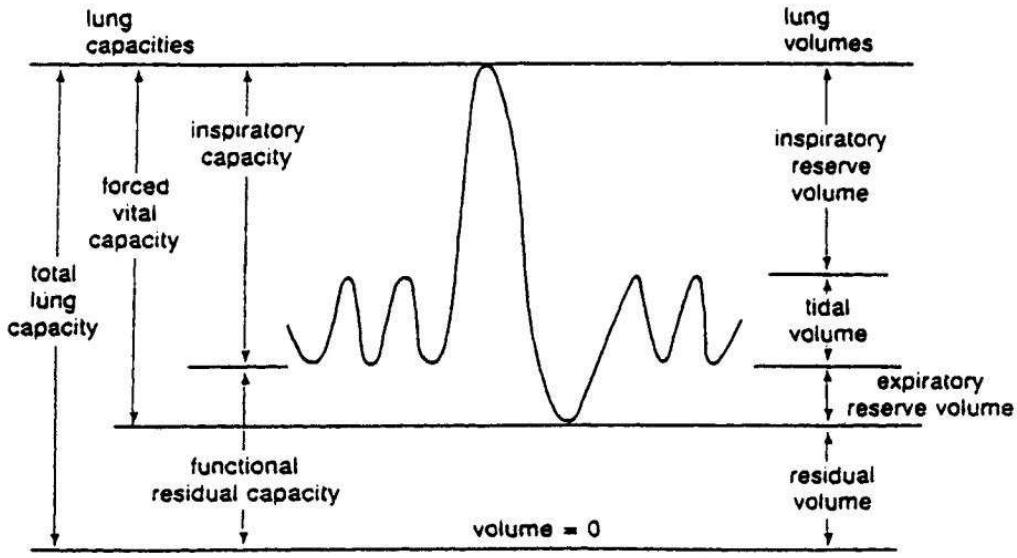


**Figure 2.34**: Lung capacity and lung volume relationship (from [109])

The Total Lung Capacity (TLC) is the volume of gas contained in the lungs at maximal inspiration and the Vital Capacity (VC) is the volume of gas that can be exhaled by a maximal expiration from total lung capacity. The Residual Volume (RV) is the volume remaining in the lung after maximal expiration.

The Tidal volume (Vt) refers to the normal respiratory volume excursion and the lung volume at the end of a normal expiration is the Functional Residual Capacity (FRC). The Inspiratory Reserve Volume (IRV) is the maximal amount of gas that can be inspired as extra inspiration from the high peak tidal volume. The Expiratory Reserve Volume (ERV) is the maximal amount of gas that can be expired as extra expiration from the low peak tidal volume. [107-109]

A large number of respiratory monitoring methods and their implementations that measure

[5] Muscles that surround the thoracic cavity that move the rib cage in and out

different physiological respiratory variables have been published [110] each with its advantages and disadvantages. The techniques for lung function monitoring include the Electrical Impedance Pneumography [111], the Respiration Inductive Pneumography [112, 113], the spirometry [107] and the Electrical Impedance Tomography (EIT). Of special interest for this thesis is the use of the EIT for monitoring the lungs function due to the vicinity to MIT [114, 115]. A short description of EIT is given in Appendix 2.

The EIT has been considered for monitoring the lung function due to the difference in conductivity and permittivity between the human tissues, the blood and the air. To monitor the lung function a set of electrodes is placed around the chest of the patient and an image of the conductivity distribution is produced [116]. The research conducted for examining the use of EIT as a lung function monitoring tool has shown that EIT can be considered as a suitable method for lung function monitoring [117, 118]. Until the date this thesis was submitted two EIT systems for lung function monitoring were commercially available [119, 120].

However there are still problems with the application of EIT for lung function monitoring associated with the electrode placement and localisation, the electrode-tissue contact, the current-tissue injection and the image reconstruction.[11]

### 2.6.5 MIT systems for detecting the cardiac activity and lung function

#### 2.6.5.1 Single channel system

A single channel system was developed in [121] to investigate the possibility of measuring the cardiac stroke volume and the conductivity changes in the head without coming into contact with the human body. In this review the measurements concerning the head will not be covered.

The coil configuration of the system comprised three coils forming a differential transformer (also called linear variable differential transformer). The excitation coil was placed in the centre and the two detection coils were placed at each side of the excitation coil. The detection coils were connected in series phase opposition to cancel the voltage induced by direct coupling. The coil configuration is shown in figure 2.35.

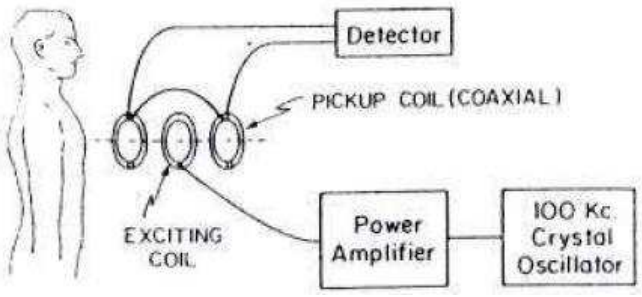


**Figure 2.35**: The coil configuration of the single channel system described in [121]

The coils used were coaxial, 13 cm in diameter, with 10 layers of 10 turns per layer and spaced 5.2 cm apart with respect to their centres. The coils had about 2.5 mH self inductance, 3.5 Ω DC resistance and resonated at about 610 kHz. In the article a model to calculate the dimensions of the coils was given however it was mentioned that it was not used to calculate the coil dimensions because the coil configuration was prepared before the model was developed.

The excitation signal of 100 kHz generated by a crystal oscillator and was the input to a power amplifier that amplified it. The signal was then band-passed and low-passed filtered to keep the frequency as centred as possible to 100 kHz to achieve the cancellation between the coils. It was stated that in normal circumstances (which were not clarified) the current at the excitation coil was 250 mA and the voltage induced at the detection coils was about 60 $mV_{RMS}$.

A synchronous detector was used to obtain the conductivity changes at the output of the detection coils network. The synchronisation signal was generated by the crystal oscillator used for the excitation signal. The output of the synchronous detector was fed to an oscilloscope and a chart recorder.

The experiments regarding the torso covered static and dynamic measurements. The static measurements were performed in an attempt to determine the effective average resistivity of the human chest. A headless and limbless model terminated at the waist was constructed which contained 30 litres saline of 87.5 Ωcm at 26 degrees C. The model was used to record measurements of the resistivity at various distances from the coil configuration. A live human subject was also used to record measurements at the same distances.

A formula was given in the article for calculating the effective average resistivity from the unbalanced voltages obtained from the model and the human subject however it must be noted that it is unique to that coil configuration and thus is largely unsuitable for use in

other coil configurations.

The dynamic measurements were performed in an attempt to record the cardiac stroke volume of human subjects. In the experiments participated six male human subjects which were placed in various positions and distances above the coil configuration. According to the authors the results showed that when the subjects breathed at a random point in the respiratory cycle there were considerable variations in the magnitude and the waveform as shown in the figure below and the repeatability of the records was poor. An example of the conductivity changes recorded at normal breathing is shown in figure 2.36.

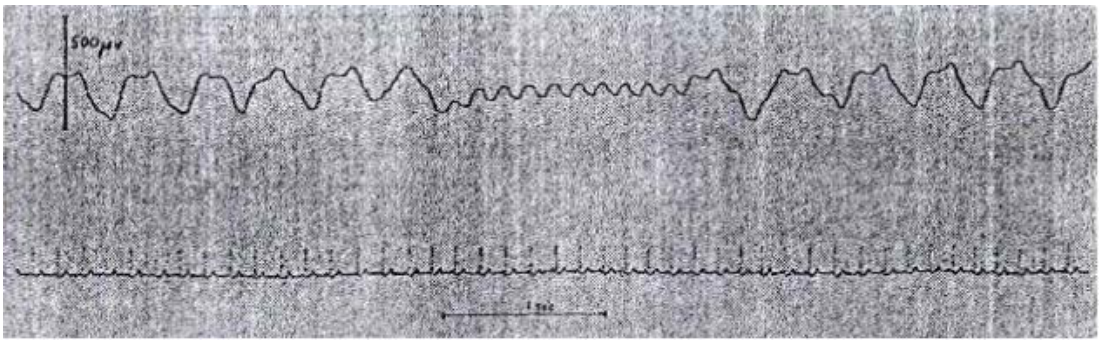

**Figure 2.36**: Conductivity changes recorded when the subject was breathing normally as recorded in [121] (In the centre of the graph the subject hold its breath)

When the subjects held their breath at the maximum inspiratory level the authors stated that the records resembled ventricular stroke-volume curves. However when the subjects were taking short breaths until the maximum inspiratory level was reached the authors commented that the records showed considerably larger successive changes in the magnitude and the waveform than those occurring in ventricular volume curves as a result of breathing. The distance of the heart from the coil configuration was pointed out as a cause of reducing the induced signal level and thus the amplitude of the recorded conductivity changes.

Based on the results the authors stated that the changing volume of the heart was probably the biggest factor in producing the conductivity changes however other factors which included the periodic changing of the hearts shape and the distance of heart from the coil configuration may have attributed. It was also stated that the developed coil configuration was not optimal for cardiac stroke volume measurements and alternative coil configurations were proposed as shown in figure 2.37.

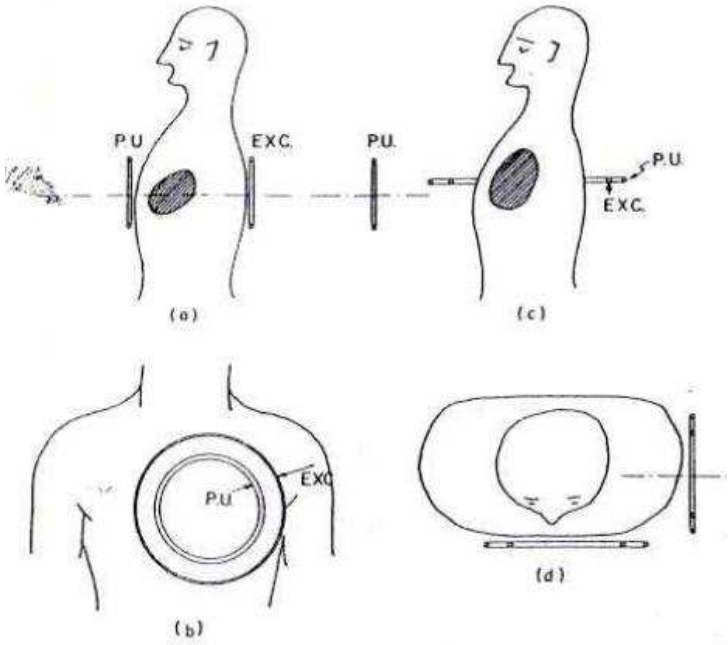


**Figure 2.37**: Alternative coil configurations for conductivity changes recording at the torso area as proposed in [121] (EXC is the excitation coil, PU is the detection coils)

### 2.6.5.2 Single channel planar coil

A single channel planar coil which comprised a pcb printed coil with 3.5 cm radius, the RF and the measurement electronics enclosed in a plastic case was used in [20] to record the thoracic conductivity.

The coil was attached to an oscillator of finite internal impedance and so the human body was seen by the oscillator as a resistive load. Any change in the load resistance due to the conductivity of the human body caused the amplitude of the oscillation to vary. Since the characteristics of the oscillator, the geometry of the coil and the characteristics of the human body were known then the conductivity was calculated from the measured change in the oscillations amplitude.

An in-vivo experiment was performed with a 50 year old male human subject suffering with occasional arrhythmias in the supine position. The arrangement was placed above the subjects clothing and was held in place with an elastic belt. Although it did not touch the thorax of the subject the way it was placed compromised the contactless nature of the arrangement the authors claimed it had.

The experiment showed that the coil configuration recorded the conductivity changes in the human torso due to the cardiac activity and include an illustration showing a pattern of peaks which followed the R wave of the ECG wave. The pattern is shown in figure 2.38.

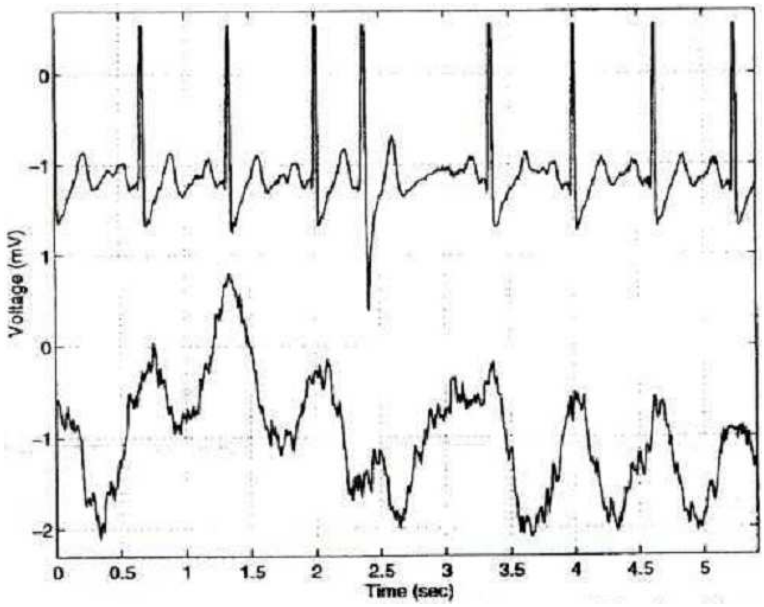


**Figure 2.38:** Conductivity changes in comparison with the ECG of the subject as recorded in [20]

A sensitivity analysis was performed using an eccentric spheres model which showed that the parameters affecting more the electromagnetic signal were the haematocrit and the heart – thorax walls distance. The latter was considered as a problem which required a multichannel approach.

### 2.6.5.3 Multichannel system MUSIMITOS

The development of a multichannel system dubbed the Musimitos aiming to record the heart and lung activity was described in [24] and [68]. The technical characteristics of the system was examined in section 2.4.4.2 and so they will not be repeated here.

A preliminary result from testing the system was included in [24] in the form of the figure 2.39 which captured the respiration activity measurement of a human subject. More information regarding the test were not given. The figure shows that there is a pattern of similar behaviour between the output of the MIT system and the respiration activity of the subject although in the opposite way (when airflow is high the magnetic induction is low and vice versa).

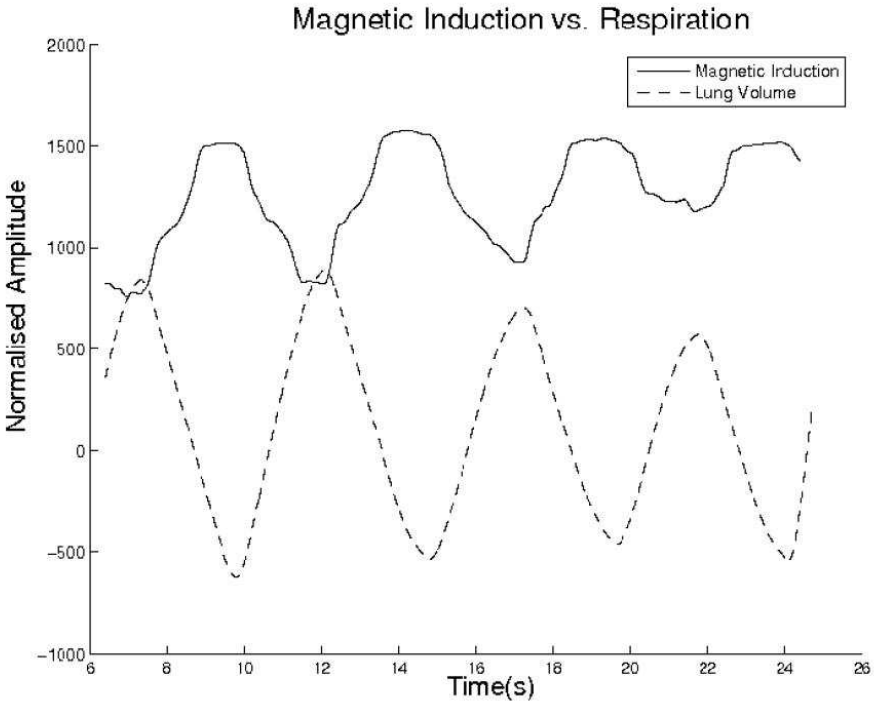


**Figure 2.39**: The comparison of airflow and magnetic induction performed in [24]

The system was used in [68] to record the heart and the lung activity of a human subject. For the measurements the system used two excitation coils and three measurement coils providing six independent channels of inductive coupling. Simultaneously to the MIT system recordings the signals from a photoplethysmograph (PPG) device and an airflow sensor attached to the human subject were also recorded. An overview of the signals measured is shown in figure 2.40.

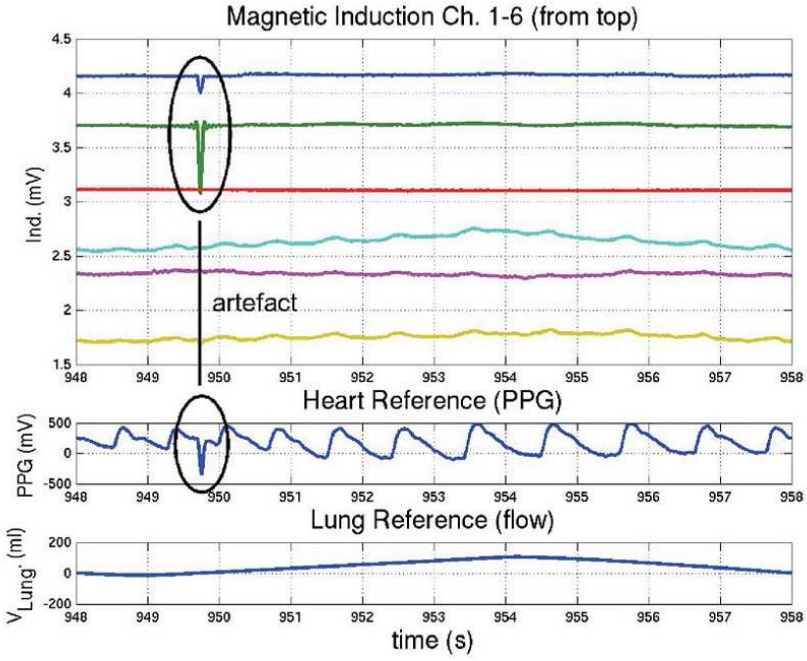


**Figure 2.40**: An overview of the signals measured simultaneously in [68]

The human subject was placed on four different positions (supine, prone, right lateral, left lateral) above the sensor head. The distance of the sensor head from the subjects thorax was not quoted.

The study showed that the MIT system could detect the signal components produced by the cardiac and lung activity without coming into contact with the subjects body. The authors claimed that the system could perform what it was designed for however they acknowledged that further work is required for the system to detect the respiratory and the heart rate.

Furthermore it must be mentioned here that the PPG device was used to provide the heart reference to compare the recordings of the MIT system. However a PPG device produces a waveform which is similar to the arterial pressure waveform [122] and thus the results of the system were compared to the volumetric changes at the body part where the device was placed and were related only to the mechanical and not the electrical function of the heart.

#### 2.6.5.4 Multichannel MIT system

The development of a 12 channel parallel processing MIT system intended for the recording of human vital signs was described in [42]. The technical characteristics of the system was examined in section 2.4.2.3 and they will not be repeated here.

For the measurements the human subject was lying on a bed with the chest central above the planar array at a distance of about 5 cm above the coils. The human subject started with normal breathing and then held the breath for a few seconds to record a single heartbeat signal similar to one of the processes in [121].

An ECG/breathing device was used to record the ECG and the respiratory activity of the subject. The MIT system and the device were synchronised for time-locked comparison. System results compared against the subject's ECG and airflow is shown in figure 2.52.

The results showed that the system could detect the cardiac activity and the lung functioning without coming into contact with the human subject. For the cardiac activity the induction channels closer to the excitation coil had their peak when the R wave of the ECG wave occurred similar to the results in [121]. For the lung function the induction channels closer to the excitation coil followed the pattern of the airflow but in the opposite way (when airflow was high the magnetic induction was low and vice versa) similar to the respiration activity graph included in [24].

Finally in the article it was stated that a decentralized multichannel system with synchronous parallel data acquisition and integrated data processing is a precondition for real time observation in the medical care area.

### 2.6.5.5 Single channel portable system

The Portable Impedance Measurement System (PIMS) developed in [123] was based on the Musimitos system described in [24] and [68]. The system targeted the everyday use by professionals like bus drivers or office workers that sit on a chair. The block diagram of the system is shown in figure 2.41.

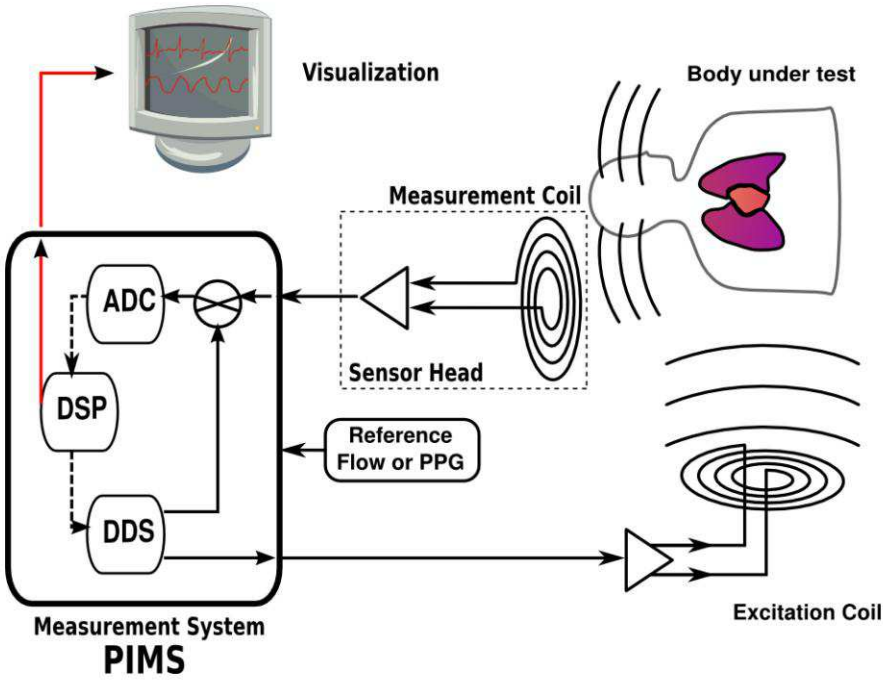


**Figure 2.41**: The block diagram of the portable impedance measurement system developed in [123]

The coil configuration consisted of an excitation coil which had two windings of 35 mm diameter and used 752 mA of excitation current and the detection coil which had eight windings and had a 35 mm diameter. The coils were arranged in orthogonal configuration and along with the pre-amplifiers were called the sensor head.

The dedicated computer used for the demodulation in the Musimitos system was replaced by a Digital Signal Processor. The system was equipped with one extra channel for measuring the heart activity with a PPG device or with a flow reference for breathing detection. The rest of the circuitry and the principle of operation was kept the same as in the Musimitos system and so it will not be repeated. The excitation frequency used was 10 MHz.

The system was experimentally used for detecting the respiration activity of five human subjects lying on a divan on the prone position with their chest directly over the sensor head at a distance of 7 cm from the excitation coil. Three different breathing behaviours were measured which were the shallow, the normal and the very deep breathing. During the recordings a flow sensor was used to measure the subjects breathing synchronised with the inductive measurement.

The results showed that the system could detect the lung functioning without coming into contact with the human subject. The normal breathing pattern was similar to those already published in [24, 42, 68, 121]. The authors claimed that the amplitude of the measured signals corresponded directly to the measured breathing behaviors which appears to be correct. The results of the system are shown in figure 2.42.

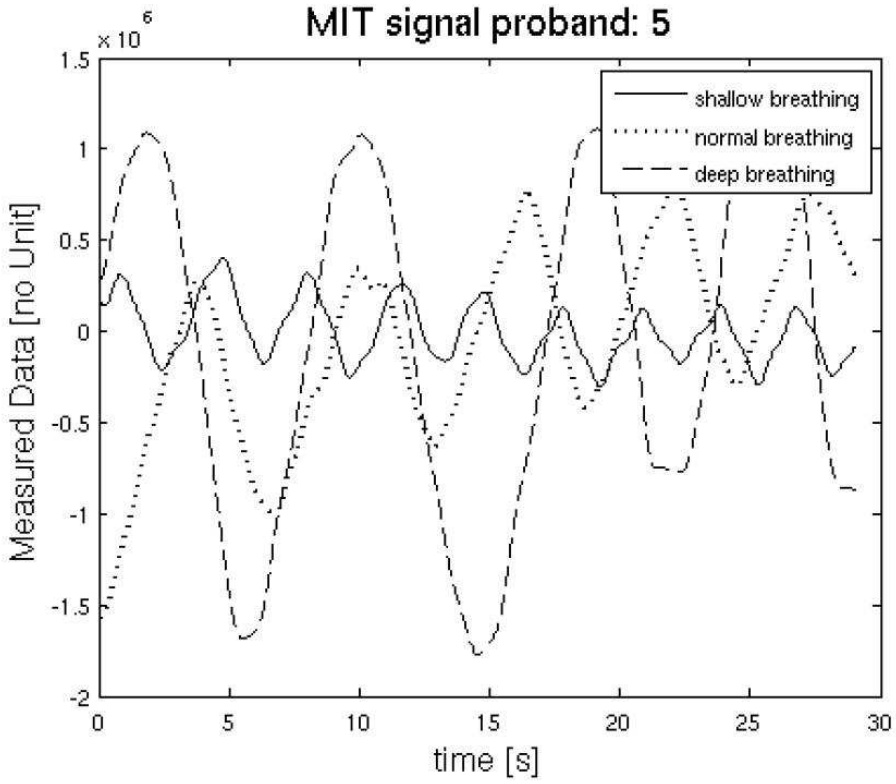


**Figure 2.42**: Shallow, normal and deep breathing of a subject captured by the system developed in [123]

The authors stated that artifacts mainly due to motion may have compromised the measurements and that they could be a major issue in a real life implementation of the system. It was also stated that the use of digital filters for signal separation could result to the calculation of the respiration rate although it was not demonstrated.

## 2.7 Summary and identified areas of further research work

This section provides a summary of the findings from the literature review conducted and presented in the previous sections.

In section 2.1 the review performed set the essential requirements for the design and the development of MIT systems. The review showed that an MIT system is required to operate at a frequency range which depends on the physical characteristics of the object and that a phase measurement section must be employed for determining the conductivity. Furthermore it showed that measurement of the induced signals amplitudes is required to determine the permittivity. These factors complicate the design of MIT systems and demand the design and the development of specialised MIT instrumentation.

In section 2.2 the literature regarding the MIT system's architecture, characteristics, components and noise was reviewed. Four proposed descriptions of the MIT system architecture were examined. The review showed that a new architecture description which will use a clearer and more descriptive terminology for the MIT subsystems may be required.

A review of the components comprising an MIT system was then conducted. The review showed that the excitation coils and the detection coils number affect the speed and the spatial resolution of the MIT system. It was further shown that the configuration of the phase measurement subsystem has a great impact on the speed of the system.

The review on the noise showed that it depends mainly on the construction of the coil array, the signal conditioning electronics and the phase measurement system. It was further shown that a reduction in the noise can be achieved if low noise components are used for implementing the MIT system.

In section 2.3 the phase measurements in MIT were examined. The review on the sinusoidal wave characteristics showed that the frequency variations from the electronic devices' noise create amplitude noise and phase noise on the signals. The review further showed that the phase precision and the phase drift which are calculated by the phase measurement performed by the MIT system can be used as quality markers for the system performance.

In section 2.4 the phase measurement techniques used in MIT and some of their implementations were reviewed. The review showed that at 10 MHz the direct digitisation

technique exhibited the best results in respect to phase precision and phase drift at the cost of a very low frame rate (less than 1 fps).

In terms of speed at 10 MHz only the zero crossing technique seems to have the potential to reach a frame rate of 10 fps when employed by a multichannel system. The review showed that the development of a parallel multichannel zero crossing MIT system operating at 10 MHz. have not been reported yet and thus the development and the characterisation of its performance could be a subject for research work.

In section 2.5 the literature review examined the multiphase flow measurements (MPF) in oil pipes which is a possible low conductivity industrial application for a fast MIT system. The review examined the requirements and the available techniques currently in use. The review showed that a good spatial resolution and a high frame rate (tens of frames) are required to consider a tomographic technique for MPF measurements.

The only multichannel high frequency MIT system [29] used for the application was examined. The system detected the stratified flow however it achieved a very low frame rate (1 frame every 90 seconds). The zero crossing technique was considered as a possible solution for the low frame rate. The review showed that an investigation for the development and the characterisation of a fast multichannel MIT system operating at 10 MHz aiming at low conductivity industrial applications such as the MPF measurements could be a subject for research work.

In section 2.6 the literature was examined concerning the detection of the cardiac activity and the lung function which are two possible low conductivity biomedical applications for a fast MIT system. The review first examined the electrical properties of the living tissues and it was showed that the tissues are frequency dependent. The tissue conductivity increases with frequency while the tissue permittivity decreases however both have an upper frequency limit. The review showed that the excitation frequency used by an MIT system should be in the order of 10 MHz to use the conductivity changes for detecting the cardiac and the lung activity.

The review then examined the physical aspects of the heart and the lung and their monitoring. The review for the heart monitoring showed that there is a number of techniques that can record the ECG however they all require physical contacts with the patients. A true contactless ECG monitoring technique would be advantageous in the clinical setting however it does not yet exist. Contactless techniques for measuring the

heart rate have been implemented and are commercially available.

The review of the lung activity showed that a large number of techniques exist for monitoring the lung function. Of special interest for the thesis is the EIT due to the proximity it has to MIT. The literature review showed that the EIT is used for the monitoring of the lung function and two systems are commercially available. However it still suffers from inherent problems due to the electrodes use which was partially solved with thorax electrode belts.

The critical examination of two single channel and two multichannel MIT systems for the detection of the cardiac activity and the lung function followed which showed that MIT systems can detect the cardiac activity and the lung function. However it also showed that the use of MIT in this field is still at a very primary level and that an investigation on the development and the characterisation of a fast MIT system targeting the cardiac activity and the lung function could be a subject for research work.

In summary the following experimental areas have been identified from the review for further research work and will be addressed in this thesis:

- The design, the development and the performance characterisation of a single channel zero crossing phase measurement subsystem capable for fast phase measurements. This is addressed in chapter 3.
- The design, the development and the performance characterisation of a multichannel parallel zero crossing phase measurement subsystem based on the single channel system. This is addressed in chapter 4.
- The design, the development and the performance characterisation of a fast parallel zero crossing MIT multichannel system targeting low conductivity industrial applications requiring a high frame rate such as the multiphase flow measurements in oil pipes. This is addressed in chapter 4.
- The design, the development and the performance characterisation of a fast MIT zero crossing single channel system targeting low conductivity biomedical applications requiring a high frame rate such as the detection of the cardiac activity and the lung function. This is addressed in chapter 5.

# 3. The zero crossing phase measurement subsystem

This chapter presents the work performed for the design, the development and the characterisation of a low cost single channel phase measurement subsystem based on the zero crossing technique. It analyses the theoretical and practical aspects for the design of the subsystem and provides the required technical details and information regarding the implementation of the subsystem. The characterisation results of the subsystem in terms of the phase precision, the phase drift and the recording rate are provided.

The chapter begins with section 3.1 where the background leading to the required work is examined briefly and the minimum requirements that the phase measurement subsystem was expected to satisfy are given. In section 3.2 the work performed for the design of the subsystem is presented and in section 3.3 some theoretical aspects of the subsystem are covered.

In section 3.4 the practical work for the development and the implementation of the single channel phase measurement subsystem is described. In section 3.5 the characterisation of the developed single channel phase system in terms of phase precision, phase drift and recording rate is presented and the characterisation results are given. The chapter ends with section 3.6 that summarises the work performed.

## 3.1 Background and requirements

The general conclusion of the review conducted in chapter 2 was that further research is required for the development of MIT systems capable of achieving a high data acquisition rate and the precision required for certain applications. These factors are very important as they affect the speed for a fast MIT multichannel system and the quality of the image reconstruction.

Considering these two factors the review in chapter 2 showed that a phase measurement subsystem based on the zero crossing technique can achieve a high recording rate and good

precision. This was demonstrated in [13] with a single channel phase measurement system implementation tested at 10 MHz. In fact it emerged that the zero crossing technique can provide the highest data acquisition rate when compared to other phase measurement techniques. Since this thesis is interested in the design and the development of high speed MIT systems the zero crossing technique seemed to be a good choice to use for the development of the phase measurement subsystem.

The zero crossing technique was realised in the field of MIT in two different ways. In [32] with the use of discrete analogue components and a microcontroller which served as the phase detector and the counter for the time interval and in [13] with the use of discrete analogue components, an XOR gate as the phase detector and a commercially available counter and an oscilloscope for measuring the XOR pulse time interval.

Both realisations were single channel configurations and it is noted here that there are not any references in the literature about a multichannel phase measurement subsystem based on the zero crossing technique. The phase measurement subsystem in [32] was used in the Moscow multiplexed multichannel MIT system but the phase measurement subsystem in [13] was not used in an MIT system.

The heavy use of discrete components for the realisation of the subsystems in [13] and [32] increases the difficulty of scalability for a multichannel implementation. Furthermore the use of a commercial counter and an oscilloscope in [13] increases the cost of the implementation.

Therefore to design and develop a single channel zero crossing phase measurement subsystem that at least matches the performance of the previously designed systems a general set of requirements must be set which is given below:

- High recording rate – above 50 phase difference values per second
- Phase precision in the order of millidegrees – ideally below 10 millidegrees at 100 $mV_{pp}$ input signal in single channel configuration
- Capability to operate with excitation frequencies from 1 MHz to 20 MHz
- Easy scalability to a multichannel version for use in a parallel multichannel MIT system
- Low cost

## 3.2 Design

This section covers the design of the zero crossing phase measurement subsystem. It examines the architecture of the system and the parts of the system in detail.

### 3.2.1 General architecture

In the requirements set in section 3.1 it was stated that the single channel phase measurement subsystem should be based on the zero crossing technique. Thus it should accept two periodic sinusoidal signals as inputs, detect the zero crossing and measure their phase difference. To realise the subsystem an analogue stage for processing the sinusoidal signals followed by a measurement stage for performing the measurement are required. The concept diagram of the phase measurement subsystem is given in figure 3.1.

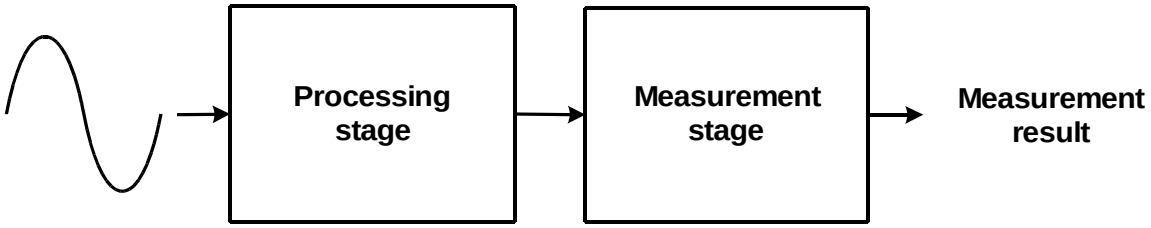


**Figure 3.1**: The concept diagram of the phase measurement subsystem configuration

The processing stage requires two analogue signal chains to process the sinusoidal signals. To introduce the minimum phase measurement error into the signals' original phase difference the signal chains should be identical in terms of circuit construction.

The measurement stage serves two purposes. The first is to detect the phase difference between the reference signal and the detected signal and the second is to measure it. The first purpose is achieved with a phase detector and the second purpose with a counter. These components form the measurement chain and they are cascaded with the phase detector placed in front of the counter.

The measurement stage requires only one measurement chain since it will compare the two input signals to each other. A notable difference from the processing stage however is that the measurement stage can be developed from digital components as well as analogue components.

The single channel configuration can be easily scaled up to a multichannel version. Assuming that an MIT system employs a coil array with C detection coils then C+1 signal chains are required to process the detection signals and the reference signal concurrently. The processing stage becomes a multichannel parallel processing stage by adding more

analogue signal chains.

For C+1 signal processing chains however only C measurement chains are required because the phase detector will use the output of one signal processing chain as the reference and the rest as the detection signals.

Thus the number of the detection channels define the number of the signal processing chains and the measurement chains required for a multichannel version of the subsystem. The simplest form of the configuration will result when C equals 1 which is the single channel configuration. The concept diagram for the hardware required for the multichannel version is shown in figure 3.2.

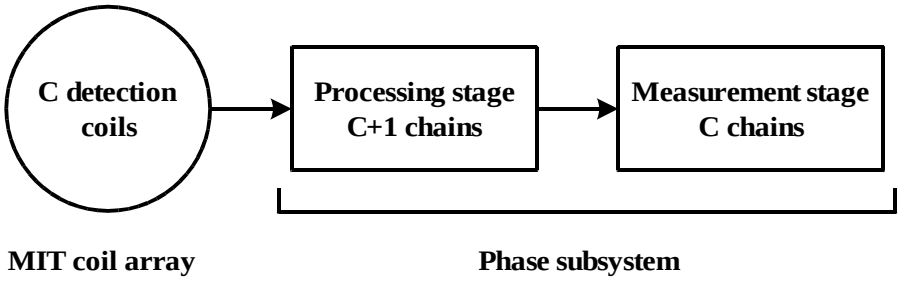


**Figure 3.2**: Block diagram of the hardware required for the multichannel version

The scalability of the phase measurement subsystem can be an easy task provided that certain provisions are taken during the development of the subsystem. These are related to the selection of the electronic components used, the circuit design and the circuit realisation.

### 3.2.2 Implementation details for the analogue processing stage

The literature review in chapter 2 showed that the zero crossing technique can be implemented in a variety of approaches. One approach is to convert the sinusoidal signals into square waves which transforms their phase difference to time difference. The phase difference is then calculated by

$$\Delta \varphi = 2\pi f t \qquad (3.1)$$

where f is the frequency of the sinusoidal signals and t is the time difference of the square waves.

Analogue solutions that can be used to convert a sinewave to square wave include the use of an amplifier wired as a Schmitt trigger, the use of a comparator circuit and the use of cascaded stages of high gain amplifiers. In [13] and [32] the latter was used and thus it was decided to use the same solution for this subsystem as well.

The amplifiers are implemented with a high closed loop gain (for example a gain of 33 was used at each amplifier stage in [13]). When the sinusoidal wave is outputted from each amplifier it “clips” due to the high gain. With each new high gain amplifier stage added the sinewave “clips” more and more and as a result the sinewave eventually is overclipping and is turned into a square wave.

In [11] (from the same author as in [13]) an in depth investigation resulted in the conclusion that the use of cascaded stages of high speed amplifiers with high gain can convert a sinewave to a square wave while maintaining the zero crossings.

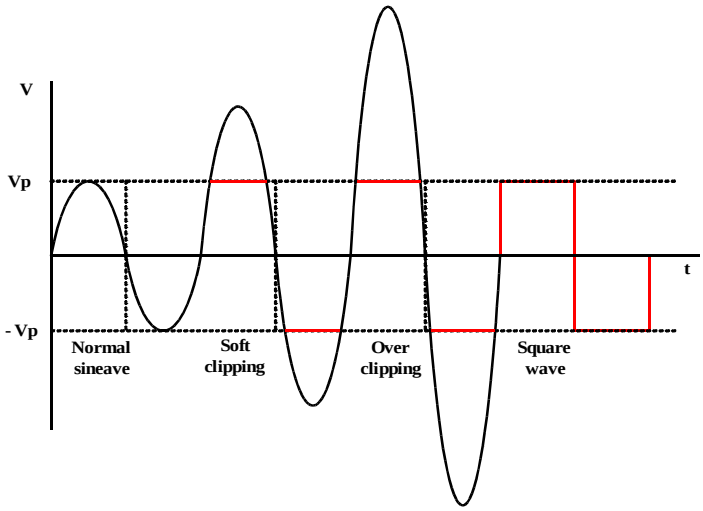


**Figure 3.3**: Sinewave to square wave conversion using high gain saturated amplifiers

The use of high speed amplifiers however is not problem free. Although high speed amplifiers offer a wide bandwidth at unity gain the use of the excessive gain limits their bandwidth. Hence as the frequency of the sinusoidal signals increases it will exceed the amplifiers bandwidth and the conversion will fail. Depending on the gain used the amplifier bandwidth can be as low as tenths of kHz. This prevents the connection to MIT coil arrays that use excitation frequencies in the region of MHz and hence to be used in MIT systems aiming at low conductivity applications.

The use of the excitation frequency in the MHz region introduces another problem. The time difference between the squares waves lies in the region of μs which makes the measurement a challenging task. This is shown below. Assume two noiseless sinusoidal signals $V_1(t)$ and $V_2(t)$ both at frequency f where $t_1$ and $t_3$ are the zero crossing for signal $V_1(t)$ and the $t_2$ and $t_4$ are for signal $V_2(t)$ as shown in figure 3.4.

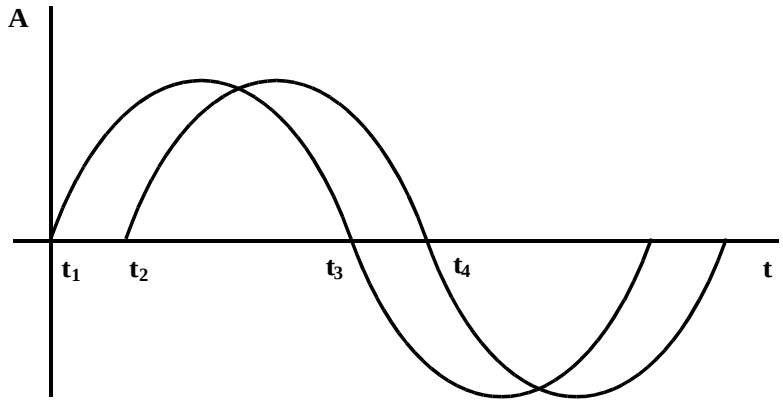


**Figure 3.4**: The two sinusoidal signals having 45 degrees phase difference and their respective zero crossings

If $V_1(t)$ and $V_2(t)$ have a phase difference of 45 degrees between them then their zero crossings can be calculated (Table 3.1 for frequencies from 10 kHz to 10 MHz).

**Table 3.1**: Calculation of the zero crossings of the sinusoidal signals of figure 3.4

| f (kHz) | T (ms) | $t_1$ (ms) | $t_2$ (ms) | $t_3$ (ms) | $t_4$ (ms) | $t_2 - t_1$ (ms) | $t_4 - t_2$ (ms) |
|---|---|---|---|---|---|---|---|
| 1 | 1000 | 0 | 125 | 500 | 625 | 125 | 125 |
| 10 | 100 | 0 | 12.5 | 50 | 62.5 | 12.5 | 12.5 |
| 100 | 10 | 0 | 1.25 | 5 | 6.25 | 1.25 | 1.25 |
| 1000 | 1 | 0 | 0.125 | 0.5 | 0.625 | 0.125 | 0.125 |
| 10000 | 0.1 | 0 | 0.0125 | 0.05 | 0.0625 | 0.0125 | 0.0125 |

From the table it can be seen that at 10 kHz the difference between the zero crossings of the sinusoidal signals is 12.5 ms but at 10 MHz it is 1000 times smaller and becomes only 12.5 μs. The latter obviously requires a huge effort by the measurement section to measure it in comparison with the time difference at 10 kHz. This is especially true if the aim is to measure a phase difference around 10 millidegrees or lower (factor 4500 lower).

To remedy these problems a solution can be provided with the use of the heterodyne technique which is used for shifting the frequency of a sinusoidal signal to a lower frequency or as commonly referred to downconvert the sinusoidal signal (Appendix 1). Downconversion allows the phase measurement subsystem to connect to MIT coil arrays operating in the region of MHz than being limited only to coil arrays operating in the region of kHz. Based on the findings in table 3.1 it was decided to downconvert the input signals to 10 kHz which would ease the phase measurement and at the same time it would not have a big impact on the subsystem's speed.

### 3.2.3 Implementation details for the measurement stage

The purpose of the measurement stage was to detect and measure the phase difference

between the squares waves outputted by the analogue processing stage. The phase difference detection is performed by a phase detector. It is a circuit that senses two periodic inputs and produces an output value proportional to the phase difference between them.

Ideally the phase detector input/output characteristic is a straight line with a slope called the gain and denoted as $K_{PD}$ (unit is V/rad). However in practise a phase detector can exhibit a non-linear and non-monotonic input/output characteristic. [124]

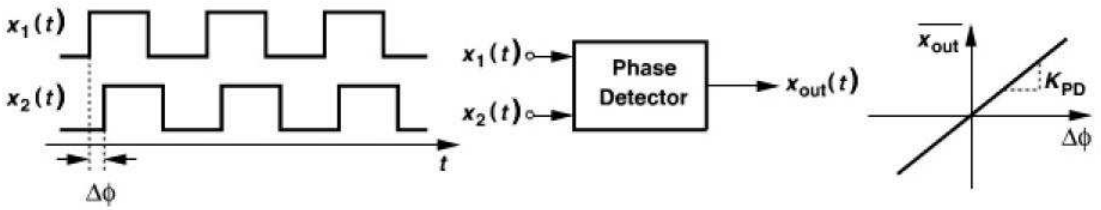


**Figure 3.5**: The ideal phase detector (from [124])

Phase detectors can be electronic circuits like the balanced mixer or electronic components like the flip-flop and the Exclusive OR (XOR) gate [124, 125]. In MIT a microcontroller was used in [32] as a phase detector and an XOR gate in [13]. The latter offers a simple and low cost solution which can reach a good precision in MIT [13]. Furthermore it does not have any apparent effect on the speed of the phase detection other than the XOR gate time delay. Thus it was decided to use it in the phase measurement subsystem. The operation of the XOR gate as a phase detector is quite simple and it is shown in figure 3.6.

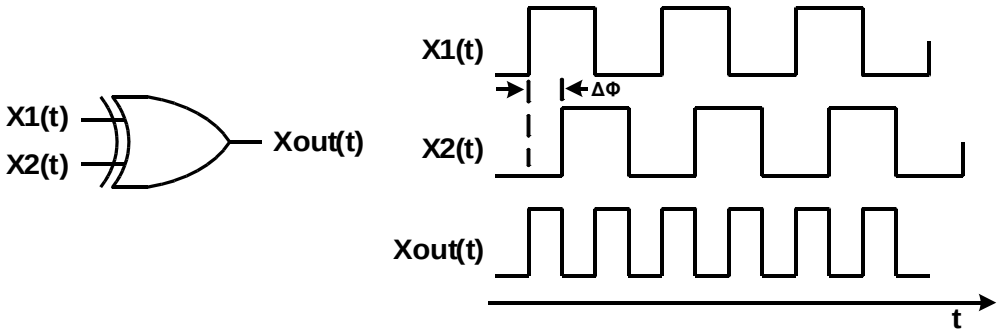


**Figure 3.6**: The XOR phase detector (from [124])

Two square waves with a distinct phase difference are fed to the XOR gate. In chapter 2 it was explained that when the XOR output is high (logic 1) the output pulse width represents the time difference between the signals. Hence by measuring the pulse width the phase difference can be calculated. The XOR gate phase detector can produce a train of pulses as long as the signals to both inputs are maintained. [124, 125]

The input/output characteristic of the XOR phase detector output is proportional to the phase over a π radians range. This means that at a phase difference of 0° the output of the

XOR phase detector is constantly a logic low (0) and at a phase difference of 180° the output of the XOR is constantly a logic high (1). Between these two values the output of the XOR phase detector changes according to the phase difference between the two input signals.

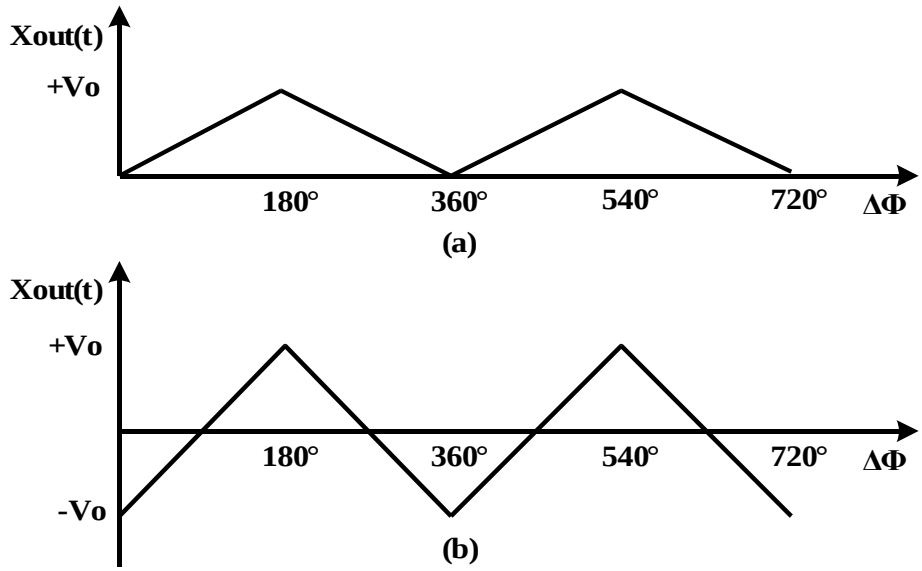


**Figure 3.7**: The input/output characteristic of the XOR phase detector with (a) single-ended output and (b) differential output (from [124])

This input /output characteristic can be a problem in differences that are greater than 180° because it has the same output for different values of the phase difference. Since in MIT the phase difference that is to be detected is in the region millidegrees the input/output characteristic of the XOR phase detector does not affect the phase measurement. [124, 125]

Proceeding to the measurement of the phase difference it is important to realise that in essence what was required was to measure the time interval of the XOR phase detector pulse width output and use that measurement to calculate the phase difference.

Thus what was required was to perform a time interval (TI) measurement which is defined as the measurement of the elapsed time between a designated start phenomenon and a later stop phenomenon [126]. In the case of the XOR phase detector the start phenomenon is the rising edge of the XOR pulse and the stop phenomenon is the falling edge.

A plethora of TI measurement techniques exist that can measure time intervals with single shot, short term or long term measurements capability. They can be realised with analogue or digital components. The latter offers some advantages such as the ease of implementation, fast operation, low noise, reproducible behaviour and ease of scalability. [127]

The TI measurement technique used is expected to measure the XOR pulse time interval with a precision down to millidegrees and as fast as possible. Such a technique is the coarse counting [127] which involves the use of a counter driven by a reference clock of a period $T_{clk}$.

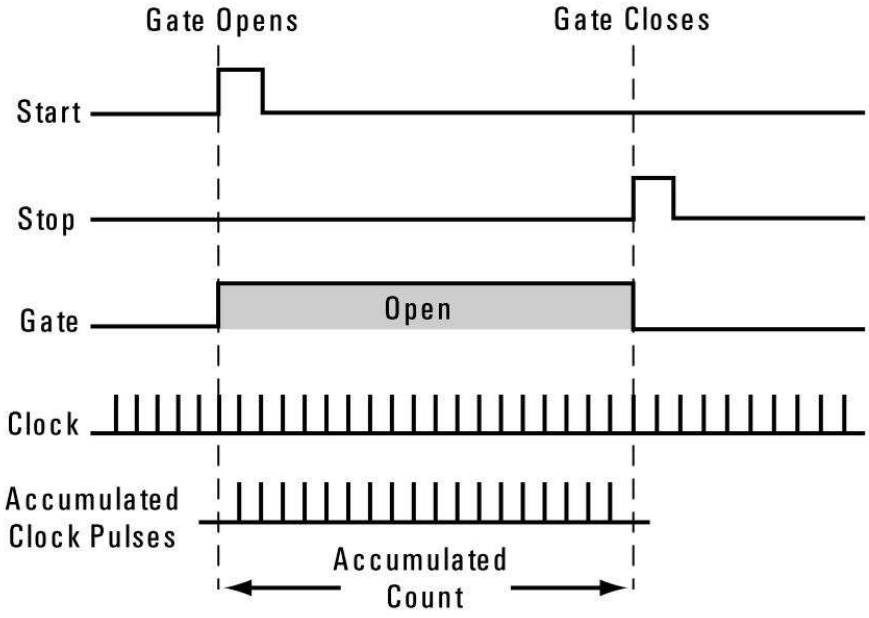


**Figure 3.8**: Time interval measurement (from [126])

The use of the coarse counting technique has four advantages:

1. It is a very fast way of measuring the pulse width because the counter has to measure only the rising (or falling) edges of the clock.
2. The counter design can be kept simple and faults due to complex design can be avoided.
3. The output of the measurement section is an integer something that results in simpler and faster phase calculations in comparison with the use of floating point calculations.
4. The precision of the measurements depends on the amount of clock edges that "fit" in the XOR pulse time interval thus it can be assumed that for a constant XOR pulse time interval the more clock edges fit the better the precision will be.

However the coarse counting technique suffers from four types of error that affect the measurement: [127, 128]

1. The internal trigger error which occurs when the counter fails to acknowledge the start and the stop phenomena to start and end the measurement
2. The time base error which depends on the accuracy of the clock used by the counter and it may occur in the measurement of long time intervals.

3. The systematic error due to the electronic components and circuits used. This error may include differences in the propagation time and errors in the trigger level settings of the start and the stop phenomenon.
4. The ±1 count error which appears to all digital measurements.

The first three errors affect the calculation of the phase value indirectly. The first error can be avoided completely with careful design of the process and the measurement circuit. The second error can be compensated up to a point with the use of accurate clocks with low time jitter figure. The third error is caused by the hardware used and up to a point this also can be compensated if electronics components and circuits with low noise figures are used.

The ±1 count error however affects the calculation of the phase value directly. This is specifically noticeable when a single shot measurement is taken. As shown in figure 3.9 the XOR time interval $T_{XOR}$ is equal to 4.5 clock periods.

Since the counter output is an integral then depending on the start phenomenon it can be equal to either 4 clock periods ($T_1$) or 5 clock periods ($T_2$) or in other words $T_1 < T_{XOR}$ and $T_2 = T_1 + T_{clk}$ [127]. The ±1 count error cannot be avoided however it can be compensated if an even number of consecutive XOR pulses is averaged [127, 128].

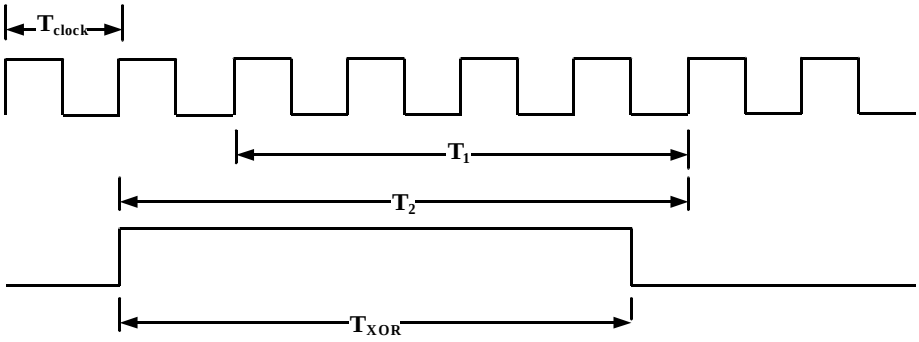


**Figure 3.9**: The ±1 count error

A benefit is that both the XOR phase detector and the coarse counting technique can be implemented completely with digital components. Thus the measurement stage of the phase system can be realised completely with the use of a digital device such as an FPGA provided that an analogue processing stage precedes it.

## 3.3 Theoretical aspects of the subsystem's operation

This section presents the work performed to analyse theoretically some aspects of the zero crossing phase subsystem operation.

### 3.3.1 The equation for calculating the phase difference

To calculate the phase difference by measuring the XOR pulse width time interval with the use of a counter a relationship between the two must be established. The coarse counting technique involves the use of a counter driven by a reference clock of a period $T_{clk}$. For a single XOR pulse the result of the counting is given by [127]

$$t_{XOR} = kT_{clk} \tag{3.2}$$

where k is the decimal number of the clock rising edges per time interval.

In chapter 2 it was shown that the phase difference can be calculated in rad[6] by

$$\Delta\varphi = \omega_s t \quad \text{or} \quad \Delta\varphi = 2\pi f_s t \tag{3.3}$$

where $f_s$ is the signal frequency and t is the time interval.

Since the time interval t is now the $t_{XOR}$ then the equation (3.3) becomes

$$\Delta\varphi = t_{XOR} f_s 2\pi \tag{3.4}$$

Substituting equation (3.2) into (3.4) gives

$$\Delta\varphi = k T_{clk} f_s 2\pi \tag{3.5}$$

which can be used for the calculation of the phase difference for a single XOR pulse i.e. for a single shot measurement.

The accuracy of the counter measurement can be improved by measuring an even number of XOR pulses and averaging them. This compensates for the variation in the offsets and the threshold levels mentioned in chapter 2 and also for the ±1 count error mentioned in section 3.2.3. A very good description on averaging in TI measurements is given in [128].

Instead of measuring the length of each individual XOR pulse and then averaging them it is more efficient to count the total number of the clock rising edges (or falling clock edges) over all XOR pulses and divide that by the number of the XOR pulses. Since one rising (or falling) edge means one clock pulse period then the total time of the XOR pulses train is given by

$$t_{total} = M T_{clk} \tag{3.6}$$

where M is the counted total sum of the clock rising edges over N XOR pulses.

It is stressed here that $t_{total}$ is not equal to the multiplication of $t_{XOR}$ with M because of the

[6] To calculate for degrees the term 2π must be replaced by 360°

±1 count error. Thus the average duration of the XOR pulses train is given by

$$t = \frac{t_{total}}{N} = \frac{M\,T_{clk}}{N} = \frac{M\,T_{clk}}{N} \qquad (3.7)$$

where N is the number of the XOR pulses to be measured

Substituting the term t in equation (3.3) results in

$$\Delta\varphi = \frac{M}{N} T_{clk}\, f_s\, 2\pi \qquad (3.8)$$

The equation (3.8) shows that by measuring M then the averaged phase result of an even number N of XOR pulses can be calculated provided that $T_{clk}$ and $f_s$ are known. The result becomes more accurate as more XOR pulses are averaged however the penalty for that is the prolonged measurement time [127].

### 3.3.2 The measurement stage standard deviation

The average standard deviation of the measurement stage for a single shot measurement is given by [127]

$$\sigma_{avg} = \frac{\pi\, T_{clk}}{8} \qquad (3.9)$$

When averaging is used then if an even number N of XOR pulses is averaged and if N is large enough then $t_{total}/N \approx t_{XOR}$ and the quantization error $t_{total}/N - t_{XOR}$ approaches to zero. Hence the random error of $t_{total}$ becomes smaller by $\sqrt{N}$ compared to the single shot measurement and so the maximum standard deviation for an averaged measurement is given by [127]

$$\sigma_{Nmax} = \frac{T_{clk}}{2\sqrt{N}} \qquad (3.10)$$

and the average standard deviation by [127]

$$\sigma_{Navg} = \frac{\pi\, T_{clk}}{8\sqrt{N}} \qquad (3.11)$$

The equations (3.9), (3.10) and (3.11) can be used to determine the maximum and average standard deviation of a measurement performed by the measurement stage. The maximum and average standard deviation expressed in degrees shows the phase precision the measurement stage.

The values of the standard deviation for an averaged measurement calculated by equations

(3.10) and (3.11) can be expressed into degrees with equation (3.8) by assigning values to $T_{clk,}$ N and $f_s$. Table 3.2 shows the values calculated when $f_s$ is assigned the value of 10 kHz.

**Table 3.2**: The theoretical standard deviation of the measurement stage for averaged measurement

| $T_{clk}$ (ns) | N | $\sigma_{Nmax}$ (s) | $\sigma_{Navg}$ (s) | $\sigma_{Nmax}$ (degrees) | $\sigma_{Navg}$ (degrees) |
|---|---|---|---|---|---|
| 20 | 100 | 1 | 0.785 | 0.0036 | 0.0028 |
| 20 | 1000 | 0.316 | 0.248 | 0.0011 | 0.0009 |
| 10 | 100 | 0.5 | 0.393 | 0.0018 | 0.0014 |
| 10 | 1000 | 0.158 | 0.124 | 0.0006 | 0.0004 |

From the table 3.2 it can be seen that theoretically the measurement stage can achieve a maximum phase precision below 1.2 millidegrees when averaging 1000 XOR pulses (time constant 50 ms) and a maximum phase precision below 4 millidegrees when averaging 100 XOR pulses (time constant 5 ms).

### 3.3.3 The measurement stage recording time

The time required by the measurement stage to measure one phase difference value depends on two factors. The first is the XOR pulses number that will be averaged and the second is the period of the input signal. From figure 3.10 it can be seen that for every period the XOR gate produces two XOR pulses.

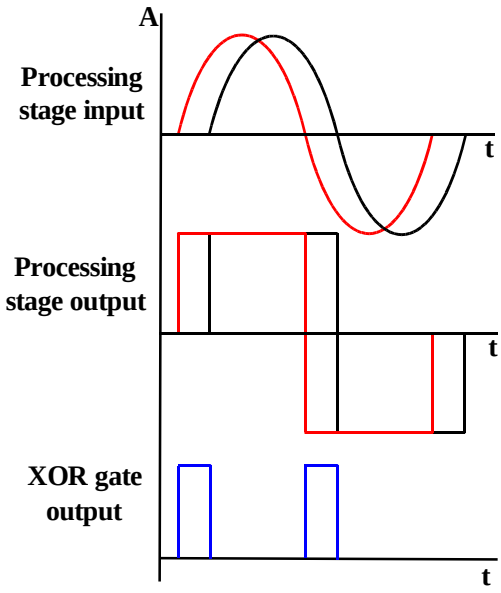


**Figure 3.10**: The XOR pulses and the input signal

Thus the phase measurement time required to measure one phase difference value is given by

$$PMT = \frac{N}{2} \times T_S = \frac{N}{2f_S} \qquad (3.12)$$

where $T_S$ is the period of the input signals, N is the XOR pulses number averaged and $f_S$ is the inputs signals frequency.

The data transmission time required to transmit the data produced when one phase difference value is measured and the overhead data bits from the communication protocol used is given by

$$DTT = \frac{PDB + OVR}{BR} \qquad (3.13)$$

where PDB is the number of the data bits produced when one phase measurement is measured, BR is the bit rate used for the transmission and OVR is the protocol overhead in of the extra bits.

Therefore the recording time MST required by the measurement stage to measure one phase difference value and transmit it to the computer is given by

$$MST = PMT + DTT = \frac{N}{2f_S} + \frac{PDB + OVR}{BR} \qquad (3.14)$$

Equation (3.17) shows the result for MST when a new phase measurement only starts if the data transmission of the result of the previous phase measurement has finished. In other words the DTT is in series with the PMT and this can be denoted by $MST_{series}$.

However when the data transmission of the previous measurement result takes place at the same time as the new phase measurement is executed then the data communication time is completely eliminated from the (3.14) and the MST is equal to the PMT. Thus the DTT is in parallel with the PMT and this is denoted by $MST_{parallel}$ which can be realised only under the condition that PMT ≥ DTT. This condition is essential to be fulfilled otherwise there is a danger to mix the data transmitted to the computer and thus contaminate the phase difference calculation.

### 3.3.4 The resolution of the phase measurement subsystem

The resolution of the phase measurement subsystem defines the minimum measurable XOR pulse width and therefore the minimum phase difference that can be detected. The phase measurement is performed by the measurement stage thus its resolution is directly connected with the standard deviation of the measurement stage. Therefore equations (3.9), (3.10) and (3.11) given in section 3.3.2 for calculating the measurement stage standard

deviation can also be used to calculate the subsystem resolution.

As was pointed in section 3.3.2 the standard deviation of the measurement stage depends on the clock period $T_{clk}$ used in the measurement stage and the measurement performed (single shot or mean averaged). In table 3.2 (section 3.3.2) it was shown that a small $T_{clk}$ combined with the mean averaged phase measurement gives a small subsystem resolution value which in turn permits the measurement of smaller phase differences.

However if a large number of XOR pulses is averaged aiming for a small resolution then the penalty will be the prolonged measurement time which will make the subsystem more precise but slower in comparison when having a larger resolution. Therefore depending on the application a trade off between resolution and speed may be required.

### 3.3.5 The subsystem phase precision and phase drift equations

The phase precision defines the phase measurement precision performed by an MIT system or a phase measurement subsystem expressed in degrees. This is calculated by statistically processing a number of the phase difference values produced during that measurement.

The phase precision can be calculated by using the standard deviation of a repeated set of calculated phase difference values and is expressed in degrees. The equation for the standard deviation is modified to suit the need for calculating the phase precision of the subsystem and becomes

$$Phase\ precision = \sqrt{\frac{1}{n}\sum_{i=1}^{n}\left(\Delta\varphi_i - \bar{\Delta}\varphi\right)^2} \qquad (3.15)$$

where n is the number of the phase measurement sample, $\Delta\Phi$ is the phase difference and $\bar{\Delta}\varphi$ is the mean of the phase difference values population which is given by

$$\bar{\Delta}\varphi = \frac{1}{n}\sum_{i=1}^{n}\Delta\varphi_i \qquad (3.16)$$

The equation (3.15) is the statistical processing of a number of the phase difference values calculated with the use of equation (3.8) and it is used as a performance marker for the complete phase measurement subsystem.

The phase drift shows the fluctuation of the phase difference values during a phase measurement over a period of time due to the thermal drift of the components which causes phase noise, phase jitter and phase shift [11]. The phase drift is expressed in degrees and in [11] it was stated that the phase drift should be calculated for a period of at least 1

hour.

The maximum phase drift of the phase measurement set over a period of time is given by

$$Phase\ drift_{max} = \Delta\varphi_{max} - \Delta\varphi_{min} \qquad (3.17)$$

where $\Delta\Phi_{max}$ is the maximum phase difference value in the set and $\Delta\Phi_{min}$ is the minimum phase difference value in the set.

To smooth out the short term noise a simple moving average (SMA) can be used prior the phase drift calculation. In such case every n phase difference values of the phase measurement set are averaged using

$$\Delta\varphi_{avg} = \frac{\Delta\varphi_1 + \Delta\varphi_2 + \ldots + \Delta\varphi_n}{n} \qquad (3.18)$$

The averaged values $\Delta\Phi_{avg}$ create a new phase measurement set and the average phase drift is calculated from that set using equation (3.17).

## 3.4 Implementation of the zero crossing phase measurement subsystem

This section covers the work performed for the development and realisation of the single channel zero crossing phase measurement subsystem which consists of the analogue processing stage and the measurement stage.

In section 3.2 the theoretical background of the zero crossing phase measurement subsystem was analysed in detail. From that analysis it resulted that the analogue processing stage can be implemented with a downconversion stage followed by cascaded stages of high speed amplifiers with high gain. Furthermore it was decided to downconvert the input signals to 10 kHz.

It was further shown that the measurement stage can be implemented with an XOR gate as the phase detector and a coarse counter for measuring the XOR pulse width. Also it emerged that the measurement stage can be implemented completely with digital components or in a digital device such as an FPGA. The latter was deemed as the most suitable solution for the implementation of the measurement stage and thus was selected.

The use of an FPGA had a number of advantages such as the ease of implementation, level of integration, the fast operation, the low noise, the reproducible behaviour and the ease of scalability. However at the same time care was required for the signal level translation between the two stages, the calculation of the phase difference using the equation (3.8)

developed in section 3.3.1 and the storage of the calculated phase values for image post-processing.

The FPGA device selected for implementing the measurement stage was the Spartan-3 FPGA (Xilinx Inc., California, USA) [129]. The Spartan-3 device was selected because it offered a high logic density and a high input/output count. This ensured that a device change would not be necessary for implementing an up-scaled version of the phase measurement subsystem thus avoiding code migration which would result in a reduced prototyping time. Furthermore the Spartan-3 device low cost and the free programming tools provided by the vendor formed a low cost implementation platform. To realise the measurement stage the Spartan-3 system board (Digilent Inc., Washington, USA) was selected which had an on-board Spartan-3 featuring 1 million gates [130].

### 3.4.1 The analogue processing stage

The purpose of the analogue processing stage is to downconvert the sinusoidal signal received from the MIT coil array while preserving its zero crossing points, to transform it into square pulses and then to transform the square waves into pulses.

#### 3.4.1.1 The downconversion

A way to implement the downconversion is to use a mixer as in [13] and [32]. In [13] two TUF1 passive mixers from Mini-circuits were used successfully in the single channel zero crossing subsystem presented there.

Another way to implement the downconversion part instead of using mixers is to use an analogue multiplier. If the input ($V_x$, $V_y$) and output ($V_{out}$) signals are voltages then the output is the product of the two input voltages divided by a scaling factor K and is given by [131]

$$V_{out} = \frac{V_x V_y}{K} \qquad (3.19)$$

Mathematically multiplication is considered a "four quadrant" operation meaning that the inputs can be positive or negative as can be the output. A multiplier that utilises this it is called a four-quadrant multiplier. However there are one-quadrant multipliers whose inputs and the output must be unipolar and two-quadrant multipliers whose one of the inputs is unipolar and the other input and the output are bipolar.[131]

The analogue multiplier AD835 [132] (Analog Devices Inc., Massachusetts, USA) which

is a four-quadrant, voltage output analogue multiplier was examined for use. It markets a low input noise of 50 nV/√Hz , a settling time of 20 ns, an output swing voltage of ± 2.5 V, an input voltage of ± 1 V, (2 $V_{pp}$), a bandwidth of 250 MHz, a very simple layout with very few external components required and a small 8-pin SOIC casing which can save space at the board level.

The data sheet features combined with a preliminary testing of the device showed that it could replace the TUF1. The main reasons for selecting the AD835 was the low noise figure, the bandwidth, the low cost (however not significantly lower than the TUF1), the ease of implementation and the small casing.

The AD835 has a translinear core supported by three linearised voltage to current converters at the inputs of the device (X, Y, Z) and the load driving output amplifier at the output (W). The scaling voltage U is provided by a band gap reference which as claimed in the data sheet has been designed for ultra noise performance. The X port and Y port are used by the input signals while the Z port provide a summing feature. The functional block of the AD835 is given in figure 3.11.

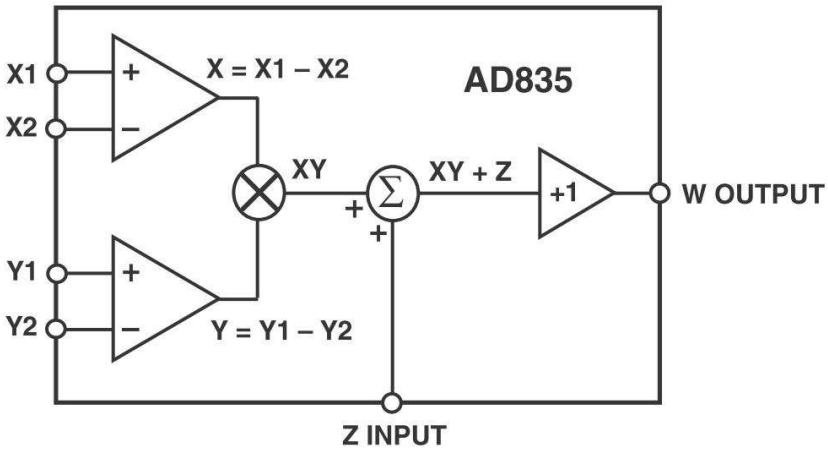


**Figure 3.11**: The AD835 functional block diagram (from [132])

The basic function of the AD835 is given by

$$W = \frac{(X_1 - X_2)(Y_1 - Y_2)}{U} + Z \qquad (3.20)$$

where W, X, Y, Z and U are all expressed in volts.

For a simple multiplier application where $X=X_1-X_2$ and $Y=Y_1-Y_2$ the scaling voltage U is set to 1 V and Z is set to 0. Thus the output W is expressed by

$$W = XY = (X_1 - X_2)(Y_1 - Y_2) \qquad (3.21)$$

However it was empirically observed that when the AD835 was connected in the simple multiplier application and the $X_2$,$Y_2$ and Z inputs were grounded then the equation (3.21) became

$$W = \frac{XY}{2} = \frac{(X_1 - X_2)(Y_1 - Y_2)}{2} \qquad (3.22)$$

Equation (3.22) allows the AD835 to be used as a mixing device for applications that require downconversion as in this case.

To employ the AD835 as a simple multiplier the configuration shown in figure 3.12 was implemented. The pin $Y_1$ was used as the input for the MIT coil array signal and the pin $X_1$ as the input for the downconversion sinusoidal signal. The pins $X_2$, $Y_2$ and Z were tied to ground thus becoming 0 and considering the scaling voltage U as 1 V then the output W obeyed equation (3.22).

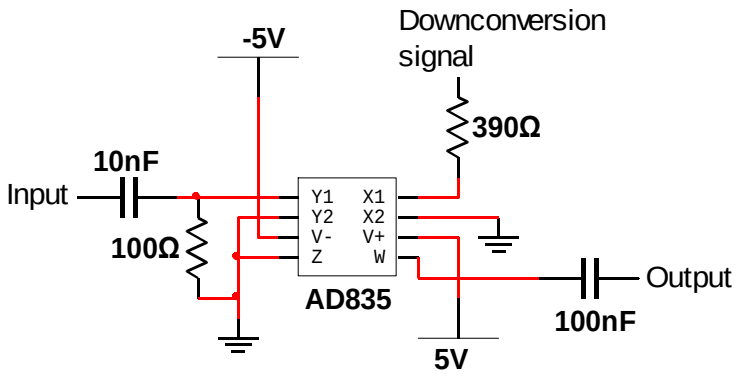


**Figure 3.12**: Implementation circuit of the AD835 multiplier

A first order RC high pass filter with a cut off frequency at 159 kHz was placed in front of the multiplier connected to pin $Y_1$ to remove or at least reduce any low frequency components in the input signal. A 390 Ω resistor was placed in front of pin $X_1$ to provide protection to the multiplier and a 100 nF capacitor was placed at the output to remove any DC component from reaching the gain section.

During the preliminary tests for the AD835 circuit implementation it was investigated whether the RC filter, the 390 Ω resistor and the 100 nF capacitor had any impact on the input sinusoidal signal. For the tests the arbitrary generator AFG3022B (Tektronix Inc., Oregon, USA) for generating the input and the downconverted sinusoidal signals and the digital storage oscilloscope TDS2024B (Tektronix Inc., Oregon, USA) for observing the signals were used.

The input sinusoidal signal was connected to the $Y_1$ pin of the AD835 circuit and its

amplitude was varied from 20 $mV_{pp}$ to 1.8 $V_{pp.}$ The signal frequency was set at 1 MHz, 10 MHz and 20 MHz. The downconversion sinusoidal signal amplitude was 2 $V_{pp}$ and was connected to the $X_1$ pin. The signal frequency was set at 0.9 MHz, 9.99 MHz and 19.99 MHz to downconvert the output signal to 10 kHz. The results of the tests showed that the RC filter, the 100 nF capacitor and the 390 Ω resistor did not affect the input sinusoidal signal at any amplitude or frequency range.

The power pin V- was powered with -5 VDC and the V+ with 5 VDC. Both were decoupled with a 10 nF X7R capacitor placed as close to them as possible and with a 10 μF tantalum capacitor placed at the origin of the power track powering them. The gain function of the AD835 was not realised as was not deemed necessary since the required gain would be provided by the gain section.

### 3.4.1.2 The gain section

The operational amplifier selected for use was the dual AD8056 [133] (Analog Devices Inc., Massachusetts, USA) because it features a 300 MHz unity gain bandwidth, a very low input noise of 6nV/√Hz, a 1400 V/μs slew rate, a 20 ns settling time and it is dual which means that it saves space on board level. It has also been used in [13]. The AD8056 functional block diagram is shown in figure 3.13.

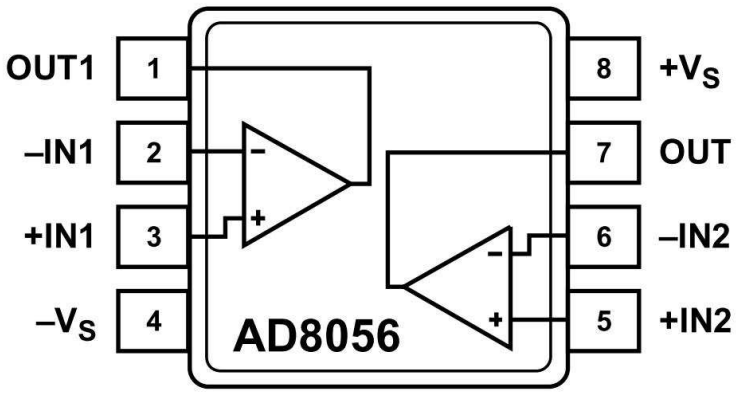


**Figure 3.13**: The AD8056 functional block diagram (from [133])

The gain stage was implemented with four cascaded stages of high speed operational amplifiers with high gain and it is shown in figure 3.14. Each stage comprised an AD8056 in inverting configuration with the $R_g$ at 160 Ω and the $R_f$ at 3300 Ω. Between each stage a 100 nF X7R capacitor was placed to remove any DC component from reaching the next stage. The power pins $-V_s$ and $+V_s$ were powered with -5 VDC and 5 VDC respectively. Both were decoupled with a 10 nF X7R capacitor placed as close to them as possible and with a 10 μF tantalum capacitor placed at the origin of the power track powering them.

In the first three stages a 1 nF X7R capacitor was placed in parallel to the $R_f$ to form a first order low pass active RC filter with a cut off frequency of 48 kHz for removing or smoothing any high frequency components.

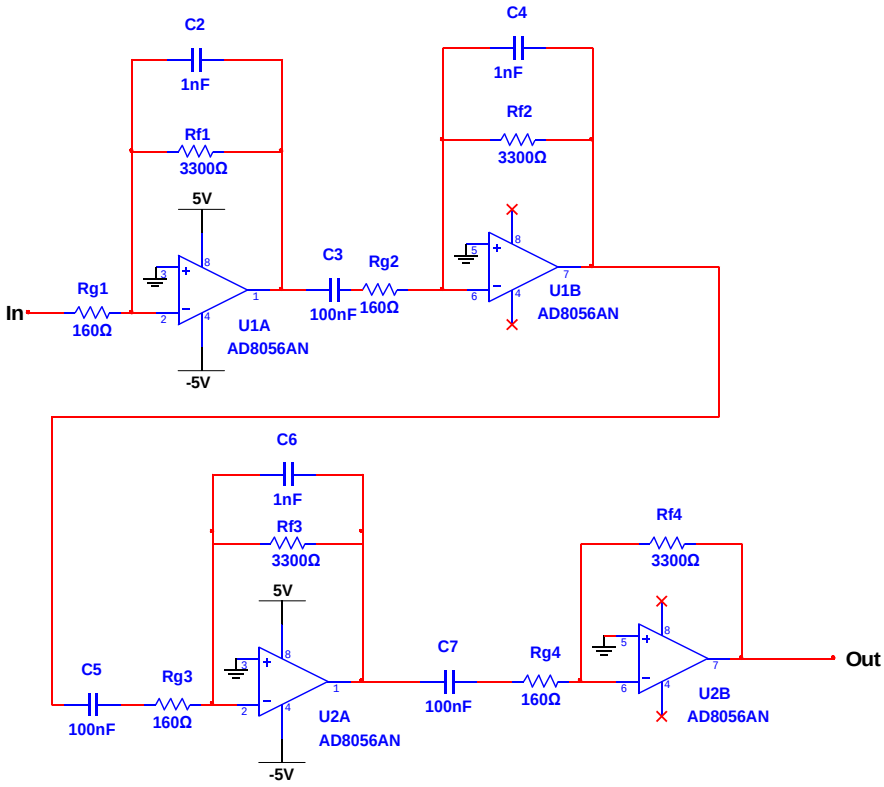


**Figure 3.14**: The implementation of the gain section

The gain of each of the first three stages is given by [134]

$$\frac{Vout}{Vin} = -\frac{X_C \| R_f}{R_g} \qquad (3.23)$$

The $X_c$ is the capacitors impedance which is given by [134]

$$X_C = \frac{1}{2\pi f C} \qquad (3.24)$$

where f is the downconversion frequency.

The fourth stage is an inverting amplifier and its gain is given by [134]

$$\frac{Vout}{Vin} = -\frac{R_f}{R_g} \qquad (3.25)$$

Using equations (3.23), (3.24) and (3.25) the gain for each of the first three stages was calculated to be 17.082 at a frequency of 10 kHz and for the fourth stage was calculated to be 20.625. Thus the total gain for the sinewave to square transformation part was calculated to be 102820. This gain was deemed sufficient for the sinusoidal to square transformation.

To test the performance of the gain section signal chain the arbitrary generator AFG3022B (Tektronix Inc., Oregon, USA) for generating the input downconverted sinusoidal signal and the digital storage oscilloscope TDS2024B (Tektronix Inc., Oregon, USA) for observing the signals were used. The input sinusoidal signal was connected to the inverting input of the first AD8056 circuit (U1A in figure 3.14) and its amplitude was varied from 20 $mV_{pp}$ to 1.8 $V_{pp.}$ The signal frequency was set at 10 kHz to simulate the downconversion frequency.

The output of the gain section was a series of square pulses with a period of 100 μs. The amplitude of the square wave was about 7 V due to the voltage swing of the AD8056 when powered by a ±5 V power supply. The output of the gain stage is shown in figure 3.15.

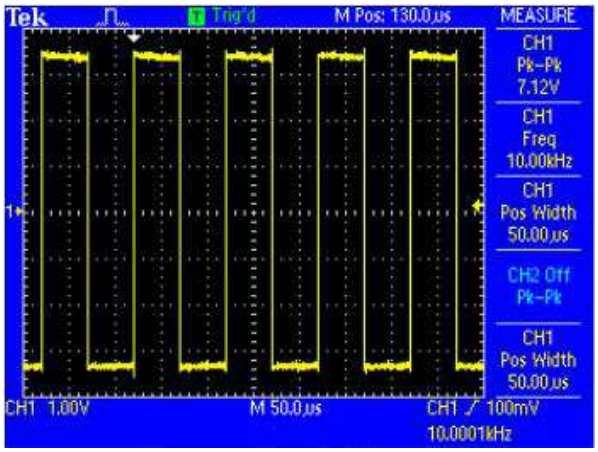


**Figure 3.15**: The output of the analogue processing stage

To give the square wave sharper edges the LT1016 comparator [135] (Linear Technology Corporation, California, USA) was used. The LT1016 was selected because it has 10 ns settling time, it does not require a minimum input slew rate and has a common mode input range of –3.75V to 3.5V with supply voltages of ±5 VDC. The LT1016 was also used in [13] where an investigation showed that when compared to zener diodes it presented superior performance. The LT1016 functional block diagram is shown in figure 3.16.

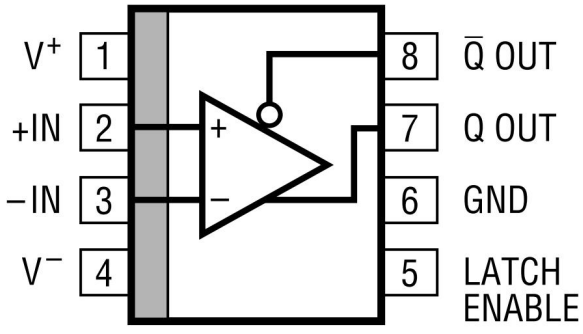


**Figure 3.16**: The LT1016 functional block diagram (from [135])

The LT1016 was implemented as shown in figure 3.17. It was powered by a ±5 VDC power supply with 1 nF X7R decoupling capacitors placed as close as possible to the power pins 1 and 4 and 10 μF electrolytic capacitors placed at the origin of the supplies. The Latch Enable (pin 5) was tied to the ground because a continuous operation for the data was required instead for the device to retain the input data. The $\bar{Q}OUT$ (pin 8) was not required and thus was left unconnected. The output of the LT1016 was a square wave with 100 μs period and 5 V amplitude.

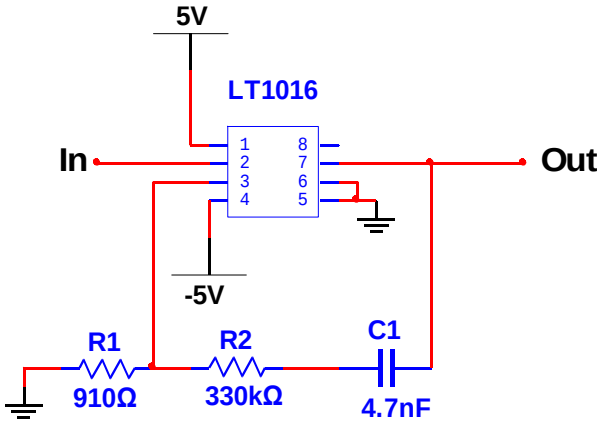


**Figure 3.17**: The implementation of the LT1016 comparator

The use of the Spartan-3 FPGA meant that the 5V output of the LT1016 was required to be voltage translated [136] down to 3.3 V (CMOS level). A cheap solution was to use resistors in a voltage divider configuration. This approach was examined however it was rejected because the amplitude of the level translation was sometimes not steady.

Another solution was the use of the octal bidirectional transceiver 74LVC245[7] [137] which provided asynchronous communication between the data bus A and the data bus B. The direction of the communication depended on the logic level of the DIR pin. When logic low is applied to the output enable input $\bar{O}E$ the device is disabled and bus A is isolated from bus B. The 74LVC245 had a maximum signal propagation delay of 7 ns.

The 74LVC245 was powered by a single 3.3 V power supply. A 1 nF X7R decoupling capacitor was placed close to pin 20 ($V_{CC}$). Since the data transmission direction was required to be from bus A to bus B the DIR pin was tied permanently to 3.3 V. The output enable input was tied to ground to ensure constant communication between the two buses. The unused pins of the device were tied to ground. The output of the 74LVC245 was a square wave with 100 μs period and 3.3 V amplitude. The 74LVC245 pin configuration

[7] This component is manufactured by various manufacturers

and connection diagram is shown in figure 3.18.

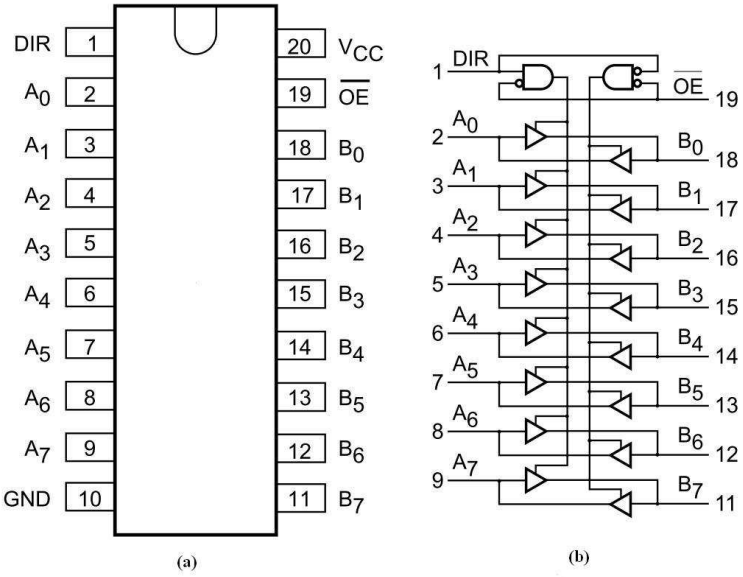


**Figure 3.18**: 74LVC245 pin configuration(a) and connection diagram (b) (from [137])

The level translation of the interface is shown in figure 3.22. The output of the LT1016 (yellow trace) had an amplitude of 5 V. The output of the 74LCV245 (purple trace) retained the pulse width of the input square wave however it lowered the amplitude of the input from 5 V to 3.3 V.

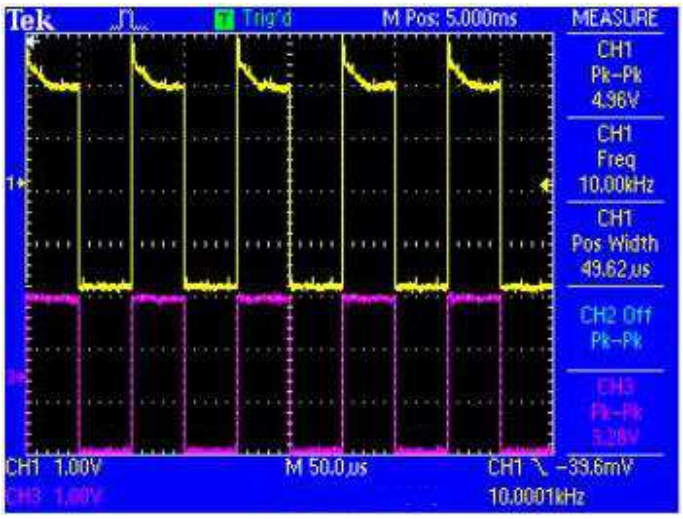


**Figure 3.19**: The level translation by the 74LVH245 – LT1016 input (yellow trace) and 74LVH245 output (purple trace)

### 3.4.2 The measurement stage

The purpose of the measurement stage is to detect the phase difference between two signals after they have been processed by the analogue processing stage, to measure and calculate their phase difference, output the result in a comprehensible manner and store it. These tasks must be performed as quickly as possible in order to achieve a high data

recording rate.

The measurement stage was decided to be implemented in an FPGA due to the advantages it offered. This meant that the measurement section was to be realised using a Hardware Description Language (HDL) which could be either VHDL or Verilog. In this case the VHDL was selected due to the familiarity of the author with it.

The measurement stage implementation was physically materialised on the Spartan-3 system board (Digilent Inc., Washington, USA) [130] which featured a Spartan-3 FPGA (Xilinx Inc., California, USA) of 1 Mgates [129]. As was mentioned in the introduction of section 3.4 the Spartan-3 device was selected because it offered a high logic density and a high input/output count. Furthermore the Spartan-3 was a low cost device and the vendor (Xilinx Inc., California, USA) provided the ISE (Integrated Software Environment) Webpack [138] for the development of the measurement stage in VHDL free of charge. For the simulations of the measurement stage during the development phase the free edition of the ModelSim simulator (Mentor Graphics Inc., Oregon, USA) [139] was used.

In section 3.2.3 it was established that the phase detection can be realised with the use of an XOR gate which produces a pulse whose time interval represents the phase difference of the two signals. It was further established that the measurement of the pulse's time interval can be achieved with the use of a coarse counter. This however covers only the phase detection and the measurement requirements for the measurement section.

To achieve the calculation, the presentation and the storage of the measurement requirements two options were considered. The first was to perform the calculation locally in the FPGA using a floating point arithmetic unit and then present the result to an external monitor (LCD or VGA) and store the measurements to an external device. This option however was considered too complicated due to the extensive and complicated VHDL programming required to realise it.

The second option was to develop an application software using a high level language on a computer to perform those tasks. The application software would offer the opportunity to automate much of the process and it could be programmed with a Graphical User Interface (GUI) to ease the interaction with the user.

The presentation of the calculations results could be on the computer monitor and the calculation results could be stored in a retrievable form on the local hard disk. However

this option required that a solid and dependable communication path should be established between the computer and the FPGA for transmitting the raw data from the FPGA to the computer.

This option was considered easier to implement than the first option and therefore it was selected which resulted in the measurement stage having two parts one for the measurement and one for the communication with the computer as shown in the block diagram of the measurement stage in figure 3.20.

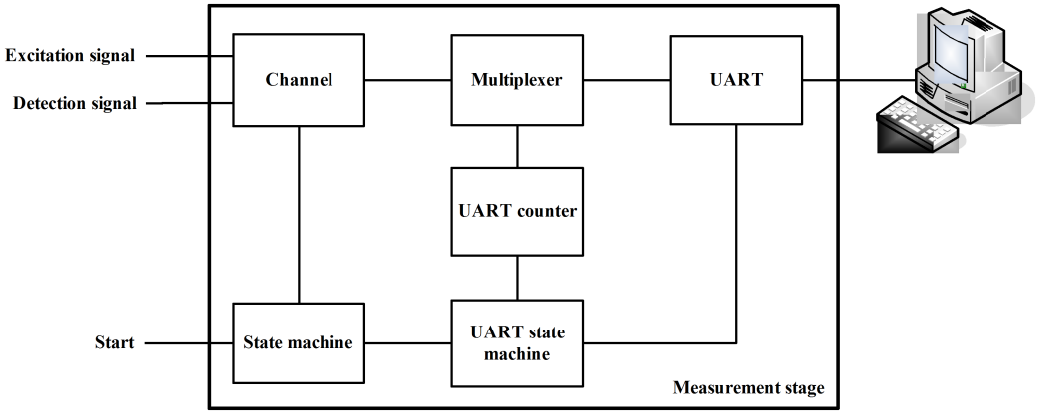


**Figure 3.20**: Block diagram of the measurement stage

### 3.4.2.1 The component channel

The implementation of the phase detector and the coarse counter in the FPGA was the first task undertaken. It was decided to implement this part in the form of a component named “channel” which was to be a black box with certain inputs and outputs. This approach would enable the component to be reproduced as required by future multichannel versions of the subsystem without requiring any change in its architecture.

The input ports to the component was the reference signal, the measured signal, the clock, the start signal, the stop signal, the reset and the measurement word which set the number of XOR output pulses to be measured. Apart from the measurement word which was assigned directly in the VHDL code the rest of the input ports were tied physically to the input signals through the FPGA pins. The reference signal was tied to the input excitation signal, the measured signal to the input detection signal, the clock to the clocking device, the start signal to the measurement stage state machine and the reset to reset signal of the measurement stage.

The output ports of the component was the measurement result and the measurement done signal. The measurement result output was tied to a multiplexer which held at its output the measurement result as long as the multiplexer selection was not changed. The multiplexer

selection was not changed while a new measurement was performed but it was changed when the measurement was done to output the new result. The measurement done signal was used to indicate to the state machine that the channel has finished the measurement.

The functional block of the component's architecture is shown in figure 3.21. However it is noted that for clarity some internal connecting wires have been omitted. The XOR gate is the phase detector. The coarse counter that measures the time interval of the XOR pulse consists of the rise edge detector (RED), the falling edge detector (FED), the measurement counter (MCN), the increment counter (ICN) and the comparator (CMP). A 32-bit (4 bytes) register (REG) was used as a temporary memory for the measurement result and the state machine (SM) controlled the whole operation of the component.

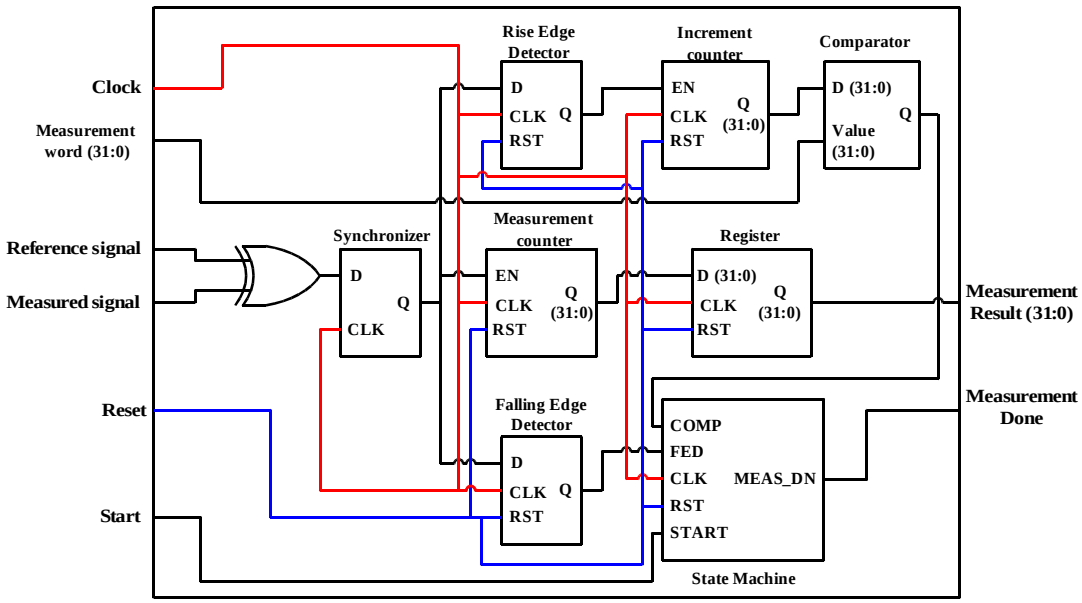


**Figure 3.21**: The functional block diagram of the component channel

The channel operates as follows. When two squared sinusoidal signals with a phase difference ΔΦ are applied to the inputs of the XOR gate a pulse representing their phase difference is generated at the output of the XOR. It is noted here that the time delays between the two signals from the time they enter the FPGA until they are fed to the XOR gate are implementation specific and are expected to be the same since they travel on the same die and thus no irregularities are inserted in their phase difference.

When the SM receive the start signal it enables the MCN which starts to count the duration of the XOR pulse by using the rising edges of the clock. The RED monitors the output of the XOR gate and increases the INC when a new XOR pulse rising edge is detected. The output of the INC is fed to the CMP which constantly compares it to the value set by the measurement word which represents the number of the XOR pulses to be measured for

averaging. If they are equal the CMP alerts the SM that the value had been reached.

When the SM is alerted by the CMP that the set value had been reached it waits for the FED to signal that it detected the falling edge of the current XOR pulse. After it disables the MCN. In this way it is ensured that the last XOR pulse was counted completely before the MCN was disabled. The SM enables the REG to get the data from the MCN and at the same time it activates the measurement done signal. The SM is implemented as a Mealy finite state machine and the flow diagram is shown in figure 3.22.

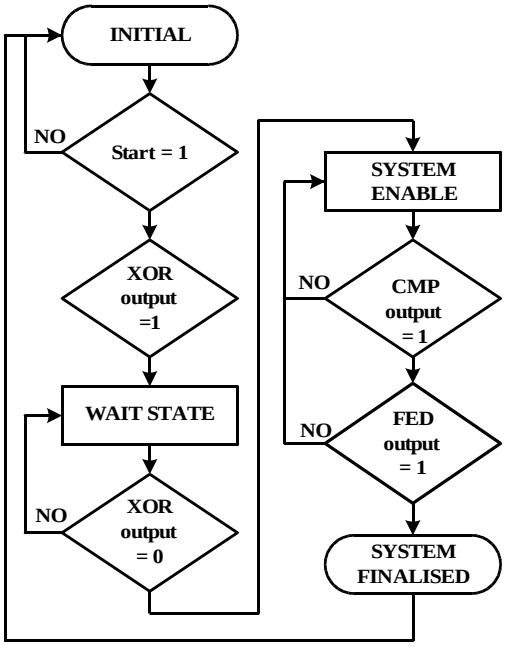


**Figure 3.22**: The channel's state machine flow diagram

In the functional block of the component channel given in figure 3.21 the XOR gate is followed by a synchroniser which is used to synchronise the asynchronous input signals with the synchronously clocked system. This was implemented in order to prevent metastability which occurs when a signal is transferred between circuits that have unrelated or asynchronous clock domains [140, 141]. In [128] this phenomenon is called direct gating and in [142] a tutorial on metastability and synchronisers is given.

This metastability phenomenon was observed by the author during the preliminary tests of the measurement section before a synchroniser was placed between the asynchronous domain (XOR gate) and the synchronous domain (coarse counter) and was recorded during repeated test phase measurements. The observed metastability is shown in figure 3.23 where a phase value is clearly out of the range of the rest phase values. The circuit in figure 3.21 is not the original circuit which creates the observed metastability shown in figure 3.23 but the new one with the synchroniser included.

Since equation (3.8) was used to calculate the phase measurement where the only measurement input is the number of the XOR pulses it was obvious that the 90 degrees value was a result of an extensive measurement of XOR pulses. This could only happen if the measurement stage was in metastability since the rest of the measurements were performed as expected. Although the time is not shown in the graph it was observed by the author that when the test suffered from metastability the test time was longer compared to tests in which metastability did not occur.

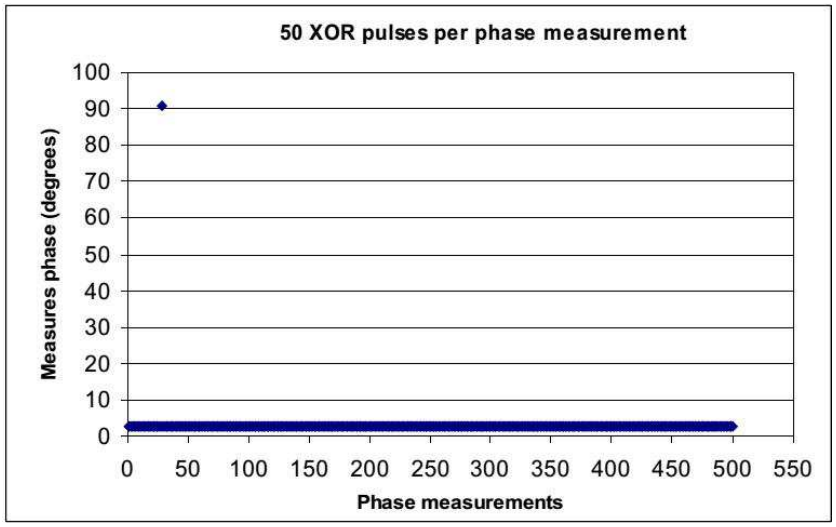


**Figure 3.23**: The metastability phenomenon recorded during the preliminary tests of the measurement section

The metastability Mean Time Between Failure (MTBF) for a flip-flop can be calculated by [140-142]

$$MTBF = \frac{e^{\frac{t_{MET}}{C_2}}}{C_1 \times f_{CLK} \times f_{DATA}} \qquad (3.26)$$

where e = 2.718281828..., $t_{MET}$ is the time delay for the metastability to resolve itself, $f_{CLK}$ is the clock frequency of the synchronous domain, $f_{DATA}$ is the frequency of the data in the asynchronous domain, $C_1$ is a constant representing the metastability catching set-up time window and $C_2$ is a constant describing the speed with which the metastable condition is resolved.

Equation (3.26) can be used to calculate the MTBF of the whole design provided that all synchronisers chains MTBF are added together. The failure rate for a synchroniser or a design is given by [141, 142]

$$failure\ rate = \frac{1}{MTBF} \qquad (3.27)$$

The solution proposed in [128, 140-142] regarding metastability is the use of D flip flops

between the asynchronous and the synchronous circuits. For the measurement section the synchroniser was placed between the XOR gate and the synchronous circuits and consisted of two cascading D flip flops which synchronised the XOR output pulse with the system clock. The use of two cascading D flip flops decreases the failure rate more than using one D flip flops and thus it was preferred. The synchroniser stage is shown in detail in figure 3.24.

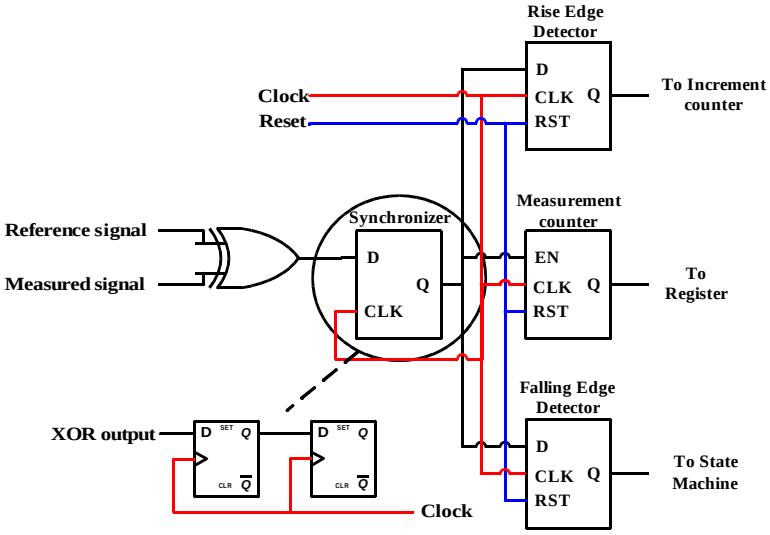


**Figure 3.24**: The synchroniser stage in detail

After implementing the synchroniser in the measurement section the metastability phenomenon was not observed again. However it is noted here that the synchroniser circuit does not remove the problem of metastability as this is impossible but it greatly reduces the probability of the measurement section to enter into a metastability state.

The failure rate calculation of a flip-flop or a design requires extensive testing for calculating reliably $C_1$ and $C_2$ and then the use of equations (3.26) and (3.27) [140-142]. This escaped the aim of this project and was not pursuit further.

### 3.4.2.2 The UART component

As was mentioned earlier in this section it was decided to use a computer for the calculation of the phase difference using equation (3.8) and for the storage and presentation of the data. A communication path was therefore required between the FPGA and the computer for transmitting the measurement raw data.

A number of communication technologies exist however the implementation of a Universal Asynchronous Receiver/Transmitter (UART) controller for setting an RS232 communication is generally simple in the FPGA. It is further eased by the abundance of ready made UART communication controllers on the Internet which can be implemented

straight away with minimal effort and preliminary testing. The Spartan-3 system board [130] provided an on-board RS232 port with the MAX3232 IC (Texas Instruments Inc., Texas, USA) [143] and thus the RS232 was selected.

A simple UART component which was posted free on the Internet under the GNU General Public Licence was used [144]. The UART component provided asynchronous communication between the FPGA and the computer. It supported the transmission of 8 bits and 1 stop bit without parity bit and it could provide bit rates up to 115200 bits per second. The top level implementation of the controller consisted of the transmit module, the receive module and the baud generator. The UART component is shown in figure 3.25.

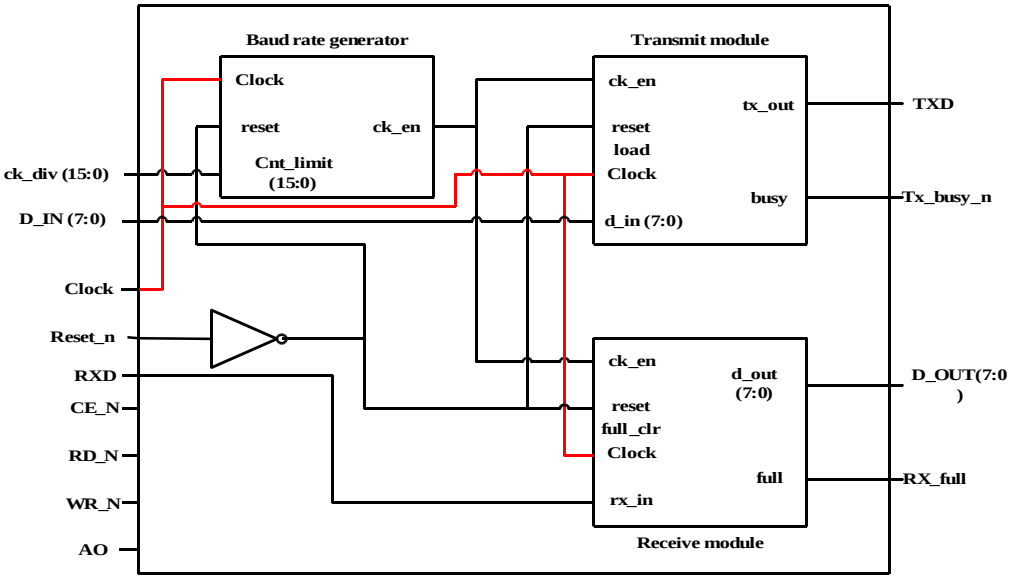


**Figure 3.25**: The UART component as implemented in the FPGA

To enable the UART component the Chip Enable (CE_N) must be set at logic low and the Reset_n at logic high. Both must be retained in the respective logic state while a receive or transmit operation takes place.

To set the UART component to receive data from the computer the Read Enable (RD_N) and the A0 must be set at logic low. The A0 is used by the UART component to set the interrupts register. Then the receive module reads the data byte from the RXD pin and transforms the serial its into a logic vector and outputs the result from D_OUT. Concurrently the receive module sets the RX_full flag to logic high to indicate that a byte is ready to be read.

To transmit data to the computer the Enable (WR_N) and the A0 are set to logic low. The transmit module reads the logic vector D_IN and then transforms it into serial. It then outputs it at TXD in serial bits. While the transmission operation is used by the UART

component the Tx_busy_n flag is set high to notify that a transmission operation is taking place.

The bit rate is set with the ck_div word which is calculated by

$$ckdiv = \frac{f_{CLK}}{bit\ rate \times 3} \qquad (3.28)$$

where $f_{CLK}$ is the clock frequency clocking the UART component in the FPGA and the bit rate.

The maximum communication rate the UART component can achieve is 115200 bits per second. However it is mentioned here that the equation (3.28) sometimes produces values with decimal points which are dropped when converting the value from decimal to binary. The following table was produced for different $f_{CLK}$ which shows the actual values of the bit rate passed in the UART component and the percentage error in comparison to the theoretical bit rate.

**Table 3.3**: The actual bit rate values passed to the UART component and the bit rate error percentage

| $F_{CLK}$ (MHz) | Bit rate | Ck div calculated value (decimal) | Ck div value used (decimal) | Actual bit rate for use | Calculated bit rate error percentage |
|---|---|---|---|---|---|
| 50 | 19200 | 868.0556 | 868 | 19201 | 0.006% |
| 50 | 33600 | 496.0317 | 496 | 33602 | 0.006% |
| 50 | 57800 | 288.3506 | 288 | 57870 | 0.122% |
| 50 | 115200 | 144.6759 | 145 | 114942 | 0.223% |
| 100 | 19200 | 1736.111 | 1736 | 19201 | 0.006% |
| 100 | 33600 | 992.0635 | 992 | 33602 | 0.006% |
| 100 | 57800 | 576.7013 | 576 | 57770 | 0.052% |
| 100 | 115200 | 289.3519 | 289 | 115340 | 0.122% |

From table 3.3 it can be seen that the expected bit rate error was very small and in addition to the small distance (below 2 meters) between the Spartan-3 system board and the computer it was not expected to have any effect on the communication between them.

The component was tested at 19200, 33600, 57800 and 115200 bits per second and it operated successfully at all bit rates. To decrease the time required for the data communication the UART bit rate was permanently set at 115200 bits per second.

The 115200 bits per second bit rate means that the UART component can transmit 115 bits per ms or 11 bits every 100 μs. The measurement output of the channel was 4 bytes or 32 bits for every phase measurement result. The RS232 overhead was 2 bits per byte (start bit and stop bit, no parity) which increases the total number of the transmitted bits to 40. This

means that the UART component would require 347 µs to transmit the 4 bytes of the measurement result to the computer.

### 3.4.2.3 The measurement stage as a working unit

The measurement stage was formed into the working unit as shown in figure 3.26. The section consists of the channel block, a 32-bit to 8-bit multiplexer, a UART counter to drive the multiplexer, a pulse detector and two state machines for the UART and the overall measurement section.

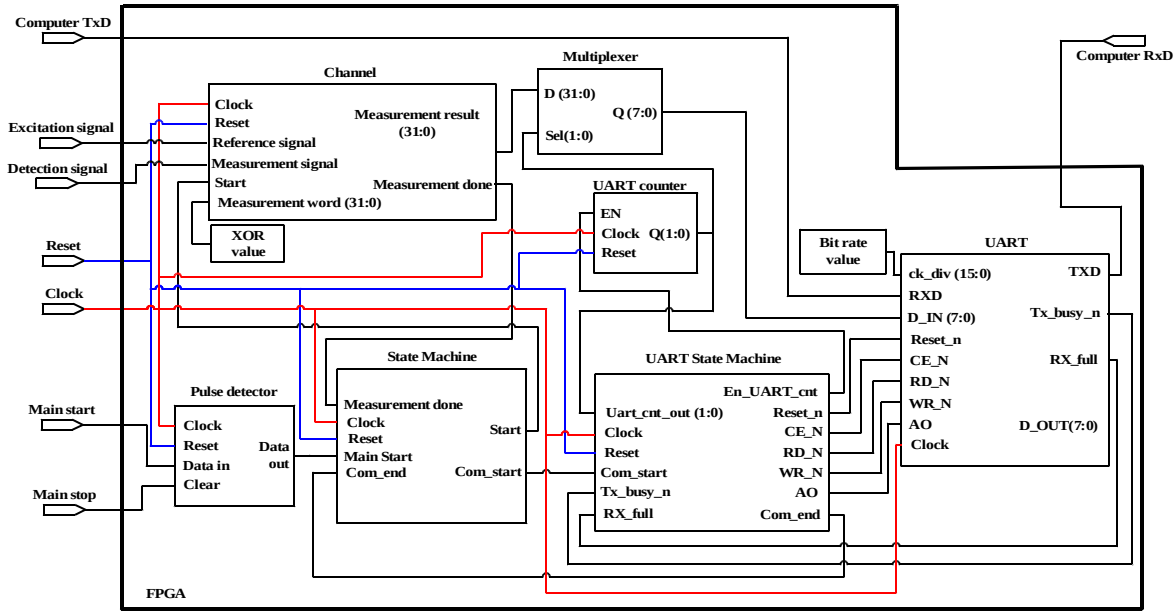


**Figure 3.26**: The complete measurement stage implementation in the FPGA

The measurement stage implementation was physically materialised on the Spartan-3 system board (Digilent Inc., Washington, USA) [130] which featured a Spartan-3 FPGA (Xilinx Inc., California, USA) of 1 Mgates [129]. The Spartan-3 system board further provided the on-board 50 MHz crystal oscillator SG-8002JF (Epson Toyocom, California, USA), 8 push buttons and an RS232 port with the MAX3232 IC (Texas Instruments Inc., Texas, USA) [143]. The inputs and the output were tied to the FPGA pins and through them to their respective inputs or outputs of the electronic components.

The clock input was connected to the on-board crystal oscillator. The excitation and the detection signal inputs were connected to the respective 74LVC245 level translation IC outputs. The reset, the main start and the main stop inputs were each connected to a push button. The component's RxD input was connected to the computer's RS232 port TxD pin and the component's TxD output was connected to the RxD pin of the computer RS232 port.

At first it was considered to use the channel state machine for controlling the computer – FPGA communication however this would invalidate the concept of having the component channel as an independent entity to facilitate easy scalability. For this reason the use of a main state machine (MSM) was considered a better choice and was implemented. Similarly instead of having the MSM performing two roles i.e. the measurement stage central control and the data transmission control it was decided to implement a UART state machine with the sole purpose to control the data transmission.

The multiplexer was used to bridge the line width mismatch between the measurement output of the channel and the UART component input. The measurement output of the channel was a logic vector (31:0) while the D_IN input of the RS232 controller was a logic vector (7:0). A multiplexer with a logic vector (31:0) input, a logic vector (7:0) output and a select line input (1:0) was selected for use.

The UART counter was an increment counter whose output was connected to the select line of the multiplexer. As the UART counter outputs increased the selected data were transferred from the multiplexer’s input to the multiplexer's output and from there to the UART component. This configuration minimized the intervention of the UART SM in the data transmission into enabling the UART counter and the transmission operation of the UART component. Thus it made the whole process more flexible and also created the provisions for the data transmission of the previous measurement result while the new measurement took place.

The pulse detector outputted the logic high of a signal appearing in its input even when that signal was not high any more until it was cleared by setting the CLEAR into logic high. The use of this component ensured that the signals that were crucial for the correct operation of the measurement section were retained at logic high until they were read by their intended recipient.

In the measurement stage the pulse detector was used to hold the logic high of the main start. The user pushed the main start push button once which set the output of the pulse detector into logic high and in turn signalled the MSM to begin a measurement. The user did not have to press the main start push button again because the pulse detector output retained the logic high of the main start and thus the MSM continued measuring. When the user pressed the main stop button the pulse detector output was cleared and set in logic low which in turn signalled the MSM to stop taking measurements.

The MSM and UART SM were Mealy finite state machine. The MSM output values relied on the external inputs from the main start push button and the channel component while the UART SM output relied on external input from the UART counter and the UART component and their current state. Both state machines were clocked by the same clock as the rest of the measurement section. The MSM flow diagram is shown in figure 3.27 below.

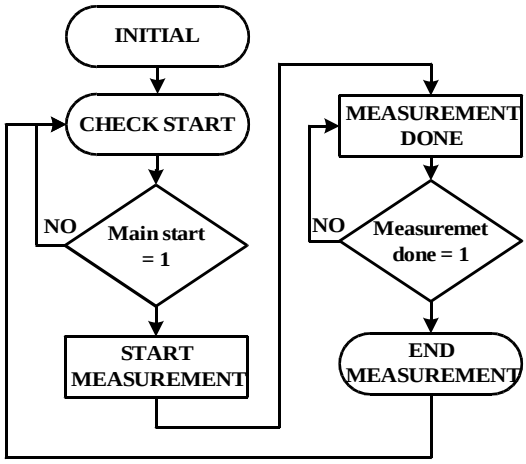


**Figure 3.27**: The main state machine (MSM) flow diagram

Prior the measurement the MSM constantly checked the main start input. When it was set to logic high then the MSM sent the start signal to the channel to begin the phase measurement. When the MSM received the measurement done signal from the channel it signalled the UART SM to start the data transmission and returned back to the main start checking state. If the main start was still on logic high the whole procedure was repeated again.

The UART SM enabled the UART counter which was connected to the select line of the multiplexer. As the UART counter value increased the multiplexer sent the measurement result to the UART component byte after byte. Concurrently the UART SM enabled the UART component for a transmission operation in which it transmitted the measurement result to the computer byte after byte. This procedure went on until the UART counter reached “00” which meant that the data transmission process was finished and the UART SM returned back to the START COMMUNICATION state.

It is worth noticing here that the two TRANSMISSION PART states were used to make sure that the byte was transferred correctly to the computer. The Finish COMMUNICATION state was used to make sure that the transmission was ended and the UART counter was reset to initial conditions. During the preliminary testing of the UART

component it was noticed that the use of a single TRANSMISSION PART state sometimes resulted in the wrong transmission of the data byte.

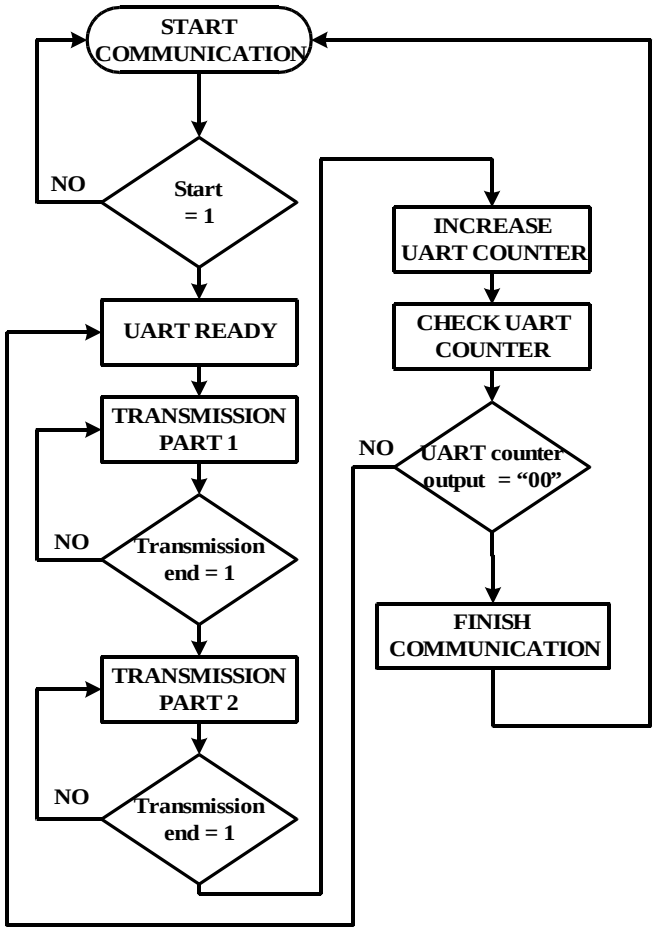


**Figure 3.28**: The UART state machine (UART SM) flow diagram

In section 3.3.3 the equations (3.12), (3.13) and (3.14) were developed to calculate the Phase Measurement Time (PMT), the Data Transfer Time (DTT) and the Measurement Stage Time (MST). These equations were used to theoretically investigate the performance of the UART component in regards to the MST.

The DTT can be calculated using equation (3.13) and was calculated to 347 μs at the end of the section 3.4.2.2. The PMT however is calculated by the values of N and $f_{DC}$. The table 3.4 can be produced for the MST for a limited number of N and $f_{DC}$ combinations. It is reminded that for the $MST_{series}$ the previous phase measurement result is transmitted before the next phase measurement start. For the $MST_{parallel}$ the transmission of the previous phase measurement result is transmitted while the new phase measurement is taken provided that the PMT ≥ DTT.

**Table 3.4**: Measurement stage time for various values of N and $f_{DC}$

| $f_{DC}$ (kHz) | N (XOR pulses) | PMT (μs) | DTT (μs) | $MST_{series}$ (μs) | $MST_{parallel}$ (μs) |
|---|---|---|---|---|---|
| 100 | 100 | 500 | 347 | 847 | 500 |
| 100 | 50 | 250 | 347 | 597 | PMT < DTT |
| 100 | 10 | 50 | 347 | 397 | PMT < DTT |
| 50 | 100 | 1000 | 347 | 1347 | 1000 |
| 50 | 50 | 500 | 347 | 847 | 500 |
| 50 | 10 | 100 | 347 | 447 | PMT < DTT |
| 10 | 100 | 5000 | 347 | 5347 | 5000 |
| 10 | 50 | 2500 | 347 | 247 | 2500 |
| 10 | 10 | 500 | 347 | 847 | 500 |

From the table it can be seen that for the $MST_{series}$ the UART component satisfies the transmission demand for the data load from the channel block for all $f_{DC}$ and N. For the $MST_{parallel}$ the UART component satisfies most of the transmission demand except when the $f_{DC}$ is higher than 50 kHz and at the same time the value of N is equal or lower than 50 XOR pulses.

### 3.4.2.4 Synthesis of the measurement stage

The measurement section was synthesized using the ISE Webpack 13.0. The target device was the Spartan-3 FPGA on-board the Spartan-3 system board. The Spartan-3 device has two different speed grades (-4 and -5) which are indicative figures of the worst case timing delays across all the process corners of the device. The results of the synthesis are shown in the table below.

**Table 3.5**: Synthesis results of the phase measurement subsystem

| Spartan-3 speed grade | Synthesized minimum clock period (ns) | Maximum operational frequency (MHz) |
|---|---|---|
| -4 | 7.066 | 141.52 |
| -5 | 6.089 | 164.22 |

The synthesis of the measurement stage showed that it can operate at a minimum clock pulse period of about 7 ns when a Spartan-3 grade -4 is used and with a minimum clock pulse period of about 6 ns when a Spartan-3 grade -5 will be used. Although these figures are only indicative as no Place & Route has taken place and thus no routing delays have been included they show that the measurement stage can become extremely fast.

### 3.4.2.5 The computer application software

In the introduction of section 3.4 it was stated that the option for developing an application software for calculating, presenting and storing the phase differences calculations was

made. The application software was required to serve five requirements which were to maintain a communication over RS232 between the computer and the FPGA, to process the raw data transmitted from the FPGA, to calculate the phase difference, to present and to store the calculated phase difference values.

The Labwindows/CVI 7.0 graphical C compiler from National Instruments Inc [145] was selected to develop the application software. It has a wealth of built-in libraries that eased the development and thus shortened the time required. Being a graphical compiler means that it incorporated the capability for programming a GUI. The application software was programmed with automation in mind while at the same required minimum input from the user and was used in the Microsoft Windows XP operating system. The Labwindows/CVI application software code is given in Appendix 4.

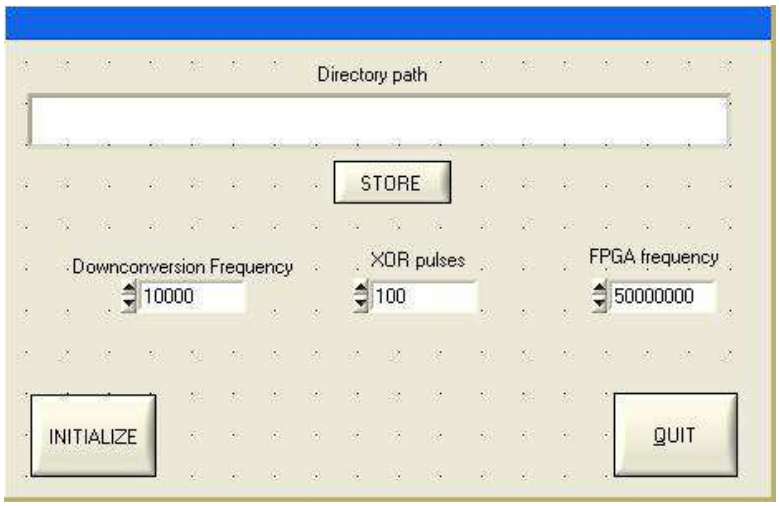


**Figure 3.29**: The application software GUI

In the GUI which is shown in figure 3.29 the user sets the directory path for storing the calculated values using the store button, sets the values for the downconverted frequency, the XOR pulses and the FPGA frequency using the numeric controls. The application software initialized by clicking on the initialization button. The downconverted frequency, the XOR pulses and the FPGA frequency were used for the phase difference calculations.

In the background the application software was programmed to execute automatically a number of operations. When the initialization button was pressed first the serial port of the computer was automatically configured to the required settings (port number, 115200 bit rate, 8 bits, 1 stop bit, no parity, in buffer size 6000 bytes, out buffer size 6000 bytes). Then the function “ComCallback” was installed by the application software to monitor constantly the serial port waiting for the data from the FPGA. A flag was raised notifying when data were present. The data bytes were read and assigned to variables which were

processed and then used for calculating the phase difference. After the calculation the calculated values were time stamped in the form of hours:minutes:seconds and then stored into a text file in the designated directory set by the user.

This procedure continued without requiring any user intervention. If for any reason there were not any data at the serial port the application software continued to monitor the serial port for new data to appear with the "ComCallback" function. The user could close the application software by clicking on the quit button.

## 3.5 Characterisation

This section presents the work performed for the characterisation of the single channel phase measurement subsystem. The characterisation results are discussed in their respective sections.

### 3.5.1 Measurement stage characterisation

The measurement stage was characterised in terms of the phase precision and the recording time it could achieve and the results were compared to the theoretical values obtained in section 3.3.

#### 3.5.1.1 Phase precision

The measurement stage was programmed in the Spartan-3 which was on-board the Spartan-3 system board [130]. The Spartan-3 was clocked by the on-board clock at 50 MHz which gave a $T_{clk}$ equal to 20 ns. For the characterisation the test set-up illustrated in figure 3.30 was used.

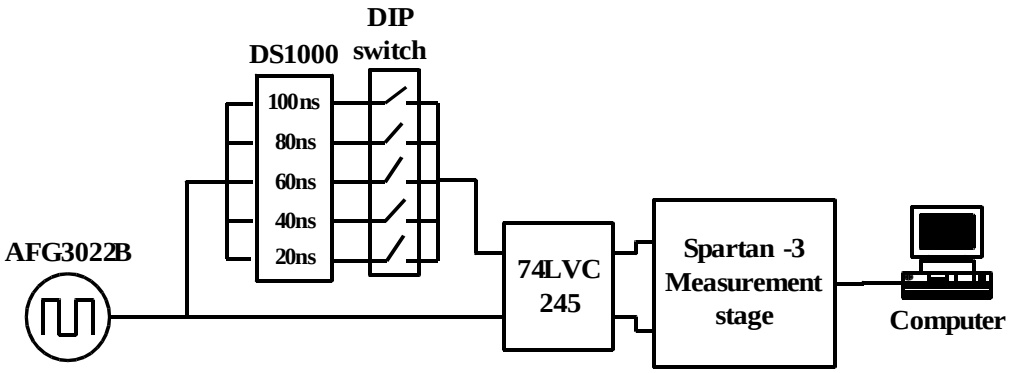


**Figure 3.30**: The test set-up for the measurement stage phase precision characterisation

The AFG3022B arbitrary function generator (Tektronix Inc., Oregon, USA) was used to provide a pulse train with 10 kHz frequency and 4 $V_{pp}$ amplitude. The pulse from the AFG3022B was divided into two paths with the one connected to the input of the delay

line DS1000 and the other connected directly to the 74LVC245.

The delay line DS1000 (Maxim Inc.) [146] was used to provide the time difference by applying a fixed time delay of 20 ns, 40 ns, 60 ns, 80 ns and 100 ns to the pulse signal which passed through it. Since all outputs of the delay line were active at the same time the DIP switches were used to select the required time delay.

A computer with the Microsoft Windows XP operating system running the LabWindows application software was used for acquiring the raw data from the FPGA and for calculating and storing the phase difference values. The raw data were transmitted to the computer through the RS232 interface at a bit rate of 115200 bits per second. The phase precision was calculated from the first 10 phase difference values in Microsoft Excel using equation (3.15).

For the measurement stage four time constants (TC) were used. The TC 0.1 ms (1 XOR pulse), the TC 0.2 ms (2 XOR pulses), the TC 5 ms (100 XOR pulses averaged) and the TC 50 ms (1000 XOR pulses averaged).

The characterisation results are illustrated in figure 3.31 below. It is noted here that for the 20 ns delay line tab the measurement stage outputted the value of the $T_{clk}$ which in turn gave a phase precision of $2.22\times10^{-16}$ degrees. This was due to the approximation of the delay line value to the $T_{clk}$.

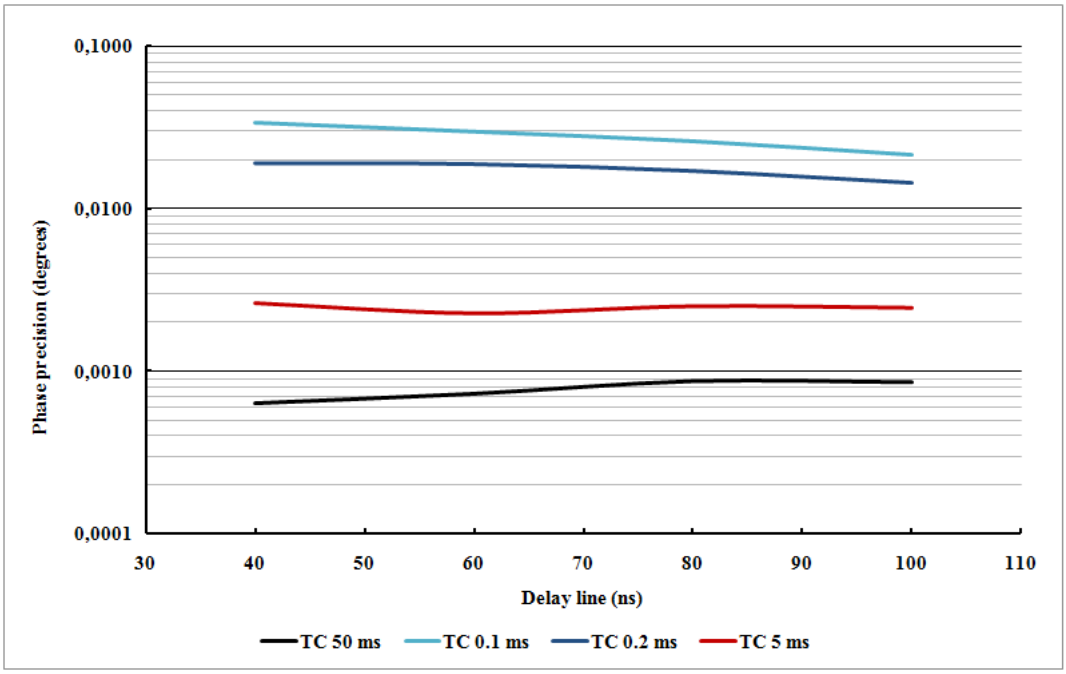


**Figure 3.31**: Measurement stage phase precision Vs delay line

From the graph in figure 3.31 it can be seen that when the measurement stage does not use

averaging (TC 0.1 ms) or averages a very small number of XOR pulses (TC 0.2 ms) the phase precision of the measurement stage is far worse than when averaging is used.

When the measurement stage used the TC 0.1 ms (1 XOR pulse) the phase precision improved over time reaching about 25 millidegrees at 100 ns delay which however was still 10 times worse than the phase precision with the TC 5 ms (100 XOR pulses averaged). This agrees with the theory where the improvement when averaging is $1/\sqrt{N}$ where N is the XOR pulses as was pointed out in section 3.3.2.

The measurement stage achieved 2.5 millidegrees phase precision when the TC 5 ms was used and 0.9 millidegrees phase precision when the TC 50 ms was used. The measurement stage theoretical values from section 3.3.2 of the average standard deviation were 2.8 millidegrees and 0.9 millidegrees respectively. For the maximum standard deviation the theoretical values were 3.6 millidegrees and 1.1 millidegrees respectively.

Comparing the theoretical values with the recorded values it can be seen that the practical values are very close to the average standard deviation theoretical values and lower than the maximum standard deviation theoretical values. This shows that the measurement stage operated as predicted by equations (3.10) and (3.11). Also it shows that both equations can be used as a performance predictors for the operational behaviour of the measurement stage.

#### 3.5.1.2 Recording rate

The recording time for the measurement section is given by equation (3.14) which is equal to the summation of the phase measurement time (PMT) and the data transfer time (DTT). When the signal frequency $f_S$ is 10 kHz and 100 XOR pulses are averaged the theoretical value of the PMT is calculated equal to 5 ms. This increases to 50 ms when 1000 XOR pulses are averaged.

To verify the calculated values the test set-up in figure 3.30 was used. The measurement stage was set to transmit while recording ($MST_{parallel}$) and a phase measurement of 1 second duration was recorded and transmitted to the computer.

The result was 200 phase difference values for the 100 XOR pulses and 20 phase difference values for the 1000 XOR averaging. The test was repeated for a number of times and the results were approximately the same. The results showed that the time constant used by the measurement stage was 5 ms when 100 XOR pulses were averaged and 50 ms

when 1000 XOR pulses were averaged.

Combining the results of section 3.5.1.1 and of this section it is clear that a trade off exists for the measurement stage regarding the data acquisition rate and the phase precision. The measurement stage can be very fast or very precise. However it cannot achieve both at the same time. Therefore depending on the application the user should select which is more important to the application.

### 3.5.2 Phase measurement subsystem characterisation

The aim of the tests was to characterise the phase measurement subsystem in terms of the phase precision, the phase drift and the recording rate. For the phase precision characterisation the subsystem was tested first without the downconversion and then with the downconversion. The first test aimed to create a phase precision baseline which would serve as comparison for the phase precision results from the second test. This would allow the investigation of the downconversion impact on the subsystem phase precision.

Since this thesis is interested for low conductivity applications requiring high recording rates it was decided to set the measurement stage time constant to 5 ms which offered a good precision and a high recording rate of 200 phase difference values per second.

The measurement stage was programmed in the Spartan-3 which was on-board the Spartan-3 system board [130] and had two physical inputs for the excitation signal and the detection signal. The Spartan-3 was clocked by the on-board clock and the $T_{clk}$ was equal to 20 ns.

#### 3.5.2.1 The phase precision of the subsystem without the downconversion

The test set-up shown in figure 3.32 was used for the characterisation.

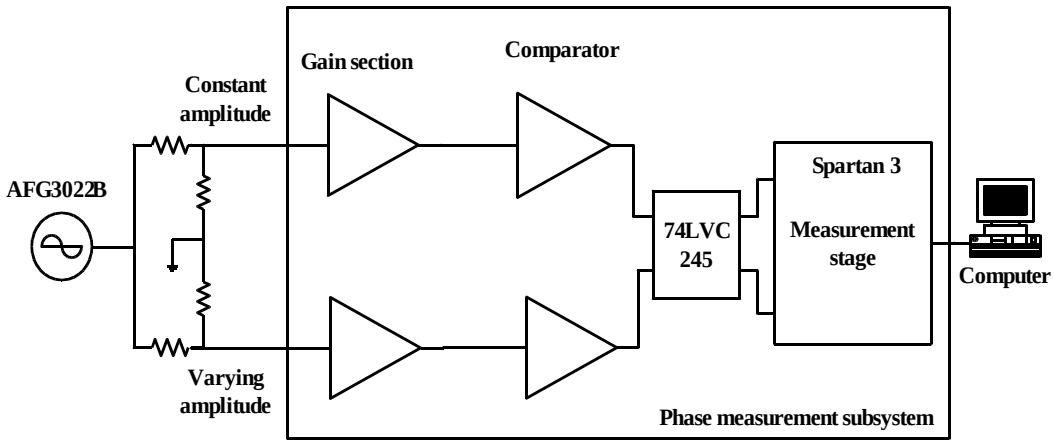


**Figure 3.32**: The phase precision characterisation test set-up for the subsystem without downconversion

The AFG 3022B provided the sinusoidal signal of 10 kHz and 2 $V_{pp}$ amplitude. The signal was divided into two paths each featuring a voltage divider in order to get the required voltage amplitude. The amplitude for the one path was kept constant at 1800 $mV_{pp}$ while the amplitude of the second path was varied from 1800 $mV_{pp}$ down to 20 $mV_{pp}$ in predefined steps. The resistors used in the voltage dividers were below 100 Ω with 0.1% tolerance to minimize the effect they would have on the signal.

Both signals were fed directly to the input of the gain stage and were processed as described in the respective section of this chapter. A computer with Microsoft Windows XP operating system running the LabWindows application software was used for acquiring the raw data from the FPGA and for calculating and storing the phase difference values. The phase precision was calculated from the first 10 phase difference values in Microsoft Excel using equation (3.15).

The characterisation results are illustrated in figure 3.33 below. The recorded phase precision can be divided into three different zones with regards to the amplitude. The first region extends from 1800 $mV_{pp}$ down to 500 $mV_{pp,}$ the second region from 500 $mV_{pp}$ down to 100 $mV_{pp}$ and the third from 100 $mV_{pp}$ down to 20 $mV_{pp}$.

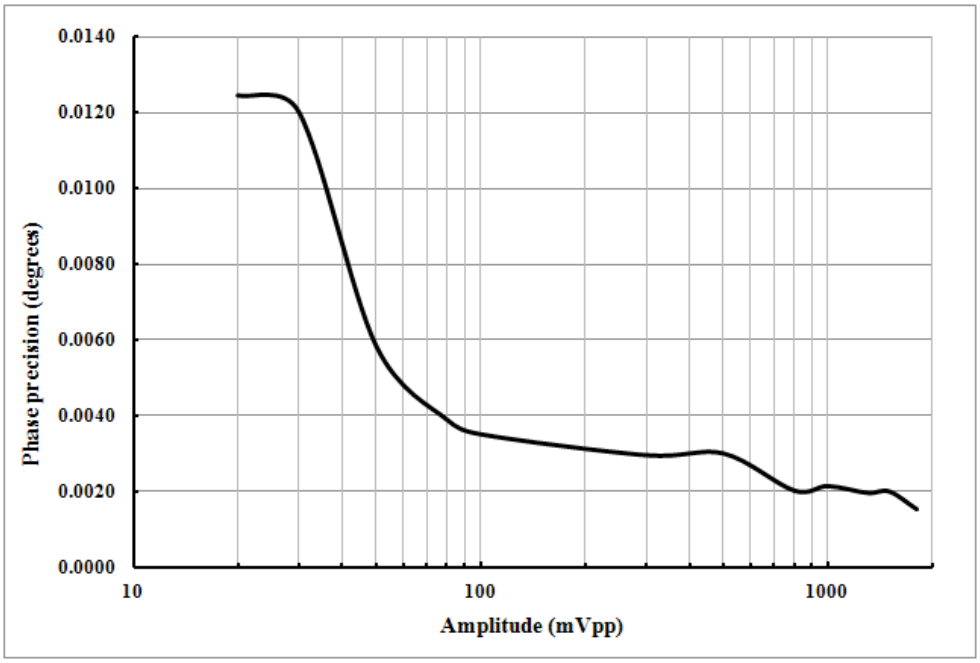


**Figure 3.33**: The subsystem without downconversion phase precision at 10 kHz

The first region is actually composed by two sub-regions. The first sub-region from 1800 $mV_{pp}$ down to 800 $mV_{pp}$ is characterised by a rather constant phase precision at about 2 millidegree. The second from 800 $mV_{pp}$ down to 500 $mV_{pp}$ is characterised by an increase from 2 millidegrees to almost 3 millidegrees.

The phase precision of the whole region corresponds well with the performance of the measurement stage when the 5ms time constant was used as shown in section 3.5.1. Furthermore it was well within the limits predicted by the average standard deviation of the measurement stage which was 2.8 millidegrees for the 5 ms time constant. The phase precision during the first region shows that the gain stage without the downconversion had almost no impact on the performance of the measurement stage.

The second region from 500 $mV_{pp}$ down to 100 $mV_{pp}$ shows an almost constant behaviour. However it increases slightly to almost 3.5 millidegrees. This shows that as the amplitude was decreased the gain stage pushed the measurement stage to reach the predicted value of 3.6 millidegrees of the maximum standard deviation for the 5 ms time constant. However once again the impact of the gain stage was not significant. Actually this zone presents the most constant behaviour from the three regions.

The third region from 100 $mV_{pp}$ down to 20 $mV_{pp}$ shows a rapid increase of the recorded phase precision from 3.6 millidegrees to almost 12.5 millidegrees. Although the recorded phase precision at 50$mV_{pp}$ is below 6 millidegrees which it can be considered as a good performance the overall phase precision increase shows that the gain stage have a significant impact on the phase precision when very low amplitudes are used as inputs.

This deterioration in the performance of the analogue processing stage in the third region could in part be the result of the extensive amplification used for converting the sinusoidal signal into square wave.

### 3.5.2.2 The phase precision of the subsystem with the downconversion

The test set-up shown in figure 3.34 was used for the characterisation.

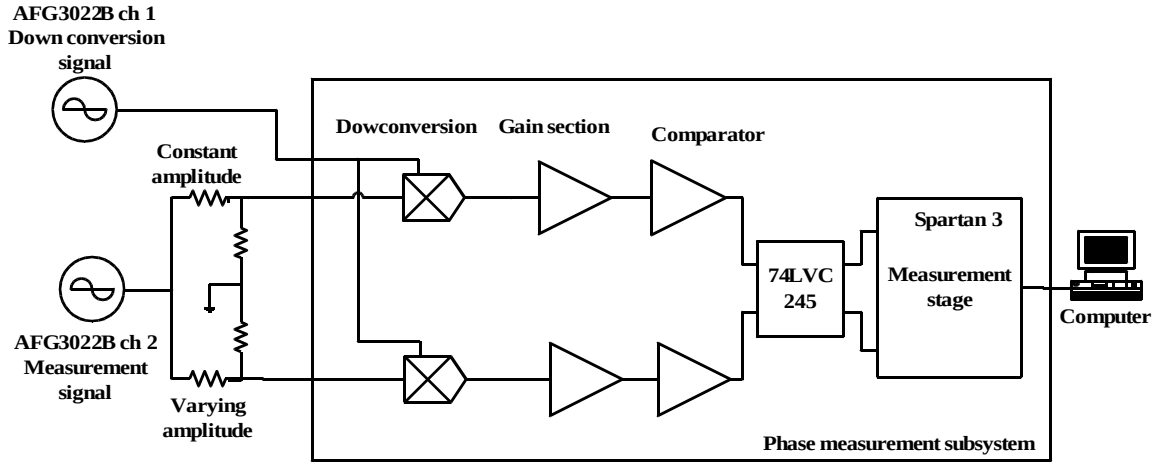


**Figure 3.34**: The phase precision characterisation test set-up for the subsystem with the downconversion

The first channel of the AFG 3022B was set to provide a sinusoidal signal of 1 MHz, 10 MHz and 20 MHz frequency and 2 $V_{pp}$ amplitude. The second channel was set to provide the downconversion sinusoidal signal of 0.99MHz, 9.99 MHz and 19.99 MHz frequency and 2 $V_{pp}$ amplitude.

The first sinusoidal signal was divided between two paths. The sinusoidal signal of the first path was applied to the subsystem's excitation input and was kept constant at 1800 $mV_{pp}$. The sinusoidal signal of the second path was applied to the subsystem's detection input and was varied from 20 $mV_{pp}$ to 1800 $mV_{pp}$ in predefined steps. The downconversion signal was connected directly to the respective input of the AD835 multiplier.

The two signals from the voltage dividers were downconverted by the AD835 to 10 kHz. Then they were converted to square waves and were measured by the measurement stage. The raw data were transmitted to a computer running the LabWindows application software. The phase precision was calculated from the first 10 phase difference values in Microsoft Excel using equation (3.15).

The characterisation results are graphically shown in figure 3.35 for the 1 MHz operation, in figure 3.36 for the 10 MHz operation and in figure 3.37 for the 20 MHz operation.

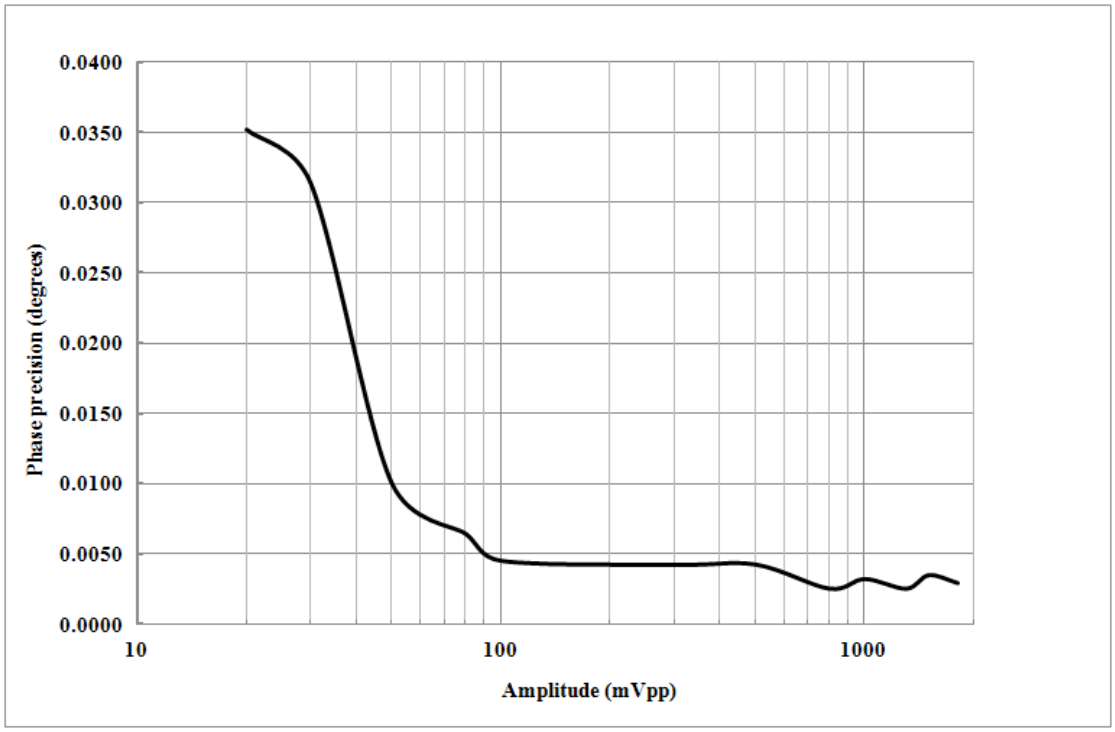


**Figure 3.35**: The complete subsystem phase precision at 1 MHz operation frequency

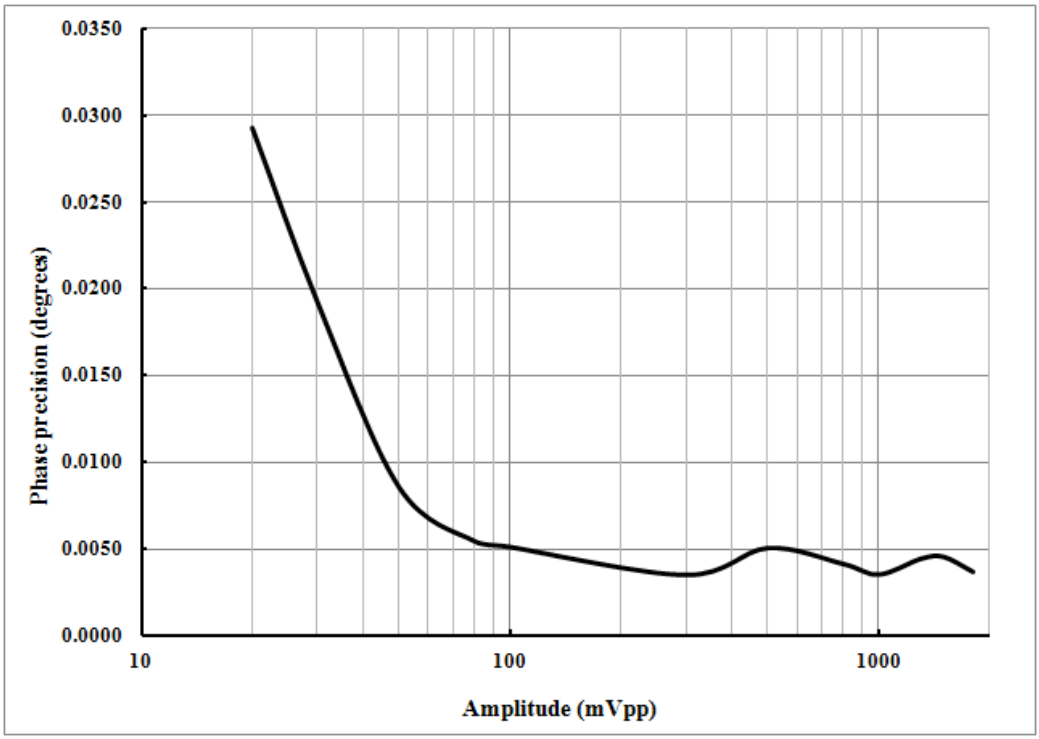


**Figure 3.36**: The complete subsystem phase precision at 10 MHz operation frequency

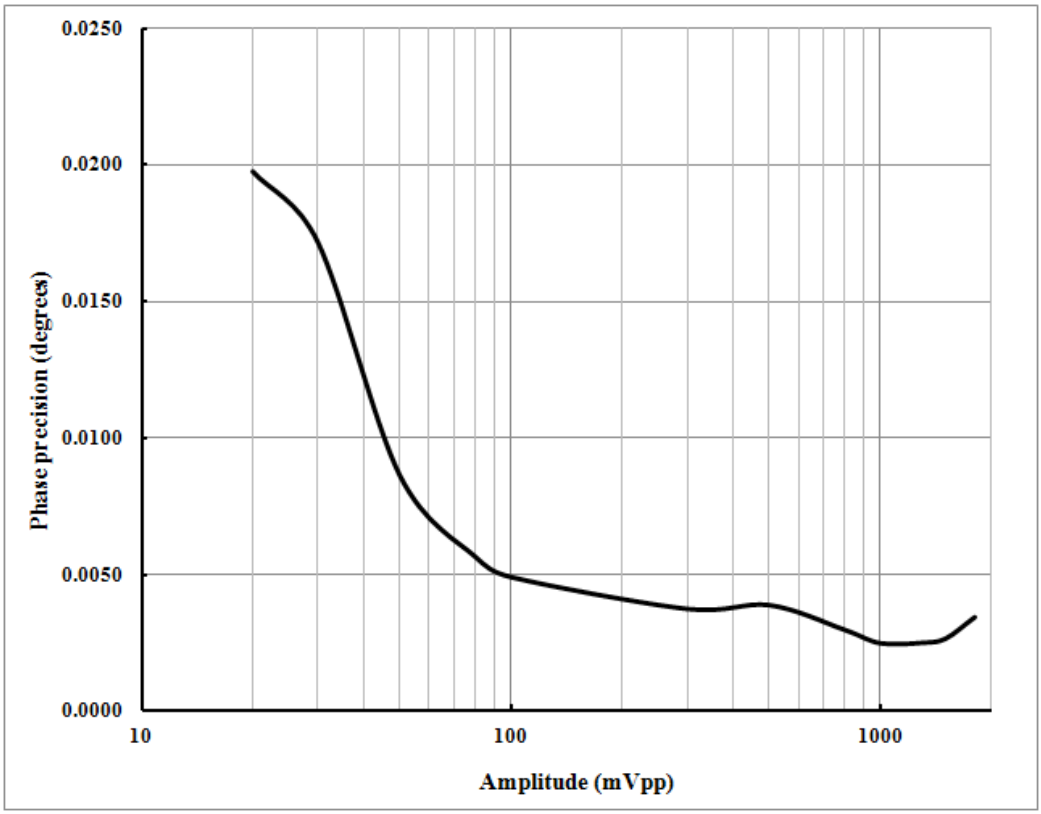


**Figure 3.37**: The complete subsystem phase precision at 20 MHz operation frequency

From the three graphs in figures 3.35, 3.36 and 3.37 it can be seen that they follow a similar pattern as that in the graph depicted in figure 3.34 which depicted the phase precision of the subsystem without the downconversion. This shows that the behaviour of

the phase subsystem is dictated by the gain section and that the addition of the downconversion part does not have any impact on this pattern.

The phase precision of the subsystem with downconversion is generally below 5 millidegrees in the region from 100 $mV_{pp}$ to 1800 $mV_{pp}$ regardless of the frequency used. This shows that the subsystem presents a steady behaviour in this amplitude region and that the frequency does not have any impact on the behaviour of the subsystem.

Comparing this behaviour to the behaviour of the subsystem without the downconversion in the same region it can be seen that the downconversion part had a minimal impact on the phase precision of the subsystem from 100 $mV_{pp}$ to 1800 $mV_{pp}$ (5 millidegrees to 4 millidegrees).

Below 100 $mV_{pp}$ however the impact of the downconversion on the behaviour of the subsystem increases. At 50 $mV_{pp}$ the recorded phase precision at any of the three frequencies used was below 10 millidegrees but above the 6 millidegrees threshold recorded when the subsystems without the downconversion was characterised.

The impact becomes even greater when the amplitude difference between the two signals is increased further. At 20 $mV_{pp}$ the phase precision was recorded to be 35 millidegrees when 1 MHz was used, almost 30 millidegrees when 10 MHz was used and just below 20 millidegrees when 20 MHz was used compared to 12.5 millidegrees without downconversion.

The behaviour of the subsystem with downconversion at low signal amplitudes with regards to the phase precision can be attributed to the combination of the downconversion impact and the gain section impact. The output of the AD835 is a sinusoidal signal that is a product of multiplying two sinusoidal signals.

Equation (3.22) states that the AD835 output signal amplitude is dictated by the lowest signal amplitude not the highest and hence applying a low amplitude signal will result into the AD835 outputting that. As was shown in section 3.5.2.1 when low amplitude signals are input to the gain section it effects the phase precision in a negative way.

However the results show that the impact of the downconversion part at 20 $mV_{pp}$ is decreased as the frequency increases. From the data sheet of the AD835 it can be seen that the harmonic distortion on the AD835 output signal is decreased as the frequency of the

input signals increases. Thus when the 20 $mV_{pp}$ signal is used the results suggest that due to the harmonic distortion the AD835 outputs a more noisier signal at 1 MHz than at 20 MHz which in turn affects the phase precision of the subsystem. In fact at 20 $mV_{pp}$ an improvement of almost 50% is seen in the phase precision when recorded at 20 MHz in comparison with 1 MHz.

From the results of this characterisation test it can be seen that by applying a very low amplitude sinusoidal signal to the AD835 it results into a reduced phase precision. However the same results suggest that a way to rectify this problem is by increasing the input signals frequency. In such case the skin penetration and other factors related to the operation of an MIT coil array related to the excitation frequency should be taken into consideration when selecting this solution.

### 3.5.2.3 Phase drift of the complete subsystem

The test set-up shown in figure 3.38 was used for the characterisation.

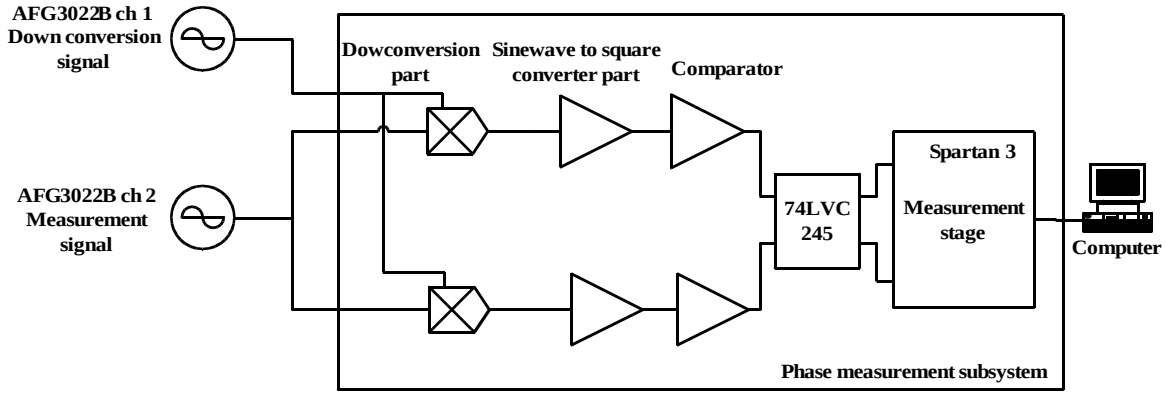


**Figure 3.38**: The complete subsystem phase drift characterisation test set-up

The first channel of the AFG3022B provided the measurement sinusoidal signal with a frequency of 10 MHz and an amplitude of 1.8 $V_{pp}$ which was divided into two paths and was use as input to the excitation and detection inputs of the subsystem. The second channel provided the downconversion sinusoidal signal with a frequency of 9.99 MHz and an amplitude of 2 $V_{pp.}$

The signals were downconverted to 10 kHz, squared by the gain section and measured by the measurement stage. The raw data were transmitted to a computer running the LabWindows application software. A phase difference value was recorded every minute for 5 hours which created a data set of 300 phase measurement values.

The maximum phase drift was calculated from the data set in Microsoft Excel using

equation (3.16). The data set was processed with a moving average algorithm of 10 given in equation (3.17) to produce a new averaged data set. The average drift was calculated from the averaged data set using equation (3.16).

The characterisation results are graphically shown in figure 3.39. The maximum phase drift over 5 hours was 37 millidegrees and the average phase drift was 14 millidegrees using a moving average algorithm of 10.

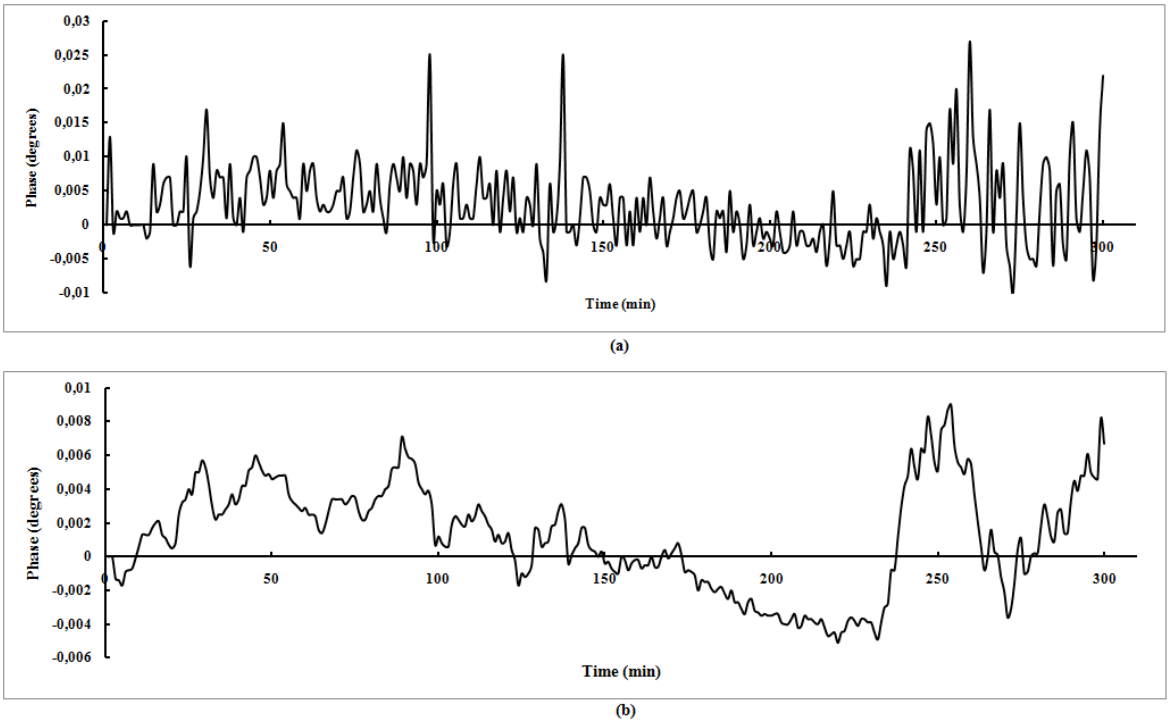


**Figure 3.39**: The subsystem phase drift over 5 hours showing the maximum drift (a) and the average drift (b)

### 3.5.2.4 Recording rate of the subsystem with downconversion

The procedure regarding the signals and the test set-up from section 3.5.2.2 were used for this test. For comparison purposes the time constant was set at 5 ms and at 50 ms.

A phase measurement of 1 second duration was recorded for each time constant and was transmitted to the computer. The result was 200 phase difference values for the 5 ms time constant and 20 phase difference values for the 50 ms time constant. The test was repeated for a number of times and the results were approximately the same. The frequency and the amplitude of the signals did not have any impact on the recording rate of the subsystem.

## 3.6 Summary

This chapter presented the work performed for the design, the development and the characterisation of a low cost single channel phase measurement subsystem based on the zero crossing technique. The main issues arising from the work performed are summarised

here.

In section 3.1 the background leading to the required work was examined briefly and the minimum requirements that the phase measurement subsystem was expected to satisfy were given.

In section 3.2 the work performed for the design of the subsystem was presented. The general architecture of the subsystem was analysed. An examination of the implementation details for the analogue processing stage and the measurement stage followed. The examination results in setting the foundations for the implementation of the subsystem.

In section 3.3 the theoretical aspects regarding the measurement stage and the subsystem were covered and the equations required for the subsystems operation and characterisation were developed. A theoretical analysis of the measurement stage precision showed that for 5 ms time constant the average precision was expected to be 2.8 millidegrees and for 50 ms time constant 0.9 millidegrees.

In section 3.4 the practical work performed for the implementation of the single channel phase measurement subsystem was described. The electronic components used were described and the implemented circuit diagrams were given. The technical details of the implementation were described in the necessary depth.

In section 3.5 the characterisation of the measurement stage and the single channel subsystem was presented. The measurement stage phase precision was 2.5 millidegrees for the 5 ms time constant and 0.9 millidegrees for the 50 ms time constant. The practical values were very close to the theoretical values which showed that the measurement stage operated as expected. The recording rate of the measurement stage was measured to be 200 phase difference values for the 5 ms time constant and 20 phase difference values for the 50 ms time constant.

The subsystem was tested at 10 kHz without the downconversion and achieved a phase precision below 4 millidegrees at 100 $mV_{pp}$ and below 12.5 millidegrees at 20 $mV_{pp}$.

The subsystem with the downconversion was tested at 1MHz, 10 MHz and 20 MHz. At 1 MHz the subsystem achieved a phase precision below 5 millidegrees at 100 $mV_{pp}$ and below 36 millidegrees at 20 $mV_{pp}$. At 10 MHz the subsystem achieved a phase precision of 5 millidegrees at 100 $mV_{pp}$ and below 30 millidegrees at 20 $mV_{pp}$. At 20 MHz the

subsystem achieved a phase precision of 5 millidegrees at 100 $mV_{pp}$ and below 20 millidegrees at 20 $mV_{pp}$.

The maximum phase drift of the subsystem with downconversion over 5 hours was 37 millidegrees and the average phase drift was 14 millidegrees using a moving average algorithm of 10. The recording rate of the subsystem with downconversion was measured to be 200 phase difference values for the 5 ms time constant and 20 phase difference values for the 50 ms time constant.

The characterisation results showed that the developed single channel zero crossing phase measurement subsystem can be very fast and precise. Its development does not require expensive tools and the implementation can be realised with low cost electronic components. The subsystem fulfilled and in some cases such as the phase precision and the recording rate exceeded the requirements that was set. The design of the single channel allows easy scalability with low cost.

# 4. The Cardiff Mk2c MIT system

This chapter presents the work performed for the design, the development and the characterisation of an eight channel parallel Magnetic Induction Tomography system operating at 10 MHz for low conductivity industrial applications requiring a high data acquisition rate. The analysis of the theoretical aspects and the practical details for the design and the implementation of the system are given. The results of two experiments conducted to prove the suitability of the system for low conductivity industrial applications are given.

The chapter begins with section 4.1 in which the operational requirements that the system was expected to satisfy are set and continues with section 4.2 where two theoretical aspects regarding the system's operation are covered. In section 4.3 the design of the system is presented and in sections 4.4 and 4.5 the implementation of the coil array and the multichannel phase measurement subsystem respectively is presented.

The Cardiff MK2c is presented in section 4.6 as a complete working system. In section 4.7 the characterisation results of the multichannel SPMU are given and in section 4.8 the characterisation results are presented. In section 4.9 the system's performance results when a saline volume flows through an inclined water pipe phantom inserted in the system's coil array are presented. The chapter ends with section 4.10 that summarises the work performed.

## 4.1 Requirements and specifications

The aim of this project was to investigate and develop practical and inexpensive high speed Magnetic Induction Tomography (MIT) instrumentation to provide a solution to low conductivity applications requiring high data acquisition rate. Such a low conductivity industrial application is the multiphase flow (MPF) measurement in the oil industry.

Therefore to design and develop an MIT system targeting that application it was necessary

to lay down a general set of requirements. These set is given below:

- Parallel tomographic multichannel system
- At least 8 excitation channels and 8 detection channels
- Excitation frequency at 10 MHz
- High frame rate – ideally 10 frames per second
- Using a multichannel zero crossing phase measurement subsystem based on the single channel developed in chapter 3
- Low cost

The parallel processing was adopted since this was essential to provide the required acquisition speed with the factors affecting acquisition speed discussed in detail in section 4.2.2.

The literature review in chapter 2 showed that a 16 channel MIT system generally exhibits a two times better spatial resolution than an 8 channel system but is two times slower. Since speed is a requisition and industrial applications in general do not require the tomographic image quality of biomedical applications it was considered a good compromise to select 8 excitation coils and 8 detection coils.

The review showed that the detection signal is proportional to the excitation frequency and that for low conductivity applications an excitation frequency in the order of MHz would be required. However due to skin penetration the excitation frequency can not extend into tens of MHz. Therefore the 10 MHz excitation frequency was considered as a good compromise between acquiring a large enough detection signal and the skin penetration.

The target overall frame rate of the system of 10 frames per second (fps) was selected arbitrarily. It is not clear at present the exact frame rate required as this will depend on the specific industrial application. Frame rates well in excess of 1 fps are likely to be necessary for industrial flow imaging. The adoption of 10 fps is selected as a realistic target.

To achieve the target frame rate of 10 fps the multichannel phase measurement subsystem for the Cardiff Mk2c was required to be fast. The characterisation results of the single channel zero crossing phase measurement subsystem in chapter 3 showed that it can achieve a low time constant of 5 ms which allows it to acquire 200 phase difference values per second. Therefore a multichannel scale up of the single channel was selected for realisation.

## 4.2 Theoretical aspects

This section takes a closer look on two aspects concerning the MIT system. The first is an general overview of the components of the MIT system and the second an examination of the factors affecting the acquisition speed of the MIT system.

### 4.2.1 The MIT system architecture

In chapter 2 the architectural approaches presented in [19], in [28], in [11] and in [30] regarding the MIT system architecture were examined. These approaches differ in chronological order with the latter being the most recent with regards to this thesis. It can be said that they signify the progress achieved in knowledge regarding the development of practical MIT systems.

The operation of an MIT system is performed by fulfilling three main tasks. It uses coils to generate the primary magnetic field and to detect the secondary magnetic field, it uses electronics to process the signals from the coils and to measure their phase difference and it process the measurement data to produce a tomographic image or other data processing procedure. These main tasks reflect to the subsystems used.

Any other tasks required for the operation of the MIT system are secondary to the main tasks and thus the devices that perform them are modules to the subsystems. The architecture of a practical MIT system can be therefore better described by a new description which can be graphically illustrated using the block diagram below.

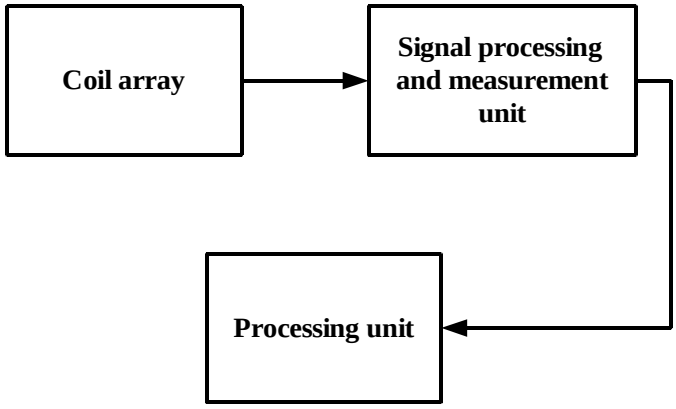


**Figure 4.1**: The proposed architecture for a practical MIT system

This proposed approach divides the complete MIT system into three distinct subsystems which are the coil array, the signal processing and measurement unit and the processing unit. Each subsystem serves a distinct purpose as given below:

- the coil array is the sub-system that generates the primary magnetic field and

detects the primary and any resulting secondary magnetic field produced by samples.

- the signal processing and measurement unit (SPMU) is the sub-system that process the signals produced by the coil array and measures their phase difference
- the processing unit (PU) is the subsystem that process the phase measurements to produce an image or processes the data into some other useful form

This proposed approach differentiates from the approach in [11] which was used in chapter 2 to describe the MIT systems on the fact that unifies the signal conditioning electronics and the phase measurement system into a single unit. The reasoning is that each phase measurement system requires its individual signal processing and thus the two form one unit.

From now on the terminology given here will be followed in this thesis when referring to the MIT subsystems.

### 4.2.2 Factors affecting the MIT system frame rate

Since high data acquisition frame rate is a primary requirement it is important to identify and describe all factors affecting the frame rate of an MIT system. The term frame rate is related in the MIT field with the time $T_M$ required by an MIT system to perform a complete measurement with the use of all the excitation coils and detection coils and output a result. Hence it results that the number of complete measurements per second that an MIT system can achieve or frame rate is given by

$$Frame\,rate = \frac{1}{T_M} \qquad (4.1)$$

An analysis for determining the frame rate during the design phase of an MIT system irrespective of the phase measurement technique used would be very valuable as it could be used as a guide during the system design but also in the selection and erection of the components required for the system's implementations. From the authors best knowledge such analysis for the general MIT system does not exist in the literature yet and thus it was performed in the context of this work.

To be exact on the identification and analysis of the time delays the excitation signal chain and the detection signal chain were treated separately. The detection signal chain was further separated into the detection line employed by a parallel MIT system and the detection line employed by a multiplexed MIT system due to their differences. The time

delays for each case are given in the following figures and tables.

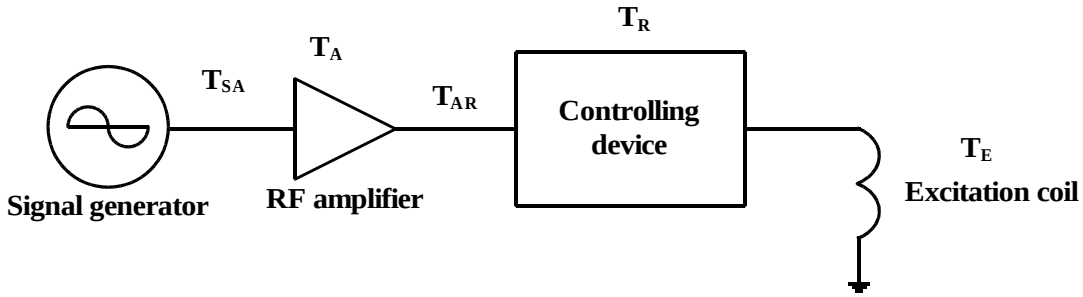


**Figure 4.2**: The excitation signal chain time delays

**Table 4.1**: The excitation signal chain time delays

| Symbol | Description |
|---|---|
| $T_{SA}$ | Propagation time required by the excitation signal to travel from the signal source to the RF amplifier |
| $T_A$ | The time required by the RF amplifier for amplifying and transmitting the detected signal |
| $T_{AR}$ | Propagation time required by the excitation signal to travel from the RF amplifier to the controlling device which switches the excitation coil on and off |
| $T_R$ | The time the controlling device must maintain the excitation coil active for a projection to take place |
| $T_E$ | The time required by the excitation coil to generate the primary magnetic field |
| $T_{EX}$ | The total time required by the excitation chain line to make an excitation coil active |

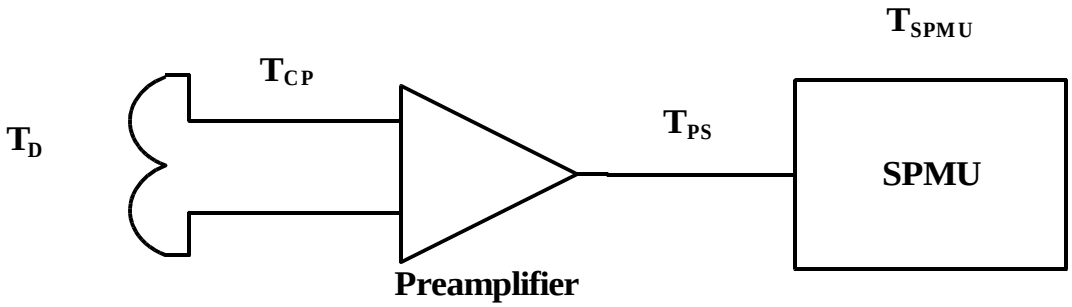


**Figure 4.3**: The parallel MIT system detection signal chain time delays

**Table 4.2**: The parallel MIT system detection signal chain time delays

| Symbol | Description |
|---|---|
| $T_D$ | The time required by the detection coil to generate the detected signal after the primary magnetic field has been generated |
| $T_{CP}$ | Propagation time required by the detected signal to travel from the detection coil to the preamplifier |
| $T_P$ | The time required by the preamplifier for amplifying and transmitting the detected signal |
| $T_{PS}$ | Propagation time required by the detected signal to travel from the preamplifier to the signal processing measurement unit (SPMU) |
| $T_{SPMU}$ | The time required by the SPMU for the signal processing and the phase measurement of the detected signal |

| Symbol | Description |
|---|---|
| $T_{Dpar}$ | The total time required by the detection chain to process the signals and perform the measurement |

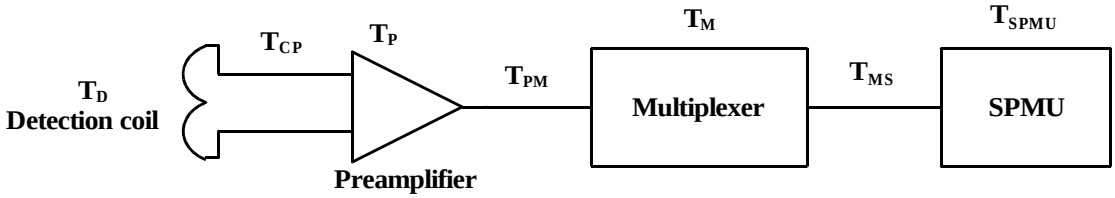


**Figure 4.4**: The multiplexed MIT system detection signal chain time delays

**Table 4.3**: The multiplexed MIT system detection signal chain time delays

| Symbol | Description |
|---|---|
| $T_D$ | The time required by the detection coil to generate the detected signal |
| $T_{CP}$ | Propagation time required by the detected signal to travel from the detection coil to the preamplifier |
| $T_P$ | The time required by the preamplifier for amplifying and transmitting the detected signal |
| $T_{PM}$ | Propagation time required by the detected signal to travel from the preamplifier to the multiplexer |
| $T_M$ | The time required by the multiplexer for transmitting the detected signal |
| $T_{MS}$ | Propagation time required by the detected signal to travel from the multiplexer to the SPMU |
| $T_{SPMU}$ | The time required by the SPMU for the signal processing and the phase measurement of the detected signal |
| $T_{Dmux}$ | The total time required by the detection chain to process the signals and perform the measurement |

**Table 4.4**: Time delays for the data transfer and the image processing

| | |
|---|---|
| $T_{DI}$ | The time required for the data transfer from the SPMU to the processing unit (PU) |
| $T_I$ | The time required for the real time processing by the PU |

From table 4.1 it occurs that the time $T_{EX}$ which is required by the excitation chain line to make an excitation coil active and thus have a projection is given by

$$T_{EX} = T_{SA} + T_A + T_{AR} + T_R + T_E \qquad (4.2)$$

For an MIT system employing a single excitation coil the required excitation time for a projection is given by equation (4.2). However if the excitation coil is used for continuous projection during the operation of the MIT system then a controlling device is usually not required and thus $T_R$ becomes zero. In such case $T_{EX}$ is the sum of the time delays of the remaining factors.

For an MIT system employing a number of m excitation coils i.e. a multichannel system

the total excitation time $T_{TEX}$ required to perform the complete measurement is given by

$$T_{TEX} = (T_{EX} + T_{TRANS}) \times m \qquad (4.3)$$

where $T_{TRANS}$ is the transmission time taken between two sequential projections.

If the next projection begins directly after the previous projection ends then $T_{TRANS}$ is zero and $T_{EX}$ is the result of the multiplication of $T_{EX}$ times m. For a system aiming at a high data acquisition rate $T_{TRANS}$ must be kept as low as possible or ideally zero.

For a multichannel MIT system there is another aspect resulting from equation (4.2) and equation (4.3). Because there are more than one excitation coils a controlling device is required on each excitation coil to ensure the separation of the projections. This means that to calculate $T_{EX}$ the time delay $T_R$ must be taken into consideration. Through $T_{EX}$ however $T_R$ affects $T_{TEX}$ which in turn affects the total time required for the complete measurement.

Therefore it becomes clear that if the target for a multichannel MIT system is an increased data recording rate then a fast controlling device with a low $T_R$ must be used at each excitation coil.

For a parallel multichannel MIT system it results from table 4.2 that the time delay $T_{Dpar}$ is given by

$$T_{Dpar} = T_D + T_{CP} + T_P + T_{PS} + T_{SPMU} \qquad (4.4)$$

The total detection time required by all the detection signal chains employed by the system is actually equal to the time required by one detection signal chain ($T_{Dpar}$). This is because the signals from all the detection chains are processed and measured in parallel. Therefore the number of the detection signal chains used by the MIT system does not increase the time required for the measurement in a parallel MIT system.

For an MIT system employing a number of m excitation coils then the total time delay $T_{TDpar}$ of the detection signal chains is given by

$$T_{TDpar} = T_{Dpar} \times m \qquad (4.5)$$

However the $T_{TDpar}$ runs in parallel to the $T_{TEX}$ and therefore it does not add any extra time delay. Thus the time $T_{HMpar}$ required by the hardware part of the parallel MIT system for a complete measurement is given by

$$T_{HMpar} = T_{TEX} = (T_{EX} + T_{TRANS}) \times m \qquad (4.6)$$

Combining the data from table 4.4 and equation (4.6) the time $T_{Mpar}$ required by the

complete parallel MIT system to produce a real time result is given by

$$T_{Mpar} = T_{HMpar} + T_{DI} + T_I \qquad (4.7)$$

Hence the frame rate of the complete parallel MIT system is given by

$$Frame\,rate = \frac{1}{T_{Mpar}} = \frac{1}{T_{HMpar} + T_{DI} + T_I} \qquad (4.8)$$

For a multiplexed multichannel MIT system however things are a bit more complicated. The table 4.3 suggests that the time delay $T_{Dmux}$ of the detection chain is given by

$$T_{Dmux} = T_D + T_{CP} + T_P + T_{PM} + T_M + T_{MS} + T_{SPMU} \qquad (4.9)$$

Comparing equation (4.9) to equation (4.4) it can be seen that the detection chain of the multiplexed MIT system has an additional time delay caused by $T_{PM}$, $T_M$ and $T_{MS}$ which in the parallel MIT system is the propagation time delay $T_{PS}$.

Furthermore the phase measurement in the multiplexed MIT system is performed sequentially. This means that the signal from the excitation channel is compared to the signal from a detection channel one at a time. Therefore the total detection time $T_{TDmux}$ depends not only on the number of the excitation coils but on the number of the detection channels as well and is given by

$$T_{TDmux} = (T_{Dmux} \times m) \times n \qquad (4.10)$$

where n is the number of the detection coils used by the MIT system

As can be seen from equation (4.10) a time delay is inserted in the phase measurement equal to n times. Thus the time $T_{HMmux}$ required by the hardware part of the multiplexed MIT system to perform a complete measurement is given by

$$T_{HMmux} = T_{TEX} \times n = (T_{EX} + T_{TRANS}) \times m \times n \qquad (4.11)$$

Thus from table 4.4 and equation (4.10) it results that the time $T_{Mmux}$ required by the complete multiplexed MIT system to produce a tomographic image is given by

$$T_{Mmux} = T_{HMmux} + T_{DI} + T_I \qquad (4.12)$$

and therefore the frame rate of the complete multiplexed MIT system is given by

$$Frame\,rate = \frac{1}{T_{Mmux}} = \frac{1}{T_{HMmux} + T_{DI} + T_I} \qquad (4.13)$$

Comparing equation (4.13) to equation (4.8) it is obvious that what differentiates the time

between a compete parallel MIT system and a complete multiplexed MIT system is the time required by the hardware part of the system to perform a complete measurement given that $T_{DI}$ and $T_I$ are the same for both systems.

In comparison to time $T_{HMpar}$ the time $T_{HMmux}$ is increased by three additional time delays related to the multiplexer used and by the number of the detection channels used by the system. The latter is actually the most significant contributor of the increase observed in $T_{HMmux}$. However at the same time it is the most difficult part to minimise due to the impact it will have on the spatial resolution of the tomographic image.

Thus if all are kept equal and n is the number of the detection channels then a complete parallel MIT system will have a frame rate which would be at least n times greater than the frame rate of a complete multiplexed MIT system.

## 4.3 Design of the Cardiff Mk2c system

This section describes the design of the Cardiff Mk2c MIT system and covers the system architecture and the implementation considerations. As this thesis is targeting only the development of the hardware subsystems of a practical MIT system the design of the processing unit (PU) was not addressed.

### 4.3.1 System architecture

The analysis in section 4.2.2 was used to decide if the system will have an increased frame rate by selecting the number of the excitation and the detection coils and the measurement nature (parallel or multiplexed). Using that analysis and assuming that the time delays $T_{DI}$ and $T_I$ are the same for a parallel and a multiplexed system then the frame rate of each system is affected solely by $T_{HMpar}$ and $T_{HMmux}$ respectively.

As was shown in section 4.2.2 $T_{HMpar}$ is smaller than $T_{HMmux}$ due to the fewer time delays it has and because the number of the detection coils does not affect it. Thus for an increased frame rate the obvious choice was a parallel system.

The number of the excitation coils affects in a linear way the total excitation time $T_{TEX}$ of the system as indicated in equation (4.3) which in turn affects the $T_{HMpar}$. An increase to the number of the excitation coils causes an increase of $T_{TEX}$ and $T_{HMpar}$ and in turn a decrease to the frame rate. If all is kept equal apart from the number of the excitation coils then a system with 8 excitation coils has twice the frame rate than a system with 16 excitation

coils. Thus for an increased frame rate a small number of excitation coils is preferred.

However the number of the excitation and detection coils affect the spatial resolution of the system. As was shown in [11] the spatial resolution of a system is directly proportional to the number of the excitation and detection coils used and a small number of excitation and detection coils will result in a poor resolution. The number of the coils used therefore depends on the target application.

For most industrial applications the requirement for tomographic images is not that demanding as it is for biomedical applications. Since the system was aimed at industrial applications requiring a fast frame rate it was decided to sacrifice some of the spatial resolution for a higher frame rate. Thus 8 excitation coils and 8 detection coils were selected for use.

In section 4.1 it was required that the SPMU must be based on the zero crossing technique. Due to the applications the system targeted it was selected to use the system as monotonic i.e. to use only one excitation frequency when operate. It should be noted that it is possible to adapt this system to operate with at least two simultaneous frequencies however this work was not part of this study.

### 4.3.2 System components and implementation details

#### 4.3.2.1 Coil array

From section 4.3.1 it resulted that the system would consist of a coil array with 8 excitation coils and 8 detection coils. Since the system was aimed at the MPF measurements an annular coil array was selected it would fit easier around a pipe.

In the Cardiff Mk1 system [11] both excitation and detection coils were placed on the same coil formers and the coils were placed in a ring. This configuration has the advantage of simplicity but does have significant disadvantages as regards the very large signal dynamic range which must be accommodated and limitations on the shielding which may be applied to the coils.

For the Mk2c system described here it was decided to adopt the coil formation from [11] which placed the excitation coils in one ring and the detection coils in a separate ring as shown in figure 4.5. This formation was expected to offer three advantages compared to the coil array of the Cardiff Mk1 system.

The first advantage was that the separation of the excitation and the detection coil rings reduced the dynamic range of the signal. This allowed the detection amplifier to be optimized and reduced the maximum power dissipated in the detection preamplifier which was identified as a source of drift. The second advantage was that it provided more independent measurements for a given number of coils. The third advantage was that extra shielding could be applied on the excitation coils without affecting the detection coils. [11]

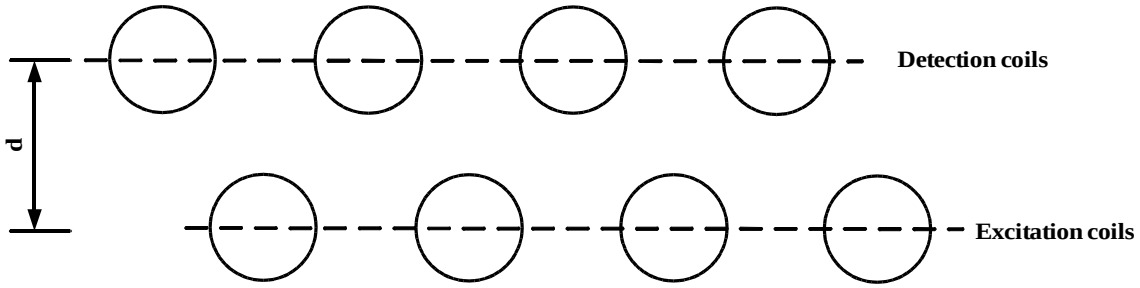


**Figure 4.5**: The coil formation used in Cardiff Mk2 (from [11])

#### 4.3.2.2 Excitation system

A consideration regarding the excitation signal was the strength of the primary magnetic field B. The Biot-Savart equation[8] dictates that the magnitude of **B** at a point P depends on the coil geometry, the distance of P from the coil and the current flowing through the coil. In the annular coil array the excitation coil geometry and the distance between the excitation coils and the detection coils are fixed and known.

In contrast the current flowing through the excitation coil can be increased (or decreased) and it is obvious that an increased value of current results in an increased magnitude of **B** which in turn will create a larger induced signal on the detection coil. A high current however cannot be obtained from signal generators intended for laboratory use and thus an RF amplifier is required to fulfil this task.

However an RF amplifier can be extremely costly and due to budget considerations it was decided to use the ZHL-3A [147] (Minicircuits Inc., New York, USA). On reviewing available amplifiers the ZHL-3A was considered to provide the best compromise between output power and cost of commercially available low-cost RF amplifier modules.

For the distribution of the excitation signal to the excitation coils it was decided to use an inexpensive daisy cable chain that would connect all the excitation coils into a ring. The activation of each excitation coil is then controlled by the use of a RF switch device which isolates the coil from the excitation amplifier when not in use.

[8] Given in chapter 2

The requirement for the control over the excitation coils can be realised with the use of an RF semiconductor switch or an RF relay. Since these devices would control the projection time and the order of the excitation coils activation it meant that they would play a crucial role on the speed of the system as stated in section 4.2.2 but also on the quality of the tomographic image. Therefore a form of central and automated control over them was required and it was decided to incorporate this into the system.

The USB-6501 (National Instruments Inc., Texas, USA) which is a low cost USB digital input/output device controlled by the application software in LabWindows CVI was first considered and used in the preliminary testing of the system. The tests showed that this configuration worked however it could not achieve the required precise control over the RF controlling devices for this application and resulted in achieving a very low frame rate (maximum 3 frames per second). Furthermore problems of synchronisation between the measurement stage and the control configuration were at times observed.

Such precise time control is possible only with hardware control because a software control can suffer from inaccuracies due to the demands on the processor by other processes taking place within the workstation operating system. It was decided to realise the automated control in the same FPGA as the measurement stage of the SPMU and have them cooperate. This was expected to provide the automated and precise control over the RF controlling devices, to solve the synchronisation problem and with the added benefit of lowering the implementation cost.

The location of the RF excitation isolation was also a point of consideration. A large distance between the device and the coil would require a long cable to connect them. This would introduce capacitance to the coil which could significantly lower its resonance frequency. So it was decided to employ a design with the selected RF excitation isolation as close to the excitation coil as possible.

#### 4.3.2.3 Detection system

The induced sinusoidal signal from the detection coils carries the phase information and thus the conductivity information of the sample. As was shown in chapter 3 the phase precision is directly related to the amplitude of the input sinusoidal signal to the SPMU which in the case of the MIT system comes from the detection coils. Depending on **B** the induced signal amplitude can be in the order of a few millivolts which makes the processing of the signal very difficult. Although the induced signal amplitude can be

increased by using more turns in the detection coil in [11] it was stated that an increased number of detection coil turns (more than 2) introduced instability and reduce the phase precision.

The **B** field depends on the power of the RF amplifier and given their cost the only remaining way to increase the induced signal amplitude enough for processing was to use a preamplifier as close to the detection coil as possible. The preamplifier would amplify the induced signal effectively to travel the distance to the SPMU for the phase measurement. Furthermore an increase to the induced signal amplitude would result in increasing the phase precision as was shown from the characterisation results of the single phase subsystem in chapter 3.

In chapter 2 the review showed that the preamplifier should have a low noise figure to minimise its contribution to the total noise of the signal chain. Thus it was decided to adopt the preamplifier from [11] which had a gain of 20 and an input noise of 3 nV/√Hz.

Apart from the induced signal the SPMU required also the excitation signal to perform the phase measurement between the primary and the secondary magnetic field. This however created the requirement to use the excitation signal from the active excitation coil rather than from the signal generator to avoid any phase errors to be introduced in the measurement.

A simple, stable and low cost solution was reported in [11] in which a reference coil was placed in close proximity to the excitation coil. The induced signal produced by the reference coil was transmitted directly to the SPMU through a cable. Due to its simplicity, its performance and its low cost it was decided to use this concept in the coil array of the Cardiff Mk2c for providing the reference signal to the SPMU.

In chapter 3 the work performed for the development of a single channel phase measurement subsystem showed that the single channel phase subsystem could evolve into a multichannel SPMU that would could satisfy the requirements of the Cardiff Mk2c system.

This however demanded the design of a new 9 channel analogue processing board for processing the signals coming for the coil array and to prepare them for the phase measurement. Also it required the scaling up of the measurement stage in the FPGA to accommodate the required 8 measurement chains and to handle the transmission of the

increased data load to the computer. The conceptual block diagram of the signal route in the Cardiff Mk2c system is given in figure 4.6.

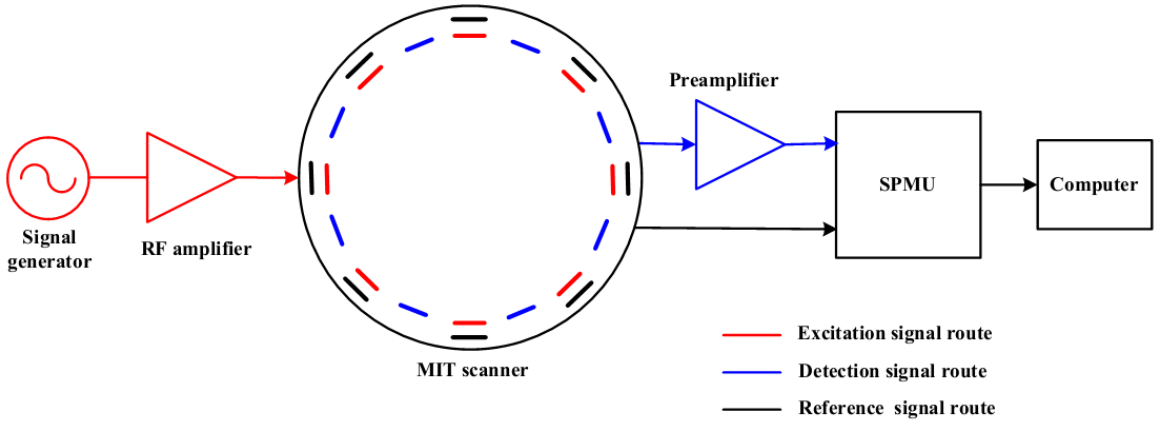


**Figure 4.6**: Conceptual block diagram of the designed signal route in the Cardiff Mk2c system

## 4.4 Implementation of the coil array subsystem

This section presents the work performed for the implementation of the coil array of the Cardiff Mk2c system. The specific details of the coil array's implementation are given in the necessary depth. The coil array implementation incorporated some of the techniques and concepts used for the Cardiff Mk2 system [11] since both coil arrays were developed in the work context of the same research group.

### 4.4.1 The coil array body

The coil array body is shown in figure 4.7 consists of the outer shield, the coil formers and the enclosures for the controlling device circuits and the preamplifier circuits.

**Figure 4.7**: The coil array of the Cardiff Mk2c MIT system

The outer shield as was pointed out in chapter 2 was used for confining the magnetic field in the boundaries of the coil array, to prevent interference from external conductive or magnetic objects, to improve the susceptibility to interference from electrical devices and as a ground plane for the electric fields generated by the coils [36]. Furthermore it provided a rigid frame for mounting the rest of the components on it.

The shield was cylindrical and it was made of aluminium of 2 mm thickness. It had an outside diameter of 34.9 cm, an inner diameter of 34.5 cm and was of 25 cm height. Due to the thinness of the aluminium used the cylindrical shape of the shield was retained with the use of two wooden rings 4 cm high and 1 cm wide placed at each end of the shield. Although the wooden rings limited the usable diameter of the screen down to 27.5 cm they were necessary as otherwise the screen would not have retained its cylindrical shape. The dimensions of the outer shield are given in figure 4.8.

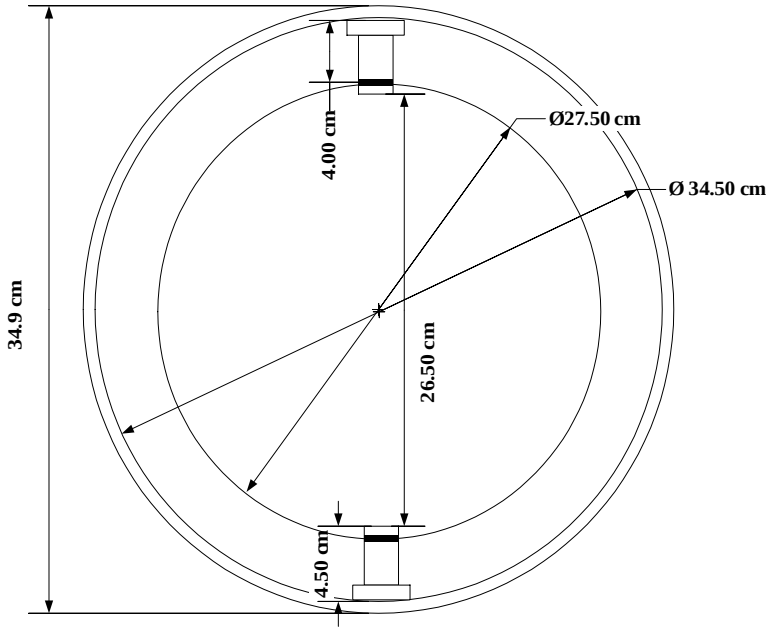


**Figure 4.8**: The dimensions of the outer screen

The coil formers were used for forming and preserving the coils shape. If the coil shape changed then the behaviour of the system would change and it would need to be characterised again. The coil formers were made of perspex plastic that did not swell by humidity and thus did not change shape. Furthermore the plastic was not conductive and thus it did not have any effect on the magnetic field generated in the coil array.

The coil formers had a cylindrical shape, they were 4.5 cm high with an outer diameter of 4.50 cm and an inner diameter of 3.5 cm and a rectangular base. The coil position was 0.5 cm wide and placed at 3.5 cm from the bottom of the former and 0.5 cm from the top. A coil former and its dimensions are shown in figure 4.9.

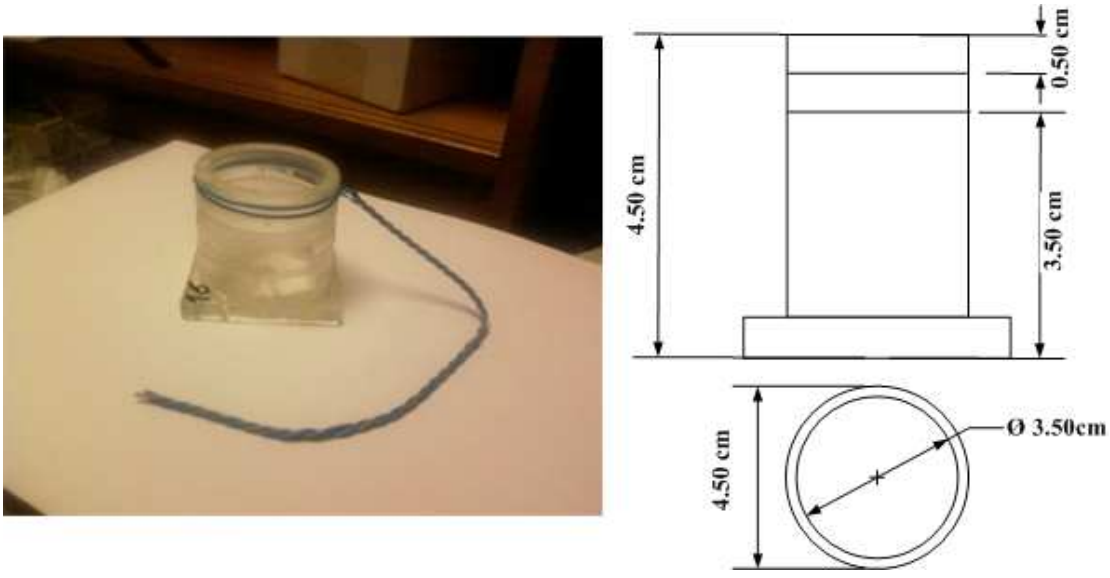


**Figure 4.9**: A coil former on the left and it dimensions on the right

The coil formers were placed into two rings on the inside of the outer shield as shown in figures 4.10 and 4.11. The one ring was used for the excitation coils formers and the other ring for the detections coils formers.

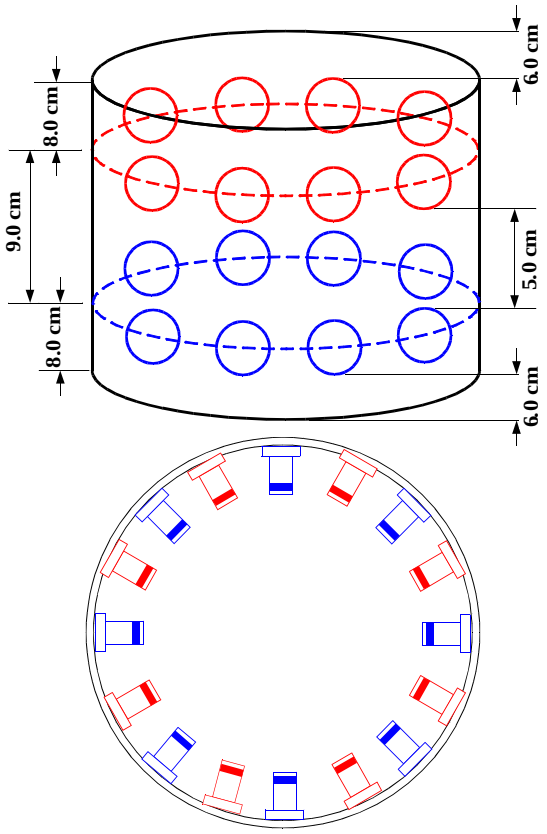


**Figure 4.10**: The coil formers' rings dimensions and placement on the outer shield (viewed from the side and from above)

The coil formers were placed in a configuration resembling a zigzag line in such a way that two coils belonging to a different ring were not placed above each other.

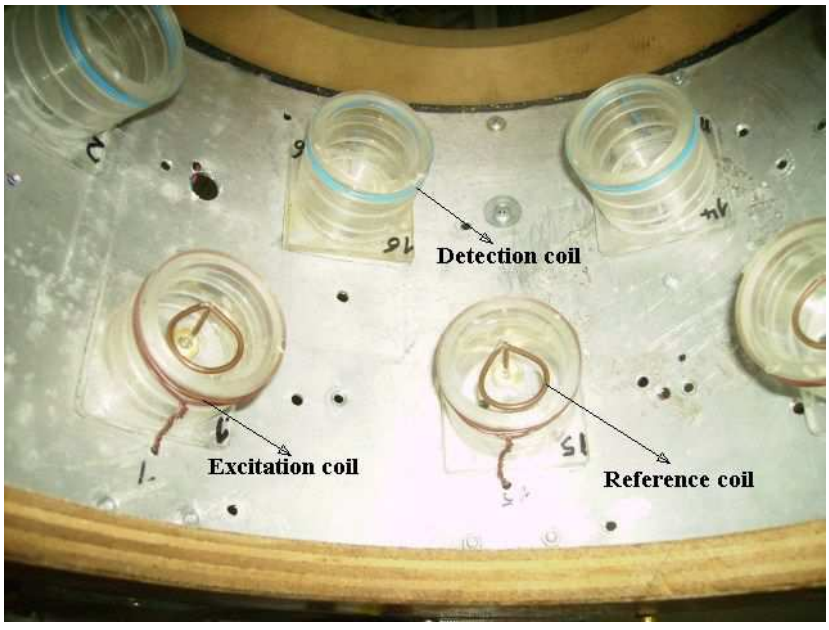


**Figure 4.11**: The coil former configuration in the coil array

The horizontal distance between two opposite coil formers in the same ring was 26.5 cm and the vertical distance between two nearby coil formers in the same ring was about 13.5 cm. The distance from the coil former to the edge of the outer shield was 6 cm and the distance between the centres of the two rings was 9 cm.

Each of the preamplifier circuits and the controlling device circuits were housed in rectangular enclosures made of aluminium with approximate dimensions of 6 cm x 5.3 cm x 2.5 cm. Each rectangular box was placed on the outside of the outer shield directly above a coil former. The position was selected for minimising the distance the signal had to travel between the circuit and the coil. The rectangular boxes had removable tops with screws that allowed direct access to the circuits.

### 4.4.2 The excitation signal circuit

The excitation signal circuit comprised the excitation coils, the signal generator, the RF amplifier, the daisy chain and the RF controlling devices.

#### 4.4.2.1 The excitation coils

The excitation coils were constructed from a single PVC insulated copper wire of 0.6 mm in diameter. Their diameter was 4.5 cm, their height was 0.5 cm and were constructed with 4 turns. The number of the turns was selected to have a large magnetic field strength as possible but at the same time to have an increased self resonance frequency since the more turns are used the lower the self resonance becomes which can create problems with the operation of the coil.

The inductance of the coils was calculated using the Wheeler formula (see Appendix 5) to be equal to 1.4 μH and the self resonance frequency was calculated to be approximately 50 MHz. The one end of the wire was connected to the controlling device circuit and the other end to the ground.

#### 4.4.2.2 The signal generator

The system required a dual signal source to provide one channel for the excitation signal and one channel for the downconversion signal. The system used the dual channel AFG3022B (Tektronix Inc., Oregon, USA) arbitrary function generator. The frequency range of the generator was from DC to 25 MHz which allowed the system to exploit the full frequency region it was intended for. The amplitude range was from 10 $mV_{pp}$ to 10 $V_{pp}$.

#### 4.4.2.3 The RF amplifier and the distribution network

The sinusoidal signal from the one channel of the signal generator was used as input to the RF amplifier ZHL-3A [147] (Minicircuits Inc., New York, USA). The ZHL-3A had a maximum power output of 29.5 dBm (about 0.90 watt).

The excitation coil inductive reactance at 10 MHz was calculated to be about 90 Ω meaning that the RF amplifier could output an excitation current up to 100 $mA_{rms}$ to the excitation coil. The maximum amplitude of the input signal to the RF amplifier allowed by the manufacturer was 10 dBm (about 2.1 $V_{pp}$). During the preliminary tests it was observed that the RF amplifier output was becoming distorted above 35 $V_{pp}$ and so it was not used beyond this signal output.

The output of the RF amplifier was used as input to the daisy chain that distributed the excitation signal to the excitation coils through the RF controlling device. In essence the daisy chain connected the excitation coils through the controlling devices into an incomplete ring. The entry point of the excitation signal was the excitation coil which was closest to the RF amplifier and the last point was the last excitation coil of the annular array. The daisy chain distribution is shown in figure 4.12.

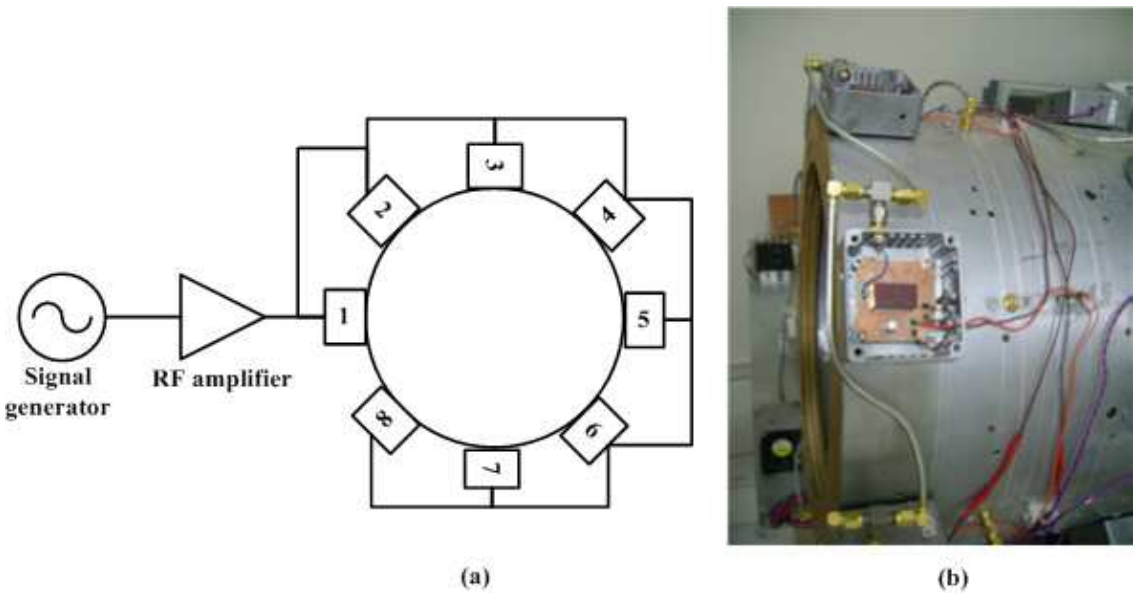


**Figure 4.12**: The daisy chain distribution of the excitation signal (a) block diagram (b) photo of the realisation

The daisy chain was realised with seven small semi-rigid RG402 coaxial cable with an SMA bulkhead at each end. A T connector was used to connect the controlling device and the RG402 cable going to the next coil with the RG402 cable coming from the previous coil.

#### 4.4.2.4 The RF controlling device circuit

The use of the daisy chain for the signal distribution required an RF controlling device to be placed on each excitation coil to isolate it when not in use. If not then the rest of the excitation coils would load and perturb the excitation field of the active excitation coil. Such RF switch had to be situated as close as possible to the excitation coil since any cabling adds capacitance and inductance. Furthermore it had to handle up to 50 $V_{pp}$ at 10 MHz and drive up to 1 A into a 50 Ω load. These specifications were set to allow the excitation signal to extend in the future.

There are two groups of RF switches which are the electromechanical (mechanical relay, reed relay) and the solid state (solid state relay, MOSFET switch, PIN diode). From the options available the mechanical relay was selected because it was simple to implement, it could easily handle the current and the voltage required, it had very good isolation properties at 10 MHz and it was cheap. However the mechanical relays can be slow with their operation time reaching to several milliseconds.

The mechanical relay ARE134H (Panasonic Inc., Osaka, Japan) was selected for the implementation because it offered 60 dB isolation at 900 MHz, good signal handling as mentioned in [11] and because it was of low cost. Apart from the isolation and the signal handling the main interest for the Cardiff Mk2c was the increased data acquisition rate and thus an evaluation was performed regarding the circuit layout used in the Cardiff Mk2 and the relay operation and release time.

The circuit layout used an NPN transistor as a switch to drive the relay. Since in the Cardiff Mk2c architecture design it was required that an automated central control should be achieved the NPN transistor input was designed to be driven by a digital pulse whose amplitude could be as low as 2.5 V.

An important aspect for every circuit incorporating a relay is the compensation circuit that is used to limit the inductive kick back of the relay coil. This can reach up to several decades of volts and damage the NPN transistor or other circuitry. An investigation was therefore performed using different compensation circuits to find the most suitable for the relay circuit. The results of the investigation are given in the following table.

**Table 4.5**: Results from the compensation used on the ARE134 mechanical relay

| Compensation used in parallel to the relay coil | Inductive kick back (Vp) | Relay operation times (ms) | Relay release time (ms) |
|---|---|---|---|
| None – from ARE134 data sheet | Not given | 10 maximum | 5 maximum |
| None – measured | 166 | 3 | 1.2 |
| 1N4004 diode | 6 | 3.4 | 3.5 |
| 1N4004 diode with BZX61 zener diode (11V) | 154 | 3.4 | 1.2 |
| 1N4002 diode with BZX79-C24 zener diode (24V) [148-150] | 30 | 3.4 | 1.2 |

However the penalty for compensating the relay was the increased relay operation and release time. From the investigation results it was clear that the best compromise between a low figure of the relay operation and release time and a reduced inductive kick back was to compensate the relay with a 1N4002 diode and a BZX79-C24 zener diode in common anode configuration.

The results when the relay was used uncompensated and when compensated with the 1N4004 diode with BZX79-C24 zener diode are shown in figure 4.13. When the relay was used uncompensated the inductive kickback could reach up to 166 V which could potentially destroy an NPN transistor.

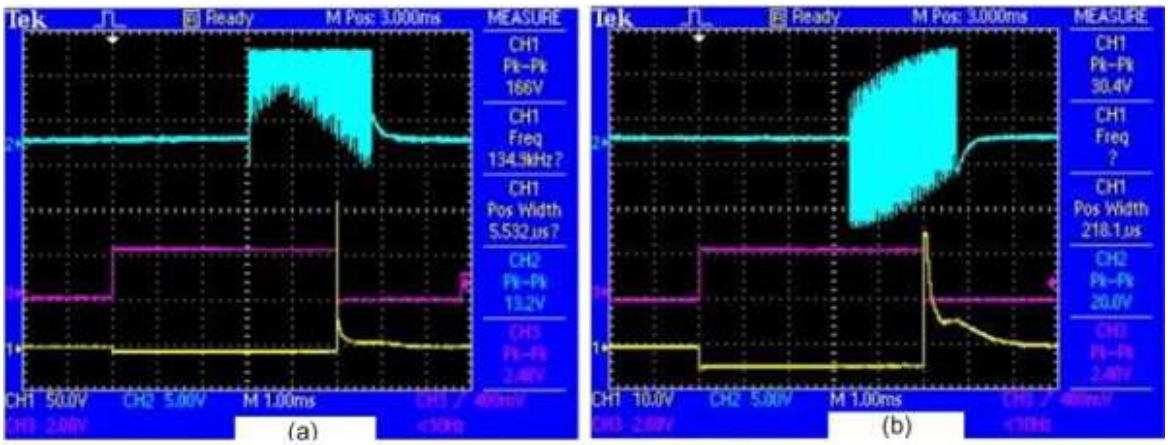


**Figure 4.13**: The input pulse (purple trace), the output of the transistor connector (yellow trace) and the relay output (blue trace) when (a) uncompensated and (b) compensated with 1N4004 diode with BZX79-C24 zener diode

The use of the relay uncompensated increased the specification demand of the NPN transistor to one that could handle the magnitude of the inductive kickback. The 1N4004 diode with BZX79-C24 zener diode compensation lowered the inductive kickback down to 30 V thus lowered the specification demand on the NPN transistor. The circuit diagram and the implementation of the RF relay are given in figure 4.14.

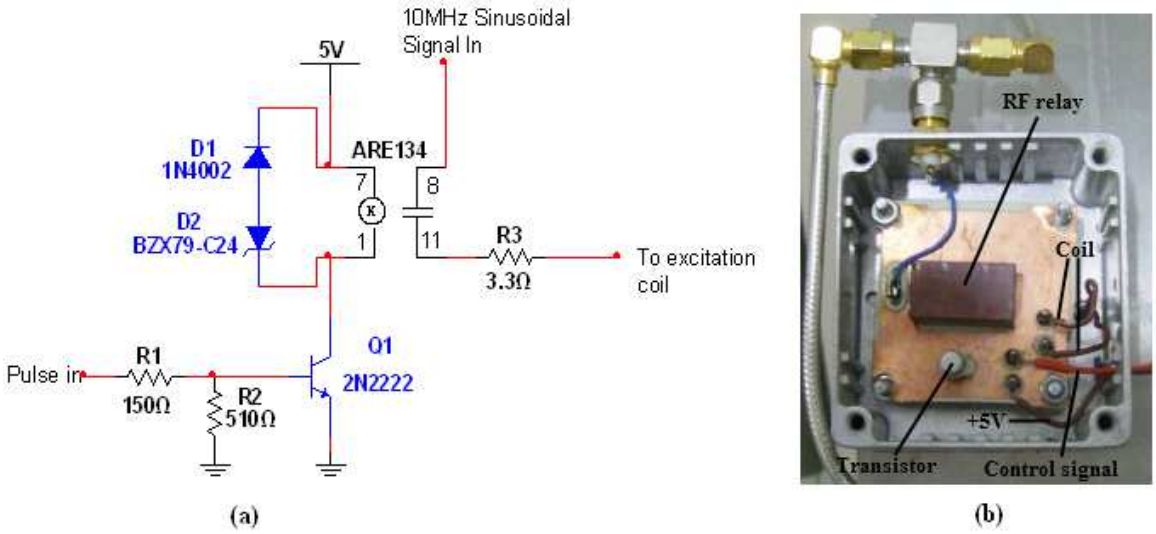


**Figure 4.14**: The RF relay circuit diagram (a) and the implementation (b)

### 4.4.3 The detection signal circuit

The detection signal circuit comprised the detection coils and the preamplifier. Each detection coils was constructed from a single PVC insulated copper wire of 0.6 mm in diameter. Its diameter was 4.5 cm, its height was 0.5 cm and it had 2 turns. A single PVC insulated copper wire of 0.60 mm in diameter was connected as a centre tab to the coil.

In [11] it was stated that detection coils with these specifications and 4 turns exhibited resonances at 30 MHz and 50 MHz. That caused significant distortion at 10 MHz and their optimal behaviour was when 2 turns were used. This was adopted and the detection coils were constructed with 2 turns. The inductance of the detection coils was calculated using the Wheeler formula (see Appendix 5) to be equal to 0.37 μH and the self resonance frequency was calculated to be approximately 56 MHz. The two ends of the coil wire were connected to the preamplifier inputs and the end of the centre tab wire was connected to the ground.

The preamplifiers used in the coil array were adopted from [11] and the circuit diagrams is shown in figure 4.15. The preamplifier design has been already described in chapter 2 and it will not be repeated here. The output of the preamplifier was connected with a semi-rigid RG402 coaxial cable directly to the input of the respective SPMU analogue signal chain. The RG402 was used because it provides excellent phase stability performance due to its high mechanical stability and high isolation.

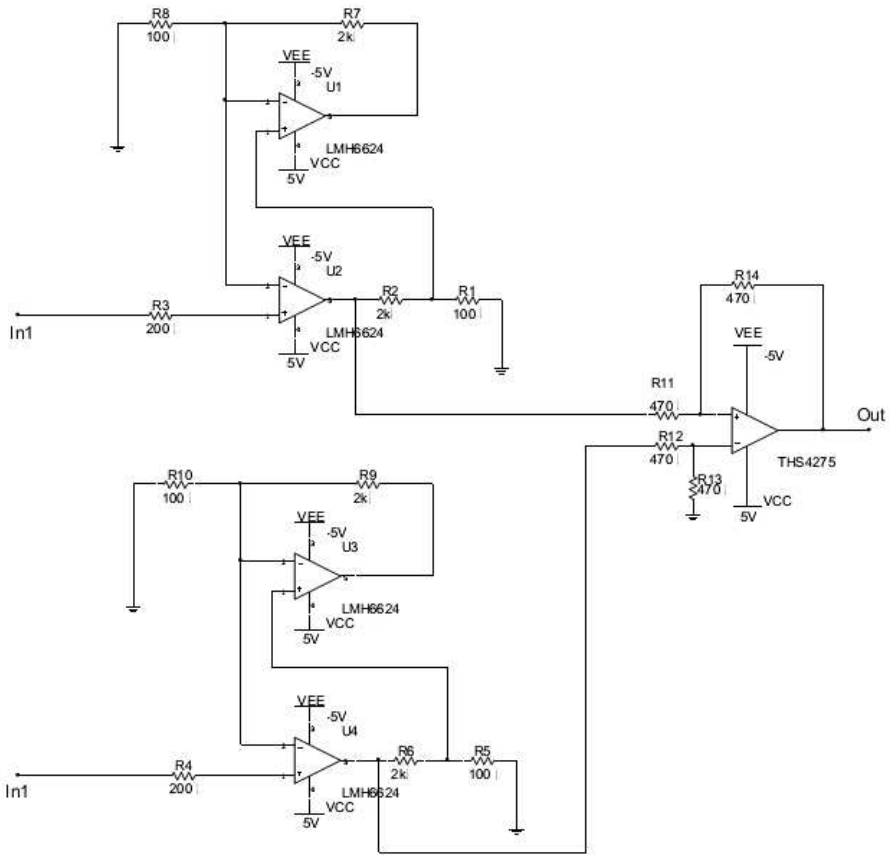


**Figure 4.15**: The low noise preamplifier used in the Cardiff Mk2c (from [11])

### 4.4.4 The reference signal circuit

The reference circuit was adopted from [11]. A reference coil was placed inside the excitation coil and then a power combiner was used to transfer the reference signal to the SPMU. The reference coil is shown in figure 4.16.

**Figure 4.16**: The reference signal coil used in the Cardiff Mk2c

Each of the reference coils was constructed from RG405 semi-rigid coaxial cable with 2

cm diameter single-turn coil. The one end of the inside conductor that form the coil was directly soldered on the outside conductor. The other end was soldered on the pin of an SMA connector on which the outside conductor was also soldered. The SMA was then screwed on the shield.

The power combiner selected was the ZFSC-8-1-S+ (Minicircuits Inc., New York, USA) which had 8 inputs and 1 output. A semi-rigid RG402 coaxial cable was used to connect a reference coil with an input of the power combiner. The use of the power combiner was based on the reasoning that although during a projection all reference coils induce signal the output of the power combiner is dominated by the signal from the reference coil that is inside the active excitation coil.

### 4.4.5 The power supply

A dedicated board was constructed comprising two 7805 regulators for outputting the regulated+5 VDC and two 7905 regulators for outputting the – 5VDC. The regulators had a maximum current output of 1 A and required an input of at least ± 9 VDC to operate correctly which was provided by the dual channel power supply GPC-3030D (GW Instek).

The board was used to power the preamplifier boards with ± 5 VDC and the RF relay circuit boards with 5 VDC. The board was placed inside a metal enclosure and a fan on the top provided forced cooling.

## 4.5 Implementation of the multichannel SPMU

This section covers the work performed for the development of the multichannel signal processing and measurement unit (SPMU) intended for the Cardiff Mk2c.

### 4.5.1 Architecture and implementation considerations

The multichannel SPMU is based on the design of the single channel described in chapter 3 and is a multi-channel implementation of this single-channel design. As such it maintains the two main stages of the single channel system which are the analogue processing stage and the measurement stage.

The latter maintains the measurement part and the communication part however a notable difference from the single channel is the addition of a third part called the excitation section to satisfy the implementation requirement regarding the automated control over the RF relays stated in section 4.3.2. The block diagram in figure 4.17 depicts the general

architecture of the measurement system.

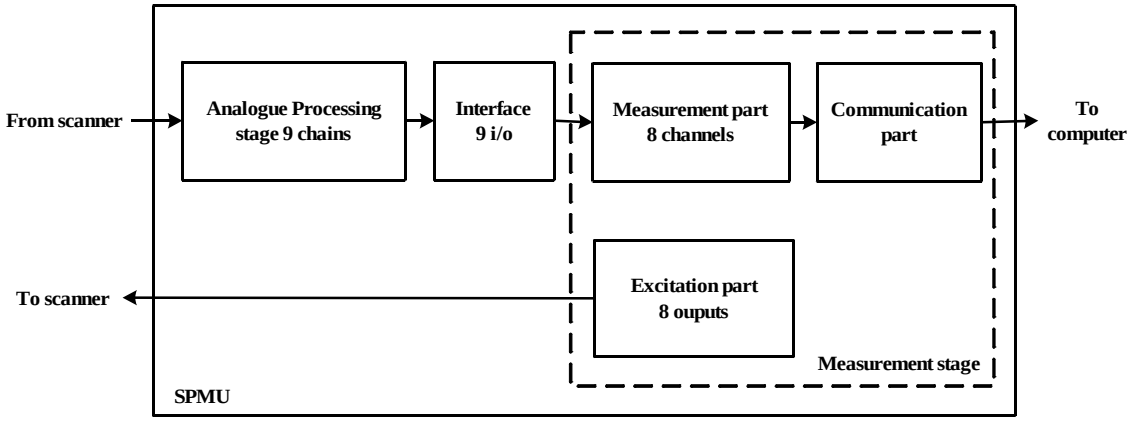


**Figure 4.17:** Block diagram of the SPMU general architecture

The scale up of the analogue processing stage from 2 signal chain lines to 9 signal lines (8 channels plus the reference) created the need for developing and constructing a new pcb board.

Each signal chain line connected to the coil array using one SMA socket directly soldered on the pcb board. The same connectors were used in the coil array. To connect the pcb board to the Spartan-3 system board a 40 pin male connector was placed on the pcb board for direct connection to the 40 pin female expansion connector of the Spartan-3 system board. This eliminated the need for using connecting cables that could introduce time delays to the signals. Two readily available 74LVC245 octal bidirectional transceivers were used to provide the level translation between the comparators and the Spartan-3.

The signal generator channel output which provided the downconversion signal was connected with an RG402 cable directly to an SMA socket placed on the board. From there the downconversion signal was distributed to the inputs of the multipliers with a pcb track.

To implement the excitation part in the FPGA the findings of section 4.4.2.4 were taken into consideration. There it was shown that the compensated RF relay circuit used in the coil array had an operation time of 3.4 ms and a release time of 1.2 ms. This created the requirement to allocate time for the relay operation time before the projection and for the relay release time after the projection.

### 4.5.2 The analogue stage of SPMU

The analogue processing stage was a scale up of the analogue processing stage of the single channel subsystem described in chapter 3. It used the same signal chain as in the single channel with the same components and the same layout. However in this case 9

signal chains were used instead of 2 signal chains. The signal chains were placed in parallel on a double sided pcb board as shown in figure 4.18.

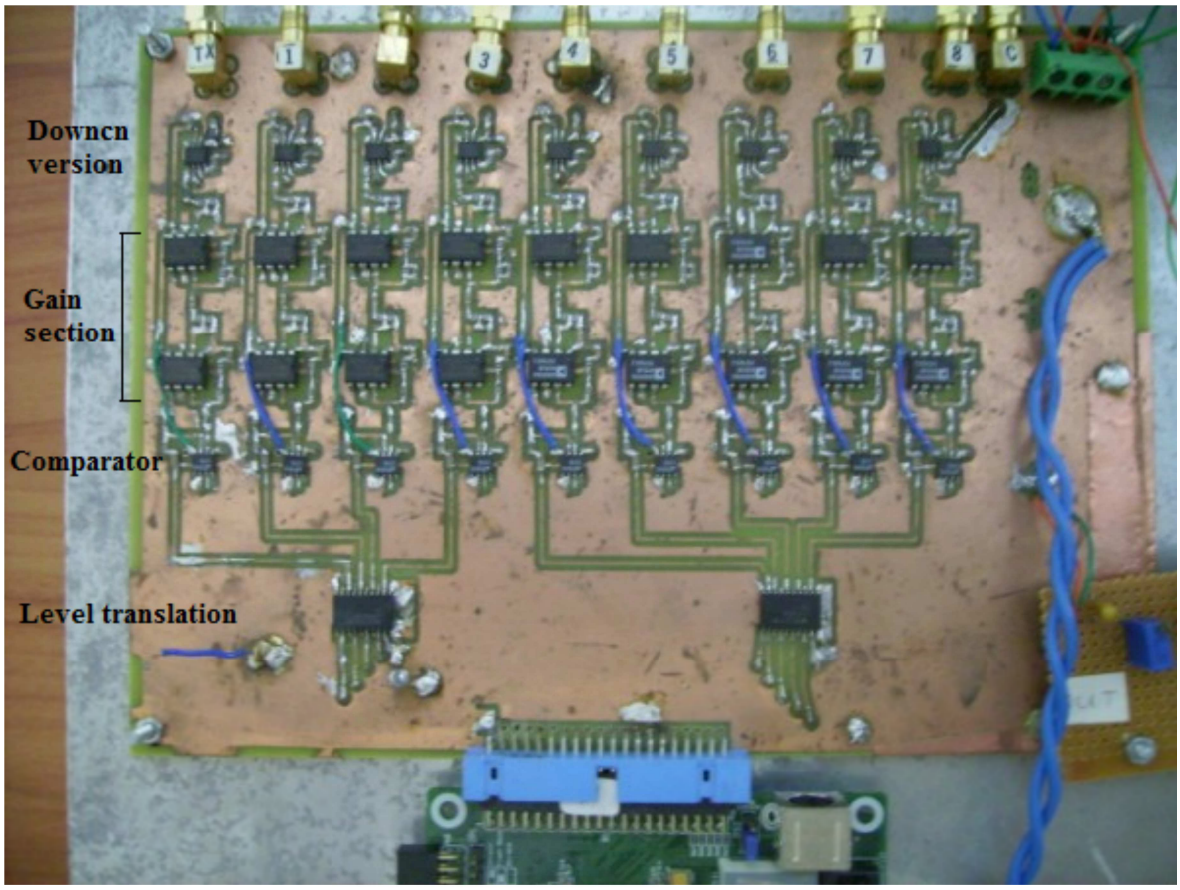


**Figure 4.18**: The implemented analogue processing stage of the multichannel SPMU

The upper side was used for the component placement, the signal tracks and some of the power tracks that did not fit on the bottom side while the bottom side was used for the power tracks and the ground plane. The reference signal chain was placed on the left hand side and the rest of the signal chains intended for the detection coils were placed next to the reference signal chain progressively. The downconversion signal SMA socket was placed last after the signal chain 8. This implementation required the least board space and eased the distribution of the signals, the power supply and the downconversion signal. The latter was implemented as in the single channel.

The board required three DC voltages to operate which are ±5 VDC for the AD835, the AD8056 and the LT1016 and 3.3 V for the 74LVC245. When the board was first implemented it included three voltage regulators for providing the DC voltages required. However they were removed shortly after the first operation of the board due to the excessive heat they produced when operating which could result in causing thermal drift to the other components. A small power pcb board comprising the three voltage regulators was implemented separately and connected permanently to the board through copper wires.

### 4.5.3 The measurement stage of SPMU

The measurement stage had to fulfil three tasks simultaneously. The first was to measure the phase difference of the 8 channels, the second was to transmit the measurement to the computer and the third was to precisely control the RF relays. It was required to perform these tasks very fast to minimise the operation time and thus contribute to increasing the frame rate.

#### 4.5.3.1 The measurement section

The measurement section was used to measure the phase difference between the activated excitation coil and the detection coils. To achieve this the component block “channel” from chapter 3 was used as the main building component and it is shown in figure 4.19.

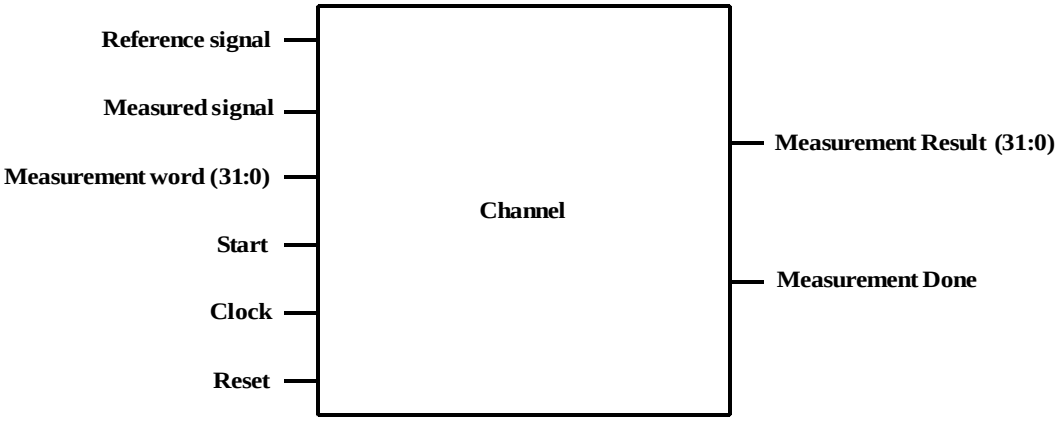


**Figure 4.19**: The component channel presented as a black box

For the implementation of the measurement section 8 channel blocks were required. Apart from the input “Measured signal” which was the signal from the detection coil the other 5 inputs to the channel were common to all 8 channels. Thus only 5 signal lines were required to communicate the input signals to all channels.

Handling the output of the channels however was not that simple. Each channel outputted the “Measurement Result” and the “Measurement Done” signal which signified that the channel had ended the measurement. The latter was used by the measurement stage as a flag to start the transmission of the measurement result to the computer.

Since 8 channels were used the measurement stage state machine not only should acknowledge all of them but should also wait for all of them to finish the measurement before the data transmission started. This avoided any confusion of the measurement results.

To simplify the acknowledgement of the “Measurement Done” signal by the measurement stage state machine an 8-input AND gate was used to output a logic 1 when all its inputs

were logic 1. Thus the state machine would have to acknowledge only one signal to know that all the channels has finished the measurement.

The design above however required that all channels should output the “Measurement Done” signal at the same clock edge and that all signals should arrive concurrently to the input of the AND gate. If this did not happen then the AND gate would output a logic 0 and the state machine would not be aware that the measurement was finished. The failure of the circuit when operated in this configuration was verified with repeated real measurements because it did not happen very often.

The required level of synchronization to eliminate failures due to the issue described above could be achieved with two ways. Either to introduce a time delay on the logic high of all the “Measurement Done” signals or to use a kind of temporary memory to remember the high state of the “Measurement Done” signals.

Although the former was achievable it was considered to be a more complicated solution than the latter. Thus to implement the temporary memory the component “pulse detector” was used. It was implemented as a state machine that acknowledged an input logic 1 with a logic 1 at its output until it was reset by an external controller.

A pulse detector was placed at the output of the “Measurement Done” signal of each channel prior to the input of the AND gate. A pulse detector was also placed at the output of the AND gate to make sure that the measurement stage state machine would have the time to acknowledge the logic 1 of the AND gate.

After the measurement stage machine acknowledged the logic 1 at the AND gate output it reset the pulse detectors. This mechanism composed of the AND gate and the pulse detectors before and after the AND gate provided a fail safe operation of the measurement part. The measurement section is shown in 4.20.

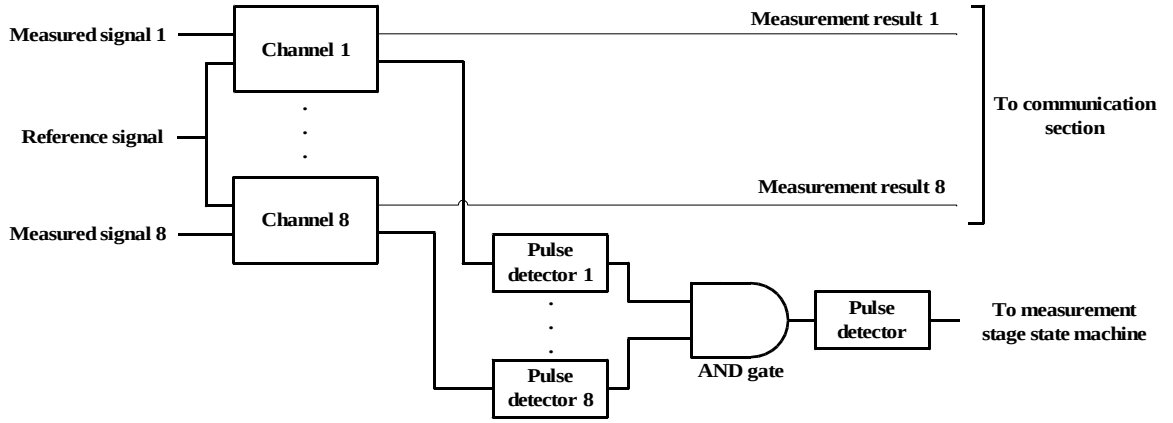


**Figure 4.20**: Block diagram of the measurement section as implemented in the SPMU measurement stage

The measurement result of each channel was 4 bytes. Thus the data load from the measurement part to the communication part was 32 bytes for each activated excitation coil. The total number of the data bits produced by the measurement part for a complete frame was given by

$$DL_{frame} = channel\ output\ bits \times m \times n \qquad (4.14)$$

where m is the number of the excitation coils used in the coil array and n is the number of the detection coils used in the coil array.

The phase measurement time (PMT) required by the measurement part to measure one phase difference value when one excitation coil is used was given by equation (3.12) in chapter 3. However when more than one excitation coils are used then the phase measurement time of the complete frame is given by

$$PMT_{frame} = \frac{N}{2f_{DC}} \times m \qquad (4.15)$$

where $f_{DC}$ is the downconversion frequency, N is the number of the XOR pulses averaged and m is the excitation coils number.

### 4.5.3.2 The communication section

The communication section of the SPMU measurement stage used the same components as the communication section of the single channel described in chapter 3. Some of the communication part components were upgraded to accommodate the increased requirements for the multichannel subsystem. These components were the multiplexer and the counter. The block diagram is shown in figure 4.21.

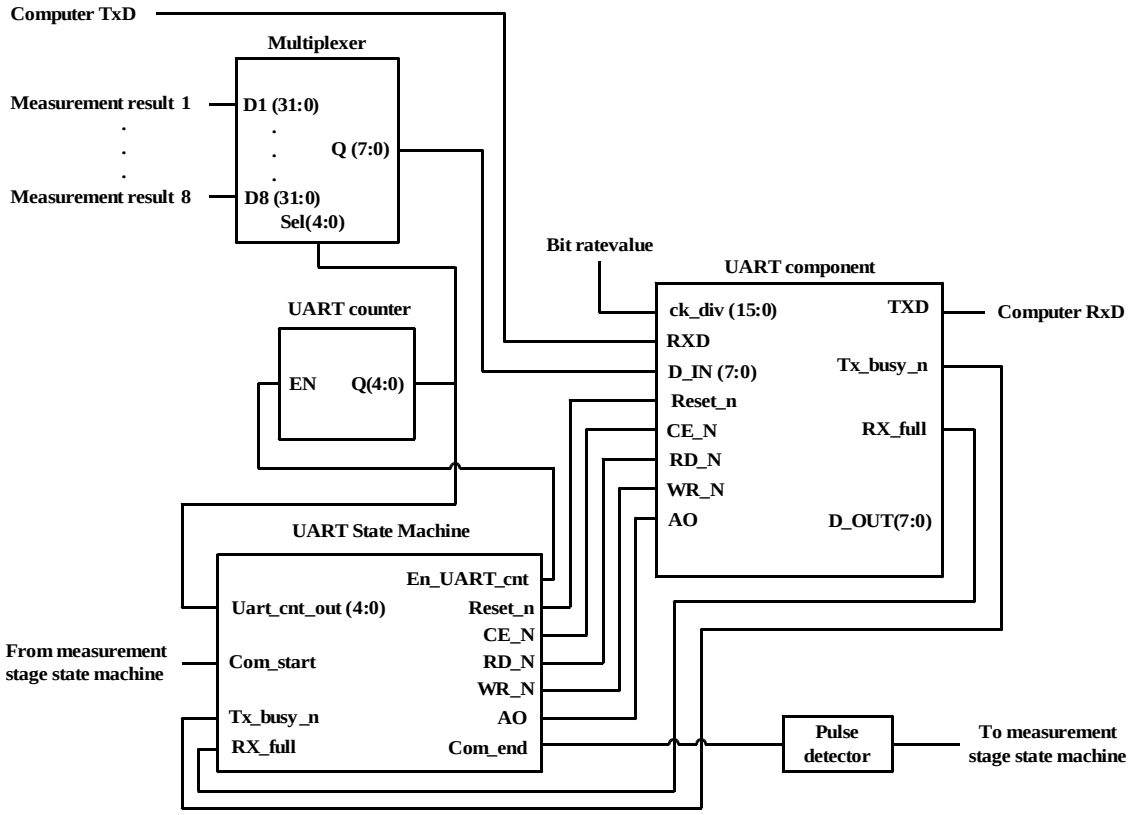


**Figure 4.21**: Block diagram of the communication section implementation

The multiplexer was increased from a 32 bit input to a 256 bit input to accept concurrently the measurement results from the 8 channels. The multiplexer select line Sel was also increased to 5 bits which allowed for 32 eight bit data to be outputted. The Sel was controlled from the UART counter whose output was equally increased to 5 bits.

These changes affected the UART State Machine regarding the input of the increased logic vector (4:0) from the UART counter output. Otherwise the UART SM remained the same as the one used in the single channel phase measurement subsystem. The UART SM flow diagram is shown in figure 4.22.

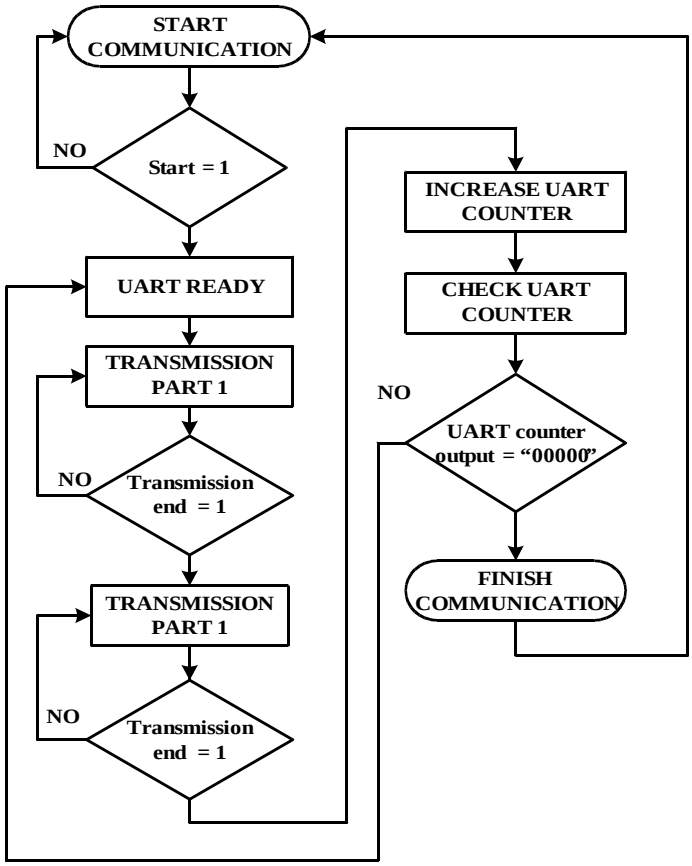


**Figure 4.22**: The communication section state machine

Equation (3.13) from chapter 3 can be used to calculate the data transmission time required for transmitting the results of a phase measurement for one activated excitation coil. However the total data transmission time required to transmit the data load for one frame is given by

$$DTT_{SPMU} = \frac{DL_{frame} + OVR}{BR} \qquad (4.16)$$

where $DL_{frame}$ is the frame data load in bits from the measurement part for one frame, BR is the bit rate used and OVR is the protocol overhead in of the extra bits.

#### 4.5.3.3 The excitation section

The excitation section of the SPMU was developed to replace the USB-6501 aiming to provide a low cost, automated and precise control over the RF relays. To achieve this two requirements were needed to be satisfied. The first was to allow the required time period for the relay operation time which is the transition time $T_{TRANS}$ between the projections. The second was to activate the RF relay controlling the excitation coil right after $T_{TRANS}$ has elapsed, maintain the excitation time for the phase measurement and de-activate it when the measurement for that excitation coil was finished.

To allow for $T_{TRANS}$ a simple design called the transition counter was developed which comprised a counter and a comparator. The counter was enabled by the measurement stage state machine and its output was constantly compared by the comparator with a set value. When the counter output reached that set value the comparator outputted a logic 1 through a pulse detector to the state machine signifying that the value had been reached. This indicated to the state machine when the $T_{TRANS}$ had elapsed. The state machine then disabled and cleared the transition counter. The block diagram of the transition counter is shown in figure 4.23.

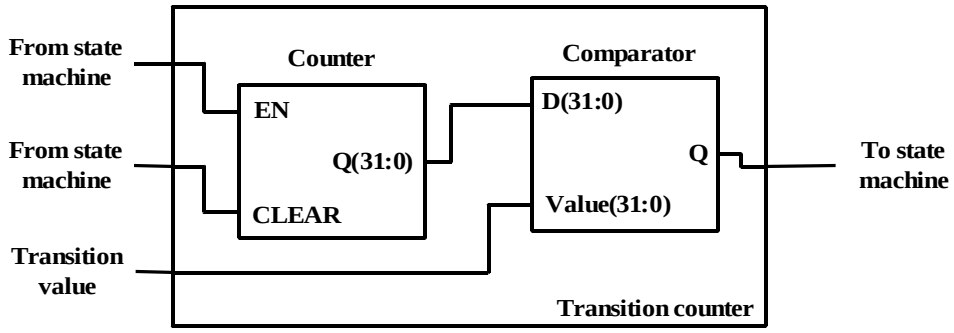


**Figure 4.23**: The transition counter

The transition value is calculated by

$$Transition\,value = \frac{T_{TRANS}}{T_{clock}} \qquad (4.17)$$

where $T_{TRANS}$ is the transition time in s and $T_{clock}$ is the clock period used to clock the transition counter in s.

To activate and de-activate the RF relays a simple circuit configuration comprised by a counter (called excitation counter) and a decoder was used (figure 4.24). The counter output was connected to the decoder's select line Sel(3.1). The select line Sel(0) was controlled directly from the measurement stage state machine. The decoder output D(7:0) was connected to the 8 output FPGA pins which were connected to the transistor base of the RF relay circuit (see section 4.4.2.4).

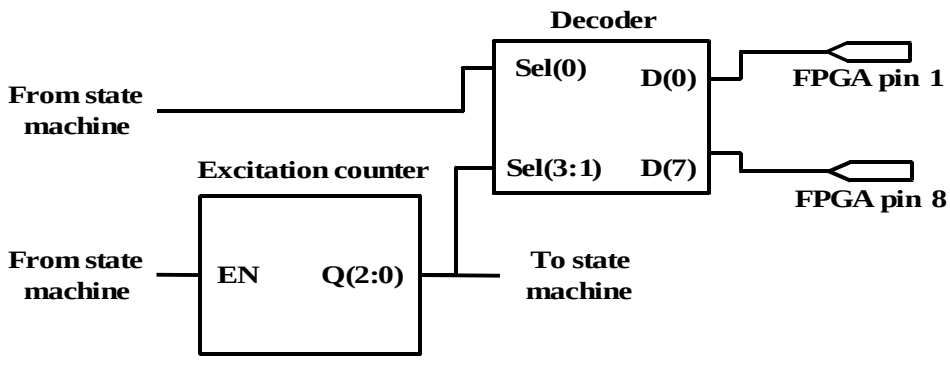


**Figure 4.24**: The circuit for activating and deactivating the RF relays

After the transition counter signalled the state machine with a logic 1 that $T_{TRANS}$ had elapsed the state machine enabled the counter and set the Sel(0) to logic 1. The decoder outputted the value that corresponded to the combined Sel(3:0) as shown in the truth table in table 4.6. This activated the respective RF relay and the excitation coil controlled by it. At the same time the output of the counter was transmitted back to the state machine.

**Table 4.6**: The decoder truth table

| Sel(0) | Sel(3:1) | D(7:0) |
|---|---|---|
| 1 | 000 | 00000001 |
| 1 | 001 | 00000010 |
| 1 | 010 | 00000100 |
| 1 | 011 | 00001000 |
| 1 | 100 | 00010000 |
| 1 | 101 | 00100000 |
| 1 | 110 | 01000000 |
| 1 | 111 | 10000000 |
| 0 | XXX | 00000000 |

#### 4.5.3.4 The measurement stage state machine

The measurement stage state machine is similar to the state machine used for the single channel measurement stage with two notable differences which will be explained here. The remainder of the state machine operation has been already explained in chapter 3. The measurement state machine flow diagram is shown in figure 4.25.

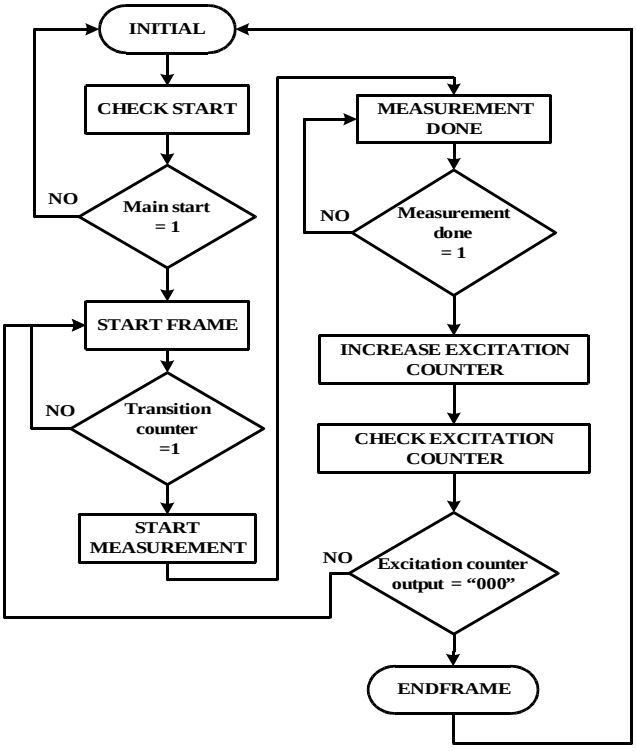


**Figure 4.25**: The measurement stage state machine

The first difference was the state START FRAME which checked whether the transition counter had finished counting and thus the activation of the excitation coil which meant that the phase measurement could start.

The second difference were the states INCREASE EXCITATION COUNTER and CHECK EXCITATION COUNTER involved with the activation of the excitation coils. The first state increased the output of the excitation counter by 1 and the second checked if its output has reached the value “000” which meant that all 8 excitation coils were activated and a frame had been captured. If the excitation counter output was “000” then the END FRAME state set the decoder's Sel(0) to logic 0 and returned to the INITIAL state which set the measurement stage to initial conditions.

## 4.6 The Cardiff Mk2c as a complete system

The previous sections presented the work performed for the design and the implementation of the coil array and the signal processing and measurement unit (SPMU) for the Cardiff Mk2c system. This section presents the Cardiff Mk2c as a complete system and calculates its expected frame rate based on the constraints introduced by each hardware component.

### 4.6.1 The hardware part of the system

The block diagram of the hardware part of the Cardiff Mk2c system is given in figure 4.28. The implemented hardware part of the system conforms to the architecture described in section 4.2.1. The two architectural hardware subsystems which are the coil array and the SPMU are clearly visible and easy to identify. The Cardiff Mk2c system implementation is shown in figure 4.26 and the detailed block diagram in figure 4.27.

**Figure 4.26**: The Cardiff Mk2c system

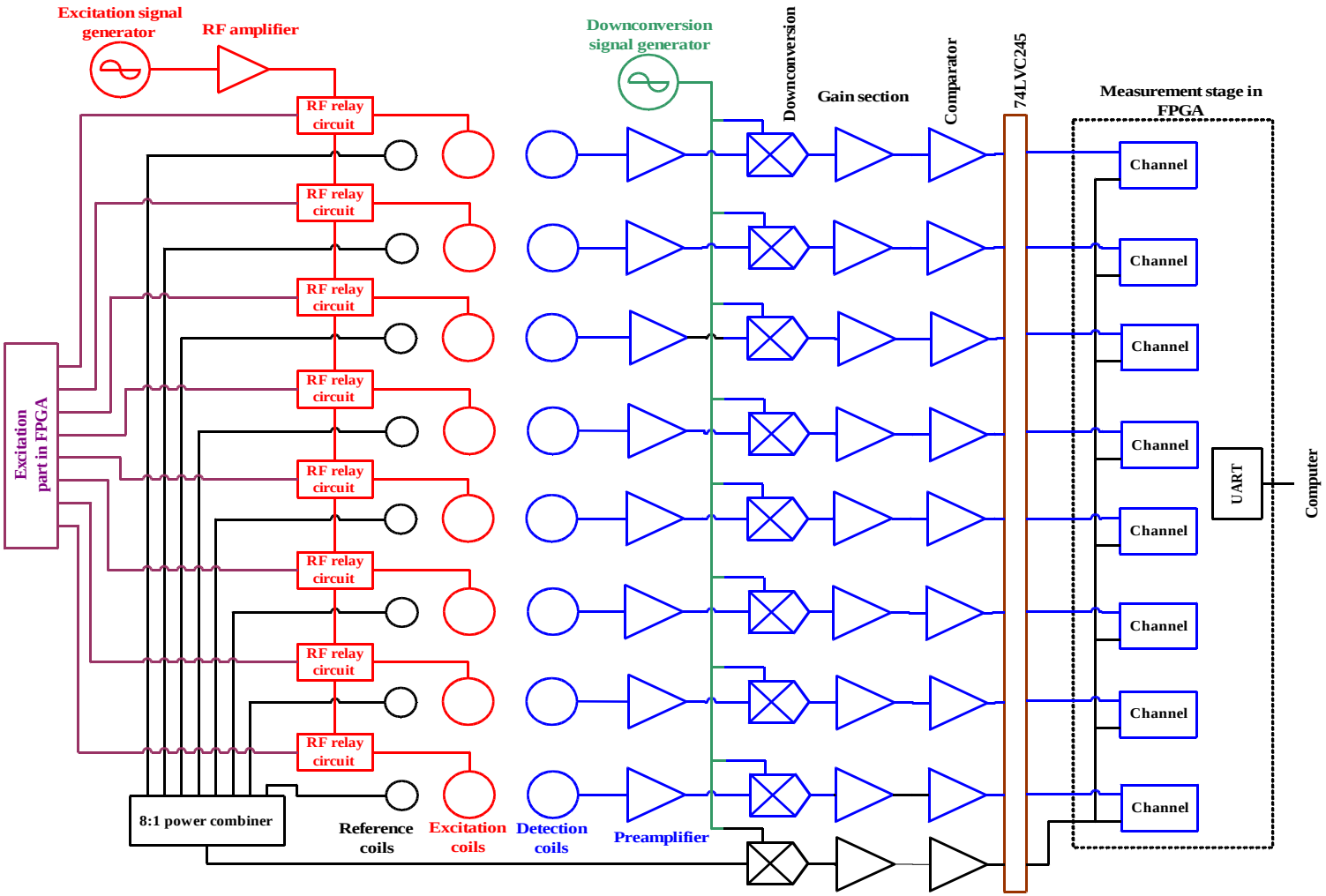


**Figure 4.27**: Block diagram of the CardiffMk2c as a working unit

The implemented hardware subsystems were fixed on an aluminium basis for the experimental part of the study (figure 4.26). This provided easy and quick access to the hardware parts and allowed for measurements on the circuits used. Although this structure can be useful for experimental conditions it is debatable whether it would be useful for a possible implementation of the system in a real industrial environment. In such case a different way of securing the hardware parts may be required.

Every effort was made to keep the connecting wires and the cables used for transferring the signals between the subsystems as small as possible. This was achieved with the longest cable being shorter than 1 m.

### 4.6.2 Calculation of the frame rate of the hardware part

The equations developed in the analysis for the MIT system frame rate in section 4.2.2 were used to calculate the expected frame rate of the Cardiff Mk2c at 5 ms time constant and 50 ms time constant. The calculations and the results are described in this section.

For the calculations the Cardiff Mk2c was set as a parallel system with 8 excitation coils (m=8) and 8 detection coils (n=8). The downconversion frequency was set at 10 kHz and the clock period $T_{clk}$ for the SPMU measurement stage was set at 20 ns. The propagation times were considered to be less than ps therefore they were not included in the calculations.

The transition time $T_{TRANS}$ was the RF relay operation and relay release time which in section 4.4.2.4 were measured to be 3.4 ms and 1.2 ms respectively. During the implementation of the excitation part in the FPGA the relay release time of the previous relay was coincided with the relay operation time of the next relay therefore practically the $T_{TRANS}$ time was equal only to the RF relay operation time. Therefore for 8 excitation coils the cumulative transition time was $T_{TRANS}$ = 27.2 ms.

For the Cardiff Mk2c system the cumulative $T_R$ time for m channels is actually the phase measurement time (PMT) given by equation (4.15). For 5 ms time constant the $T_{EX5ms}$ = 40 ms and for 50 ms time constant the $T_{EX50ms}$ = 400 ms.

Thus the total excitation time $T_{TEX}$ required to perform the complete measurement was calculated with equation (4.3) to be $T_{TEX5ms}$ = 67.20 ms and $T_{TEX50ms}$ = 427.20 ms.

The time $T_{HMpar}$ was calculated with equation (4.5) which for 5 ms time constant it gives

$T_{HMpar5ms}$ = 67.20 ms and for 50 ms time constant it gives $T_{HMpar50ms}$ = 427.20 ms.

Thus with the use of equation (4.1) the maximum frame rate for the hardware part was calculated to be 14.88 frames per second for 5 ms time constant and 2.34 frames per second for 50 ms time constant.

## 4.7 Characterisation of the multichannel SPMU

The multichannel SPMU was characterised in terms of phase precision, phase drift and the frame rate it could achieve. The characterisation aimed to identify the best performance the SPMU could reach.

### 4.7.1 Test set-up

The test set-up for the characterisation test is given in the figure 4.28.

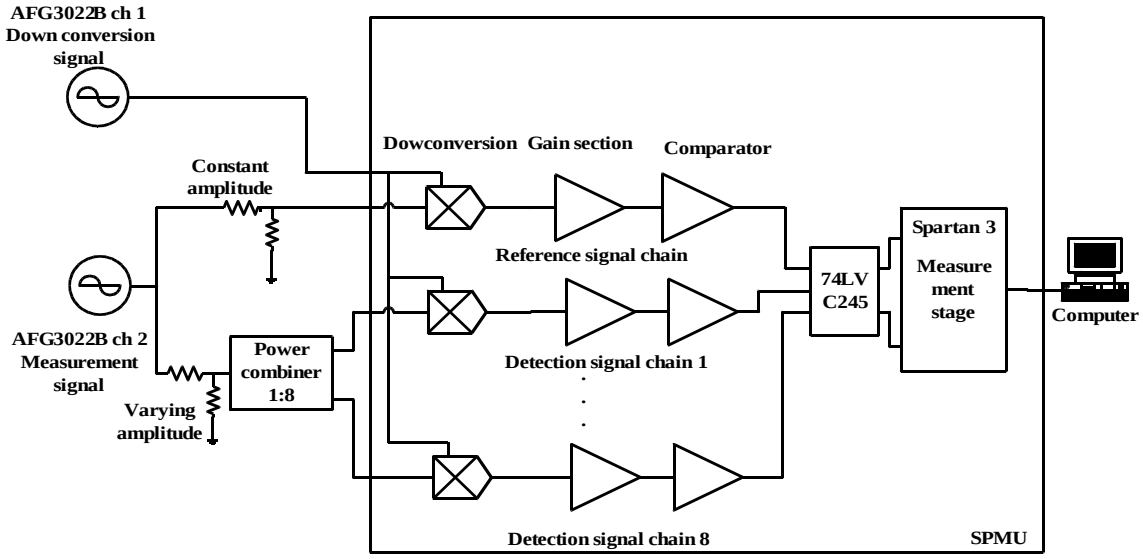


**Figure 4.28**: The test set-up for the 8 channel SPMU characterisation

The measurement stage was programmed in the Spartan-3 on-board the Spartan-3 system board and clocked with 20 ns $T_{clk}$. The time constant was set to 5 ms.

One channel of the AFG3022B provided the measurement sinusoidal signal with a 10 MHz frequency of and amplitude of 10 $V_{pp}$ which was divided into two signals. The first signal was passed through the voltage divider where it was divided down to 1.8 $V_{pp}$ and was fed directly to the reference signal chain. It was retained at 1.8 $V_{pp}$ until the end of the measurements.

The second signal was passed through a voltage divider and divided in predefined steps from 1.8 $V_{pp}$ to 20 $mV_{pp}$. Then it was fed to the single input of the power combiner ZFSC-

8-1-S+ that provided the eight signals for the inputs to the detection signal chains. It was observed that the power combiner reduced the input signal from the voltage divider by a factor of 5 therefore the input to the power combiner was increased by a factor of 5 to retain the balance.

The second channel provided the downconversion sinusoidal signal with a frequency of 9.99 MHz and amplitude of 2 $V_{pp.}$ The raw data were transmitted to a computer running the LabWindows application software in the Windows XP operating environment.

### 4.7.2 Phase precision

The phase precision was calculated from the first 10 phase difference values in Microsoft Excel using equation (3.15). The phase precision characterisation results are graphically shown in figure 4.29.

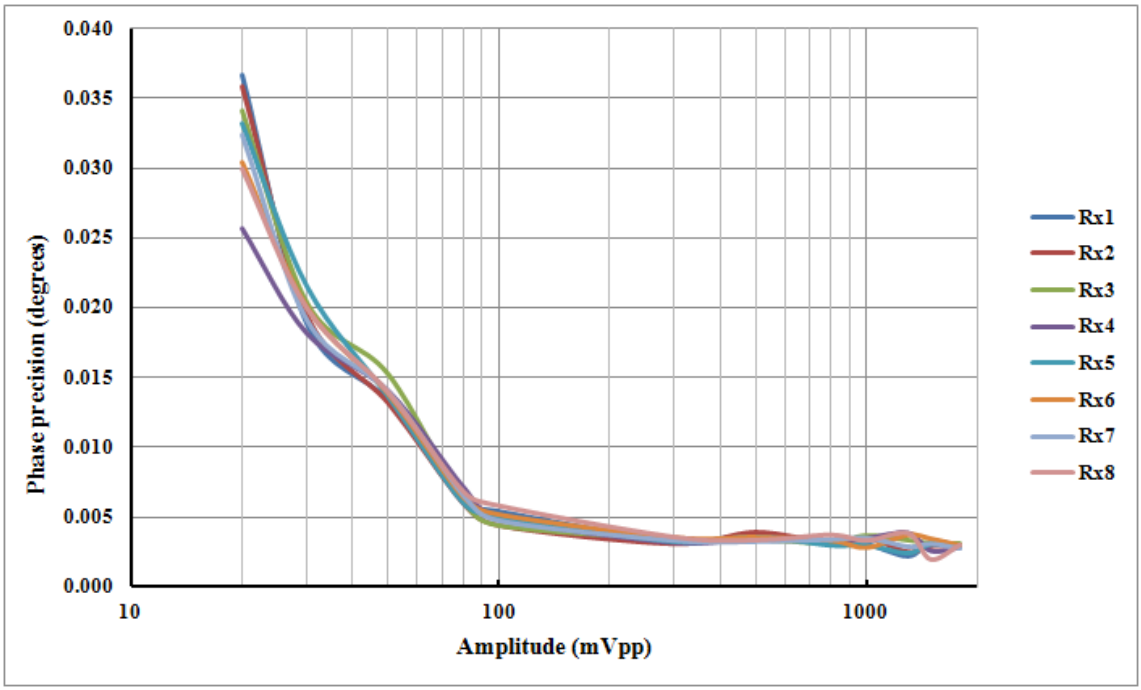


**Figure 4.29**: SPMU phase precision Vs input amplifier graph

From the figure it can be seen that the 8 channel SPMU exhibits the same graphic pattern as the phase precision graphs of the single channel phase measurement subsystem. This was anticipated since the multichannel SPMU is a scale-up version of the single channel. However it also shows that the work performed in chapter 3 regarding the single channel was successful since one of the requirements was the scalability of the single channel.

From 1.8$V_{pp}$ down to 100 $mV_{pp}$ the phase precision for all channels was below 6 millidegrees, at 50 $mV_{pp}$ was below 15 millidegrees, at 30 $mV_{pp}$ was below 23 millidegrees and at 20 $mV_{pp}$ was below 36 millidegrees. For the single channel characterised at 10 MHz

the phase precision was below 5 millidegrees from $1.8V_{pp}$ to 100 $mV_{pp}$, below 10 millidegrees at 50 $mV_{pp}$, below 20 millidegrees at 30 $mV_{pp}$ and below 29 millidegrees at 20 $mV_{pp}$. The results show a slight deterioration of the phase precision achieved by the SPMU at the same amplitudes in comparison to the single channel. This increases as the amplitude is getting smaller.

To investigate this a measurement with the multichannel SPMU measurement stage alone was taken. The test set-up of figure 3.34 was used (shown in figure 4.30) with the time delay tab set to 100 ns, the frequency set at 10 kHz and the time constant to 5 ms. The results showed that the SPMU measurement stage exhibited the same phase precision at all channels as the single channel measurement stage when used with the same settings.

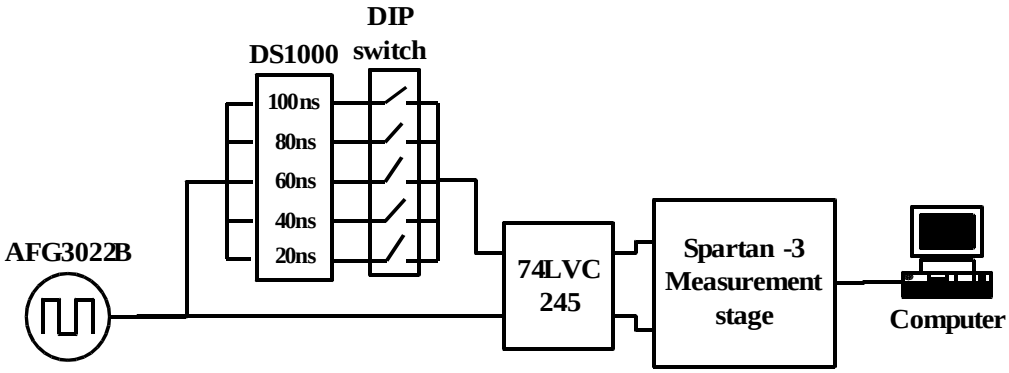


**Figure 4.30**: The test set-up for the measurement stage phase precision characterisation

Thus the phase precision deterioration was attributed to the analogue processing stage and the fact that noise due to crosstalk between the 9 analogue signal chains contaminated the measurements especially at low amplitudes. However the phase precision difference between the single channel and the multichannel SPMU is not that critical considering that the multichannel SPMU uses 7 more analogue signal chains in comparison to the single channel.

### 4.7.3 Phase drift

For the phase drift characterisation of the multichannel SPMU the test set-up shown in figure 4.28 was used. The maximum phase drift was calculated from the data set using equation (3.16) in Microsoft Excel. The data set was processed with a moving average algorithm of 10 given in equation (3.17) to produce a new averaged data set. The average drift was calculated from the averaged data set using equation (3.16) in Microsoft Excel.

The input sinusoidal signal at the reference chain and the eight detection chains was 1.8 $V_{pp}$ at 10 MHz, the downconversion sinusoidal signal was 2 $V_{pp}$ at 9.99 MHz, the $T_{clk}$ was

20 ns and the time constant was 5 ms.

The average maximum phase drift of all channels over 5 hours was 149 millidegrees and the average phase drift using a simple moving average of 10 for all channels was 78 millidegrees. The phase drift results obtained for 5 hours for the single channel phase subsystem was 37 millidegrees and 14 millidegrees respectively. Comparing the results for the multichannel SPMU with the single channel it emerges that the maximum phase drift of the SPMU was increased by a factor of 4.

The results suggest that the multichannel SPMU displays significantly higher drift in comparison to the single channel. The increase in the phase drift may be due to factors such as reduced cross-channel isolation and increased parasitic capacitance and inductance on the PCB of the multichannel system in comparison to the single channel system.

### 4.7.4 Recording rate

The procedure regarding the signals and the test set-up from section 4.7.2 were used for this test. For comparison purposes the time constant was set at 5 ms and at 50 ms.

A phase measurement of 1 second duration was recorded for each time constant and was transmitted to the computer. The result was 200 phase difference values for the 5 ms time constant and 20 phase difference values for the 50 ms time constant. The test was repeated for a number of times and the results were approximately the same. The frequency and the amplitude of the signals did not have any impact on the recording rate of the subsystem.

The results showed that the recording rate of the multichannel SPMU was exactly the same as the single channel despite the fact that 8 detection signal chains were used instead of 1. This stressed the fact that the use of the parallel configuration for the SPMU can create a fast multichannel phase measurement subsystem and that a parallel configuration for the SPMU is a requirement for a fast system.

## 4.8 Characterisation of the Cardiff Mk2d system

This section presents the results of the performance tests and the characterisation of the Cardiff Mk2c MIT system in terms of the phase precision, the phase drift and the frame rate. The system was warmed up for half hour prior the tests.

### 4.8.1 Performance of the coil array

The coil array task was to generate the primary magnetic field using the excitation coil and

detect the secondary magnetic field with the detections coils. However the detection signals and the reference signals from the coil array were used as inputs to the multichannel signal processing and measurement unit (SPMU) which performed the phase measurement. The coil array output affects the performance of the SPMU and thus the phase measurement.

To investigate the coil array impact on the behaviour of the SPMU it was decided to measure the amplitude of the sinusoidal signal from a detection coil and at the same to measure the reference signal from the activated excitation coil. Both signals were measured at the input of the SPMU. The TDS2024B (Tektronix Inc., Oregon, USA) was used to measure the signal amplitudes of the detection coils number 3 and number 7. The RF amplifier output used was 30 $V_{pp}$.

The investigation results showed almost identical results for both detection coils. Thus it is safe to assume that they apply to the rest of the detection coils as well. The detection coils exhibited the highest induction voltage (about 2.5 $V_{pp}$) when the excitation coil closest to them was activated (excitation coil 1 and 3 respectively). The reference signal from the excitation coil 3 (yellow trace) and the detection signal from the detection coil 3 (blue signal) are shown in figure 4.31.

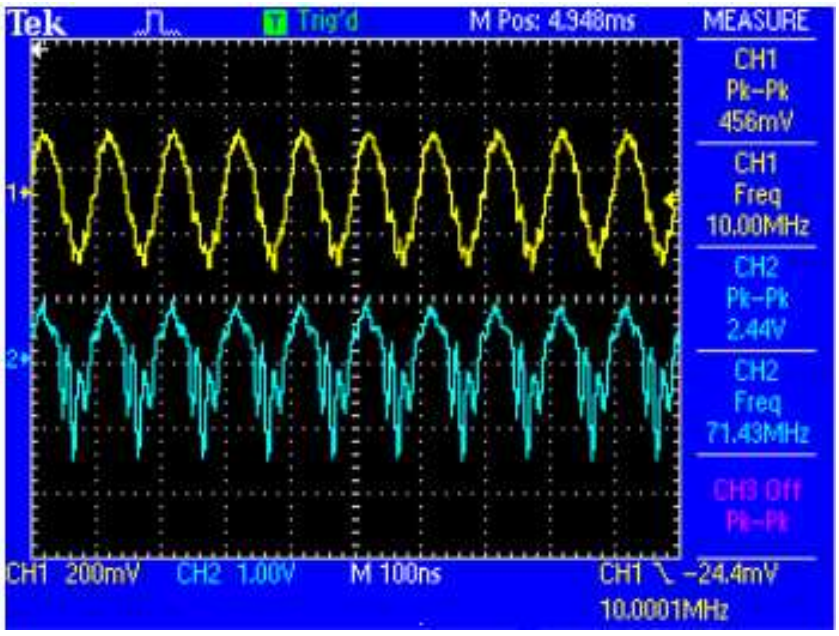


**Figure 4.31**: The reference signal from excitation coil 3 (yellow trace) and the detection signal from the detection coil 3 (blue signal)

The signal amplitude however was decreased as the distance between the detection coils and the activated excitation coil was increased reaching its minimum value when the activated excitation coil was the one farthest away from the detection coil. The reference

signal from excitation coil 7 (yellow trace) and the detection signal from the detection coil 3 (blue signal) are shown in figure 4.32.

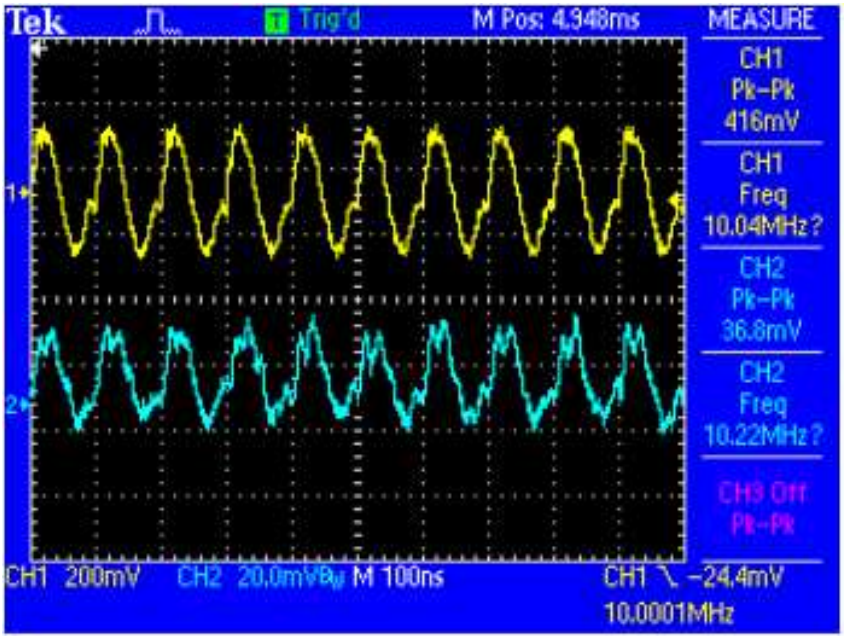


**Figure 4.32**: The reference signal from excitation coil 7 (yellow trace) and the detection signal from the detection coil 3 (blue signal)

The detection signals waveform shape appears to be noisy irrespective from which detection coil it was captured or which excitation coil used to generate it. Since the zero crossing technique requires the sinusoidal zero crossings to be well defined then it is expected that these noisy waveforms will have an impact on the behaviour of the system.

The amplitude of the reference signals was not the same for all excitation coils. It varied with the excitation coil 5 showing the smallest reference signal at about 360 $mV_{pp}$ and the excitation coil 1 showing the highest at 600 $mV_{pp}$. The reason for this is not clear since theoretically they should have the same amplitude. Further investigation on this matter is therefore required.

### 4.8.2 Frame rate

In section 4.6.2 the maximum frame rate was calculated to be 14.88 frames for a time constant of 5 ms and $T_{TRANS}$ equal to 3.4 ms and 12.5 frames for a time constant of 5 ms and $T_{TRANS}$ equal to 5 ms. For the operation of the Cardiff Mk2c the time $T_{TRANS}$ was set at 5 ms to provide a margin of safety for the relay operation time since the requirement for a frame rate of 10 fps was satisfied.

To verify the number of frames a measurement of 1 minute was taken and then the total number of the frames recorded was divided by 60 which gave the frame rate. This

procedure was repeated for 2 and 5 minutes in different days. The excitation frequency was 10 MHz however different RF amplifier outputs were used to investigate if the RF amplifier output would affect the frame rate.

The results showed that the system achieved the 12.5 fps frame rate with a time constant of 5 ms regardless the RF amplifier output used.

The same procedure as before was repeated to identify the frame rate when the time constant was set at 50 ms and the system achieved a frame rate of 2.2 fps.

The results provided the empirical proof for the theoretical frame rate calculation in section 4.6.2 and for the analysis in section 4.2.2. It further showed that the Cardiff MK2c could fulfil the requirement for a frame rate of 10 fps when the time constant used was 5 ms.

### 4.8.2 Phase precision

This test aimed to characterise the Cardiff Mk2c system in terms of the average phase precision for 5 ms time constant and 50 ms time constant at different RF output amplitudes. The average phase precision was calculated from the first 10 phase difference values of a frame. For the calculations the equation (3.15) was used in Microsoft Excel. The results are graphically presented in figure 4.33 where the average phase precision is presented over the output voltage of the RF amplifier.

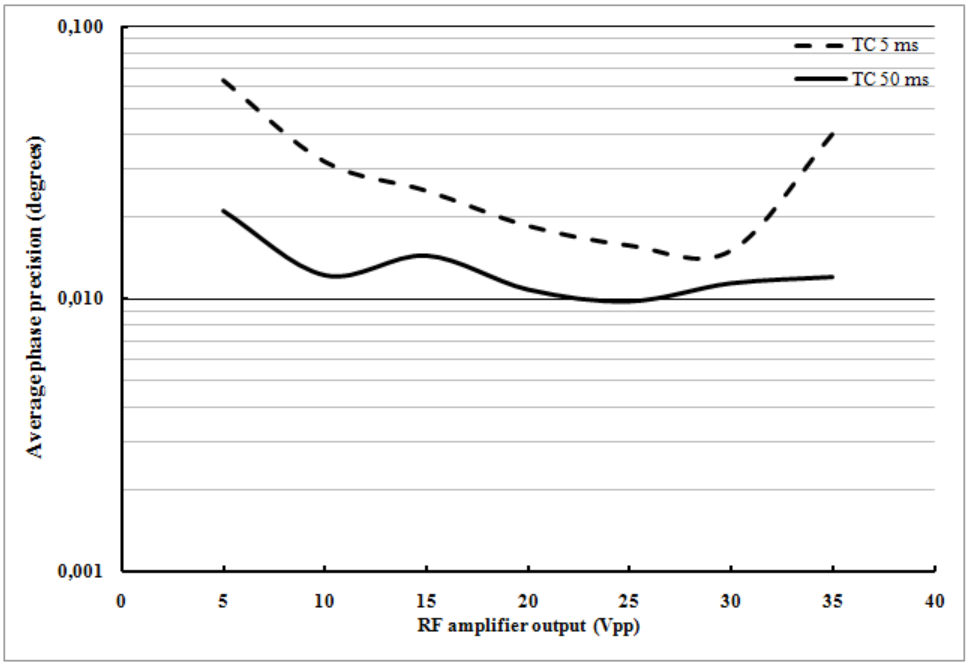


**Figure 4.33**: Average phase precision Vs RF amplifier output

From figure 4.33 it can be seen that for both time constants the system appears to have the

best overall phase precision in the region between 20 $V_{pp}$ and 32 $V_{pp}$. Below and above this voltage region the phase precision is significantly deteriorating which indicates that the system is practically unusable at these regions. For the 5 ms time constant the lowest average phase precision achieved by the system was 15 millidegrees at 30 $V_{pp}$. For the 50 ms time constant it was 10 millidegrees at 25 $V_{pp}$.

Both graphs show that the RF amplifier output plays a crucial role on the performance of the system. The phase precision increases as the RF amplifier output increase however it reaches a maximum from which it starts to deteriorate. This point differs depending on the time constant used.

At high RF output this is because a stronger magnetic field is produced and thus a higher signal to noise ratio is achieved. This suggests that the use of a more powerful RF amplifier than the ZHL-3A could benefit the system in terms of the phase precision.

From the test results it can be seen that the RF amplifier output displays its optimal excitation power from 25 $V_{pp}$ to 30 $V_{pp}$ when the time constant is set to 5 ms and thus the system should be used in that range.

### 4.8.2 Phase drift

The Cardiff Mk2c system was characterised in terms of the maximum phase drift and the average phase drift. The RF amplifier output was set at 25 $V_{pp}$ and the time constant was set at 5 ms.

The maximum phase drift was calculated from the data set using equation (3.16) in Microsoft Excel. The data set was processed with a moving average algorithm of 10 given in equation (3.17) to produce a new averaged data set. The average drift was calculated from the averaged data set using equation (3.16) in Microsoft Excel. A 1 hour phase drift measurement was taken with a phase difference result recorded every second.

The average maximum drift was 259 millidegrees and the average drift with moving average of 10 was 220 millidegrees. The lowest channel maximum drift was 73 millidegrees and the highest was 530 millidegrees.

The system drifts more than the multichannel SPMU. This deterioration of the phase drift is attributed to the coil array and the low amplitude sinusoidal signal it produces.

## 4.9 Water pipe phantom flow measurements

This section presents the measurements performed with an inclined water pipe phantom placed in the coil array for detecting the flow of saline.

### 4.9.1 Test set-up

A possible application for fast MIT systems such as the Cardiff Mk2c system is in measurements of multiphase flows such as oil/water mixtures in oil pipelines. MIT may be suitable for this application given the relatively high conductivity of sea water (5 S/m) in comparison to oil (ranging from 80 – 1000pS/m). Two experiments were performed to investigate whether the system could detect the flow of water through a water pipe. The test set-up is shown in figure 4.34 and was the same for both experiments.

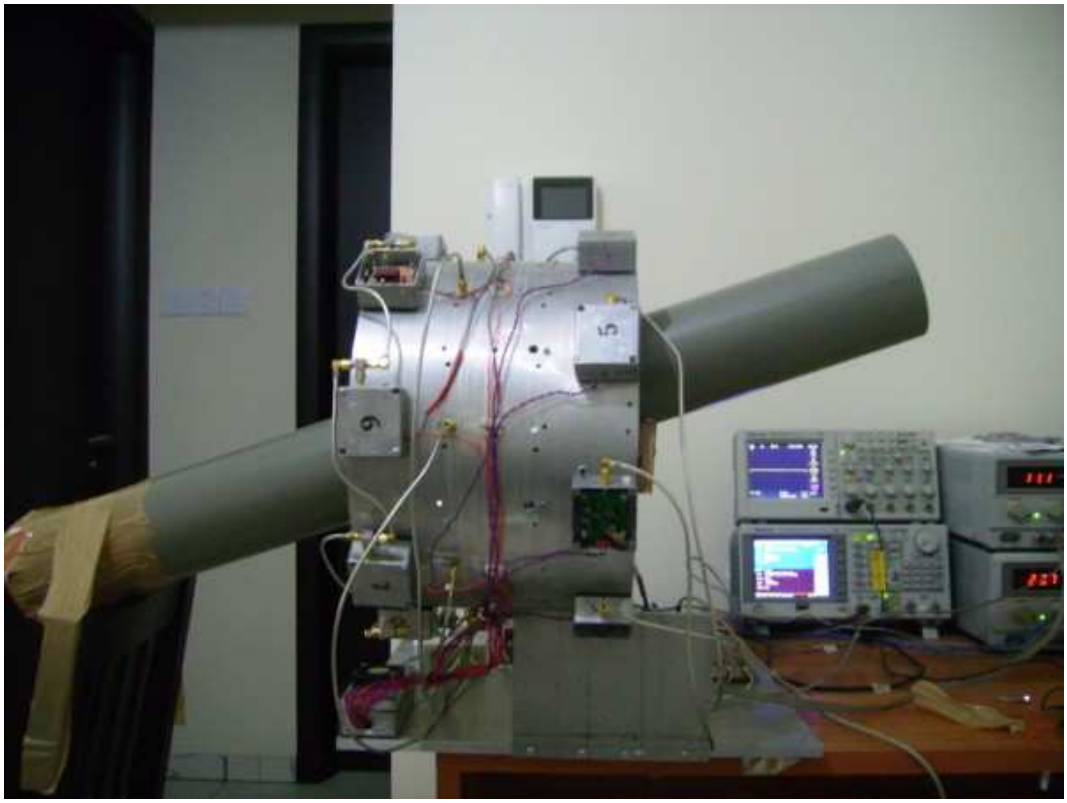

**Figure 4.34**: The test set-up for the water pipe phantom measurements

The water pipe used was a cylindrical shaped standard PVC made pipe used mainly for irrigation purposes that was open from both sides. The pipe was 97 cm long, its inner diameter was 10.3 cm and its outer diameter was 11 cm. The upper part of the pipe outside the coil array was 30 cm and the part of the pipe in the coil array was 27 cm. The pipe was placed in an inclination of 20 degrees to have a downward path to create the required flow for the saline.

In both experiments 250 ml of 3 S/m saline was used to simulate the flow of the sea water

in a pipe. It was assumed that the air in the water pipe represented the oil and the gas because oil is non-conductive compared to the sea water.

### 4.9.2 Experiment for detecting fast moving saline volume through the pipe

The experiment was intended to identify if the system would be fast enough to detect a fast moving saline volume in the water pipe as shown in figure 4.35.

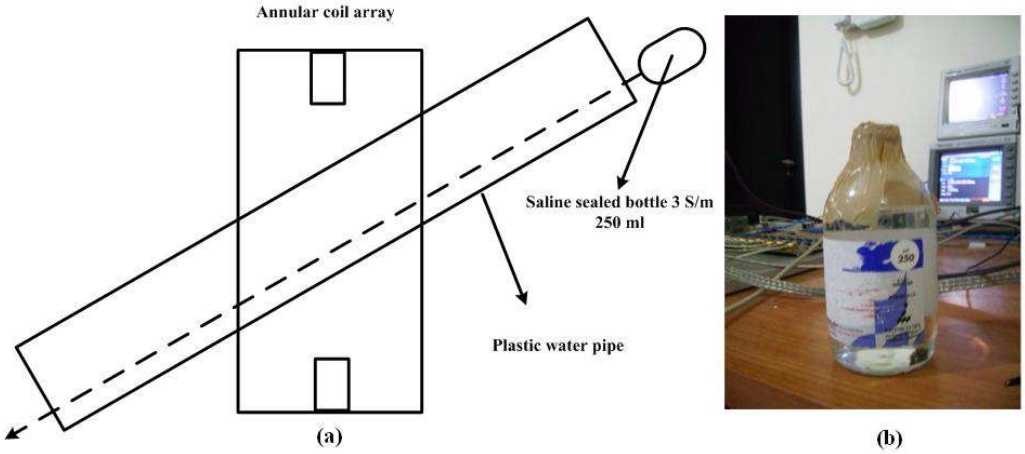


**Figure 4.35**: The saline sealed bottle in the water pipe (a) and the saline bottle used (b)

The 250 ml of 3 S/m saline were placed into a glass bottle which was subsequently sealed. The system was initiated for recording and then the saline bottle was placed at the opening of the upper part of the water pipe and pushed inside. The recording was stopped when the saline bottle exited the lower part of the pipe.

The phase difference values for each detection coil were compensated with regards to the respective detection coil baseline to create a common reference point for all detection coils. The results for all the excitation coils and detection coils are shown in figures 4.36 to 4.39.

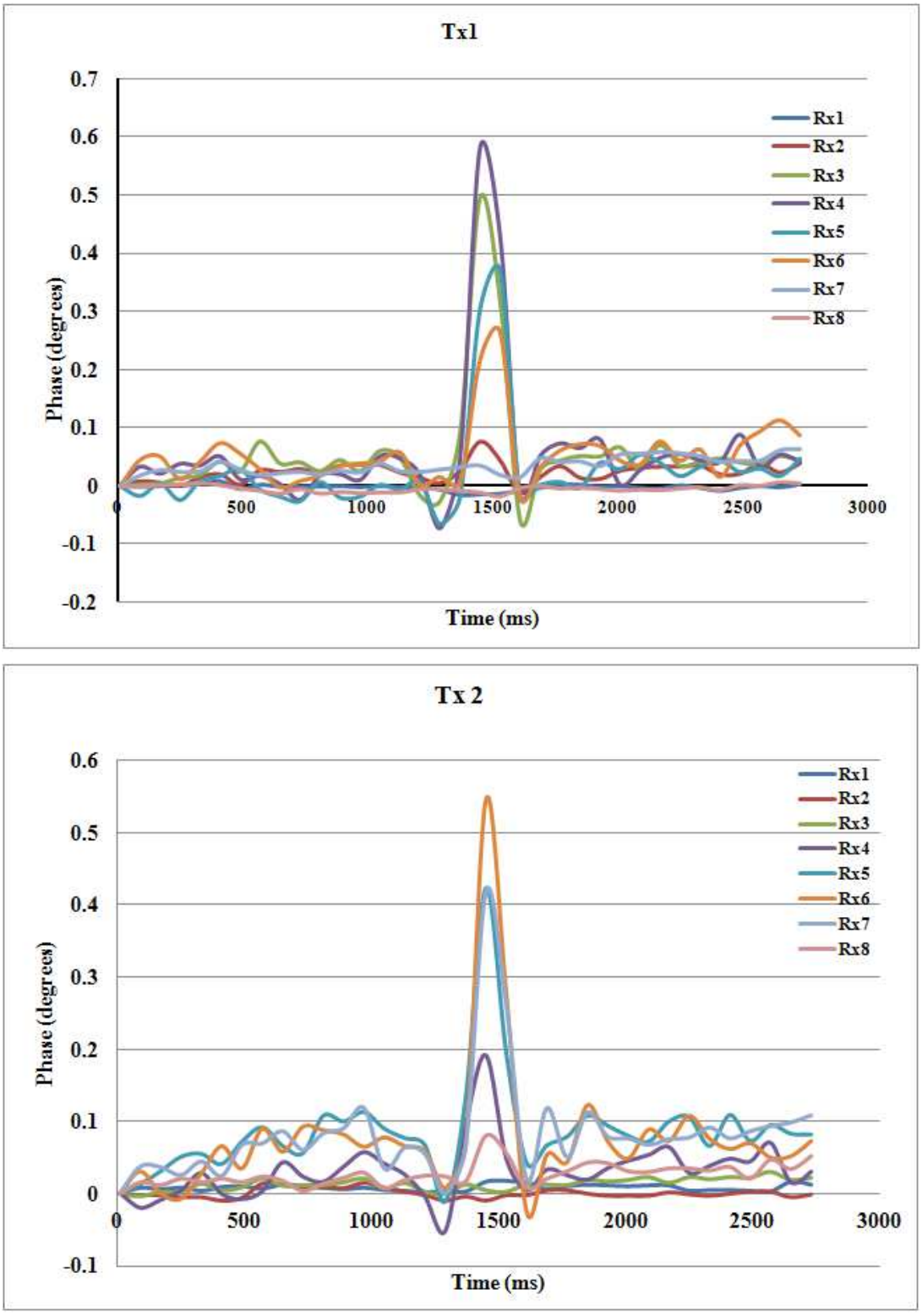


**Figure 4.36**: Saline bottle experiment – Excitation coils Tx1 and Tx2 results

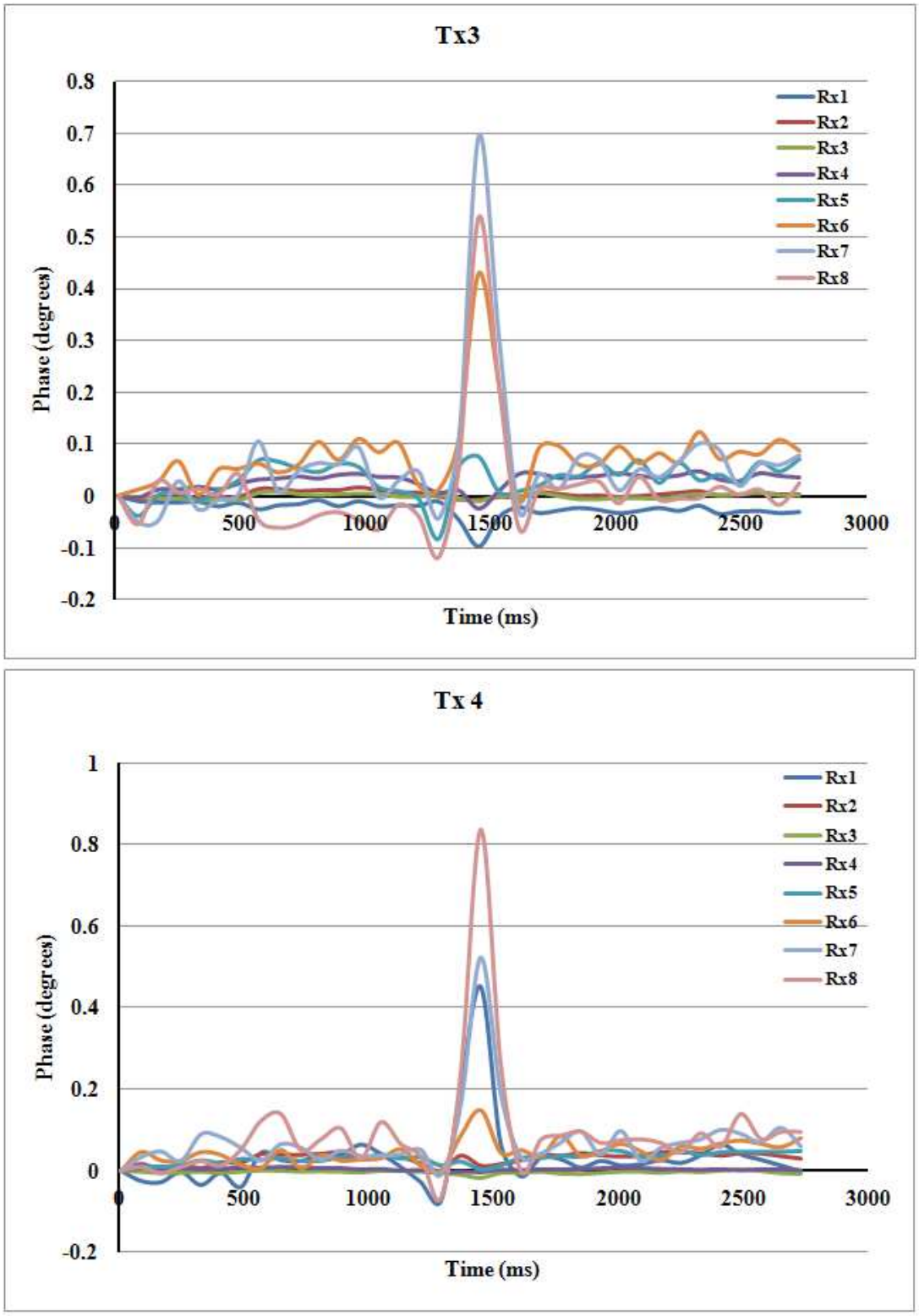


**Figure 4.37**: Saline bottle experiment – Excitation coils Tx3 and Tx4 results

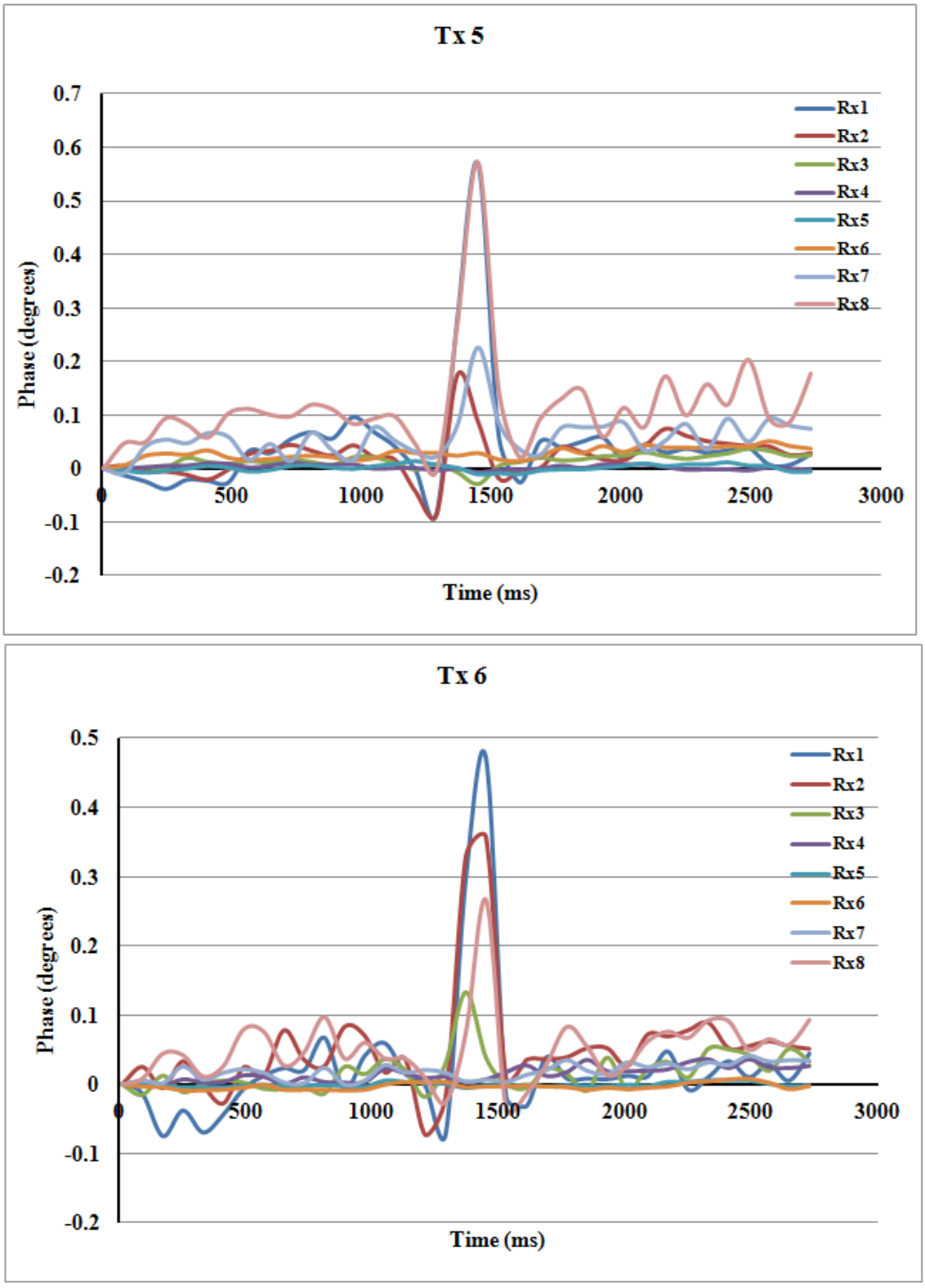


**Figure 4.38**: Saline bottle experiment – Excitation coils Tx5 and Tx6 results

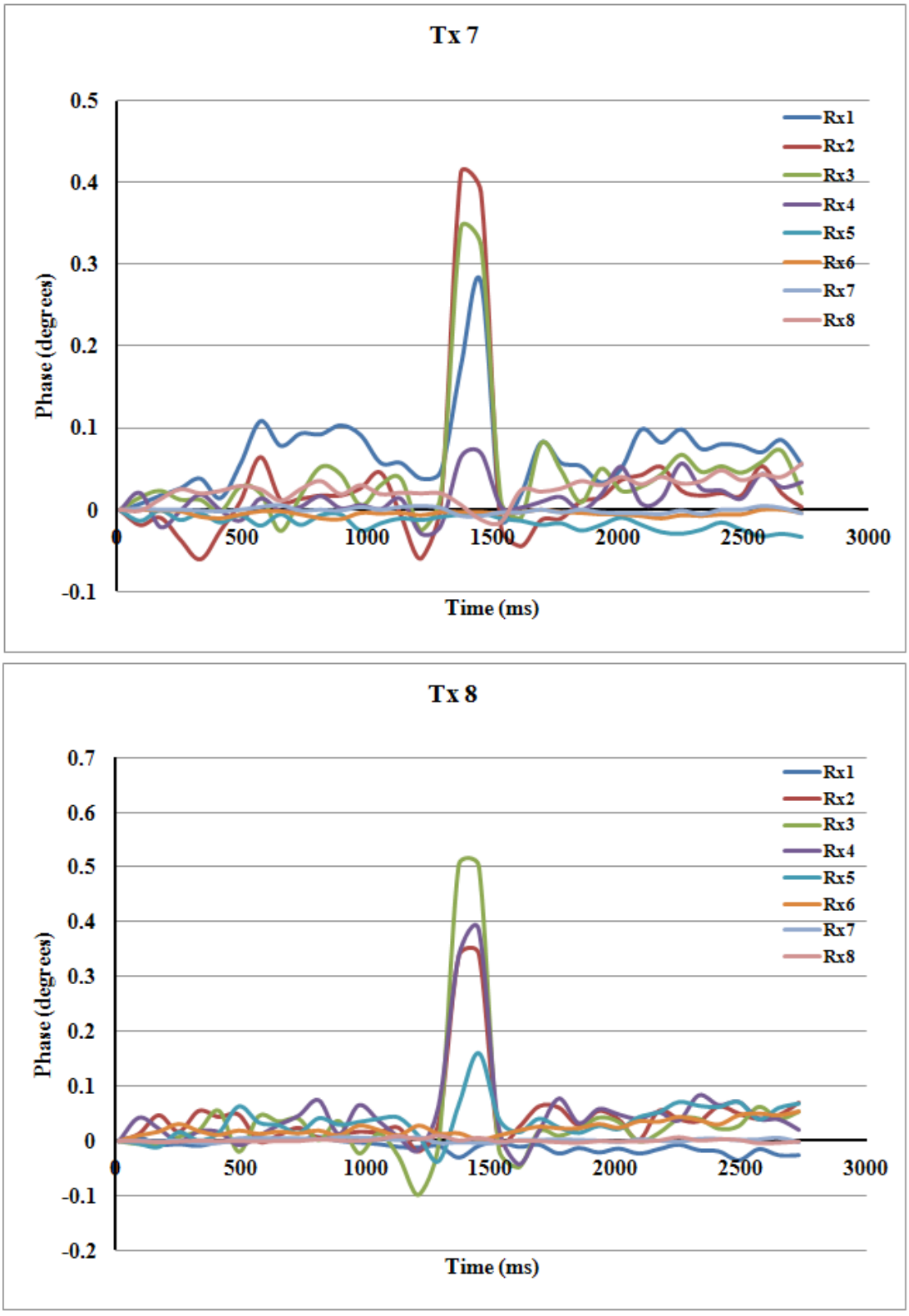


**Figure 4.39**: Saline bottle experiment – Excitation coils Tx7 and Tx8 results

The figures show that the system detected the signal created by the movement of the saline bottle in the water pipe. The signal lasted about 200 ms based on the width of the signal pulse at 0.1 degrees. The frame rate used in the experiment was 12.5 fps (80 ms per frame) so it can be said that the system can produce three frames containing the saline bottle travelling in the water pipe.

Given that the part of the pipe in the coil array was 27 cm and assuming that the saline bottle velocity in the pipe was constant then the saline bottle velocity can be calculated to be 1.35 m/s. Thus with 12.5 fps the system is fast enough to record satisfactorily the movement of a 250 ml saline volume of 3 S/m in an oil pipe travelling at velocities up to 1.35 m/s. Obviously if the frame rate is increased it is expected that the capability of the system to record saline volumes with higher velocities than 1.35 m/s will increase also.

The figures further show that the signal was recorded to be stronger at the detection coils opposite the excitation coil and almost non existent at the detection coils next to the excitation coils. This is consistent with the findings of the coil array characterisation performed in section 4.8.1.

In table 4.7 the maximum phase across all detection coils for all excitation coils and the signal to noise ratio (SNR) are given. The average noise was calculated for 1 second prior the saline measurement and the SNR was calculated by

$$SNR_{dB} = 20\log_{10}\left(\frac{max\ signal}{noise}\right) \qquad (4.18)$$

where noise is the average noise measured with empty detector and the maximum signal is the maximum value observed across all channels.

**Table 4.7**: Saline bottle experiment maximum phase and SNR for the excitation coils

| Excitation coil | Maximum phase (degrees) | Mean average noise (degrees) | SNR (dB) |
|---|---|---|---|
| Tx1 | 0.581 | 0.014 | 32.09 |
| Tx2 | 0.546 | 0.028 | 25.94 |
| Tx3 | 0.694 | 0.012 | 35.52 |
| Tx4 | 0.836 | 0.023 | 31.16 |
| Tx5 | 0.572 | 0.023 | 27.97 |
| Tx6 | 0.470 | 0.010 | 33.65 |
| Tx7 | 0.412 | 0.011 | 31.71 |
| Tx8 | 0.505 | 0.013 | 31.99 |

From table 4.7 it can be seen that the Cardiff MK2c system was observed to provide a peak SNR of 35.52 dB for a sample of 250 ml of 3 S/m saline.

### 4.9.3 Experiment for detecting free flow of saline through the pipe

The experiment was intended to identify if the system would be fast enough to detect the free flow of saline through the inclined water pipe as shown in figure 4.37.

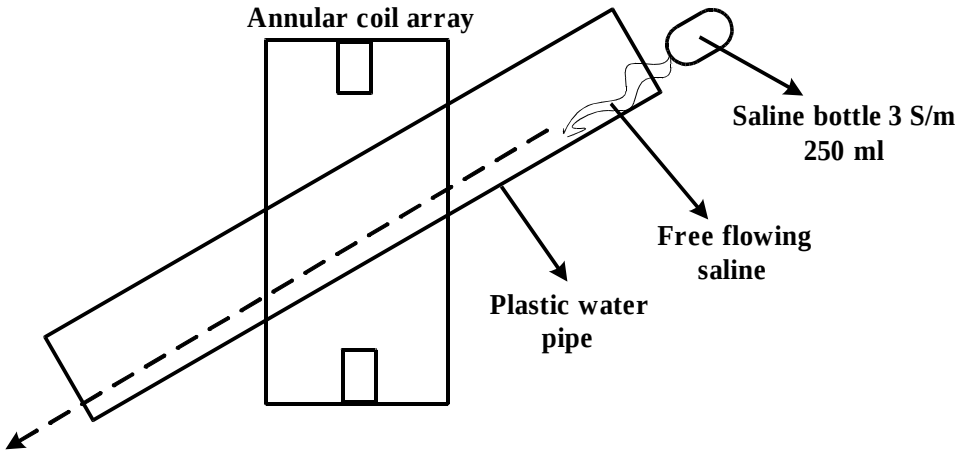


**Figure 4.40**: The saline free flow through the water pipe

The system was initiated for recording and the 250 ml of the 3 S/m saline was poured in the opening of the upper part of the water pipe and was flowing downwards. The recording was stopped when all saline exited the lower part of the pipe. It was observed that the saline did not exited the bottle in a uniform way but it left in small volumes. However it was not possible to observe the flow of the saline in the pipe due to the small time period that the flow lasted.

The results of the experiment are shown in figures 4.41 to 4.44 for all the excitation coils and detection coils.

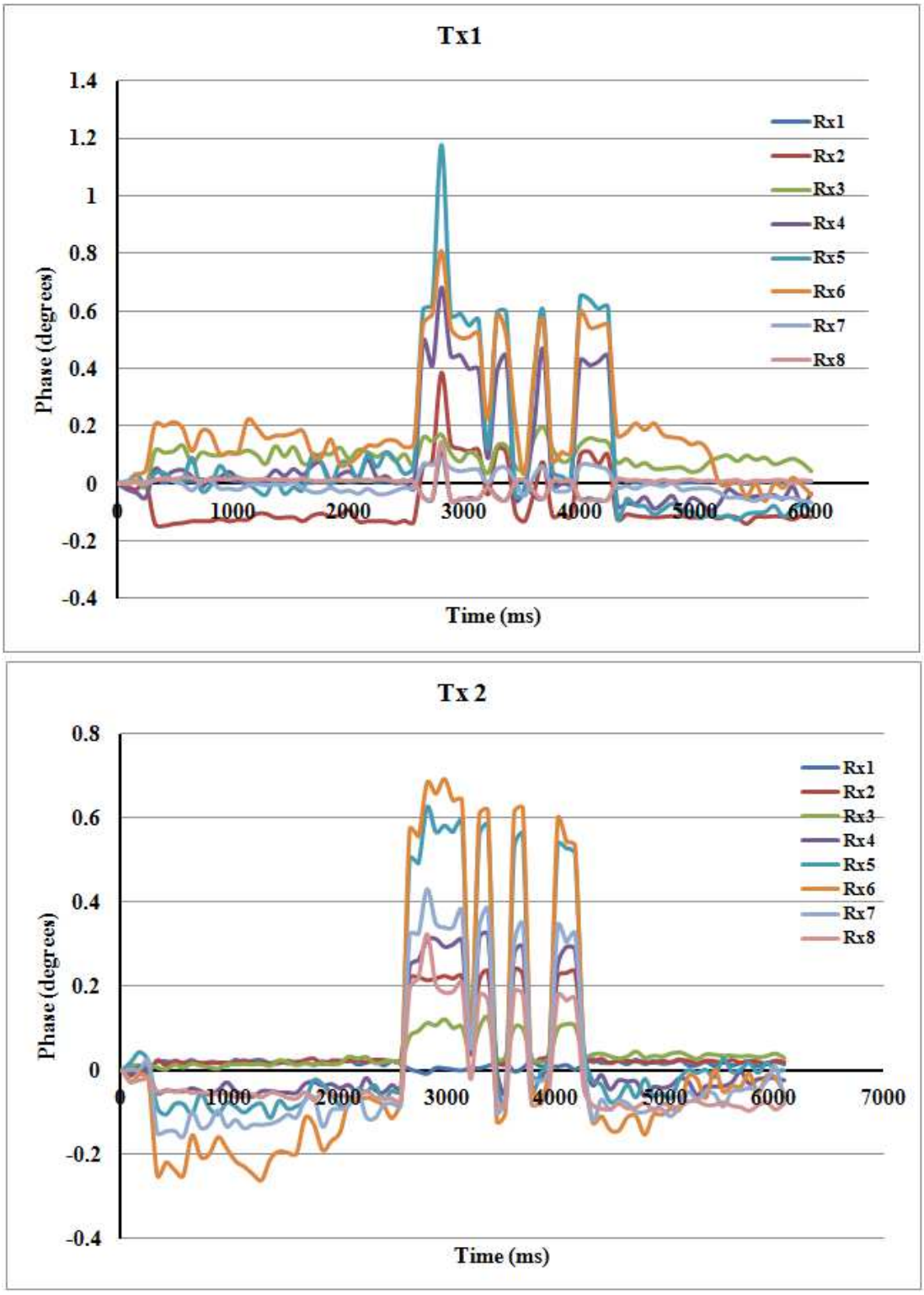


**Figure 4.41**: Saline flow experiment – Excitation coils Tx1 and Tx2 results

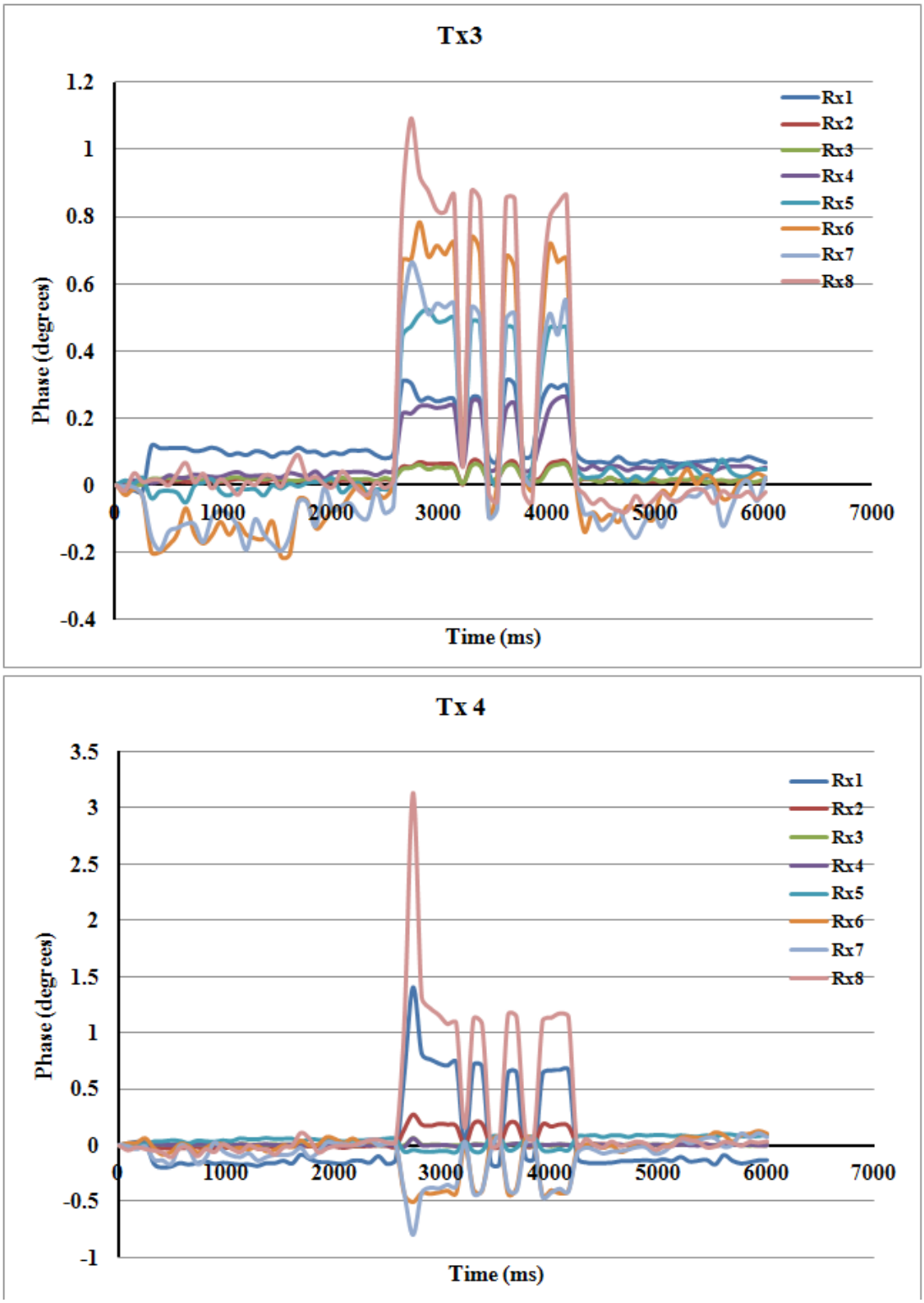


**Figure 4.42**: Saline flow experiment – Excitation coils Tx3 and Tx4 results

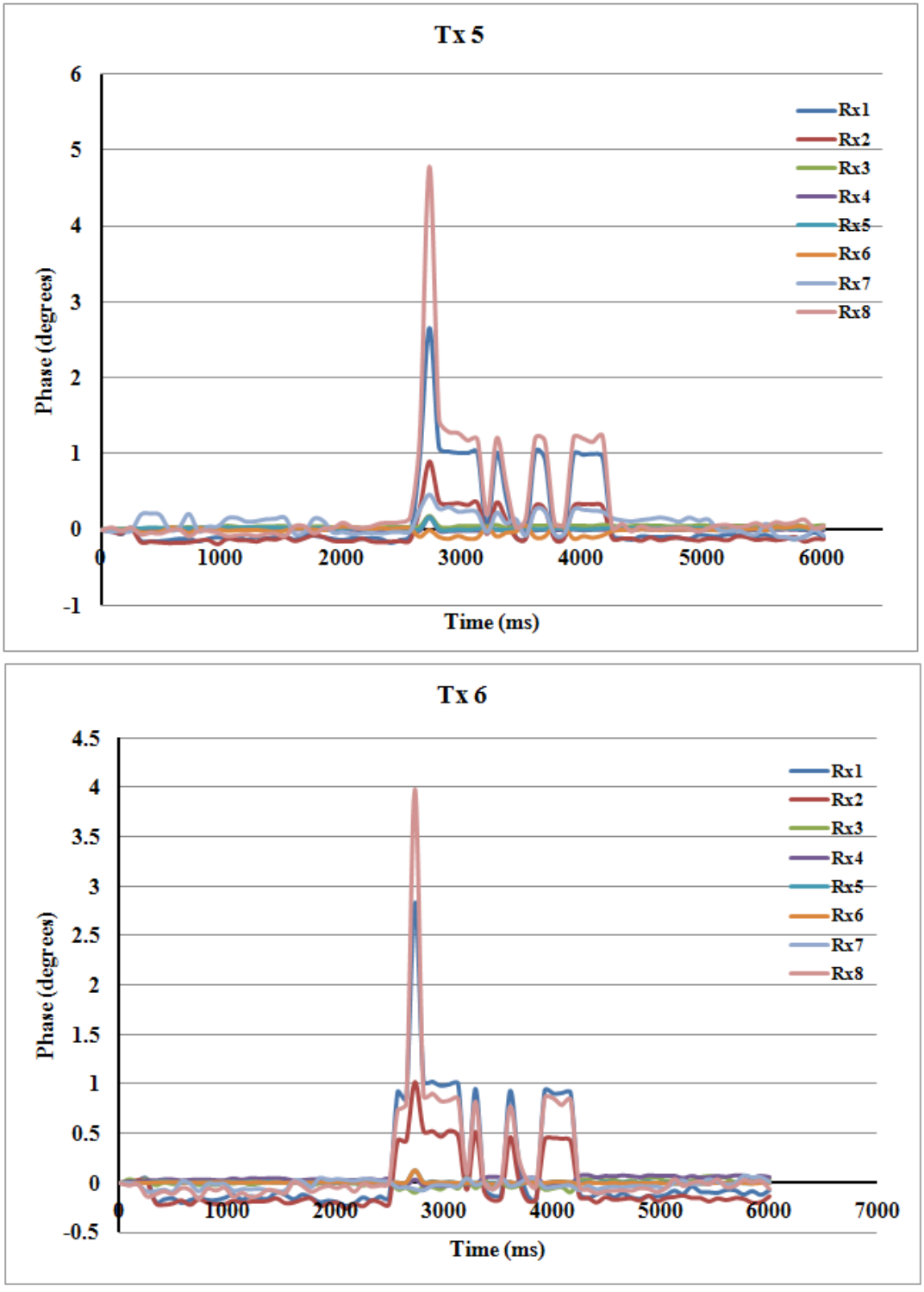


**Figure 4.43**: Saline flow experiment – Excitation coils Tx5 and Tx6 results

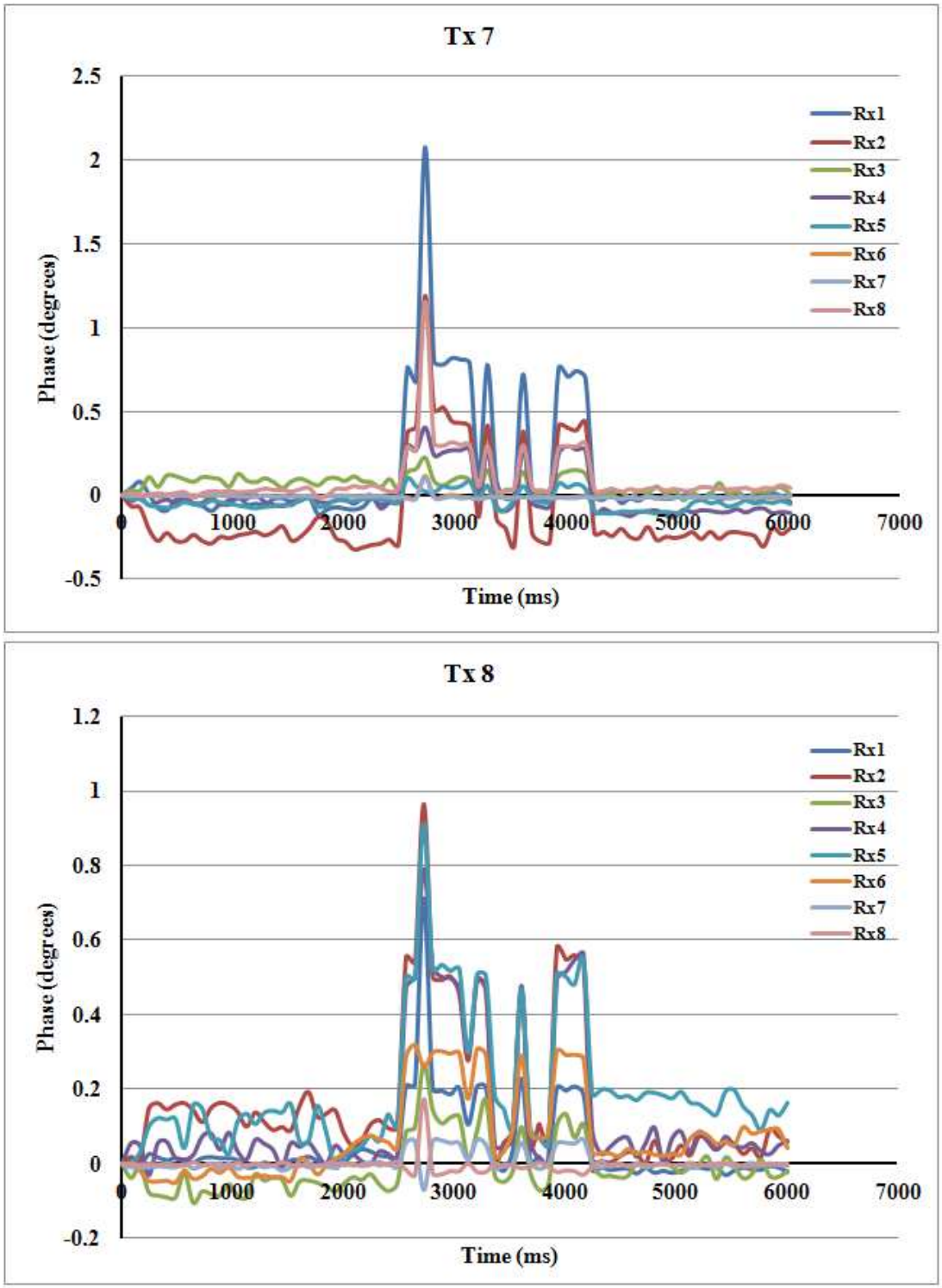


**Figure 4.44**: Saline flow experiment – Excitation coils Tx7 and Tx8 results

From the figures 4.41 to 4.44 it can be seen that the system detected the flow of the saline in the water pipe. The flow pattern was not steady through the recording time but it increased and decreased at irregular time intervals. This can be attributed to the saline exiting the bottle in small volumes than in a uniform way as was observed during the experiment.

This flow pattern was recorded to have the same phase displacement during its flow apart

from a peak of 200 ms duration which has a high phase displacement in the results of the excitation coils 1, 4, 5, 6, 7 and 8 and less visible but still there in the results of coils 2 and 3. The reason for that is not clear however it may be attributed to the way the saline exited the bottle since it appears only on the first flow interval and not in the rest.

In table 4.8 the maximum phase across all detection coils for all excitation coils and the signal to noise ratio (SNR) are given. Is is noted that the peak was removed from the maximum phase because it was of a very short duration and it was considered to be a secluded phenomenon. The average noise was calculated for 1 second prior the measurement and the SNR was calculated with equation (4.18).

**Table 4.8**: Saline flow experiment maximum phase and SNR for the excitation coils

| Excitation coil | Maximum phase (degrees) | Mean average noise (degrees) | SNR (dB) |
|---|---|---|---|
| Tx1 | 0.649 | 0.019 | 30.67 |
| Tx2 | 0.623 | 0.043 | 23.29 |
| Tx3 | 0.862 | 0.011 | 37.65 |
| Tx4 | 1.175 | 0.026 | 33.01 |
| Tx5 | 1.237 | 0.014 | 38.75 |
| Tx6 | 0.934 | 0.041 | 27.13 |
| Tx7 | 0.758 | 0.029 | 28.27 |
| Tx8 | 0.581 | 0.019 | 29.60 |

From table 4.8 it can be seen that the Cardiff MK2c system was observed to provide a peak SNR of 38.75 dB for the saline flow. This is very close to the SNR observed in the saline bottle experiment and shows that the system has a reproducible behaviour for the same volume of saline.

## 4.10 Summary

The work performed in this chapter aimed to design, develop and characterise a practical multichannel MIT system operating at 10 MHz for industrial applications requiring a high data acquisition rate. The work aimed to realise the hardware part of the system which consists of the coil array and the multichannel signal processing and measurement unit (SPMU). The processing unit (PU) was not in the work scope. The main issues arising from the work performed are summarised here.

In section 4.1 the requirements and target specifications for the MK2c MIT system were described and discussed.

Section 4.2 provided a detailed analysis on the factors that affect the frame rate of an MIT practical system which can be used as a tool in the development of MIT systems aiming in high data acquisition rates.

In section 4.3 the design of the Cardiff Mk2c system was presented. The system's architecture was analysed and covered in detail followed by an analysis of the system's components and the implementation details.

In section 4.4 the work performed for the design and implementation of the eight channel coil array was given. The various parts of the coil array and the technical details of their implementation is presented. The coil array implementation adopted some technical characteristics from the Cardiff Mk2a coil array developed in [11] since both systems were developed in the context of work of the same group.

However other system components such as the excitation control system required a significantly different design to achieve the much higher frame rates specified for the MK2c system. This was achieved by integrating control and signal processing systems within the same FPGA device and are original in the context of this work.

In section 4.5 the practical work for the design and the implementation of a multichannel signal and processing measurement unit (SPMU) was presented. The development of the SPMU was based on the work performed in chapter 3 for the design and development of the single channel zero crossing phase measurement subsystem. A number of adaptations to the single channel design were required for the multichannel system and these changes are detailed.

In section 4.6 the developed Cardiff Mk2c system was presented as a complete system. An analysis on the expected frame rate of the system based on the model developed in section 4.2 and the specifications of the components used for the implementation of the coil array and the SPMU was given.

The characterisation of the multichannel SPMU at 10 MHz was presented in section 4.7. The SPMU phase precision in the range from 1800 $mV_{pp}$ to 100 $mV_{pp}$ was 6 millidegrees which was very close to the single channel phase precision. At 20 $mV_{pp}$ the SPMU phase precision reached 36 millidegrees compared to 29 millidegrees of the single channel. This difference is not critical. An investigation showed that it was due to the increased number of the SPMU analogue signal chain lines.

The SPMU phase drift reached an average maximum drift figure of 149 millidegrees over 5 hours. The lowest channel maximum phase drift was 111 millidegrees and the highest channel maximum phase drift was 166 millidegrees. The increase in the phase drift of the SPMU may be due to increased parasitic capacitance and inductance and lower cross-channel isolation on the multichannel pcb in comparison to the single channel version.

The maximum achievable recording rate of the SPMU was verified to be 200 phase difference vales per second when the 5 ms time constant was used which was the same recording rate the single channel achieved.

In section 4.8 the characterisation of the Cardiff Mk2c system was presented. The performance of the coil array was first investigated. The Mk2c system characterization measurements showed that the detected signals at the input of the SPMU varied from 50 $mV_{pp}$ to 2.5 $V_{pp}$ depending on the location of the activated excitation coil.

The Cardiff Mk2c system phase precision when an RF amplifier output of 25 $V_{pp}$ – 30 $V_{pp}$ was used was 15 millidegrees and 10 millidegrees for measurement time constants of 5 ms and 50 ms respectively.

The Cardiff Mk2c phase drift reached an averaged across all channels maximum drift figure of 259 millidegrees for one hour measurement. The lowest channel maximum drift was 73 millidegrees and the highest was 530 millidegrees. The RF amplifier output used during the measurement was 30 $V_{pp}$.

The Cardiff Mk2c frame rate was 12.5 frames per second (fps) when the time constant was 5 ms was used and 2.2 fps when the time constant was 50 ms. The system maintained the frame rate irrespective of the RF amplifier output. From the literature review presented in chapter 2 and the authors best knowledge the 12.5 fps frame rate makes the Cardiff MK2c the fasted multichannel tomographic MIT system at 10 MHz until this thesis was submitted.

In section 4.9 two experiments were presented which aimed to investigate the performance of the system when detecting the saline flow through an inclined water pipe phantom inserted in the system's coil array. The first experiment used a sealed glass bottle containing 250 ml of 3 S/m saline which was sliding down the water pipe. The second experiment used 250 ml of 3 S/m saline which was poured in the inclined water pipe. The frame rate used by the system was 12.5 fps.

The results showed that the system detected successfully the existence and the movement of the saline in the inclined water pipe in both experiments. The detected signals for the first experiment lasted only 200 ms however the system was fast enough to record them. For the second experiment the system was fast enough to distinguish between the flow pattern of the saline through the water pipe. The system provided a peak SNR of 38.75 dB for the saline flow experiment and an SNR of 35.52 dB for the saline bottle experiment.

# 5. The Cardiff Mk2d MIT system

This chapter presents the work performed for the design, the development and the characterisation of a single channel Magnetic Induction Tomography system employing the zero crossing phase measurement subsystem for contactless detection of the cardiac activity and the lung function. Measurements on human volunteers have been performed to prove the operation of the system and the results are presented.

The chapter begins with section 5.1 in which the background for the development of the system and the requirements that were expected to satisfy are set. It continues with section 5.2 where the design, the development and the implementation of the system is given.

In section 5.3 the system characterisation in terms of phase precision, phase drift and frame rate is given and in section 5.4 the measurements conducted on human volunteers are presented. The chapter ends with section 5.5 that summarises the work performed.

## 5.1 Background and requirements

The literature review in chapter 2 showed that only the heart and the lungs are dynamically changing their conductivity at the torso area. The first due to the pumping action and the blood filling it and the second due to the breathing process. These dynamic changes reveal information for the cardiac activity and lung function.

A conductivity change will occur when the heart is filled with blood and lungs with air. Since the lungs are almost surrounding the heart a detection coil intending to capture the heart activity will capture the lung activity as well.

Given the volume of the lungs in comparison to the volume of the heart [10] it is expected that the lungs will be the major contributor to the recorded conductivity signal. Thus the sum of conductivity is expected to be high when the lungs are deflated and low when the lungs are inflated.

To design an MIT system aiming in the recording of the cardiac and the lung activity with the use of conductivity changes three factors need to be taken into consideration. The operating frequency, the positioning of the excitation coils and the detection coils and the sampling rate.

The literature review showed that the excitation frequency is required to be in the MHz region and especially from 10 MHz and up where the heart conductivity is higher than the deflated lung conductivity. The selection of the excitation frequency is confined by the skin penetration which affects the coils position. Thus the 10 MHz could be a good start.

To determine the measurement sample rate required of the Cardiff Mk2d MIT system it is necessary to define the expected range of cardiac and respiratory rates. The heart rate of a healthy resting human adult varies at about 75 beats per minute (bpm) [10] while the respiration rate varies from 12 to 18 breaths per minute [151]. The minimum MIT sample rate required is therefore set by the cardiac rate and should be of the order of twice the cardiac rate to satisfy Nyquist sampling rate requirements. A minimum sample rate of 12 Hz is therefore required and the measurement bandwidth should extend up to 4 Hz to record the heart rate up to 240 bpm.

Thus to design and develop the MIT system targeting the detection of the cardiac activity and the lung function the following general set of requirements was set:

- High sampling frequency rate – ideally 20 samples per second
- Excitation frequency set at 10 MHz
- Phase precision in the order of millidegrees – ideally below 10 millidegrees
- The phase measurement subsystem to be based on the zero crossing technique
- Low cost

It was decided to use a single excitation / detection channel to perform all measurements. This would allow the basic performance of the system and the feasibility of the system to detect respiration and cardiac rates to be assessed.

Although there are practical advantages in having a system in which both the excitation and detection coils are on the same side of the subject as for the systems of [42, 68] it was decided to investigate configurations in which the excitation and detection coils were well separated with the subjects torso between them. This configuration should produce higher sensitivity and larger dynamic changes of phase since the primary signal should be much smaller and the ratio of secondary / primary signals should be higher.

## 5.2 Design and implementation

This section describes the work performed for the design and the implementation of the Cardiff Mk2d system.

### 5.2.1 Design

The use of a zero crossing technique MIT system for cardiac activity and lung function detection has not been reported yet in the literature. Since this system would be the first attempt to investigate whether the zero crossing technique could perform this task it was decided to keep the architecture of the system as simple as possible and therefore a single channel architecture was selected. This choice was also made to reduce the cost compared to existing systems which are either multichannel systems [42, 68] or can only measure one of the two [20, 123].

The architecture for a single channel system as described before is quite simple. The excitation signal chain comprises the signal generation stage, the RF amplifier and the excitation coil. The controlling device was omitted since a single excitation coil would be used. The detection signal chain comprises the detection coil, the preamplifier and the signal processing and measurement unit (SPMU). The architecture of the system is given in the diagram of figure 5.1.

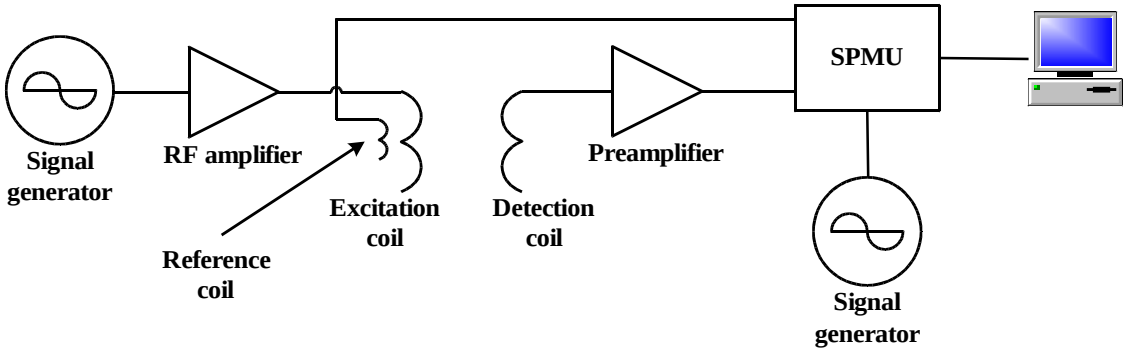


**Figure 5.1**: The Cardiff Mk2d system architecture

### 5.2.2 Implementation

#### 5.2.2.1 The coil array body

The coil array body has a Π shape form and it is shown in figure 5.2. It was constructed from three aluminium bars with the two bars being 26.5 cm long and the third bar 47 cm long. The three bars were 12.5 cm wide and 1.3 cm thick.

The two small bars were fixed opposite each other on the edges of the long bar with metal screws to form the Π shape. The coil array body was placed on a metal pole which allowed

upward and downward movement to achieve the required position where it was fixed with a securing mechanism. A ground connection was permanently connected to the coil array body.

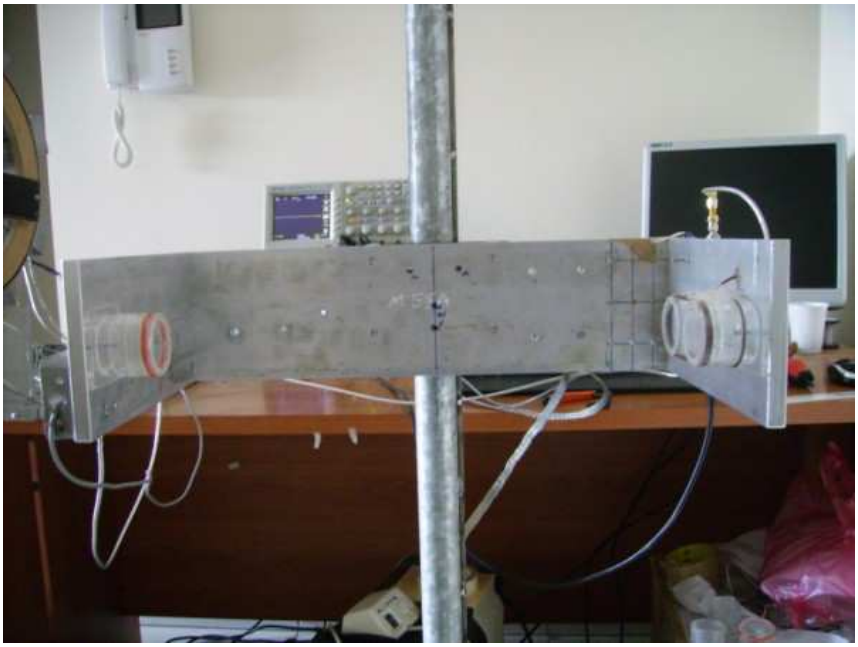

**Figure 5.2**: The Cardiff Mk2d coil array

The coil formers for the excitation coil and the detection coil were placed on the inside of the small bars. For the excitation coil two coil formers were fixed next to each other to form the single coil. For the detection coil a single coil former was used. The distance between the two coils was 38 cm.

#### 5.2.2.2 The excitation coil

The two coil formers were used to create a rectangular shape for the excitation coil which was selected to give a better homogeneity of the magnetic field on the vertical axis of the chest while using a smaller coil.

The excitation coil was constructed from a single PVC insulated copper wire of 0.6 mm in diameter and it is shown in figure 5.3. Its width was 9 cm, its height was 4.5 cm and had 4 turns. The coil was approximated as a rectangular coil and its inductance of the excitation coil was calculated with a publicly available web calculator [152] to be equal to 1.33 μH and thus the self resonance frequency was calculated to be approximately 50 MHz. The equation for calculating the inductance of the coil is given in Appendix 5.

The one wire end was soldered to the pin of an SMA connector securely fixed on the aluminium bar and the other wire end was soldered to the SMA socket. An RG402 coaxial cable was used to connect the SMA socket to the output of the RF amplifier.

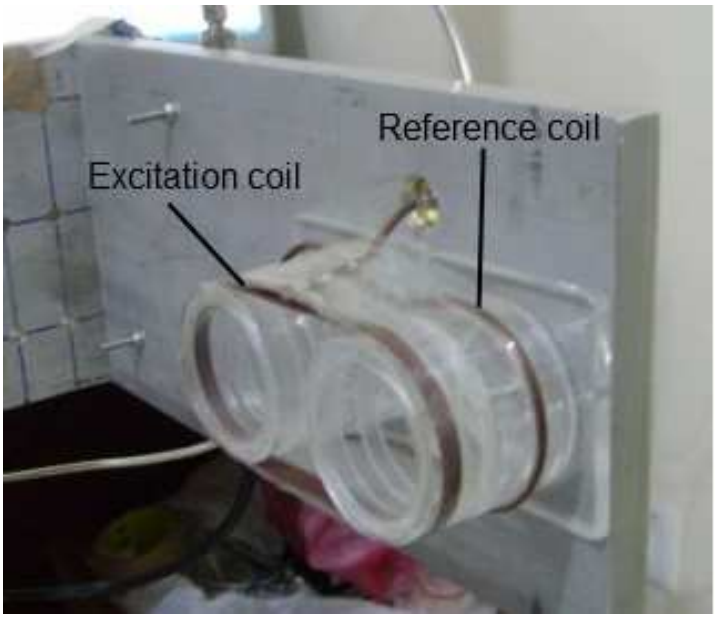


**Figure 5.3**: The excitation coil and the reference coil used in Cardiff Mk2d

#### 5.2.2.3 The reference coil

The reference coil was of the same type used in the Cardiff Mk2c system and it was placed 2 cm behind the excitation coil on the same coil former. The reference coil had a rectangular shape and it was constructed from RG405 semi-rigid coaxial cable. Its width was 9 cm, its height was 4.5 cm and had 1 turn. The reference coil is shown in figure 5.3.

The one end of the inside conductor that form the coil was directly soldered on the outside conductor. The other end was soldered to the pin of an SMA connector on which the outside conductor was also soldered. The SMA was then screwed to the aluminium bar and the reference coil was directly connected to the SPMU reference channel using a semi-rigid RG402 coaxial cable.

#### 5.2.2.4 The detection coil

The detection coil used was also of the same type as those used in the Cardiff Mk2c system. A coil former for the detection coil was screwed to the opposite bar of the excitation coil. It was constructed from a single PVC insulated copper wire of 0.6 mm in diameter. Its diameter was 4.5 cm, its height was 0.5 cm and it had 2 turns. A single PVC insulated copper wire of 0.6 mm in diameter was connected as a centre tab to the coil.

The inductance of the detection coils was calculated with the Wheeler formula (see Appendix 5) to be equal to 0.37 μH and the self resonance frequency was calculated to be approximately 56 MHz. The two ends of the coil wire were soldered to the preamplifier inputs and the end of the centre tab wire was soldered to the ground.

### 5.2.2.5 The preamplifier

For the preamplifier circuit the voltage feedback amplifier ADA4899-1 [153] (Analog Devices Inc., Massachusetts, USA) was selected for use. Its functional block is given in figure 5.4.

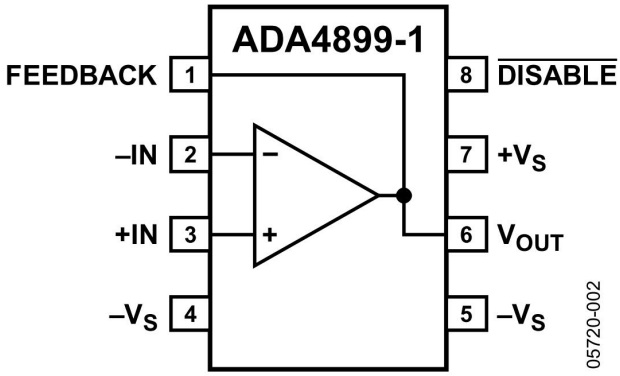


**Figure 5.4**: The ADA4899-1 functional block diagram (from [153])

The ADA4899-1 was selected for the very low noise of 1 nV/√Hz it offers, the simplicity in the implementation and the low cost compared to the preamplifier used in Cardiff Mk2c. Apart from the very low noise the ADA4899-1 offers 600 MHz unity gain bandwidth, 310 V/μs slew rate and 50 ns settling time.

The preamplifier circuit was realised as a differential amplifier as shown in figure 5.5. The closed loop differential gain was set to 32 by the resistors R1 and R3 for the non-inverting input and by the resistors R2 and R4 for the inverting input.

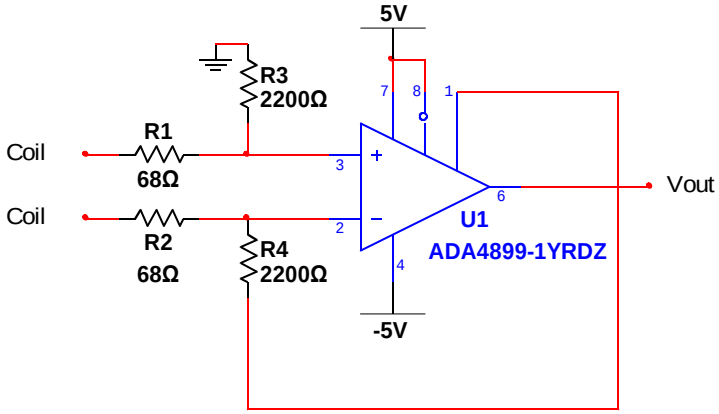


**Figure 5.5**: Implementation of the preamplifier circuit

The amplifier was powered by a dual ±5 V DC supply to utilize the dynamic performance of the amplifier. Both power pins were decoupled with a 10 nF X7R capacitor placed as close to them as possible and with a 10 μF tantalum capacitor placed at the origin of the power track powering them.

#### 5.2.2.6 Signal generation and RF amplifier

The system requires a dual channel signal source with the same requirements as for the Cardiff Mk2c system. Therefore the dual channel AFG3022B arbitrary function generator (Tektronix Inc., Oregon, USA) was used with the one channel providing the excitation signal and the other the downconversion signal.

The sinusoidal signal from the one channel of the signal generator was used as input to the RF amplifier ZHL-3A [147] (Minicircuits Inc., New York, USA) which has a maximum power output of 29.5 dBm (about 0.90 watt). The output of the RF amplifier was connected to the SMA socket of the excitation coil with an RG402 cable.

The inductive reactance of the excitation coil at 10 MHz was calculated to be about 90 Ω meaning that the RF amplifier could output an excitation current up to 100 $mA_{rms}$ to the excitation coil. The input to the RF amplifier cannot exceed 10 dBm (about 2.1 $V_{pp}$). The output of the RF amplifier appeared distorted above 35 $V_{pp}$ and so it was not used beyond that RF amplifier output.

#### 5.2.2.7 The signal processing and measurement unit

The Cardiff Mk2d system uses a single channel SPMU for measuring the phase difference based on the zero crossing technique. The single channel has been already described in detail in chapter 3. To decrease the prototyping time two signal chains from the multichannel SPMU described in channel 4 were used forming a single channel subsystem.

## 5.3 Characterisation

This section presents the work performed for the characterisation of the Cardiff Mk2d system.

### 5.3.1 Performance of the coil array

To investigate the coil array performance and its impact on the SPMU behaviour the output signal from the preamplifier and from the reference coil were measured at the input of the SPMU using the TDS2024B (Tektronix Inc., Oregon, USA). The results for the 30 $V_{pp}$ RF amplifier output are shown in figure 5.6.

The reference signal amplitude was measured about 1 $V_{pp}$ and the detected signal amplitude was measured to be 50 $mV_{pp}$. The amplitude of the detected signal is affected by four factors. The power of the RF amplifier, the distance between the coils, the turns of the detection coil and the gain of the preamplifier. An increase to the detection signal

amplitude requires the increase of at least one of these factors.

The distance between the excitation coil and the detection coil can not be decreased in this Π configuration because a person would be required to enter partially the coil array to detect its cardiac activity or the lung function.

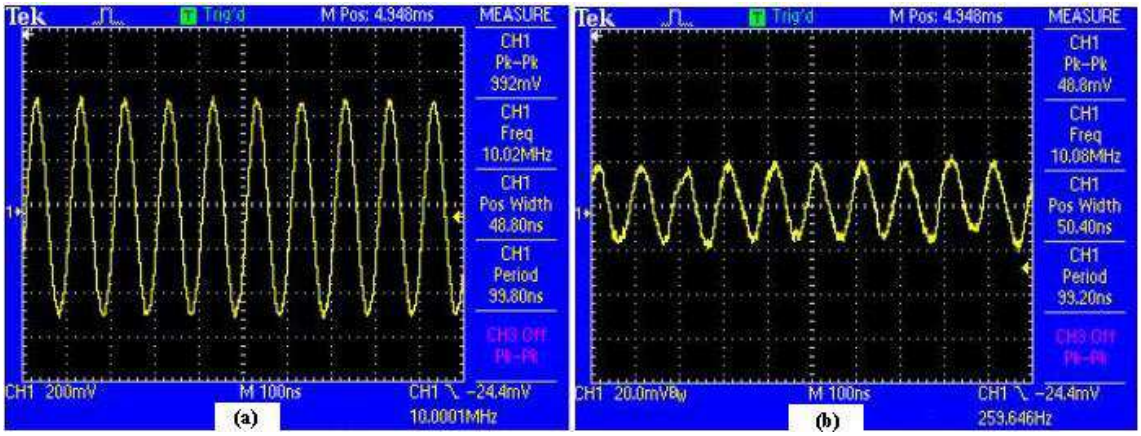


**Figure 5.6**: The reference signal (a) and the detected signal from the preamplifier (b)

An orthogonal configuration (Γ configuration) which is illustrated in figure 5.7 can be used to decrease the distance between the excitation coil and the detection coil and at the same time to allow a person to enter the coil array. The Γ configuration was tried and the amplitude of the detected signal was measured. In this case the reduction in the distance was only 8 cm and the increase to amplitude of the detected signal was 10 $mV_{pp}$.

**Figure 5.7**: The orthogonal configuration of the coil array

However the distance between the excitation coil and the detection coil cannot be reduced to a very small distance because it endangers the reduction or even the elimination of the

detection coil sensitivity as was mentioned in section 5.2.1.

In chapter 4 it was shown that the detection coils with 2 turns used in the Cardiff Mk2c were sensitive and stable. An increase to the detection coil turns would increase the detected signal amplitude but at the same time would decrease the phase stability. An increase of the preamplifier gain will certainly increase the signal amplitude but will decrease the phase stability.

The use of a more powerful RF amplifier could be the easiest way to increase the detection signal amplitude without altering the phase stability of the system or the coil array configuration.

However the increased cost and the specific absorption rate (SAR) according to the ICNIRP guidelines [154] becomes issues when more powerful RF amplifiers are considered than the one used. Due to budget considerations it was not possible to acquire a more powerful RF amplifier and thus investigate the impact it would have on the performance of the coil array.

### 5.3.2 Phase precision

This test aimed to characterise the system in terms of the phase precision at different RF output amplitudes when the 5 ms time constant (100 XOR pulses averaged) and the 50 ms time constant (1000 XOR pulses averaged) where used. The excitation frequency was 10 MHz and the phase precision for 50 measurements was calculated. The results are graphically presented in figure 5.8.

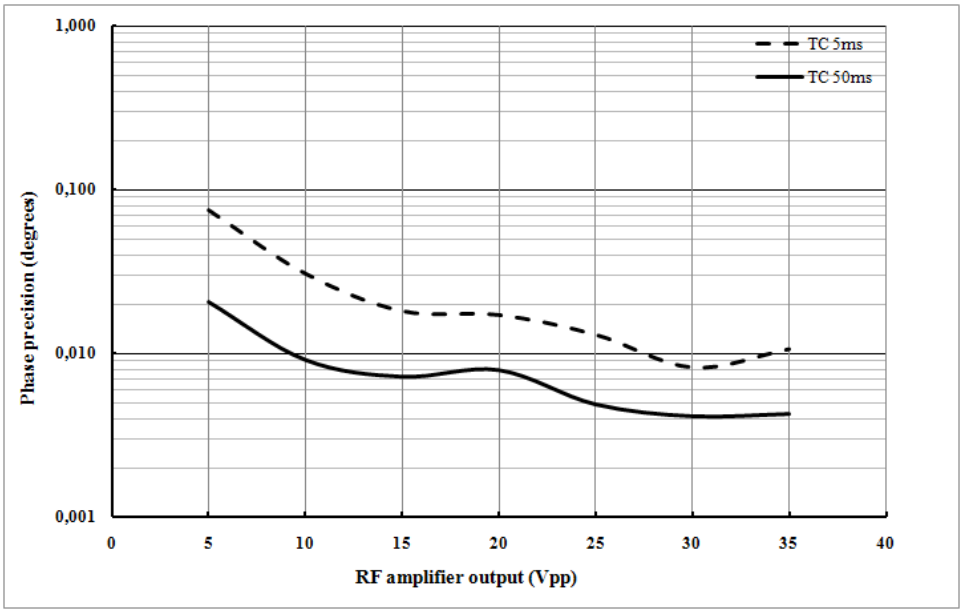


**Figure 5.8**: Phase precision Vs RF amplitude output

From figure 5.8 it can be seen that the phase precision for the 5 ms time constant goes down to 8 millidegrees at $30V_{pp}$ and for the 50 ms time constant goes down to 4 millidegrees at 30 $V_{pp}$. The results suggest that optimal results with the system are produced with 30 $V_{pp}$ RF amplitude and a time constant of 50 ms.

In chapter 3 it was shown that at 10 MHz the phase precision of the complete single channel subsystem for the 5 ms time constant was 7 millidegrees for 50 $mV_{pp}$ measured signal input (figure 3.36, chapter 3). The system's phase precision was 8 millidegrees at 30 $V_{pp}$ RF amplifier output when the detected signal was about 50 $mV_{pp}$. This shows that the system configuration has minimum impact on the capability of the single channel SPMU to measure the phase difference of a signal at 50 $mV_{pp}$.

The system exhibits a similar behaviour to the Cardiff Mk2c system in terms of the phase precision and the time constant (figure 4.33, chapter 4). This is due primarily to similar RF power values and maximum excitation-detection coil separation distances.

### 5.3.3 Phase drift

This test aimed to characterise the performance of the complete subsystem in terms of the phase drift. The excitation frequency was 10 MHz and the time constant was 5 ms. A phase difference value was recorded every minute and the measurement time was 2 hours.

The maximum phase drift was 313 millidegrees and the average phase drift was 205 millidegrees for a moving average of 10. The results show that the system drifts considerably in the 2 hours period.

Comparing the system's phase drift results with the single measurement subsystem phase drift results in chapter 3 it can be seen that the amplitude of the reference and the detected signal affect the phase drift. This shows that a contributing factor to the systems phase drift is not only the components thermal drift but also the amplitude of the detected signal and the reference signal.

Compared to the Cardiff Mk2c maximum drift across all channels which was 259 millidegrees over one hour the phase drift of the Cardiff Mk2d was better. In any case the increased observed drift is not a problem since high-pass filtering can be employed for the processing of the measurements.

### 5.3.4 Recording rate

In chapter 3 it was shown that the single channel SPMU used by the Cardiff Mk2d could achieve a recording rate of 200 phase difference values per second when the time constant was 5 ms.

To investigate the data acquisition rate achieved by a single channel of the Mk2d system samples were recorded using 5ms and 50ms time constants. Over repeated measurements the system was found to provide the expected data acquisition rates of 200 Hz and 20 Hz respectively. There is no reason to believe that similar frame rates cannot be achieved using up to 8 detector channels.

## 5.4 Measurement of the cardiac activity and the lung function

This section describes the tests performed with the Cardiff Mk2d system for recording the human cardiac activity and lung function. Two healthy male and two healthy female human volunteers participated in the tests. Due to the participation of the human volunteers all the ethical issues were considered by the appropriate committees.

### 5.4.1 Measurement set-up

The measurement set-up is divided according to the position of the detection coil in respect to the excitation coil which remained at the same position permanently. Three detection coil positions have been used and are described below.

#### 5.4.1.1 Detection coil position 1

The coil array was used in the Π configuration with the excitation coil and the detection coil facing each other. The coil array set-up is illustrated in figure 5.9.

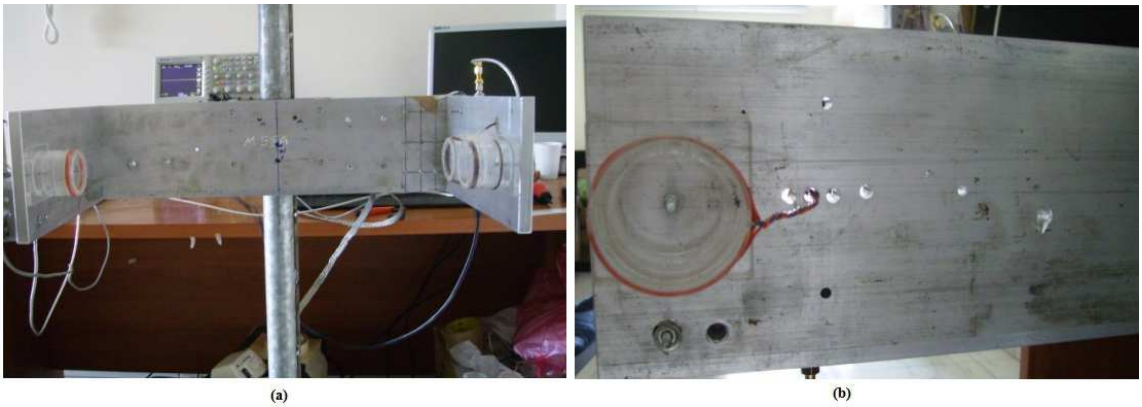


**Figure 5.9**: Position 1 coil array configuration (a) and the detection coil position (b)

The volunteer sat on the chair facing the excitation coil and having his/her back to the detection coil which was situated approximately behind the spinal column of the volunteer.

The distance between the excitation coil and the detection coil was 38 cm. The distance between the volunteer's chest and the excitation coil was 15 cm and the distance between the volunteer's back and the detection coil was 5 cm.

#### 5.4.1.2 Detection coil position 2

The coil array was used in the Π configuration with the excitation coil and the detection coil facing each other. However the detection coil was moved to be approximately behind the area between the spinal column and the scapula of the volunteer. The coil array set-up is illustrated in the figure 5.10.

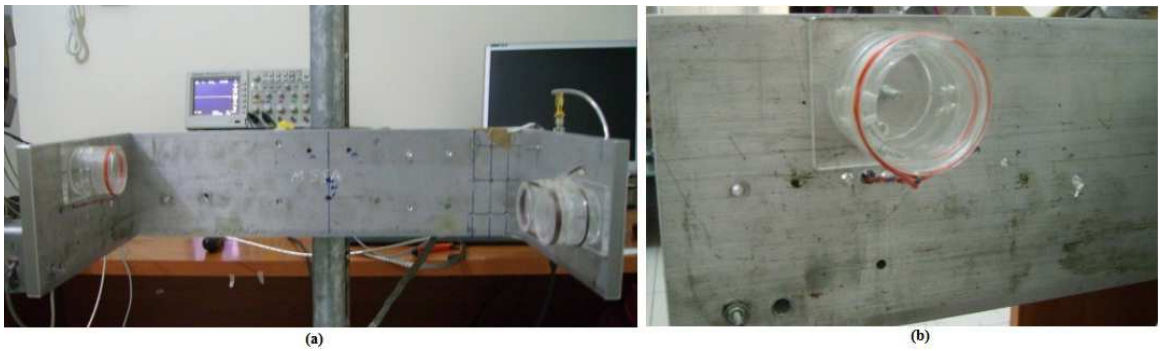


**Figure 5.10**: Position 2 coil array configuration (a) and the detection coil position (b)

The volunteer sat on the chair facing the excitation coil and having his/her back to the detection coil as depicted in figure 5.11. The distance between the excitation coil and the detection coil was 38 cm. The distance between the volunteer's chest and the excitation coil was 15 cm and the distance between the volunteer's back and the detection coil was 5 cm.

**Figure 5.11**: A volunteer in the coil array of detection coil position 2

### 5.4.1.3 Detection coil position 3

The coil array was used in an orthogonal configuration (Γ configuration) with the excitation coil on the short bar and the detection coil placed on the long bar. The coil array set-up is illustrated in the figure 5.12.

**Figure 5.12**: Position 3 orthogonal coil array configuration

The volunteer sat on the chair having the excitation coil on the left hand side and his/her back to the detection coil as depicted in figure 5.13. The distance between the excitation coil and the detection coil was 30 cm. The distance between the volunteer's side and the excitation coil was 10 cm and the distance between the volunteer's back and the detection coil was 5 cm.

**Figure 5.13**: A volunteer in the coil array of detection coil position 3

During the preliminary tests a further orthogonal coil array configuration was tested with the detection coil placed at a distance of 52 cm from the excitation coil however the

recorded SNR was very small which made the signal unusable and therefore the coil was moved to the distance of 30 cm. The reason for the very small SNR is attributed to the combination of the low power of the RF amplifier and the large distance of the detection coil from the excitation coil.

#### 5.4.1.4 The sampling rate used in the measurements

The literature review conducted in chapter 2 showed that a sampling frequency of at least 12 Hz may be required for capturing the cardiac activity up to 240 beats per minute [24].

There may be benefits in having high frame rates as it may be useful to analyse the frequency components of the cardiac MIT signal. For this project however it was considered only necessary to provide a proof of concept that the fundamental respiration and cardiac rate could be measured by magnetic induction measurements. For this reason a 20 Hz sampling rate was considered more than sufficient to detect both cardiac and respiration rates and thus the measurement time constant of 50 ms was employed.

### 5.4.2 Measurements methodology

The measurements aimed to investigate if the Cardiff Mk2d system could detect the cardiac activity and the lung function. The cardiac activity is associated primarily with the detection of the ECG trace and secondarily with the detection of the heart rate. The latter was considered to be a more achievable task for these measurements and thus it was targeted.

The lung function can be described by the lung capacity and the lung volumes relationship as shown in figure 5.14. For the lung function detection the primary target was to capture the lungs volume changes during breathing and a secondary target was to capture of the respiration rate.

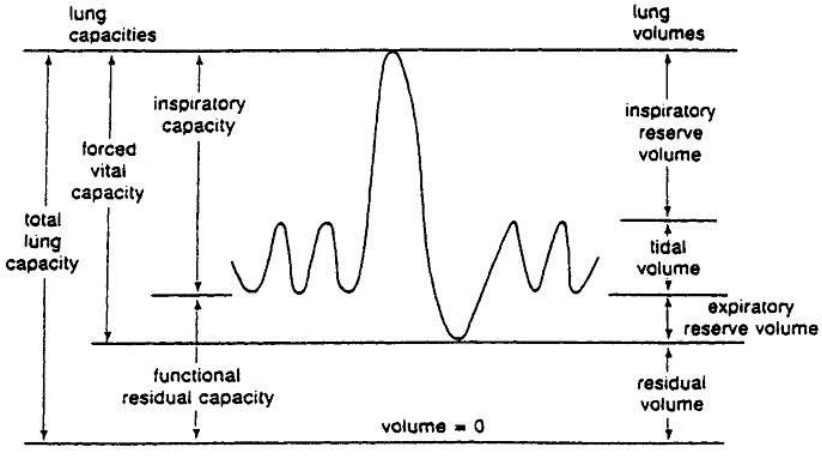


**Figure 5.14**: Lung capacities and lung volumes relationship (from [109])

The measurements were taken at different days in a time period of four weeks. Two healthy male and two healthy female human volunteers between 30 and 40 years old participated. During the measurements the volunteers were asked to remain still in the coil array to avoid measurements contamination by artefacts due to movement.

The cardiac activity and the lung function measurements were recorded by the Cardiff Mk2d concurrently. To identify that the Cardiff Mk2d could detect the cardiac activity the volunteers' ECG was recorded simultaneously to the MIT measurements using the ECG system described in [155].

The ECG system consisted of the Dyna Vision [156] ECG portable device (Techmedic International) showed in figure 5.15 and the computer application software. The sampling frequency of the device was 100 Hz. The device captured the 3-lead ECG signal with a 3-electrode wire attached to the chest of the volunteer and transmitted it wirelessly to the computer where it was displayed and stored.


**Figure 5.15**: The Dyna Vision device used for ECG recording

Due to technical incompatibilities the acquisition start of the two systems was not synchronised and the ECG system was always started 1 – 2 seconds after the Cardiff Mk2d. This however did not affect the validity of the measurements since the objective was to measure and compare the main frequency components of the MIT and ECG signals over extended periods of 1 – 3 minutes.

Before the experiments were performed an investigation was carried out to examine whether the use of the ECG portable device in the Cardiff Mk2c coil array would affect the

ECG recording. This examination was performed with the participation of the two male volunteers. The resting ECG of the volunteers was recorded while the volunteer moved in and out of the coil array in time intervals of 2 minutes. Each recording took place for 6 minutes and was performed five times for each volunteer in a time period of four hours.

The ECG recording of the time interval in the coil array was compared to the ECG recording of the time interval out of the coil array to examine whether the coil array affected the ECG recording. The investigation showed that there was not any difference of the ECG when recorded in the coil array and out of the coil array and therefore it was concluded that the ECG portable device was not affected by the coil array.

To investigate the cardiac activity and the lung function four measurement protocols were used which were the normal breath, the absence of breath (no breathing), the exercise and the breathing pattern.

In the normal breath protocol the volunteers were breathing normally. The time duration of the measurements was normally 1 minute however measurements with time duration of 2 minutes and 3 minutes were also recorded.

In the no breathing protocol the volunteers were asked to exhale the air as much as possible from their lungs and then to stop breathing for 20 seconds.

In the exercise protocol the male volunteers were asked to increase their heart rate above 100 beats per minute (bpm) and then to enter the coil array and stay in there while returning back to their normal heart rate and normal breathing.

In the breathing pattern protocol the volunteers were asked to perform a breathing sequence for 2 minutes. The breathing sequence was normal breath, no breath, normal breath, very deep breath, normal breath.

### 5.4.3 Measurements analysis

The processing of the measurements for detecting the heart rate and the respiration rate required the use of a signal analysis method. The analysis of the MIT signal and the ECG signal was performed in MATLAB. The MATLAB code is given in Appendix 6.

The MIT signal was preprocessed before the analysis. The preprocessing used averaging and subtracting instead of high pass filtering due to the lowest settling time it required.

The heart rate was extracted from the MIT signal by subtracting a smooth version of the low frequency movement. The first step was to extract the low frequency content of the MIT signal by applying a moving-average filter using an 80-point window. This removed the high frequency content. This signal was then again smooth using a 15-point moving-average filter in order to get a smooth signal representing the movement from the body and the respiration. A single combined windows was found to perform worse than the used two-stage process. Finally the smoothed signal was subtracted from the original MIT signal to provide a new signal trace containing the heart rate only.

A similar algorithm was applied to the MIT signal to extract the respiration signal. Again the MIT signal was first passed through a two-stage moving-average filter. The first stage had a 200-point window, while the second stage used a 50-point window. Larger moving-average windows were used to smooth the MIT signal in respiration preprocessing algorithm in order to get a smooth signal representing the body movement only. This smoothed signal was then subtracted from the original MIT signal to remove any low frequency movement. The resulting signal contained not only the respiration but also the heart rate signal components and was therefore again passed through a moving-average filter (10-points) to remove the heart rate signal components.

After the preprocessing the MIT-heart signal, the MIT-breath signal and the ECG signal were processed with the Fast Fourier Transform (FFT) to convert them from the time domain to the frequency domain. For the FFT a 512 point rectangular window was used.

Due to the non-stationary nature of the heart rate further analysis of the MIT-heart signal was deemed necessary. Thus the Short Term Fourier Transform[9] (STFT) was used which is a time-frequency method.

The STFT is a window function which applies the Fourier Transform (FT) in a segment of the data which is much smaller than the overall length of the waveform. The basic equation of the STFT in the continuous domain is given by [157]

$$X(t, f) = \int_{-\infty}^{\infty} x(\tau)\,\omega(t-\tau)\,e^{j\pi f \tau}\,d\tau \qquad (5.1)$$

where $\omega(t - \tau)$ is the window function and $\tau$ is the variable that slides the window across the waveform x(t).

The MIT-heart signal analysis generated a spectrogram using a 768 point window with a

[9] Also called spectrogram

512 point overlap and frequency steps of 0.05 Hz between 0.5 Hz and 4 Hz. The frequency was multiplied with 60 to give the beats per minute (bpm).

### 5.4.4 Measurement results at detection coil position 1

This section presents a selected number of the analysed measurements for detecting the cardiac activity. The four protocols were used for the measurements. It is noted here that the breathing was not recorded by an external device but it was visually monitored.

#### 5.4.4.1 Normal breathing

The normal breath response of a volunteer captured by the system is shown in figure 5.16 and the ECG signal is shown in figure 5.17. The three FFT signals are shown in figure 5.18.

The FFT was applied to the preprocessed signals to extract the heart and respiration rate. For comparison an FFT was also applied to the ECG signal. The x-axis of the FFTs are limited to the expected frequency range of the heart rate (0.5 – 4 Hz) and the breathing rate (0 – 1 Hz). To visualise the heart rate variability over time the STFT was applied to the preprocessed MIT heart rate signal which is shown in figure 5.19.

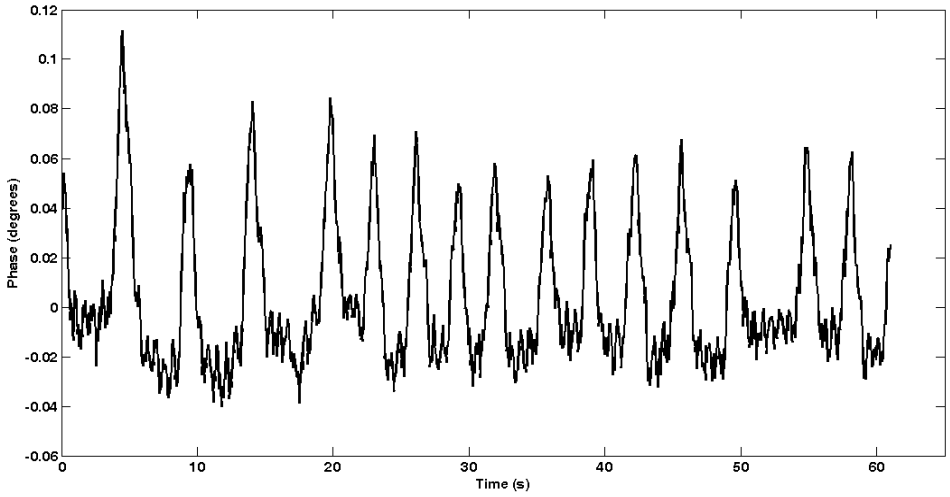


**Figure 5.16**: MIT normal breathing signal of a volunteer for 1 minute at position 1

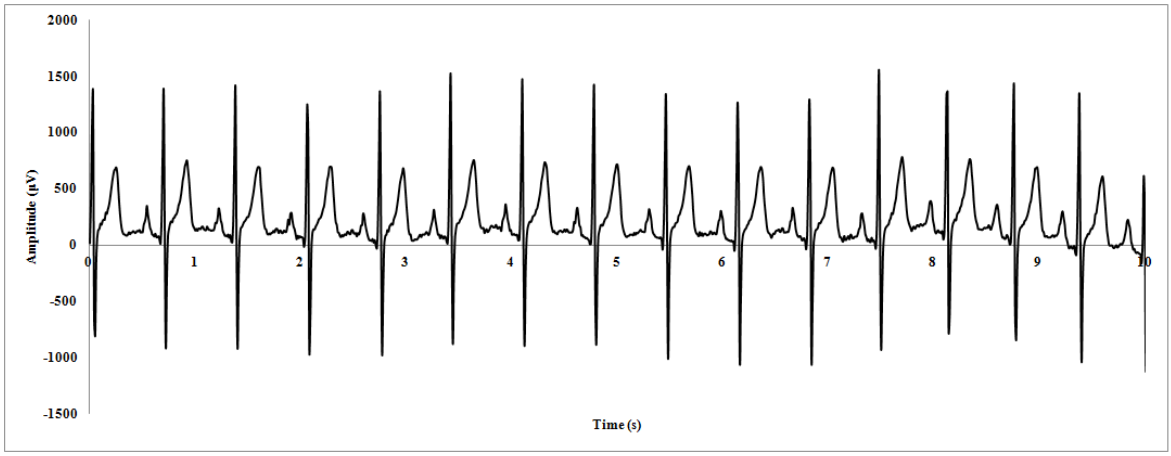


**Figure 5.17**: ECG signal of volunteer in normal breathing at position 1

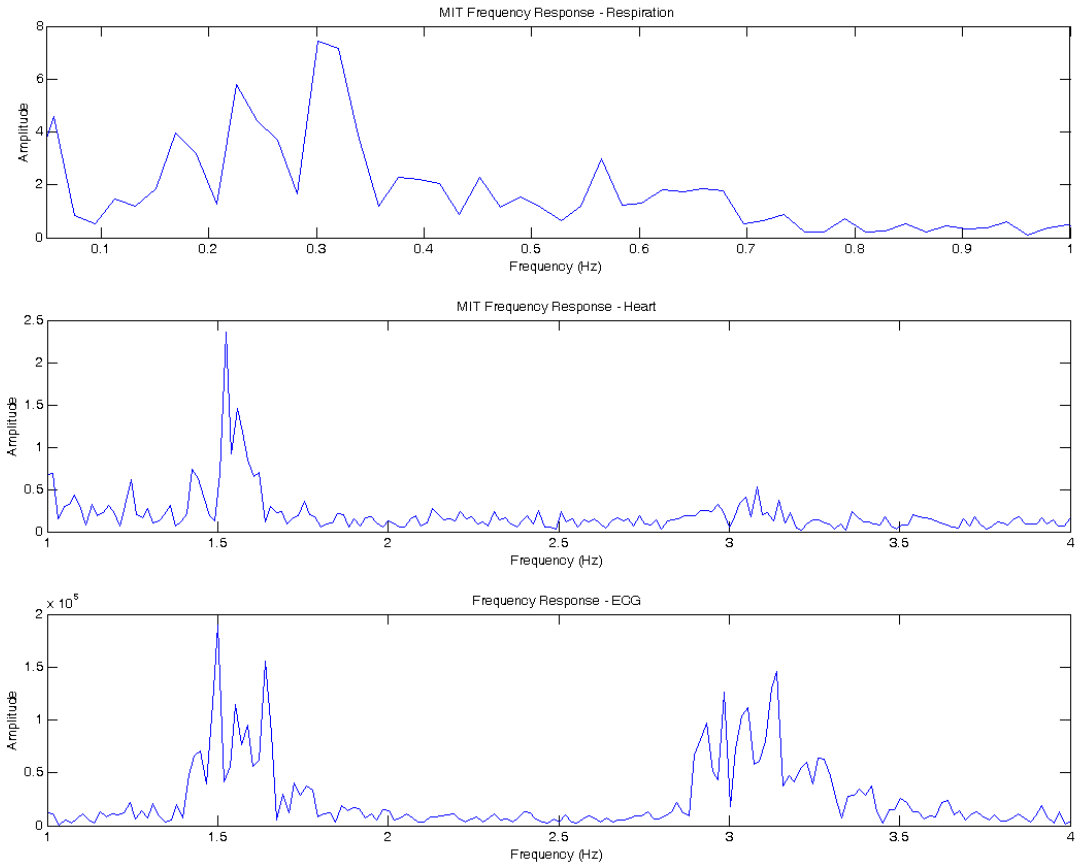


**Figure 5.18**: FFT spectrum of the MIT normal breathing signal and the ECG signal at position 1. From top to bottom: the MIT-breath signal FFT, the MIT-heart FFT and the ECG FFT.

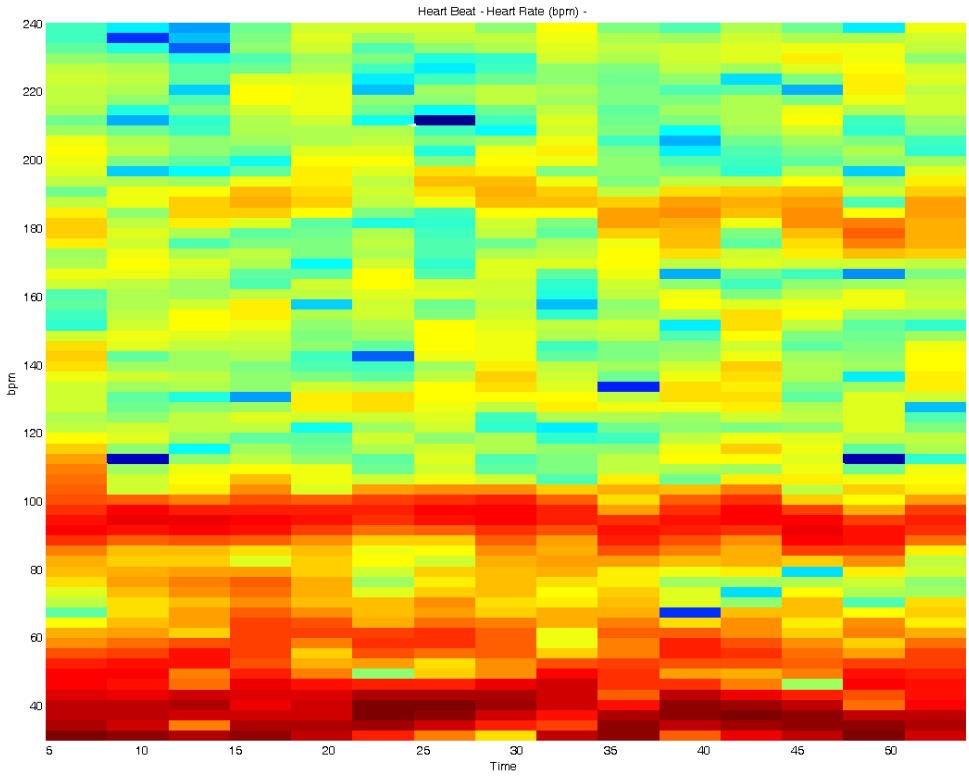


**Figure 5.19**: Heart rate spectrogram generated by the MIT normal breathing signal at position 1

From figure 5.16 it can be seen that the system captured the normal breathing of the human volunteer and distinguished between the inhalation phase which is pictured as peaks and the exhalation phase which is pictured as valleys. Comparing figure 5.16 to figure 5.14 it can be said that the system identified the respiratory waveform of the human volunteer.

The heart rate has been derived for comparison from the ECG signal (Figure 5.17) by measuring the time difference between the R waves and was found to be 96 bpm.

However from figure 5.16 it can also be seen that when the volunteer exhaled the air and only the expiratory reserve volume remained in the lungs the measurement is drifting. It is not clear if this drifting is due to the conductivity changes due to the heart movement, the air that is still in the lungs or due to the systems drift.

From figure 5.18 it can be seen that the FFT spectrum of the respiration rate has large components at 0.18, 0.23 and 0.31Hz. This corresponds to breaths per minute rates of 10.8, 13.8 and 18.6 which correspond well to the average rates expected in resting adults (12-20 breaths per minute).

From figure 5.18 it can be also seen that for the MIT signal significant frequency components can be observed between 1.5Hz – 1.6 Hz and a much smaller amplitude group between 3 Hz – 3.2 Hz. Corresponding frequency components are observed in the ECG

signal strongly suggesting that the system is detecting cardiac motion

The spectrogram in figure 5.19 appears to show a clear cardiac trace between 90 – 100 bpm. Significant noise is observed below 60 bpm however due to respiration and other physiological motion.

### 5.4.4.2 No breathing

The no breath response of a volunteer for 18 seconds captured by the system is shown in figure 5.20 and the ECG signal in figure 5.21. The MIT-breath signal FFT, the MIT-heart FFT and the ECG FFT are shown in figure 5.22.

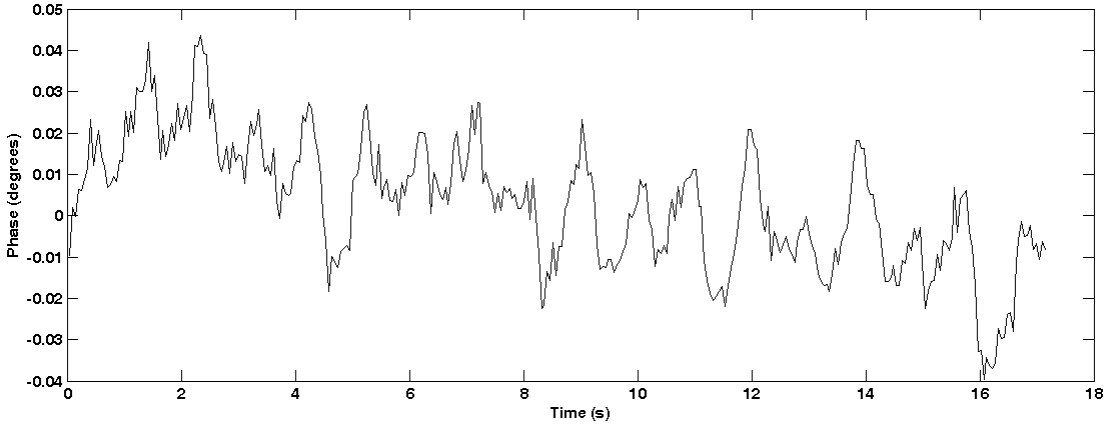


**Figure 5.20**: No breathing MIT signal of a male volunteer at position 1

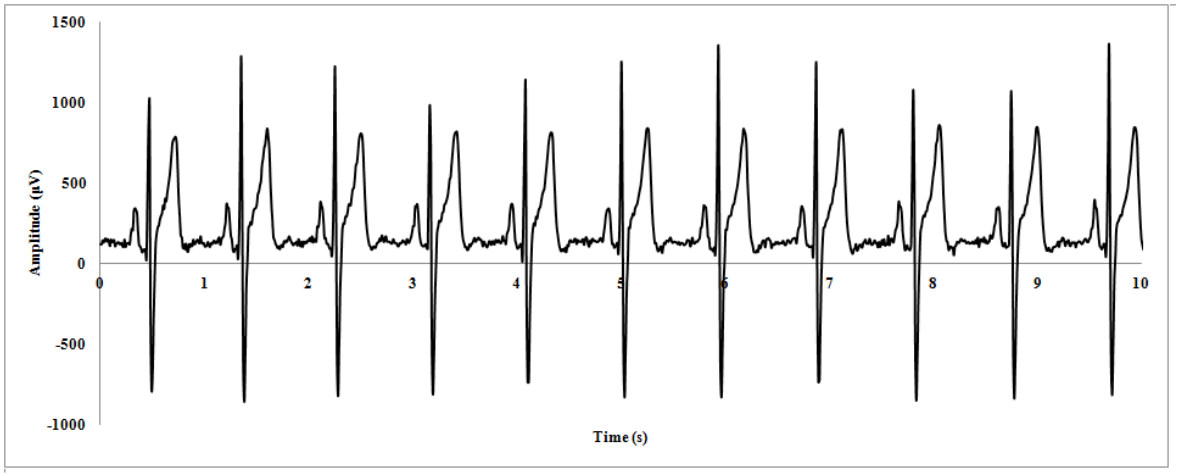


**Figure 5.21**: ECG signal when the volunteer did not breath (no breathing) at position 1

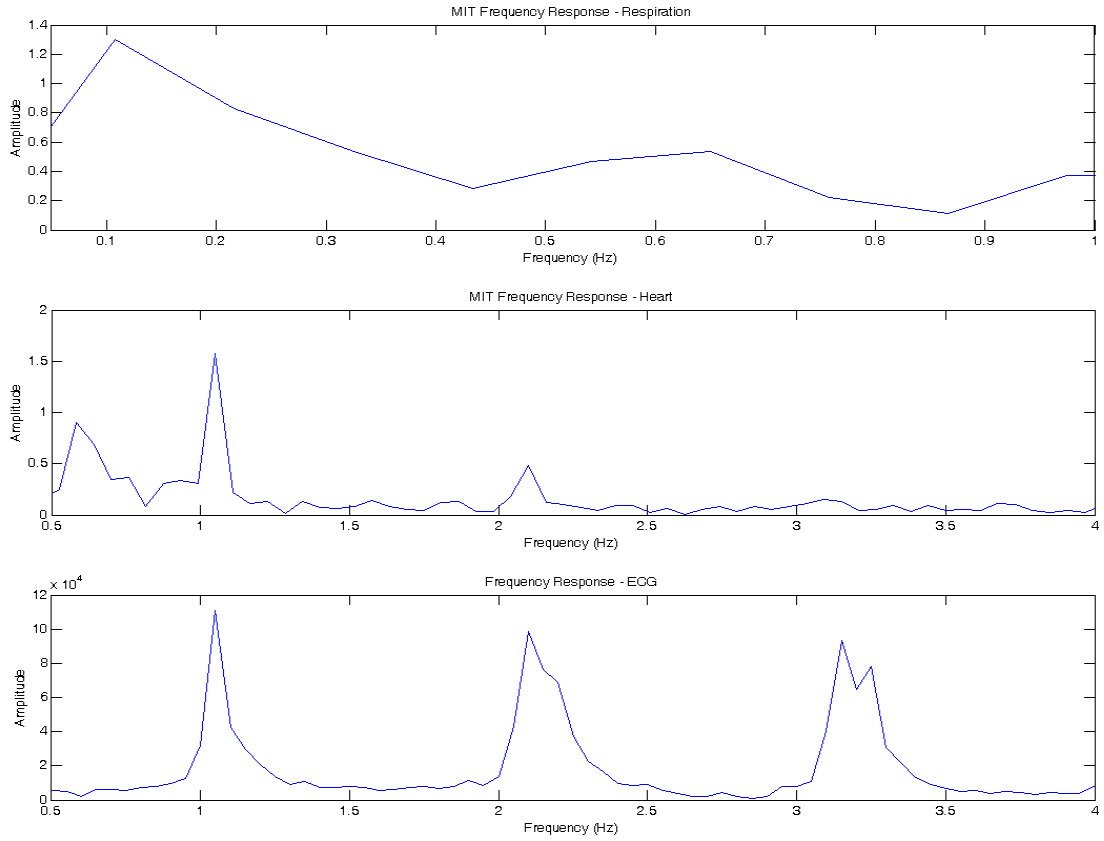


**Figure 5.22**: FFT spectrum of the no breathing MIT signal at position 1. From top to bottom: the MIT-breath signal FFT, the MIT-heart FFT and the ECG FFT.

In figure 5.20 the no breathing MIT signal is not a flat line but phase changes are recorded. The phase changes represents the conductivity changes due to the cardiac motion.

The heart rate has been derived for comparison from the ECG signal (figure 5.21) by measuring the time difference between the R waves and was found to be 66 bpm.

In figure 5.22 the FFT spectrum of the respiration rate shows the absence of breathing by the volunteer. The FFT of the MIT signal heart rate shows a large frequency component at 1.1 Hz and a smaller frequency component at 2.1 Hz. These frequency component coincide well with the frequency components of the ECG signal FFT at 1.1 Hz and at 2.1 Hz.

The MIT signal heart rate spectrogram did not provide any significant information due to the small measurement time and therefore was omitted.

### 5.4.4.3 Exercise

The MIT signal of a volunteer during the exercise protocol is shown in figure 5.23 and the ECG signal in 5.24. The signals were captured right after the exercise which aimed to raise the heart rate of the volunteer above 100 bpm. The MIT-breath signal FFT, the MIT-heart FFT and the ECG FFT are shown in figure 5.25 and the spectrogram in figure 5.26.

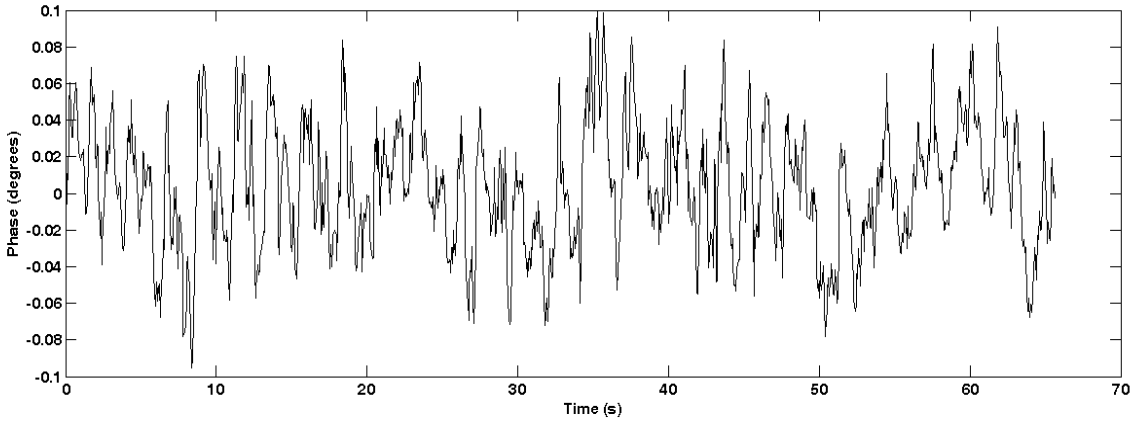


**Figure 5.23**: MIT signal of a volunteer after exercise at position 1

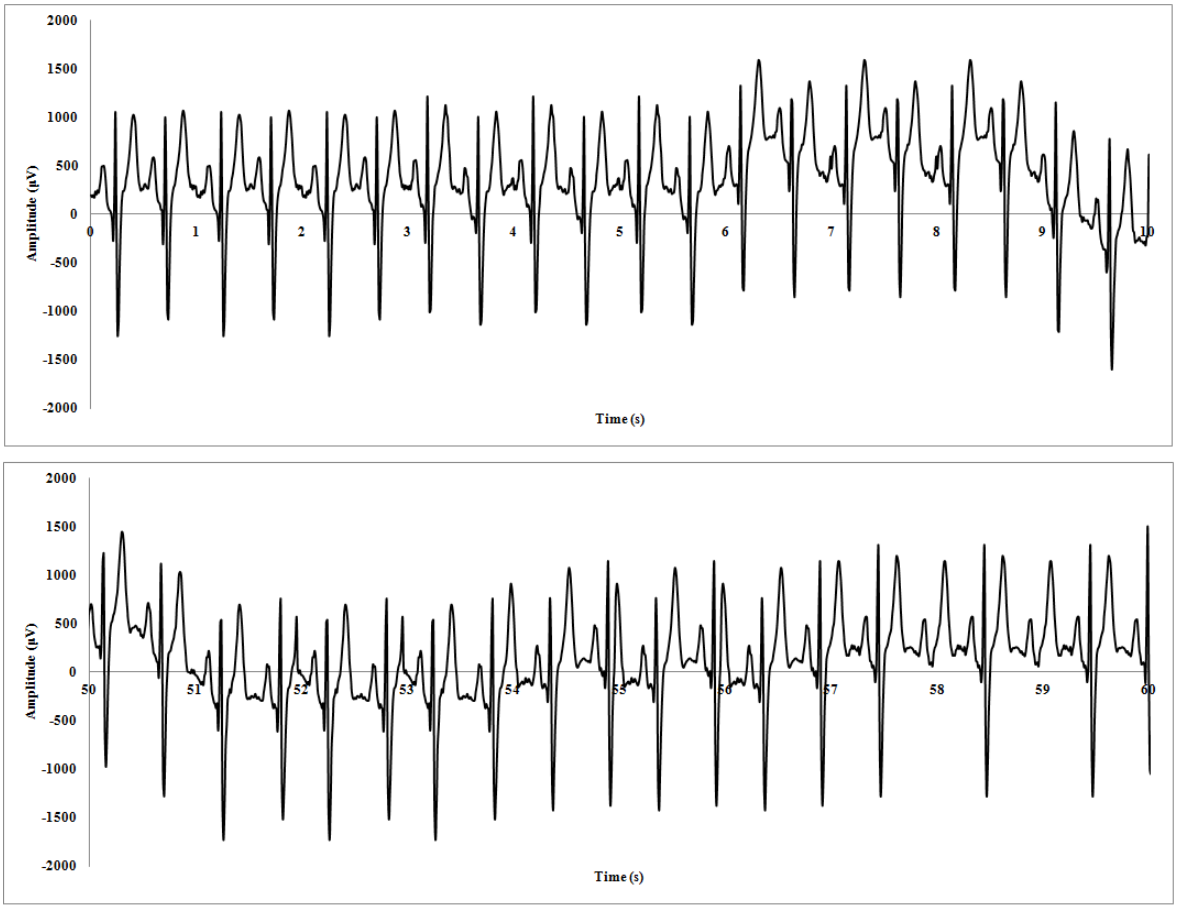


**Figure 5.24:** ECG signal of volunteer after exercise at position 1. From top to bottom: at beginning of measurement, at end of measurement

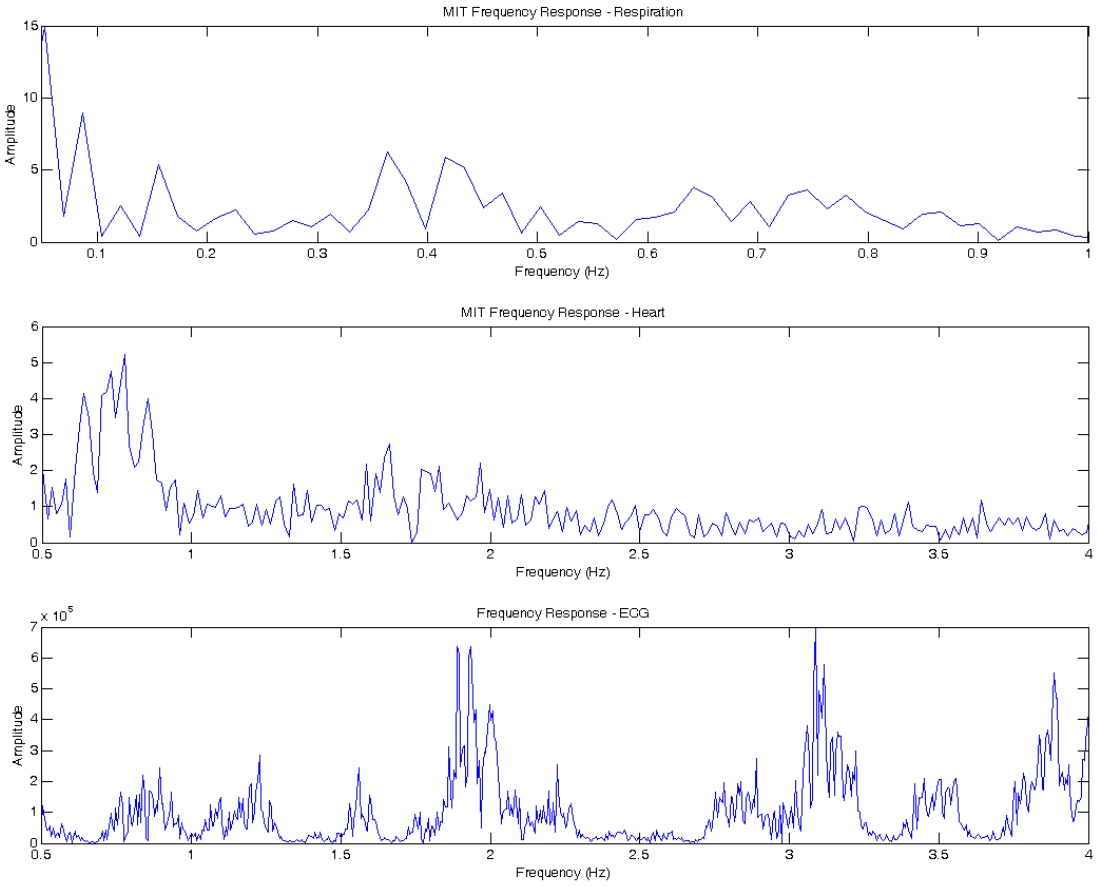


**Figure 5.25**: FFT spectrum of the MIT signal and the ECG signal after exercise at position 1. From top to bottom: the MIT-breath signal FFT, the MIT-heart FFT and the ECG FFT.

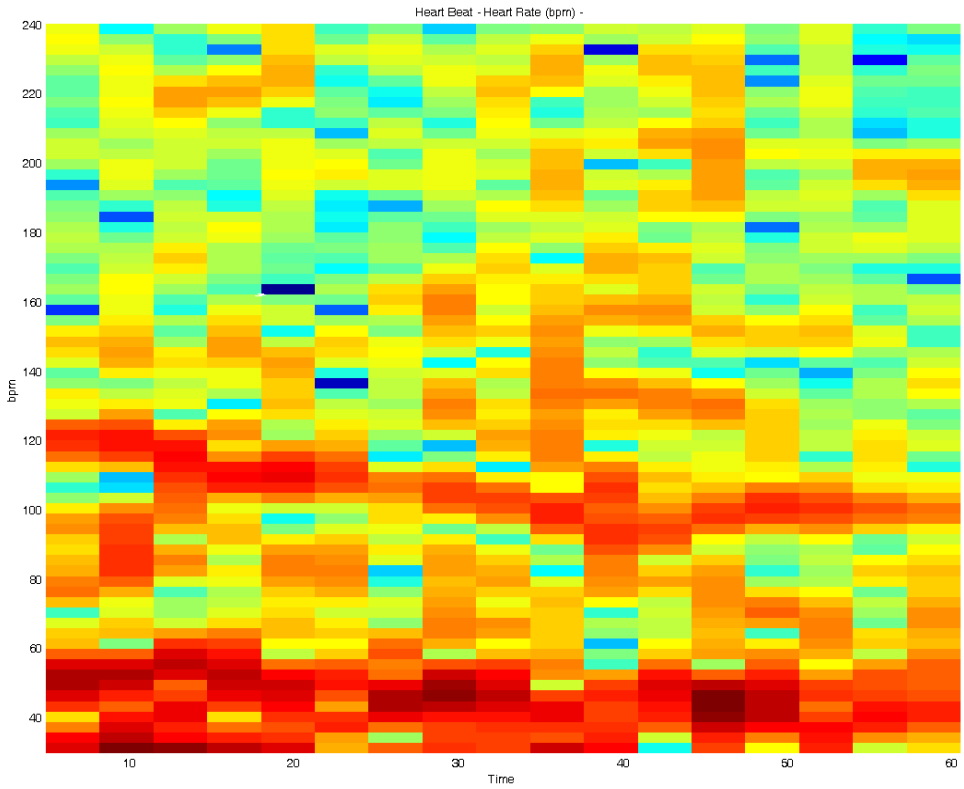


**Figure 5.26**: Heart rate spectrogram after exercise at position 1

From figure 5.23 it can be seen that the system captured the volunteer's breathing after the exercise.

From figure 5.24 the heart rate was derived at the beginning and at the end from the R waves and was found 120 bpm and 108 bpm respectively. This compares well with the spectrogram in figure 5.26.

In figure 5.25 (FFT of the MIT signal) it can be seen that the MIT signal below 1 Hz in this case appears to be much more varied and irregular in comparison to the resting MIT signal which would perhaps be expected if the volunteer was 'catching his breath' after exercise.

Large amplitude signals are also observed in the MIT signal above 1 Hz and these do not appear to correlate well with the measured ECG. It is likely that rapid breathing after the exercise produces significant higher frequency chest wall motion which overlaps and masks the cardiac frequency component in the MIT signal FFT.

The FFT of the ECG signal however compares with the information provided by the spectrogram in figure 5.26 for the MIT heart signal. The large amplitude components of the ECG FFT at 1.6, 1.85, 1.9 and 2 Hz give 96 bpm, 111 bpm, 114 bpm and 120 bpm. These ECG frequency components are illustrated in the spectrogram as well. However significant noise is present below 60 bpm.

### 5.4.5 Measurement results at detection coil position 2

This section presents a selected number of the analysed measurements taken at detection coil 2.

#### 5.4.5.1 Normal breathing

The MIT signal of a male human volunteer during normal breathing is shown in figure 5.27 and the ECG signal in 5.28. The MIT-breath signal FFT, the MIT-heart FFT and the ECG FFT are shown in figure 5.29 and the spectrogram in figure 5.30.

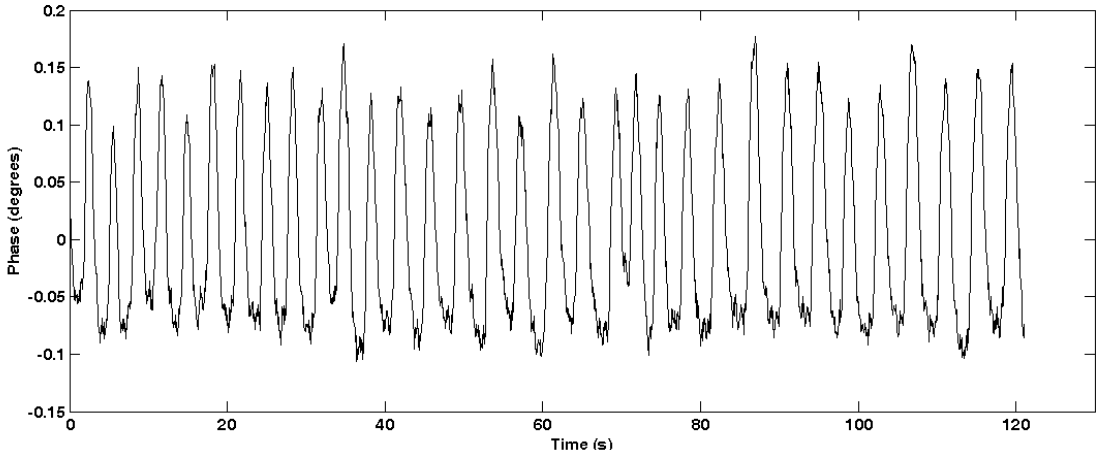


**Figure 5.27**: The MIT signal during normal breathing of a volunteer at position 2

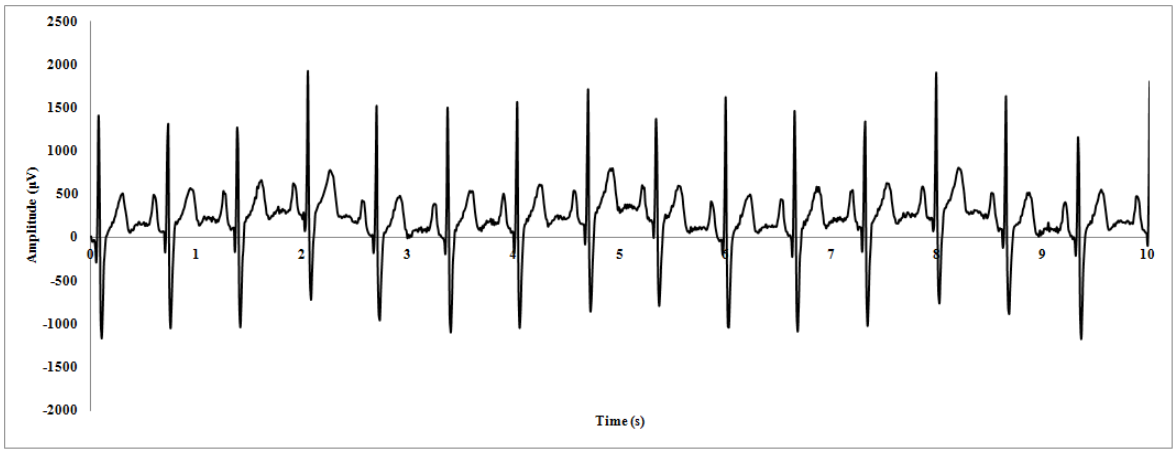


**Figure 5.28**: ECG signal of volunteer during normal breathing exercise at position 2

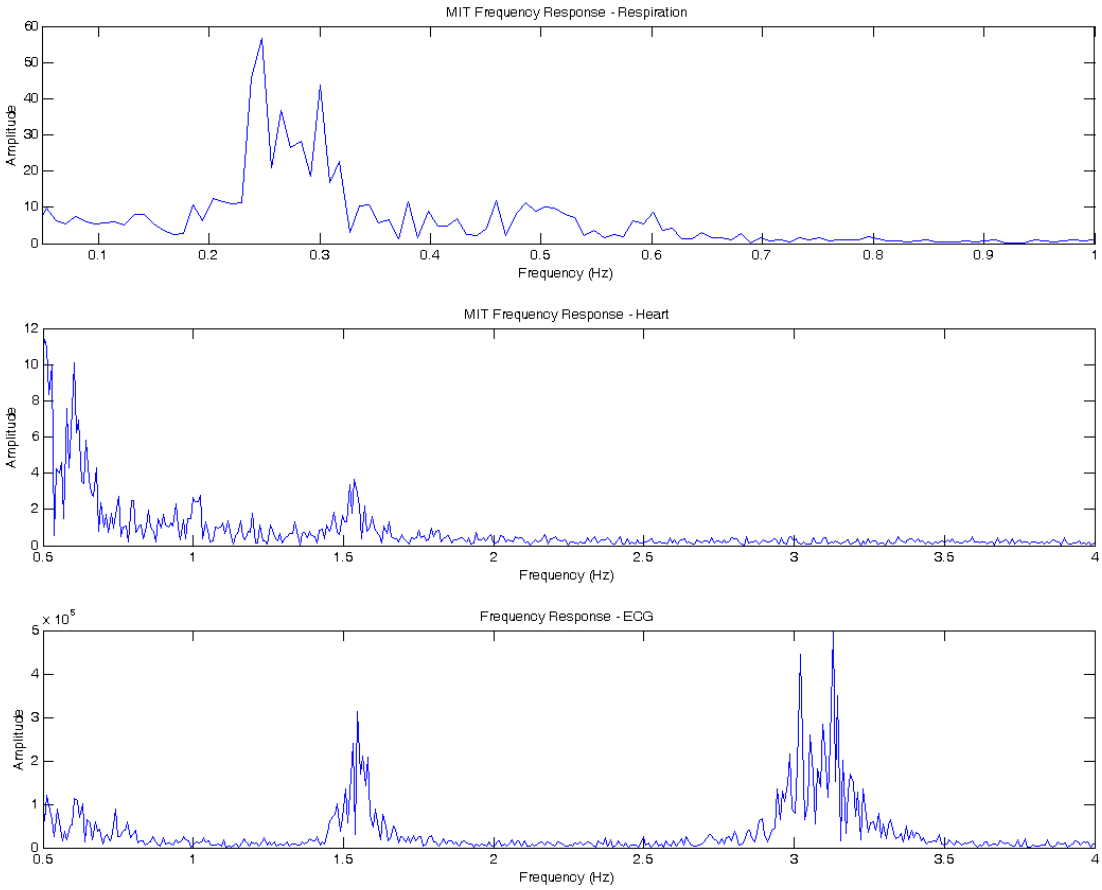


**Figure 5.29**: FFT spectrum of the MIT normal breathing signal and the ECG signal at position 2. From top to bottom: the MIT-breath signal FFT, the MIT-heart FFT and the ECG FFT.

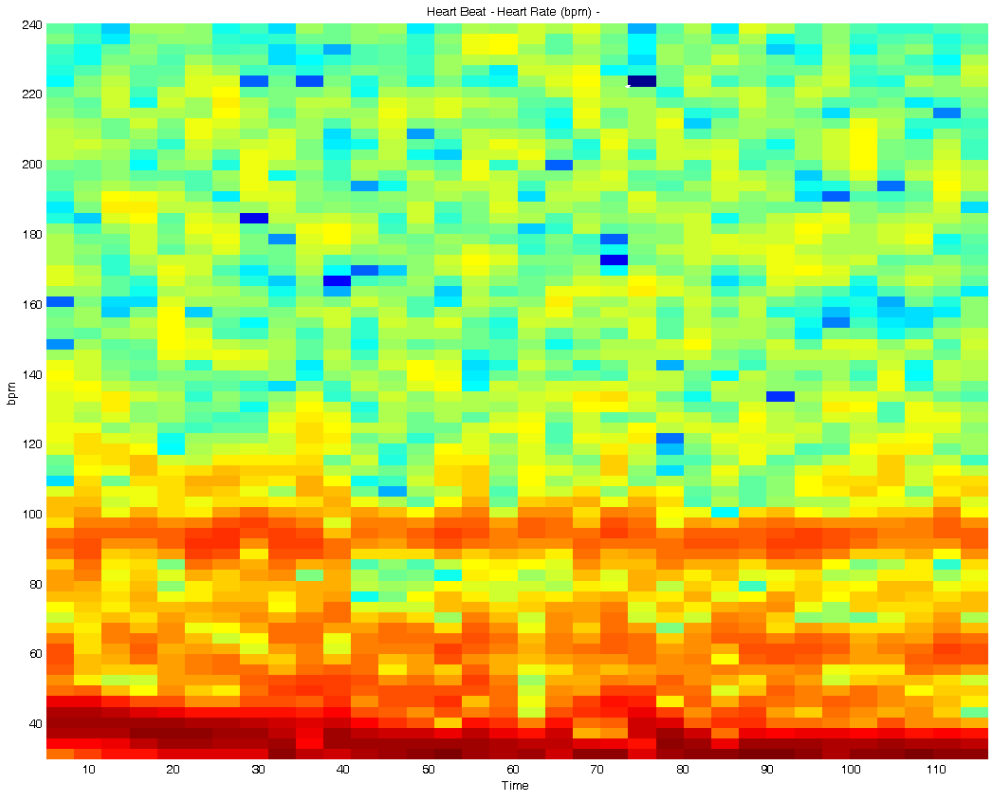


**Figure 5.30**: Heart rate spectrogram of the MIT signal during normal breathing at position 2

From figure 5.27 it can be seen that the system captured the normal breathing of the volunteer. The MIT signal captured during this measurement has a similar shape to the MIT signal illustrated in figure 5.15 for the normal breathing at position 1.

The heart rate has been derived for comparison from the ECG signal (Figure 5.28) by measuring the time difference between the R waves and was found to be 96 bpm.

From figure 5.29 it can be seen that the FFT spectrum of the respiration rate has large components at 0.23, 0.26 and 0.3 Hz. This corresponds to breaths per minute rates of 13.8, 15.6 and 18.6 which correspond well to the average rates expected in resting adults (12-20 breaths per minute).

From figure 5.29 it can be seen that for the MIT signal, significant frequency components can be observed between 1.5Hz – 1.6 Hz. Corresponding frequency components are observed in the ECG signal strongly suggesting that the system is detecting cardiac motion.

Significant noise components are observed at 0.5 Hz and 0.6 Hz in the MIT signal FFT of respiration and heart due to respiration and physiological motion.

The spectrogram in figure 5.30 appears to show a clear cardiac trace between 90 – 100 bpm. Significant noise is observed below 60 bpm however due to respiration and other physiological motion.

#### 5.4.5.2 Exercise

The MIT signal of a volunteer recorded after the exercise is shown in figure 5.31 and in more detail in figure 5.32. The ECG signal of the volunteer is shown in figure 5.33. The MIT-breath signal FFT, the MIT-heart FFT and the ECG FFT are shown in figure 5.34 and the spectrogram in figure 5.35.

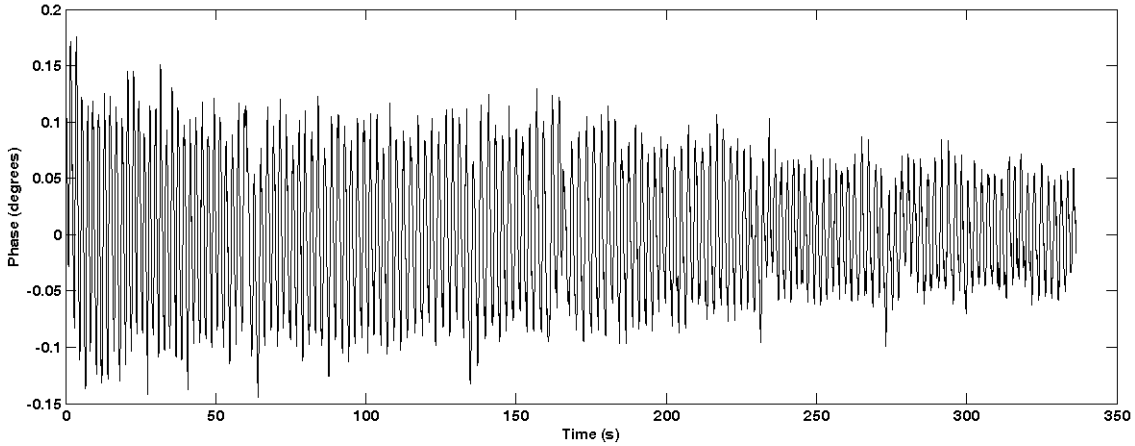


**Figure 5.31**: The MIT signal recorded after the exercise at position 2

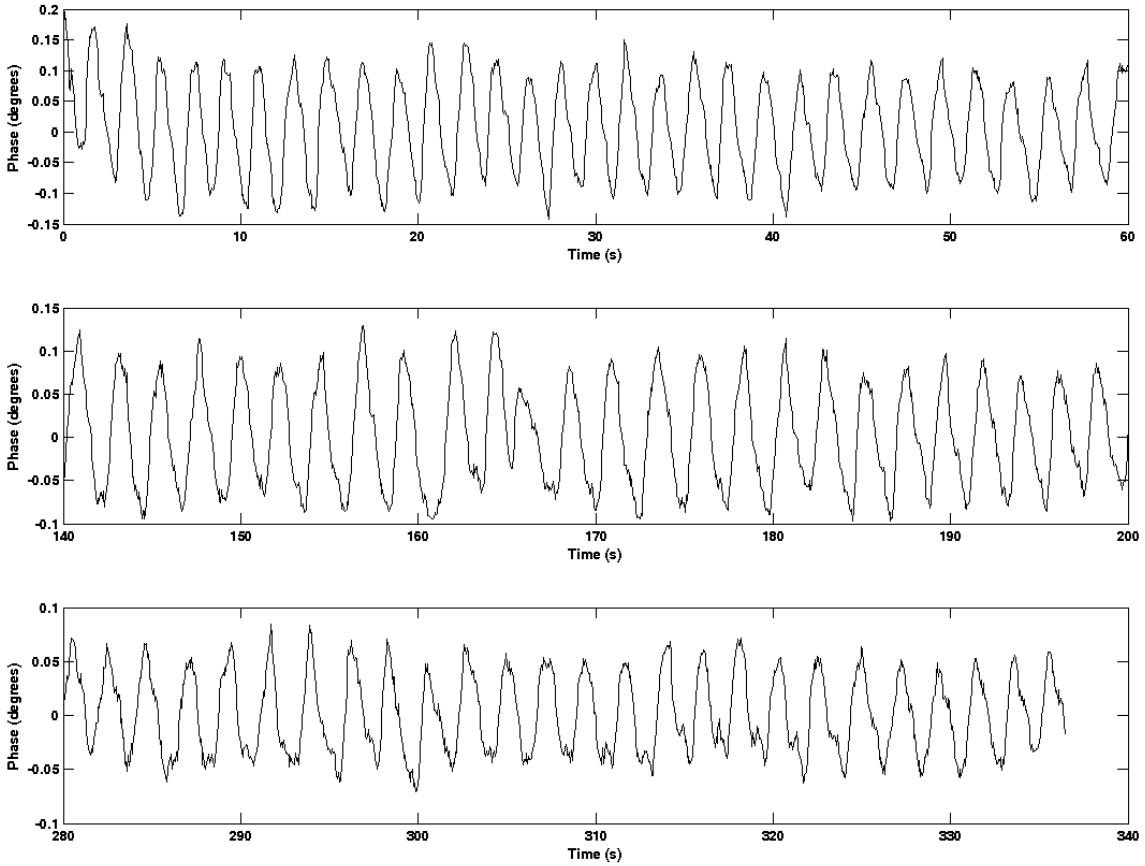


**Figure 5.32**: The MIT signal captured after the exercise at different time periods. From top to bottom: Measurement beginning, middle and end.

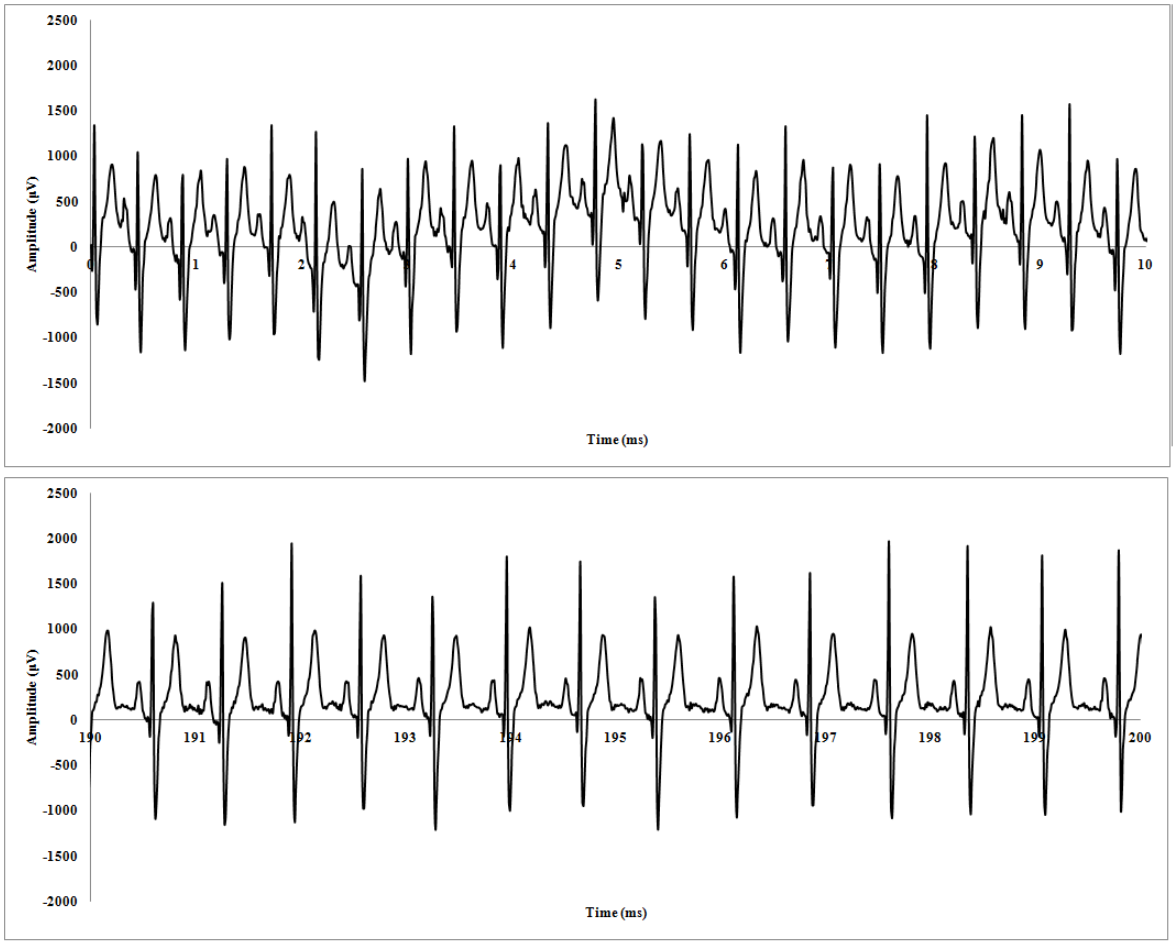


**Figure 5.33:** ECG signal of volunteer after exercise at position 2. From top to bottom: at the beginning of the measurement and in the middle

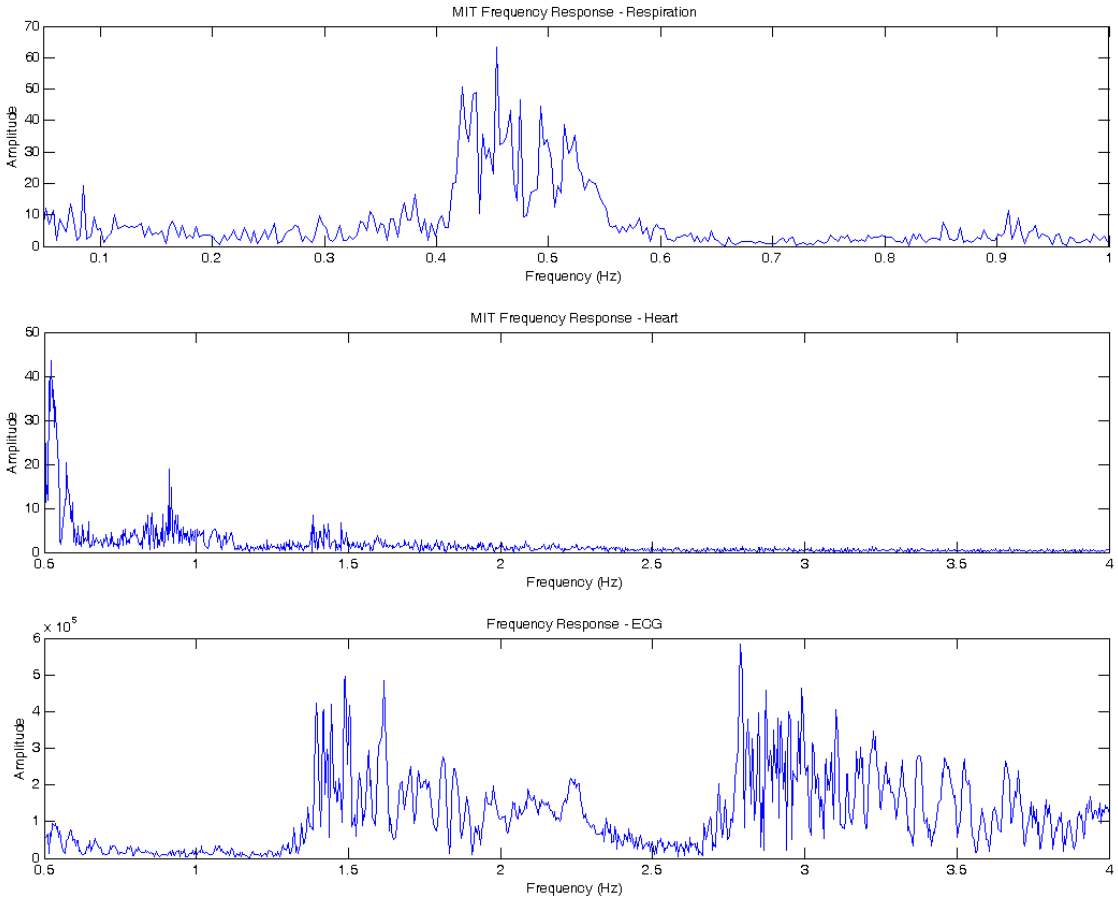


**Figure 5.34**: FFT spectrum of the MIT signal and the ECG signal after the exercise at position 2. From top to bottom: the MIT-breath signal FFT, the MIT-heart FFT and the ECG FFT.

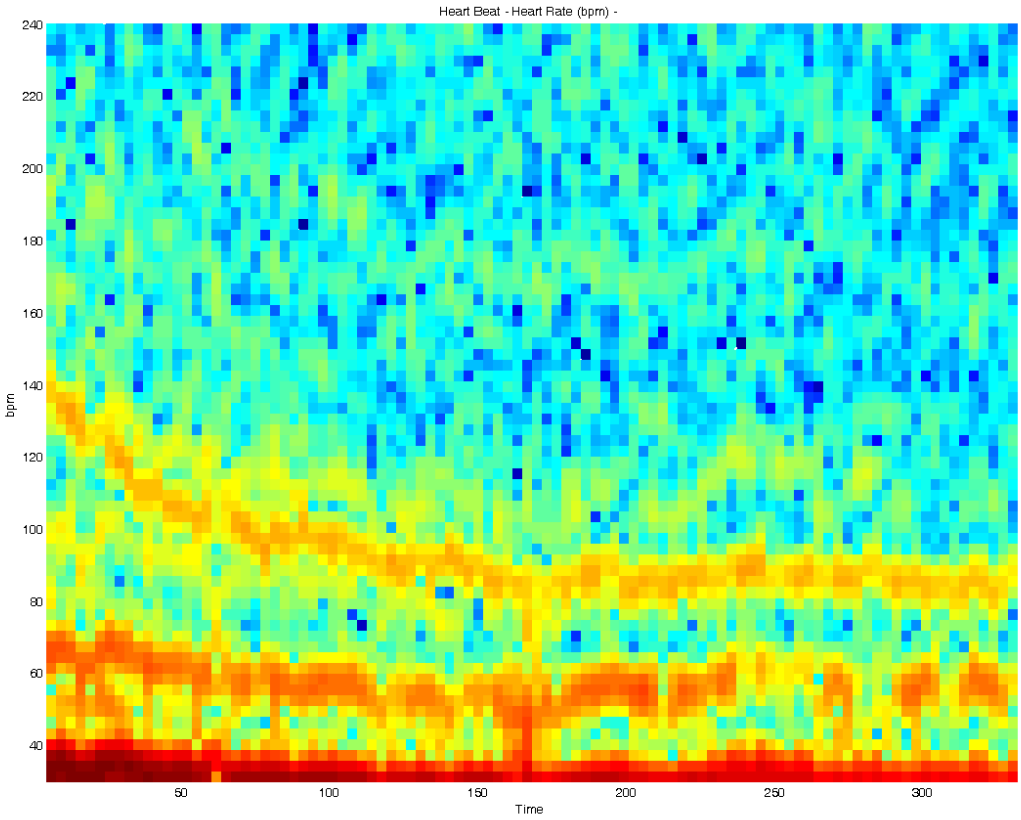


**Figure 5.35**: Heart rate spectrogram of the MIT signal after exercise at position 2

From figures 5.31 and 5.32 it can be seen that the system captured the variation in the breathing of the volunteer from deep breathing at the beginning of the measurement due to the exercise to the more normal breathing towards the end of the measurement.

The heart rate has been derived for comparison from the ECG signal (Figure 5.33) at the beginning and at the middle of the measurement by measuring the time difference between the R waves and was found to be 138 bpm and 84 bpm respectively. This compares well with the spectrogram in figure 5.35.

In figure 5.34 it can be seen that the MIT signal FFT below 1 Hz appears to have high frequency components from 0.42 Hz to 0.55 Hz which gives a variation of breath of 25-33 breaths per minute. This coincides well with the breath peaks appearing in figure 5.32.

Small amplitude signals are also observed in the MIT signal FFT at 1.5 Hz which appear to correlate well with the measured ECG. However the rapid breathing after the exercise produces significant higher frequency chest wall motion which overlaps and masks the cardiac frequency component in the MIT signal FFT.

The FFT of the ECG signal however can correlate with the information provided by the spectrogram in figure 5.35 for the MIT heart signal. The ECG signal FFT appears to have high frequency components from 1.4 Hz to 2.25 Hz which gives a variation of the heart rate from 84 to 140 breaths per minute. The heart variation is also shown in figure 5.33 of the ECG signal. This heart rate variation is illustrated in the spectrogram in figure 5.35.

#### 5.4.5.3 Breath pattern

The MIT signal of a human volunteer recorded during the breathing pattern measurement is shown in figure 5.36. The MIT-breath signal FFT, the MIT-heart FFT and the ECG FFT are shown in figure 5.37 and the spectrogram in figure 5.38.

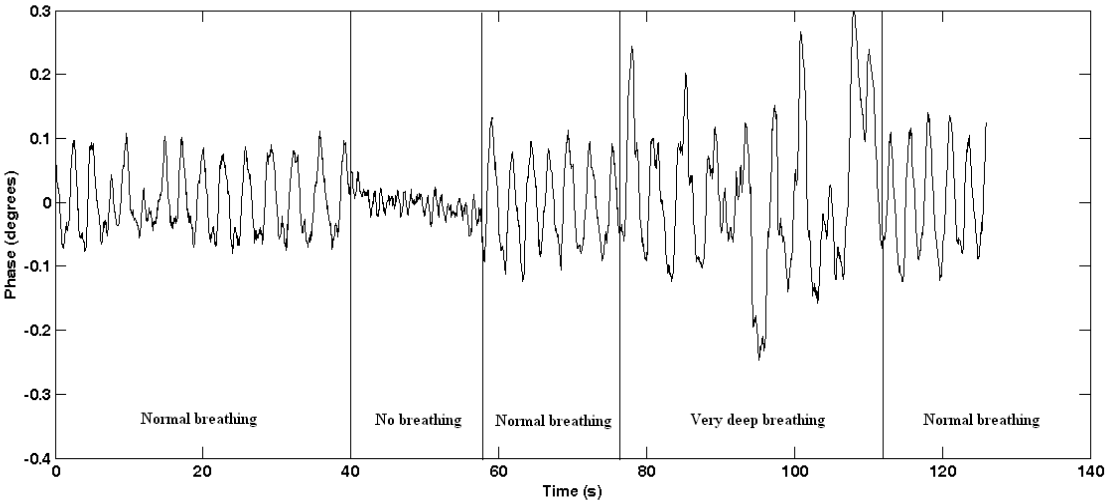


**Figure 5.36**: MIT signal of the breathing pattern at position 2

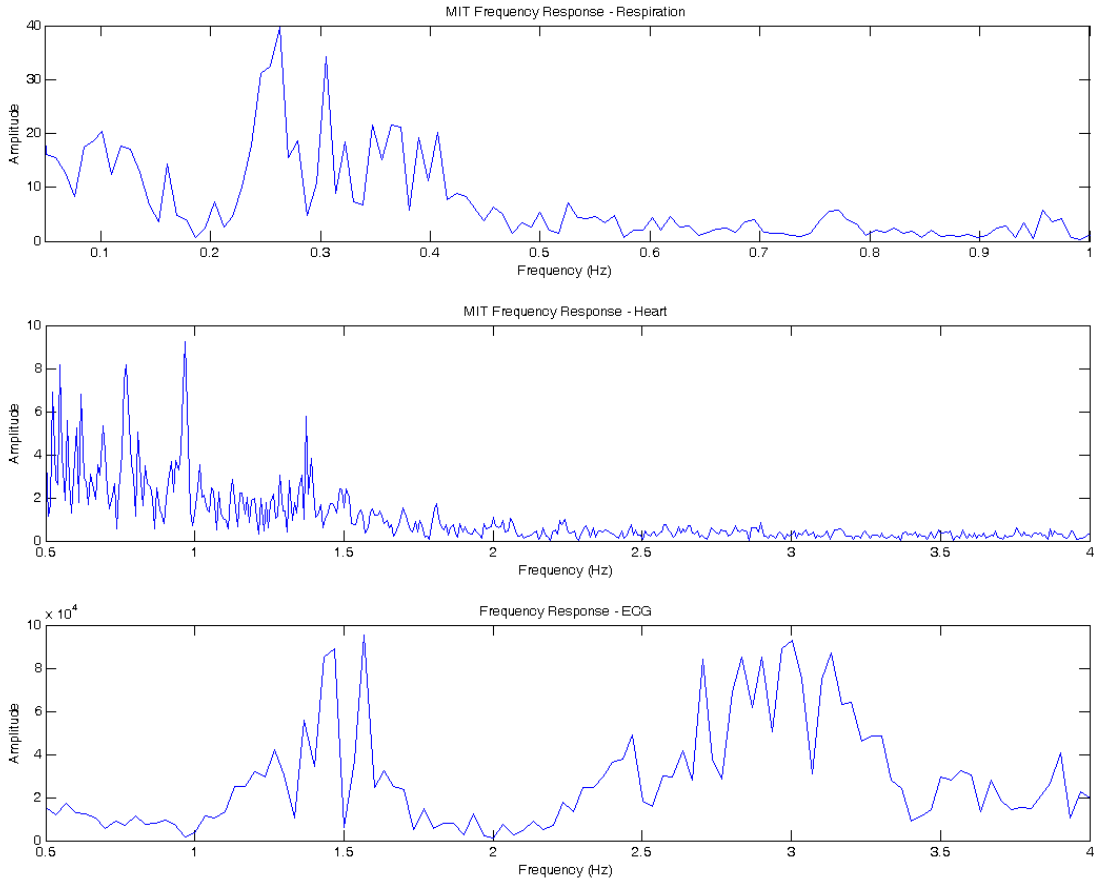


**Figure 5.37**: FFT spectrum of the MIT signal and the ECG signal of the breathing pattern at position 2

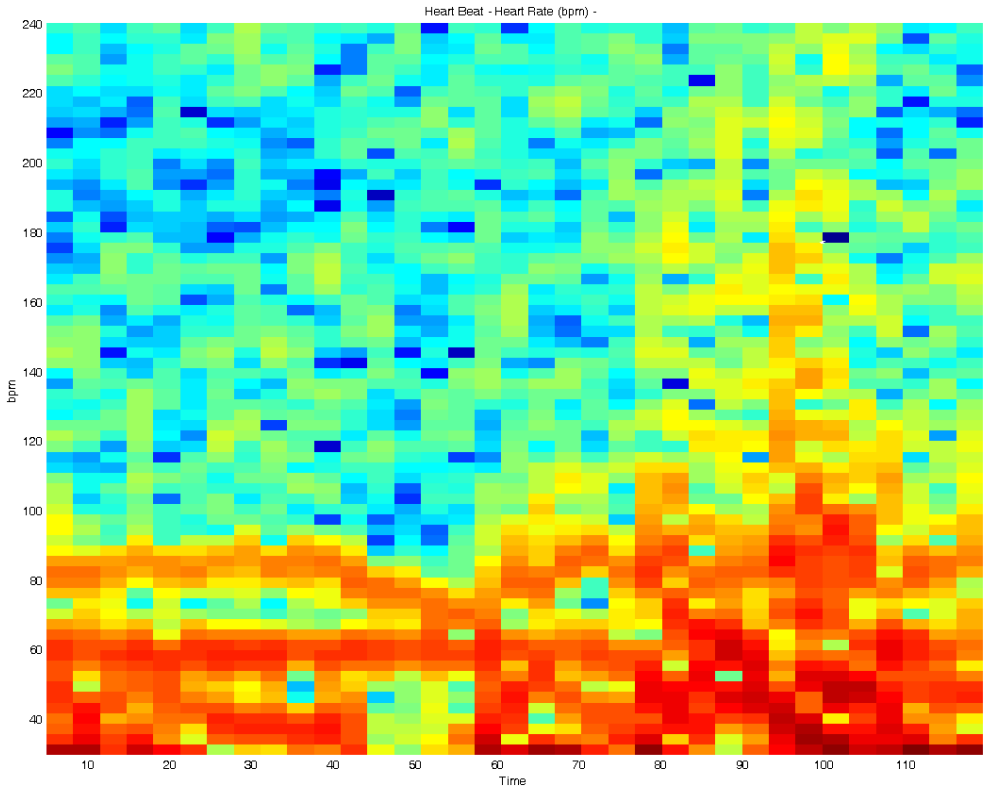


**Figure 5.38**: Heart rate spectrogram of the breathing pattern MIT signal at position 2

From figure 5.36 it can be seen that the system can capture the change between the normal breathing the absence of breathing and the deep breathing when occur sequentially.

In figure 5.37 it can be seen that the MIT signal FFT below 1 Hz appears to have high frequency components from 0.25 Hz to 0.39 Hz which gives a variation of breath of 15-23 breaths per minute.

However the rapid change in the breathing pattern and especially the physiological movement of the torso associated with the very deep breathing produces significant higher frequency components which overlaps and masks the cardiac frequency component in the MIT signal FFT as can be seen in figure 5.31. This is also clear in the spectrogram in figure 5.38.

### 5.4.6 Measurement results at detection coil position 3

This section presents a selected number of the analysed measurements taken at position 3.

#### 5.4.6.1 Normal breath

The MIT signal of a volunteer recorded during normal breathing measurement is shown in figure 5.39 and the ECG signal in figure 5.40. The MIT-breath signal FFT, the MIT-heart FFT and the ECG FFT are shown in figure 5.41 and the spectrogram in figure 5.42.

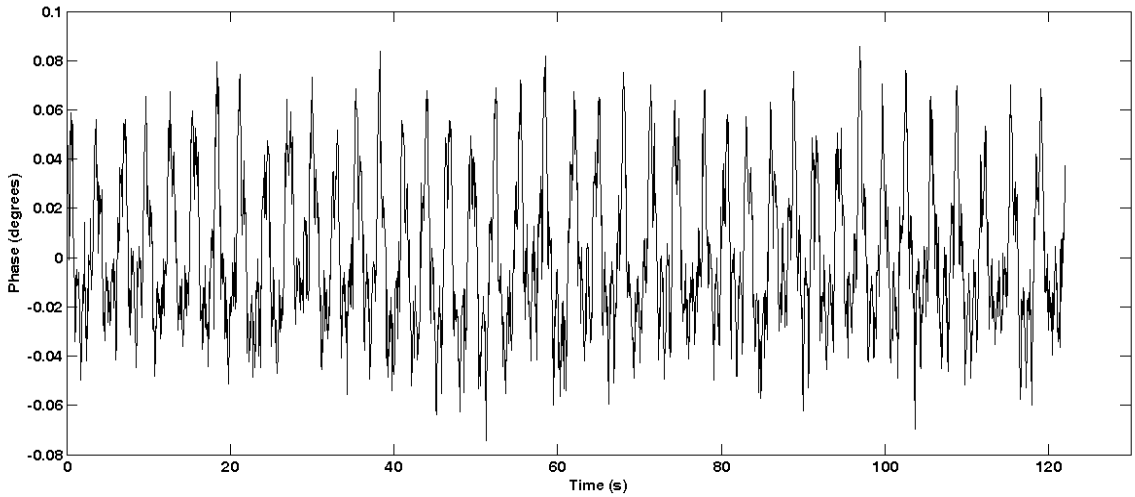


**Figure 5.39**: Normal breathing MIT signal at position 3

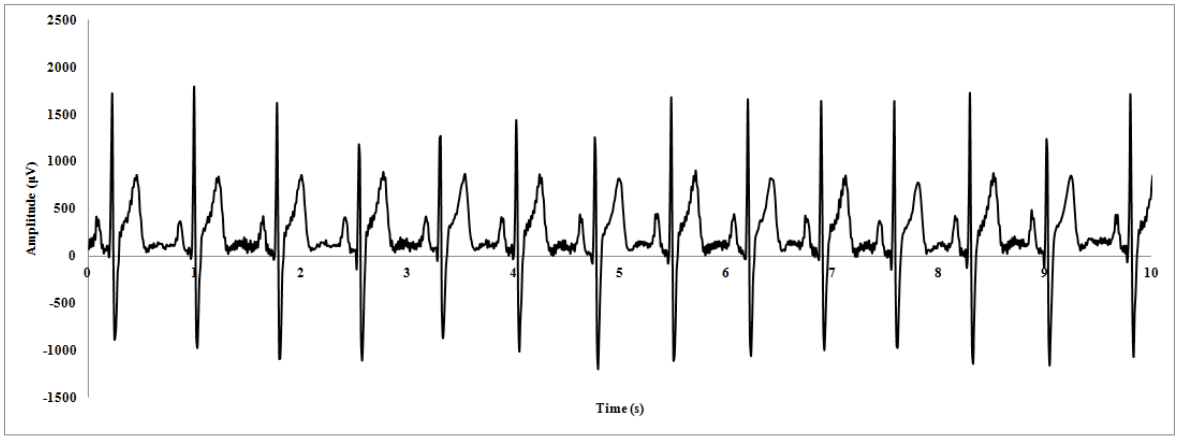


**Figure 5.40**: ECG signal of volunteer during normal breathing exercise at position 2

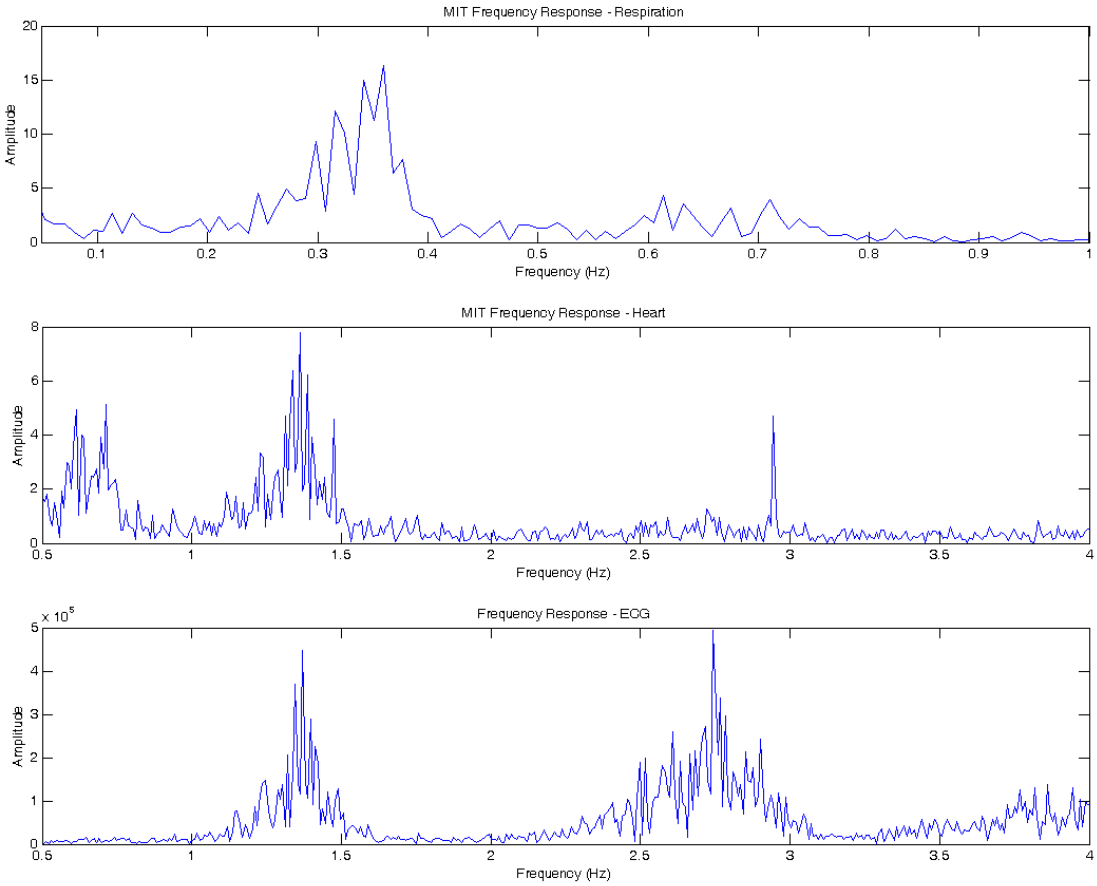


**Figure 5.41**: FFT of the MIT signal and the ECG signal during normal breathing at position 3

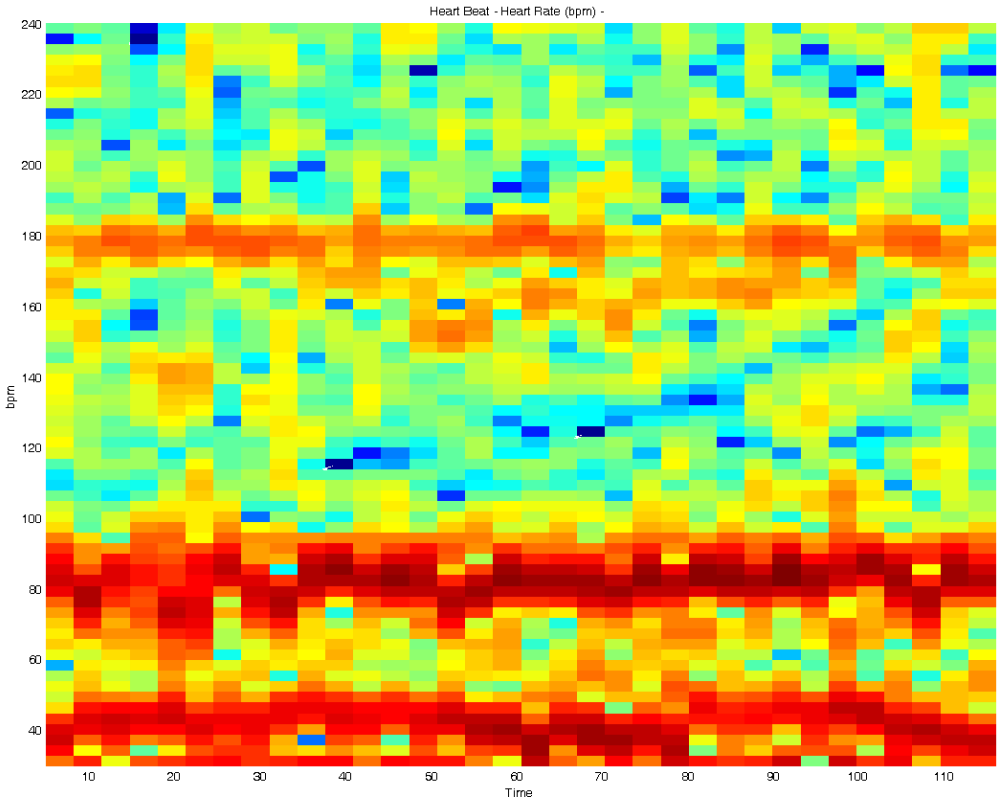


**Figure 5.42**: Heart rate spectrogram of the MIT signal during normal breathing at position 3

From figure 5.39 it can be seen that the signal has the same shape as the normal breathing MIT signals in positions 1 and 2. This shows the repeatability in the system's behaviour regarding the same input.

The heart rate has been derived for comparison from the ECG signal (Figure 5.40) by measuring the time difference between the R waves and was found to be 84 bpm.

In figure 5.41 it can be seen that the MIT signal FFT below 1 Hz appears to have the highest frequency components from 0.32 Hz to 0.36 Hz which gives a variation of breath of 19-21 breaths per minute. This variation corresponds well to the average rates expected in resting adults (12-20 breaths per minute).

From figure 5.41 it can be seen that for the MIT signal significant frequency components can be observed at 1.4 Hz and a smaller at 2.8 Hz. Corresponding frequency components are observed in the ECG signal strongly suggesting that the system is detecting cardiac motion. Significant noise components are observed at 0.5 Hz and 0.7 Hz in the MIT heart signal FFT due to respiration and physiological motion.

The spectrogram in figure 5.42 appears to show a clear cardiac trace between 80– 90 bpm. Significant noise is observed below 50 bpm however due to respiration and other physiological motion.

### 5.4.6.2 Breath pattern

The MIT signal of a male human volunteer recorded during the breath patter measurement is shown in figure 5.43. The MIT-breath signal FFT, the MIT-heart FFT and the ECG FFT are shown in figure 5.44 and the spectrogram in figure 5.45.

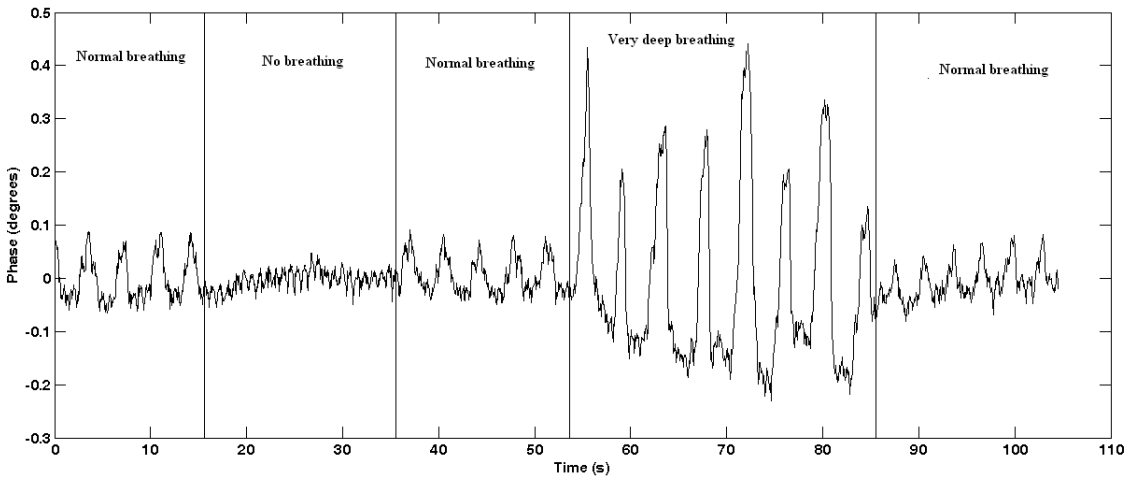


**Figure 5.43**: MIT signal of the breath pattern at position 3

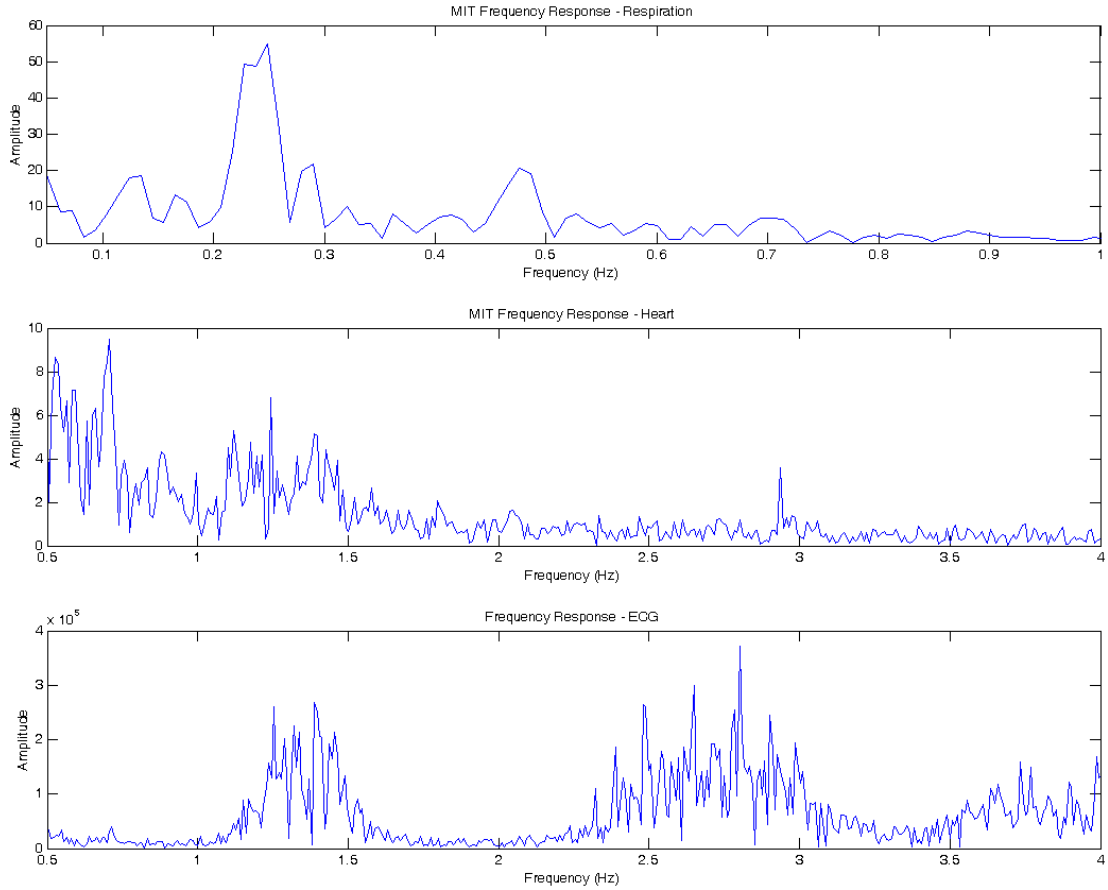


**Figure 5.44**: FFT spectrum of the MIT signal and the ECG signal during the breathing pattern at position 3

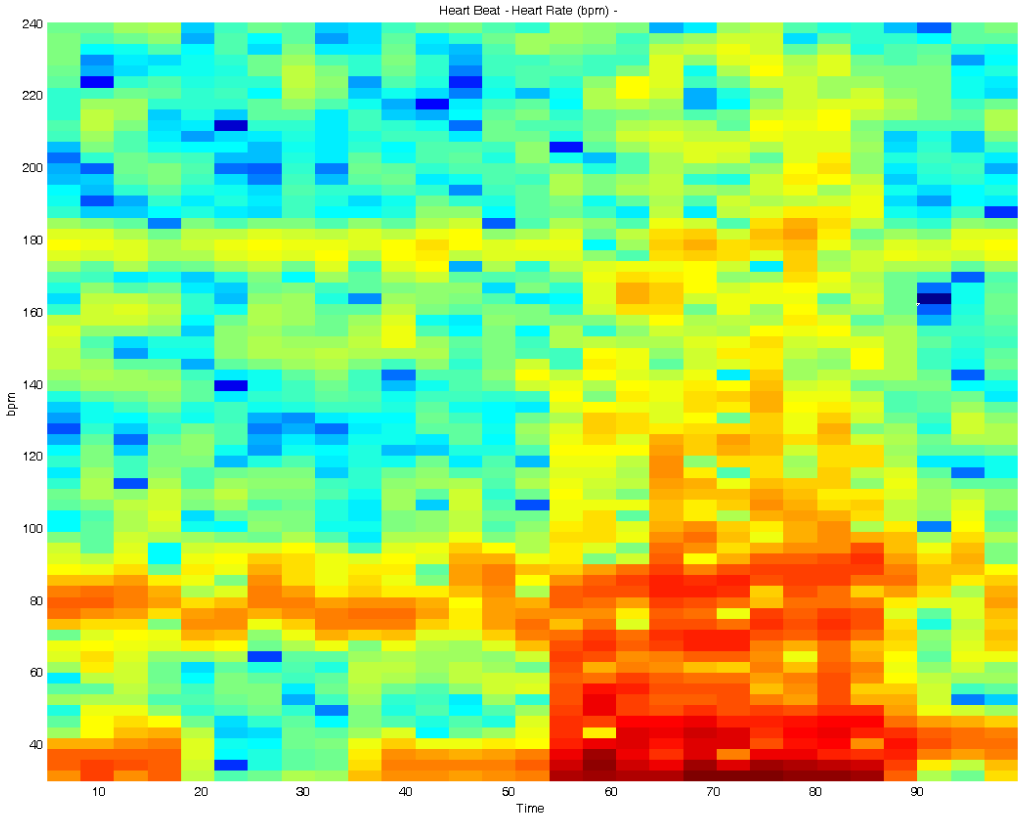


**Figure 5.45**: Heart rate spectrogram of the MIT signal during the breathing pattern at position 3

From figure 5.43 it can be seen that the system captured the breathing pattern much better than it did in position 2. This might be due to the smaller distance of the excitation coil from the volunteer (10 cm) than in position 2 (15 cm). Another possible explanation it can be that the excitation coil was situated on the side of the volunteer were the rip cage has thinner bones in comparison to the front.

In figure 5.44 it can be seen that the MIT signal FFT below 1 Hz appears to have high frequency components from 0.22 Hz to 0.23 Hz which gives a variation of breath of about 13 breaths per minute. This coincides well with the breath peaks shown in figure 5.36.

The rapid change in the breathing pattern and especially the physiological movement of the torso associated with the very deep breathing produces significant higher frequency components which overlaps and masks the cardiac frequency component in the MIT signal FFT as can be seen in figure 5.44. This is also clear in the spectrogram in figure 5.45.

## 5.5 Summary

The work performed in this chapter aimed to design, develop and characterise a practical single channel MIT system operating at 10 MHz for biomedical applications requiring a high data acquisition rate. The work aimed to realise the system and to use it for capturing the cardiac activity and the lung function of human volunteers in a contactless way.

In section 5.1 the background for the study was briefly examined and it was used to set the requirements for the system. The requirements were set to enable the targeting of the cardiac activity and the lung function.

In section 5.2 the design and the implementation of the system was presented. The design of the system was based on the knowledge and experience previously gained from the development of the single channel zero crossing subsystem (chapter 3) and of the Cardiff Mk2c (chapter 4). For the implementation of the system the existing hardware from the previous developments was used since there was not a need for developing new hardware.

In section 5.3 the characterisation of the system was given. The performance of the coil array was investigated and the results showed that the detected signal was 50 $mV_{pp}$ when the Π configuration. When the orthogonal configuration was used it increased to 60 $mV_{pp}$ due to the 8 cm decrease of the distance between the excitation coil and the detection coil.

The system achieved a phase precision of 4 millidegrees with a time constant of 50 ms and

a phase precision of 8 millidegrees with a time constant of 5 ms both at 30 $V_{pp}$ RF amplifier output. The maximum phase drift of the system was 313 millidegrees and the average phase drift was 205 millidegrees for a moving average of 10 for a measurement period of 2 hours. The increased observed drift does not consist a problem since high-pass filtering is employed for the processing of the measurements.

The recording rate achieved by the system was 200 phase difference values per second with the 5 ms time constant and 20 phase difference values with the 50 ms time constant.

In section 5.4 the measurements performed for the acquisition of the cardiac activity and the lung function were presented. For the cardiac activity the heart rate was targeted while for the lung function the detection of the lungs volume changes during breathing was primarily targeted and the respiration rate secondarily.

Furthermore to investigate the impact of the detection coil position to the capability of the system to acquire the measurements three test set-ups with different detection coil positioning were used. The sampling rate was set to 20 Hz since it was considered necessary to only prove the concept that the fundamental respiration and cardiac rate could be measured by the system. For the measurement analysis the FTT and the STFT were used. Four human volunteers participated in the measurements. To verify the heart rate results an ECG system was used in parallel to the Cardiff Mk2d. An independent monitoring of respiration was not used and thus the breathing was visually monitored.

The measurement results showed that the Cardiff Mk2d could detect the respiration and cardiac signals in normal breath and held breath measurements. For the post-exercise the respiration and cardiac signals were detected primarily with the spectrogram. The system detected the breathing pattern however it did not recorded the cardiac signal when the very deep breathing was used by the volunteers due to the physiological movement of the torso which overlapped and masked the cardiac frequency.

# 6. Discussion

The aim of this project was to investigate and develop practical and inexpensive high speed Magnetic Induction Tomography (MIT) instrumentation provide a solution to low conductivity applications requiring high data acquisition rate. To achieve this aim the previous research work conducted in the field of MIT was reviewed and the experimental areas for further research work were identified.

The requirements for a single and a multichannel zero crossing phase measurement subsystem were thoroughly reviewed and the most appropriate decisions were made during the development and implementation stages. Both systems were then characterised in terms of phase precision, phase drift and recording rate.

Two MIT systems were developed using the phase measurement systems and their performance were evaluated in two low conductivity applications: oil-in-water detection (multichannel) and the detection of the cardiac activity and lung function (single channel). After characterising each MIT system experiments were conducted with both applications. This chapter discusses the results of the investigations conducted during this study.

In section 6.1 the investigation of the theoretical aspects regarding the MIT system are discussed. These aspects formed the theoretical basis of the practical work for implementing the Cardiff Mk2c and the Cardiff Mk2d MIT systems. The investigations were based on the literature review findings.

In section 6.2 a discussion on the investigation regarding the Cardiff Mk2c is performed. The implementation and the characterisation results of the system are examined. The results of the flow experiments are discussed and conclusions are drawn. A comparison with other multichannel high frequency MIT systems is performed and the findings are critically examined.

In section 6.3 a discussion on the investigation for the Cardiff Mk2d is presented. The results of the implementation and the system characterisation are discussed. The results for the detection of the cardiac activity and the lung function are examined and the findings are critically discussed and compared to results from similar studies conducted with other MIT systems.

## 6.1 Theoretical aspects regarding the MIT system

In this section the theoretical aspects regarding the MIT system will be discussed.

### 6.1.1 The MIT architecture

The literature review conducted in chapter 2 showed that over the years four different MIT system architectures were proposed. The architectures were presented in [19], in [28], in [11] and in [30].

The architecture proposed in [19] regarded only the coil array as the MIT system. This approach in the author's opinion suffers greatly from the fact that the rest of the MIT system subsystems were not included. The coil array represents the sub-system that is used for the excitation and detection coils housing, the production of the primary electromagnetic field and the preprocessing of the detection signals. However it cannot be considered as a complete MIT system by itself because it lacks the two key components which are the phase measurement system and the image processing unit.

The architecture proposed in [28] included three subsystems which are the coil array, the signal conditioning electronics and the host computer. This approach suffers from the fact that it completely omitted a reference on the phase measurement subsystem which is a very important subsystem of an MIT system. Furthermore the term “host computer” does not define the use of that computer and it was left to the reader to assume its use from the text. Also the term “host computer” implied the use of a personal computer (PC) or similar which is not necessarily the case.

The description proposed in [11] included four subsystems which were the coil array, the signal conditioning electronics, the measurement system and the processing unit. Although this description addressed the main subsystems of the MIT system however it considered the signal conditioning electronics a subsystem which in this author opinion they are not. The signal conditioning electronics are either a part of the coil array (pre-amplifier) or a part of the phase measurement subsystem. Thus they can be considered as a module to the

subsystems but not a subsystem themselves.

The architecture description proposed in [30] includes a total of nine subsystems and was developed based on the Cardiff Mk2a MIT system. This approach suffers greatly from two problems. The first is the fact that this approach is in essence a design description of the Cardiff Mk2a system and not a description of a general MIT system architecture. This claim is supported by the fact that most subsystems included in the description were specific for the Cardiff Mk2a.

The second problem is that many of the architectural components used in the description were actually modules of the subsystems and not subsystems themselves. For example the Labview routines for controlling the coil array were considered in [30] as a subsystem. However in practise they were not a subsystem by themselves but they were a module of the coil array subsystem. These subroutines performed a secondary task amongst other secondary tasks either in parallel to them or in collaboration with them. Together all these secondary tasks realized the main task of the coil array subsystem.

Each of the four proposed architectural approaches suffered from inadequacies that prevented them from describing completely the architecture of a general MIT system. Therefore a new architecture description for MIT systems was required one which would use a clearer and a more descriptive terminology for the MIT subsystems. The new architecture was presented in chapter 4 of this thesis and the respective block diagram is repeated in figure 6.1.

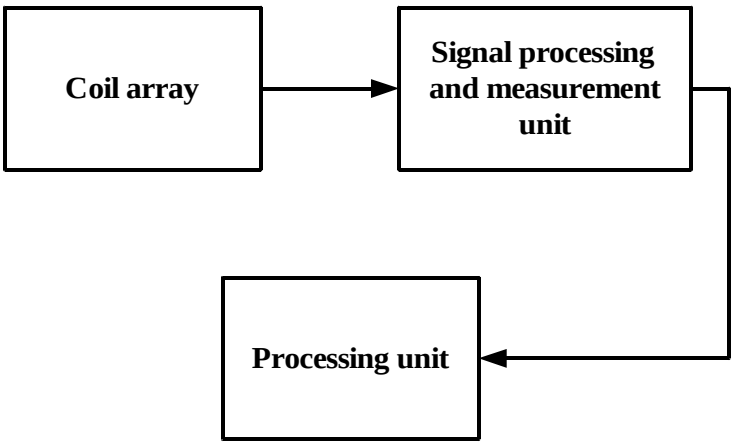


**Figure 6.1**: The proposed architecture for the MIT system

The proposed architecture was based on the realisation that the processes taking place in the MIT system can be used as a guide to describe its architecture. An MIT system in general performs three major procedures. It uses coils to generate the primary magnetic

field and to detect the secondary magnetic field, it uses electronics to process the signals from the coils and to measure their phase difference and it process the measurement data to construct a tomographic image or an indicator/indices. The block subsystems and their naming in the proposed architecture were selected to reflect these processes and to describe them in a literal but concise manner.

The MIT system architecture proposed in this thesis is the most complete to date compared to the MIT architectures previously proposed.

### 6.1.2 The MIT system frame rate

The speed of an MIT system is usually reported in the literature using two terms which are the time constant and the frame rate. The term time constant is used to denote the time required by a phase measurement subsystem or an MIT system to acquire a single phase difference value. [11]

The term frame rate is used to denote the time required by a multichannel MIT system to perform a complete set of measurements and output a result of all channel combinations. This terminology has been used extensively in the MIT field. [11]

However despite the importance of the frame rate for an MIT system an analysis of the factors affecting it and means to calculate it accurately during the design phase has not appeared in the literature yet.

Such analysis has been performed by the author of this thesis and it is given in chapter 4 (section 4.2.2). The analysis targeted the general multichannel MIT system and focused on the way the signals are processed through the system until a result is produced (tomographic image or indices). The parallel and the multiplexed signal processing chains were analysed thoroughly and all possible time delays that contribute into reducing the frame rate of an MIT system were identified.

The result of the analysis was a set of mathematical equations for calculating the maximum possible frame rate of a multiplexed or a parallel MIT system irrespective of the phase technique measurement used and the result it targets (tomographic image or indices).

### 6.1.3 Terminology used for the MIT system

#### 6.1.3.1 Consensus on terminology

From the literature review conducted in chapter 2 it emerged that at the moment there is

not a consensus on the terminology to use and the characteristics to disclose when comparing MIT systems. Thus most of the times each research group uses its own terminology and states the characteristics of an MIT system that show only the positive attributes of that system making the comparison between MIT systems difficult and sometimes impossible.

It is the authors' opinion that such consensus on the terminology and the disclosed characteristics is crucial to be established and maintained for three reasons. First it will provide the basis for meaningful comparisons of the MIT systems developed from different research groups. Second it will ease the development of new MIT systems which will address the weaknesses of the previous developed systems. Third it will help into the standardization of the MIT field knowledge and thus it will make it easier for other research groups to enter the field.

#### 6.1.3.2 Phase precision instead of phase noise

In a lot of publications presenting the implementation of MIT systems or phase subsystems the term phase noise was used to describe the short termed standard deviation of a number of phase measurements and it is given in degrees. In essence the phase noise term was used to denote the phase measurement precision of an MIT system or a phase subsystem. [11, 13, 21, 30, 37, 55]

However the term phase noise is also used in other scientific fields predominantly to describe the phase fluctuation caused by the frequency fluctuation and it is given in dBc/Hz. [47]

The phase noise affects the phase measurement precision of an MIT system however they are two entirely different quantities. The use of the same term to describe these two different quantities can be misleading and confusing. Especially when the intended use of the term in MIT is not correct.

The short termed standard deviation of a number of phase measurements is a statistical process whose figure acts as a determinant of the precision of the phase measurement performed by an MIT system. This is why it is given in degrees.

Thus it is proposed by the author of this thesis that the term phase precision describes the short termed standard deviation of a number of phase measurements better and without introducing confusion.

#### 6.1.3.3 Definition for the MIT system

From the authors' best knowledge a definition for the MIT system has not yet been stated. It is assumed that this most probably occurred because an MIT system is considered to be a tomographer and this was seemed to be a sufficient terminology.

However the term tomographer is very broad and has been used to describe Computed Tomography (CT) equipment to ultrasound machines (ultrasound tomographers). Without a doubt the term tomographer can be used to describe a capability of an MIT system but it is the authors' opinion that it is not the best description that can be used. Therefore a suitable definition for describing the MIT system could be the following.

“A Magnetic Induction Tomography system applies the principle of Magnetic Induction for producing a comprehensible measurement (numeric or tomographic image) of at least one of the passive electric properties of the object under study without having any physical contact with it.”

## 6.2 The Cardiff Mk2c system

The investigation for the Cardiff Mk2c system targeted the development of a fast multichannel MIT system for low conductivity industrial applications requiring high acquisition rate. The development of the Cardiff Mk2c system is presented in chapter 4.

An extensive literature review was conducted and is presented in chapter 2 to evaluate the phase measurement techniques that has been used in the MIT field in order to select which to use in the system. The review showed that a high excitation frequency multichannel system based on the zero crossing technique could potentially achieve a high frame rate.

To investigate the potential of the zero crossing technique a single channel phase measurement subsystem was developed and characterised. The development and characterisation of the subsystem are given in detail in chapter 3. At 10 MHz the subsystem achieved a phase precision of 12.5 millidegrees at 40 $mV_{pp}$ with a 5 ms time constant. The maximum phase drift figure at 10 MHz was 37 millidegrees over 5 hours.

The characterisation results showed that the single channel phase subsystem which was based on the zero crossing technique was fast and precise. A comparison f the subsystem developed in chapter 3 to other single channel subsystems is given in table 6.1.

**Table 6.1**: Comparison of single channel phase subsystems with time constant 20 ms or below

| Published by (authors) | Phase measurement technique | Time constant (ms) | Phase precision at lowest amplitude at 10 MHz | Maximum Phase drift over time period |
|---|---|---|---|---|
| Patz et al [60] | Direct digitisation | 6 | 7.5 millidegrees at 40 $mV_{pp}$ | 119 millidegrees over 6 hours |
| Watson et al [13] | Zero crossing | 20 | 22 millidegrees at 28 $mV_{pp}$ | 56 millidegrees over 20 minutes |
| Wei et al [61] | Direct digitisation | 6 | 4 millidegrees at 40 $mV_{pp}$ | 25 millidegrees over 5 hours |
| Subsystem in this thesis | Zero crossing | 5 | 12.5 millidegrees at 40 $mV_{pp}$ | 37 millidegrees over 5 hours |

From the table 6.1 it can be seen that the subsystem developed in this thesis compares well against single channel subsystems based on the direct digitisation.

The design of the Cardiff Mk2c required a thorough investigation on the factors affecting the frame rate of a multichannel MIT system to identify any factors that may reduce the frame rate and thus to minimise them as much as possible during the development. Most factors have been discussed before in the literature [11] and thus they were adopted.

However from the literature review it emerged that to complete the investigation an analysis on the factors affecting the signal processing chain and the time delays it could cause on the frame rate was required. Such analysis was not published in the literature therefore it was undertaken and it is presented in chapter 4.

One of the findings of the analysis was that a parallel MIT system will have a frame rate at least n times greater than the frame rate of a multiplexed MIT system if all factors are kept equal (where n is the number of the detection channels). Since speed was a major target for this study this finding created the requirement for the development of a parallel multichannel version of the single channel subsystem developed in chapter 3 to use as the signal processing and measurement unit (SPMU) in the Cardiff Mk2c.

The characterisation results of the SPMU showed that at 10 MHz it achieved a phase precision of 15 millidegrees at 40 $mV_{pp}$ with a time constant of 5 ms and an average maximum drift figure of 149 millidegrees over 5 hours. Since figures of multichannel phase measurement subsystems are not generally available in the literature a comparison of the SPMU to the single channel subsystems listed in table 6.1 shows that it drifts significantly. The drift of the SPMU may be due to the increased parasitic capacitance and inductance and lower cross-channel isolation on the multichannel pcb in comparison to the single channel version.

The characterisation of the complete Cardiff MK2c system at 10 MHz excitation frequency showed that the system can achieve a phase precision of 15 millidegrees with a time constant of 5 ms. The phase drift reached an averaged across all channels maximum drift figure of 259 millidegrees over 1 hour. The lowest channel maximum drift was 73 millidegrees and the highest was 530 millidegrees. The frame rate of the Cardiff Mk2c was 12.5 frames per second (fps) when the time constant was 5 ms was used and 2.2 fps when the time constant was 50 ms.

Overall the characterisation results show that the Cardiff Mk2c is a fast system which can provide frame rates in excess of 10 frames per second however the system suffers from significant drift. This could perhaps be controlled to a certain extend but it still is likely that drift will be significant over extended periods. The Cardiff Mk2c is therefore most suited to situations where the interest is in dynamic measurements i.e. to measure changes over short periods.

The system can be considered for industrial applications that require measurements where objects are moving in and out of the field of view of the system (with gaps for reference) such as objects on conveyor belts in food industry or an imaging metal detector.

Another industrial application that had been considered for the Cardiff Mk2c is the multi-phase flow (MPF) measurements in the oil pipes. Frame rates well in excess of 1 fps are likely to be necessary for this application and further to the speed the low conductivity nature of the application require the use of a high excitation frequency of 10 MHz. The Cardiff Mk2c characterisation results suggested that it complied with both requirements

To investigate practically the suitability of the Cardiff Mk2c for the MPF measurements application two flow experiments were conducted. The experiments are presented in chapter 4 and from the literature review and the author's best knowledge these flow experiments were not attempted before with an MIT system. The system was used with the 12.5 fps frame rate in both experiments.

For the first experiment a sealed glass bottle containing 250 ml of 3 S/m saline was used. The bottle was placed in an inclined water pipe (20 degrees inclination) and was pushed to slide downwards. The results show that the detected signal lasted only 200 ms however the system detected successfully the existence and the movement of the saline bottle through the pipe.

For the second experiment 250 ml of 3 S/m saline were poured in the opening of the upper part of the inclined water pipe and flowed out from the end of the pipe. The saline was observed to leave the bottle in small volumes but it was not possible to observe its flow in the water pipe. However the detected signal shows that the saline was flowing in volumes inside the pipe but most importantly it shows that the system can detect between different flowing volumes not only in amplitude but also in duration.

The system was observed to provide a peak SNR of 38.75 dB for the saline flow experiment and an SNR of 35.52 dB for the saline bottle experiment. It is expected that a better SNR can be achieved if a more powerful RF amplifier is used but also that the phase precision and the phase drift will be also benefited.

The two experiments demonstrated that the Cardiff Mk2c system can detect a small volume (250 ml) of 3 S/m saline as a volume and in free flow inside an inclined water pipe. Thus it is safe to state that the system will detect the stratified flow of sea water in a water pipe that is not inclined and taking into consideration the very low conductivity of oil it is safe to state that it can detect sea water in the presence of oil.

Comparing the two experiments conducted in chapter 4 to the experiment conducted in [29] where the Cardiff Mk1 was used for stratified flow detection it can be seen that the demand in terms of frame rate and saline volume detection were significantly higher in the experiments of this thesis. The successful completion of the two experiments by the Cardiff Mk2c proved that it is more suitable for MPF measurements than the Cardiff Mk1.

A comparison of the Cardiff Mk2c to other MIT systems with at least 10 MHz excitation frequency is given in table 6.2 based on the literature review presented in chapter 2.

**Table 6.2**: Comparison of multichannel MIT systems that used at least 10 MHz excitation frequency

| System | Scanner type | Channels | Phase technique | Frame rate (fps) | Average phase Precision (millidegrees) | Maximum Phase drift over all channels (millidegrees over time) |
|---|---|---|---|---|---|---|
| Cardiff Mk1 [29] | Annular | 16 | Vector-voltmeter | 0.011 | 17 | 800 over 48 minutes |
| Cardiff Mk2a [11] | Annular | 14 | Direct digitisation | 0.7 | 1 | 10 over 12 hours |
| Moscow [32] | Annular | 16 | Zero crossing | 1 | 246 | Not stated |
| Philips [67] | Annular | 16 | Downconverted direct digitisation | 0.5 (from [11]) | 80 | Not stated |
| Cardiff Mk2c | Annular | 8 | Zero crossing | 12.5 | 15 | 259 over 1 hour |

From the comparison in table 6.2 it can be seen that the 12.5 fps frame rate makes the Cardiff Mk2c the fasted multichannel tomographic high frequency MIT system until this thesis was submitted.

Furthermore the experiment results showed that the phase precision of the system is sufficient for the industrial applications it is targeted for.

Overall it can be stated that the Cardiff Mk2c fulfils the requirement for a fast system with excitation frequency of 10 MHz for low conductivity industrial applications. Furthermore the work performed for the design and the development of the Cardiff Mk2c can be used constructively by other researchers in the development of MIT systems with high frame rate.

## 6.4 The Cardiff Mk2d system

The investigation for the Cardiff Mk2d system targeted the development of a fast single channel MIT system for low conductivity biomedical applications requiring high acquisition rate. The development of the Cardiff Mk2d system is presented in chapter 5.

Two applications were targeted as proof of concept for the system. The applications were the detection of the cardiac activity and the detection of the lung function. For the cardiac activity the detection of the heart rate was targeted because it was considered to be a more achievable task than the ECG. For the lung function detection the primary target was to capture the lungs volume changes during breathing and a secondary target was the capture of the respiration rate. The Cardiff Mk2d system was the first zero crossing system in the MIT field that was used for detecting the heart rate and the respiration rate.

To investigate the capability of the Cardiff Mk2d for the cardiac activity and the lung function four measurement protocols were used. These were the normal breathing, the absence of breathing, the breathing pattern and the exercise. Four human volunteers participated in the measurements. The system configuration was tested in three different detection coil positions.

The results of the measurements showed that for resting subjects in normal breath and held breath measurements the Cardiff Mk2d system could detect both respiration and cardiac signals and the rates could be determined using FFT analysis and the spectrogram. This was possible because the much larger signals due to respiration well were separated in frequency from the smaller cardiac signals allowing both to be discriminated.

For post-exercise measurements however the MIT respiration signal was irregular and the cardiac signal could not be discriminated using the FFT analysis. However it could be discriminated using the spectrogram. In this case the respiration and exercise related chest wall motion overlapped with and dominated over the small cardiac signals masking them when FFT was applied.

The system detected the breathing pattern and distinguished between the alternate patterns of normal breathing, no breathing and very deep breathing however the cardiac signal could not be discriminated by the FFT or the spectrogram during the very deep breathing. The physiological movement of the torso associated with the very deep breathing overlapped and masked the cardiac frequency.

The very deep breathing noisy signal may require a different signal processing technique than what has been used like for example the wavelets. In general however further experimentation is required with the signal processing techniques to find the most suitable technique to use.

In the literature review it was shown that there is a small number of MIT systems that target the cardiac activity and the lung function due to increased sensitivity that is required. Most of the published system are single channels like for example [20, 121, 123]. However multichannel planar arrays have also been proposed [24, 42]. The Cardiff Mk2d system provided comparable performance to the multichannel planar arrays of [24] and [42] because they captured and processed both the cardiac signal and the respiration signal.

In [24] the measurement of the normal breathing of a human volunteer was given. The signal captured was similar to the normal breathing captured by the Cardiff Mk2d system. Information on the respiration rate were not given. The system in [24] was further developed in [68] and the cardiac signal and the respiration signal were captured. However the heart rate and the respiration rate where not disclosed. In comparison the signal processing from the Cardiff Mk2c measurements provided the heart rate and the respiration rate in all protocols apart when the very deep breathing was used.

In [42] the cardiac signal and the respiration signal were captured. The main purpose of the measurements was to capture the ECG pulse. However to capture the cardiac signal the human volunteer had to stop breathing during the measurement. Obviously this was a shortcoming of the system since for real world applications the voluntary absence of breathing would not be a common situation. The heart rate and the respiration rate were not

recorded however it is not clear if the system could measure them or not. The Cardiff Mk2c on the other hand could detect the cardiac signal while the volunteer was breathing and provided the heart rate and the respiration rate apart for very deep breathing.

A possible disadvantage of the Cardiff Mk2d is that it employs coils on either side of the subject for the Π configuration which may be less practical in comparison to the planar arrays in [24] and [42]. However the experimental use of the Cardiff Mk2 orthogonal configuration (Γ configuration) showed that it rectifies the disadvantage of the Π configuration without degrading its performance.

Overall it can be stated that the Cardiff Mk2d fulfils the requirement for a fast single channel MIT system with excitation frequency of 10 MHz for low conductivity biomedical applications. The Cardiff Mk2d is a very simple, cheap and robust system but at the same time is fast and of better performance compared to the multichannel planar arrays described in [24] and [42] as the experimental results show.

# 7. Conclusions and further work

This chapter presents the conclusions of the study in section 7.1 and provides recommendations for further work in section 7.2.

## 7.1 Conclusions

The primary aim of this project was to investigate and develop practical and inexpensive high speed Magnetic Induction Tomography (MIT) instrumentation to provide a solution to low conductivity applications requiring high data acquisition rate. All aspects of the problem definition in section 1.1 were covered in this study and the objectives of this research project outlined in section 1.2 were achieved.

The literature review has shown that high speed MIT instrumentation is required for low conductivity industrial and biomedical applications that require high acquisition rates. Such instrumentation was not available when this study begun.

The work presented in this study have demonstrated the design, the development, the implementation and the characterisation of a high speed multichannel MIT system targeting low conductivity industrial applications and a single channel MIT system targeting low conductivity biomedical applications. Their performance for the applications intended have been proved with experiments and measurements especially designed to test their capability of performing the intended tasks.

This clearly shows that the study has achieved its main objective and that the original work described in this thesis represents a significant contribution to knowledge in the field of Magnetic Induction Tomography.

The investigation in this study led to the following conclusions:

- Magnetic Induction Tomography requires high precision, high speed instrumentation to reach routine use in the industry and the clinical setting. This

study has addressed both points and has shown that such high speed and precise MIT instrumentation can be designed, developed and realised in the context of MIT.

- The design and the development of multichannel high frequency MIT systems for low conductivity applications with a frame rate in excess of 10 frames per second and high precision in the order of 15 millidegrees can be achieved. The work performed in this study for the design and the development of the Cardiff Mk2c has shown that such system can be realised and that it can target real life low conductivity applications such as the multiphase flow measurements.

- The design and the development of low cost MIT instrumentation targeting low conductivity biomedical applications such as the monitoring of the heart rate and the respiration rate can be achieved. Existing systems [24, 42] suffered from being multichannel and thus more costly and/or being only able to detect one of the two at the same time. This study has shown that the Cardiff Mk2d MIT system is capable of measuring both the heart rate and the respiration rate with a single channel at the same time. This was supported by measurements on human volunteers.

- This study showed that the zero crossing technique is suitable for high frequency MIT systems for the use in low conductivity applications. It further showed that such systems can be fast, precise and low cost. To date existing systems cannot achieve all three attributes at the same time.

- At the moment there is not a consensus on the terminology used and the characteristics to disclose when comparing MIT systems in the field of MIT. This study has identified the problem which hampers the evolution of the MIT field and has brought it into attention for further actions. A more generic MIT architecture was proposed alongside with a new terminology for characterising MIT systems phase precision. These proposed changes provide a better basis for discussions in the MIT field.

## 7.2 Further work arising from the project

This study has shown that the design and the development of high speed multichannel high frequency precise Magnetic Induction Tomography instrumentation can be achieved.

During the investigation existing instrumentation has been used in a new way and new instrumentation has been developed and realised. From the literature review and the investigations in this study the following recommendations are given for future research work in this field:

- Investigation and development of a phase drift compensation scheme for the Cardiff MK2c and Cardiff MK2d systems. Such scheme will allow the use of the systems for extended time period without small phase difference value drifting.

- Evaluation of faster relay devices for the excitation chain. This would enable an increase in the frame rate for the Cardiff Mk2c system.

- Investigation into the use of a dual excitation frequency scheme for the Cardiff MK2c and Cardiff MK2d systems. This will permit the use of the system for applications that are now restricted due to their monotonic nature.

- Investigate if a multi channel version of the Cardiff Mk2d system for biomedical applications would provide more information while keeping the cost low.

- Improve the signal processing and filtering currently used in the Cardiff MK2d system to achieve better separation of the cardiac and respiration signals

- Investigate the possibility of connecting a real time processing unit to the Cardiff MK2c for producing tomographic images in real time and to the Cardiff MK2d systems for real time calculation and display of the heart rate, the respiration rate and the subject's breathing pattern.

- Investigation of different signal processing algorithms to improve the detection of the heart and respiration rate in the Cardiff Mk2d system.

# Appendix 1

## A1.1 The heterodyne technique of frequency shifting

The aim of the heterodyne technique is to shift the frequency of a sinusoidal signal to a lower or a higher frequency. To achieve this the signal is mixed with another sinusoidal signal of different frequency. Their product is a signal which has a low frequency component created by subtracting the two sinusoidal signals and a high frequency component created by adding them. In MIT the use of the heterodyne technique is focused on the downconversion of the excitation and the detection sinusoidal signals.

As it is the case in MIT two sinusoidal signals $y_1(t)=A_1\sin(\omega_1 t+\varphi_1)$ and $y_2(t)=A_2\sin(\omega_2 t+\varphi_2)$ are applied at the inputs of a non linear device such as a mixer or a multiplier which results to [158]

$$y_1(t)\,y_2(t)=A_1\sin(\omega_1 t+\varphi_1)\,A_2\sin(\omega_1 t+\varphi_2) \qquad \text{(A1.1)}$$

From trigonometry it is known that

$$sinA\,sinB=\frac{1}{2}[\cos(A-B)-\cos(A+B)] \qquad \text{(A1.2)}$$

and thus combining (A1.1) and (A1.2) gives [158]

$$y_1(t)\,y_2(t)=\frac{A_1A_2}{2}[\cos((\omega_1-\omega_2)-(\varphi_1-\varphi_2))t-\cos((\omega_1+\omega_2)+(\varphi_1+\varphi_2))t] \qquad \text{(A1.3)}$$

To downconvert the signal to the required frequency the sum frequency component $\cos((\omega_1+\omega_2)(\varphi_1+\varphi_2))t$ is removed using low pass filtering and thus the difference component $[\cos((\omega_1-\omega_2)(\varphi_1-\varphi_2))t]$ remains. [158]

# Appendix 2

## A2.1 Electrical Capacitance Tomography

The Electrical Capacitance Tomography (ECT) is used for determining the dielectric permittivity distribution of the interior of an object using capacitance measurements. An ECT tomographic system comprises of an annular coil array, the processing electronics which includes the capacitance measuring circuit and a computer for the image processing. The coil array incorporates the measurement electrodes which must be sufficiently large to provide a change in capacitance. Typical electrode configurations include 8 or 12 electrodes. [71, 78, 159]

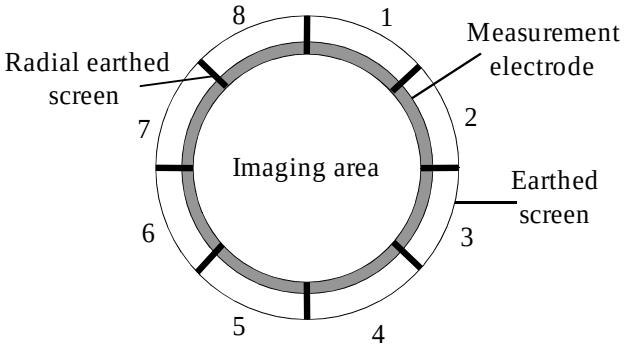


**Figure A2.1**: An 8-electrode ECT coil array (from [71])

Provided that the electrical field inside the measurement plane does not enclose free electrical charge the relationship between the capacitance and the permittivity distribution is governed by

$$\nabla \cdot [\varepsilon(x,y) \nabla \varphi(x,y)] = 0 \qquad \text{(A2.1)}$$

where $\nabla$ is the gradient operator, ε(x,y) is the permittivity distribution in the sensing field, φ(x,y) is the electrical potential distribution, and

$$C = \frac{Q}{V} = \frac{-1}{V} \int \int_{\Gamma} \varepsilon(x, y) \nabla \varphi(x, y) \, d\Gamma \qquad \text{(A2.2)}$$

where V is the potential difference between two electrodes forming the capacitance and Γ is the electrode surface.

During a measurement when one electrode is excited with a fixed voltage $V_o$ and all the other electrodes are kept at zero potential the boundary conditions are defined by $\varphi = V_o$ for the excited electrode and $\varphi = 0$ for the rest electrodes.

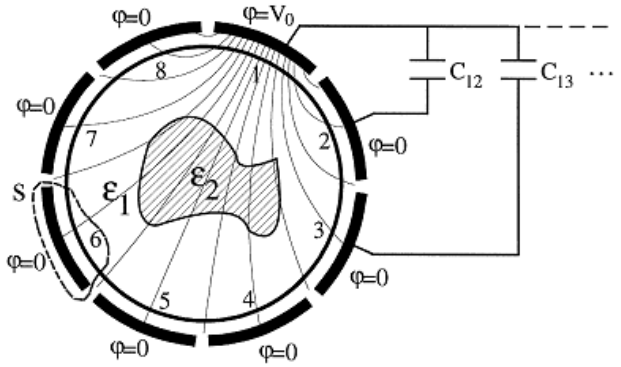


**Figure A2.2**: The ECT measurement principle (from [78])

The electrodes are excited one after the other and the capacitance values between the excitation electrode and the rest of the electrodes is measured. Thus for N electrodes the number of independent measurements M is given by [78]

$$M = \frac{N(N-1)}{2} \qquad \text{(A2.3)}$$

## A2.2 Electrical Resistance Tomography

The Electrical Resistance Tomography (ERT) is used for determining the distribution of the conductivity of the interior of an object [71, 78]. The architecture of an ERT system resembles the architecture of an ECT system. However here is a difference in the application because for MPF measurements the electrodes of the ERT system must come into direct contact with the sample [71].

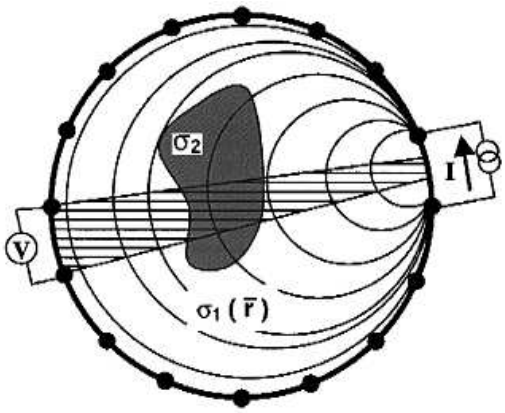


**Figure A2.3:** The ERT measurement principle
(from [78])

Similar to ECT the measurement plane in ERT can be approached as an electrostatic field problem and thus the relationship between the impedance and the conductivity distribution is given by

$$\nabla\cdot[\sigma(x,y)\nabla\varphi(x,y)]=0 \qquad \text{(A2.4)}$$

where $\nabla$ is the gradient operator, σ(x,y) is the conductivity distribution in the sensing field, φ(x,y) is the electrical potential distribution.

During a measurement in an ERT system the current is induced between one pair of adjacent electrodes and the differential potentials between the remaining pairs of adjacent electrodes are measured [71, 78]. This procedure is repeated for all pairs of adjacent electrodes until a full rotation is completed. Thus for N electrodes the number of independent measurements M is given by [78]

$$M=\frac{N(N-3)}{2} \qquad \text{(A2.5)}$$

## A2.3 Electrical Impedance Tomography

Electrical Impedance Tomography is an imaging technique in which currents are injected into the object using surface electrodes and the resulting electrical potentials created are measured by the remaining electrodes in relevance to the ground. An image of the conductivity or the permittivity distribution of the object is constructed based on these measurements. [116]

The electric potential u for an object with impedance Ω is given by [114]

$$\nabla\cdot(\sigma\nabla u)=0 \qquad \text{(A2.6)}$$

where σ is the conductivity.

For a point x of the object the electric potential is given by [160]

$$\nabla \cdot \gamma(x,\omega)\nabla u = 0 \qquad \text{(A2.7)}$$

The admittance γ is given by [160]

$$\gamma(x,\omega) = \sigma(x,\omega) + i\,\omega\,\varepsilon(x,\omega) \qquad \text{(A2.8)}$$

where σ is the conductivity, ε is the permittivity and ω is the angular frequency of the applied current.

The solution of the equations is not straightforward and mathematical models for their solution have been proposed [160, 161]. However the details of these proposed solutions escape the scope of this appendix and will not be examined further. To perform an EIT measurement a set of electrodes is placed on the surface of the object. In Table A1.1 three methods for injecting the current in an object and the resultant number of independent measurements is given.

**Table A2.1**: Some EIT measurement methods (summarized from [114])

| EIT measurement method | Independent measurements M for N electrodes | Graphical illustration |
|---|---|---|
| Neighbouring:<br>The current is applied through neighbouring electrodes and the voltage is measured successively from all other adjacent electrode pairs. | $M = \frac{N(N-3)}{2}$ | 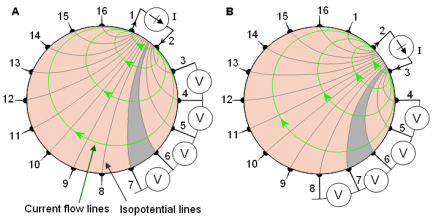 |
| Opposite:<br>The current is injected through two diametrically opposed electrodes. The electrode adjacent to the current-injecting electrode is used as the voltage reference. Voltage is measured from all other electrodes except from the current electrodes | $M = (\frac{N}{2}) \times (N-3)$ | 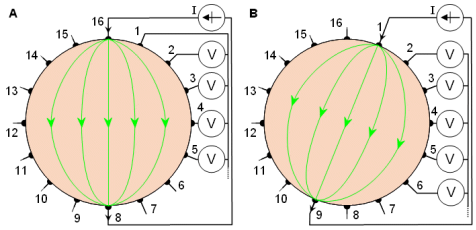 |
| Adaptive:<br>The current is injected through all electrodes and the voltages are measured with respect to a single grounded electrode. | $M = (\frac{N}{2}) \times (N-1)$ | 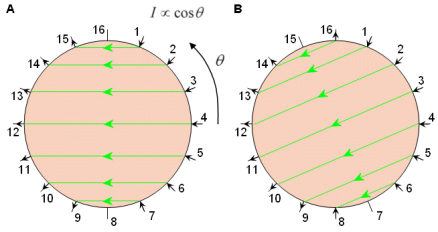 |

# Appendix 3

## A3.1 Data of the dielectric properties of some thorax tissues in the frequency range from 10 Hz to 100 MHz

The data were calculated using an online database [90] which is based on the work of Gabriel et al as published in [82, 91-93].

**Table A3.1**: Conductivity of thorax tissues and components from 10 Hz to 100 MHz

| Frequency (Hz) | Heart | Blood | Breast fat | Lung deflated | Lung inflated | Muscle | Dry skin |
|---|---|---|---|---|---|---|---|
| 1.00E+01 | 0.05368 | 0.7 | 0.015473 | 0.20279 | 0.038904 | 0.20197 | 0.0002 |
| 1.58E+01 | 0.05829 | 0.7 | 0.01849 | 0.20399 | 0.047175 | 0.20479 | 0.0002 |
| 2.51E+01 | 0.06657 | 0.7 | 0.020878 | 0.20484 | 0.057254 | 0.21122 | 0.0002 |
| 3.98E+01 | 0.0775 | 0.7 | 0.022256 | 0.20531 | 0.065574 | 0.22405 | 0.0002 |
| 6.31E+01 | 0.08731 | 0.7 | 0.022921 | 0.2056 | 0.070525 | 0.24424 | 0.0002 |
| 1.00E+02 | 0.09357 | 0.7 | 0.023239 | 0.20588 | 0.072979 | 0.26671 | 0.0002 |
| 1.58E+02 | 0.09685 | 0.7 | 0.023431 | 0.20635 | 0.074208 | 0.28446 | 0.0002 |
| 2.51E+02 | 0.09869 | 0.7 | 0.023611 | 0.20723 | 0.07506 | 0.29644 | 0.0002 |
| 3.98E+02 | 0.10029 | 0.7 | 0.023812 | 0.20887 | 0.076044 | 0.30557 | 0.0002 |
| 6.31E+02 | 0.10254 | 0.7 | 0.024016 | 0.21162 | 0.077488 | 0.31381 | 0.0002 |
| 1.00E+03 | 0.1063 | 0.7 | 0.024192 | 0.21567 | 0.079538 | 0.32115 | 0.0002001 |
| 1.58E+03 | 0.11227 | 0.7 | 0.024329 | 0.22078 | 0.082105 | 0.32709 | 0.0002002 |
| 2.51E+03 | 0.12068 | 0.7 | 0.024437 | 0.22642 | 0.08493 | 0.33162 | 0.0002003 |
| 3.98E+03 | 0.13106 | 0.7 | 0.024525 | 0.2321 | 0.08777 | 0.33517 | 0.0002008 |
| 6.31E+03 | 0.1425 | 0.7 | 0.024603 | 0.23759 | 0.090516 | 0.33813 | 0.0002018 |
| 1.00E+04 | 0.15421 | 0.7 | 0.024676 | 0.2429 | 0.093172 | 0.34083 | 0.0002041 |
| 1.58E+04 | 0.16587 | 0.7001 | 0.024747 | 0.24816 | 0.095796 | 0.34348 | 0.0002093 |
| 2.51E+04 | 0.17752 | 0.7002 | 0.024819 | 0.2535 | 0.098458 | 0.34633 | 0.0002213 |
| 3.98E+04 | 0.18939 | 0.7005 | 0.024892 | 0.25907 | 0.10123 | 0.34973 | 0.0002486 |
| 6.31E+04 | 0.20178 | 0.7012 | 0.024968 | 0.26504 | 0.10416 | 0.35442 | 0.0003107 |
| 1.00E+05 | 0.21511 | 0.7029 | 0.025048 | 0.27161 | 0.10735 | 0.36185 | 0.0004513 |
| 1.58E+05 | 0.22992 | 0.7068 | 0.025135 | 0.27914 | 0.11089 | 0.37456 | 0.0007677 |

| Frequency (Hz) | Heart | Blood | Breast fat | Lung deflated | Lung inflated | Muscle | Dry skin |
|---|---|---|---|---|---|---|---|
| 2.51E+05 | 0.24714 | 0.7155 | 0.025234 | 0.28825 | 0.11498 | 0.39591 | 0.0014735 |
| 3.98E+05 | 0.26827 | 0.7336 | 0.025354 | 0.2999 | 0.11998 | 0.42745 | 0.0030248 |
| 6.31E+05 | 0.295 | 0.7679 | 0.025517 | 0.31521 | 0.12663 | 0.46549 | 0.006355 |
| 1.00E+06 | 0.32753 | 0.8221 | 0.025757 | 0.33438 | 0.13609 | 0.50268 | 0.013237 |
| 1.58E+06 | 0.36303 | 0.8906 | 0.026112 | 0.35586 | 0.14968 | 0.53413 | 0.026628 |
| 2.51E+06 | 0.39811 | 0.959 | 0.026586 | 0.37743 | 0.16758 | 0.55951 | 0.050427 |
| 3.98E+06 | 0.432 | 1.0164 | 0.027119 | 0.39805 | 0.18778 | 0.58063 | 0.087776 |
| 6.31E+06 | 0.46594 | 1.0612 | 0.027624 | 0.41799 | 0.20745 | 0.59931 | 0.1383 |
| 1.00E+07 | 0.50137 | 1.0967 | 0.02806 | 0.43799 | 0.22524 | 0.61683 | 0.19732 |
| 1.58E+07 | 0.5394 | 1.1267 | 0.028435 | 0.45872 | 0.24144 | 0.63398 | 0.25883 |
| 2.51E+07 | 0.58084 | 1.1538 | 0.028777 | 0.4807 | 0.25689 | 0.65126 | 0.31906 |
| 3.98E+07 | 0.62638 | 1.1798 | 0.029116 | 0.50436 | 0.27236 | 0.66901 | 0.37713 |
| 6.31E+07 | 0.67676 | 1.2058 | 0.029489 | 0.53018 | 0.28846 | 0.68761 | 0.43399 |
| 1.00E+08 | 0.733 | 1.233 | 0.02996 | 0.55882 | 0.30569 | 0.70759 | 0.49122 |

**Table A3.2**: Permittivity of thorax tissues and components from 10 Hz to 100 MHz

| Frequency (Hz) | Heart | Blood | Breast fat | Lung deflated | Lung inflated | Muscle | Dry skin |
|---|---|---|---|---|---|---|---|
| 1.00E+01 | 23562000 | 5260 | 11855000 | 5497100 | 32248000 | 25700000 | 1136 |
| 1.58E+01 | 21194000 | 5260 | 7339100 | 3342500 | 24817000 | 24977000 | 1136 |
| 2.51E+01 | 16948000 | 5260 | 3766600 | 1860000 | 15765000 | 23337000 | 1136 |
| 3.98E+01 | 11344000 | 5260 | 1714500 | 1080700 | 8304100 | 20065000 | 1136 |
| 6.31E+01 | 6323600 | 5260 | 744930 | 724840 | 3891800 | 14944000 | 1136 |
| 1.00E+02 | 3163700 | 5260 | 327610 | 567080 | 1772400 | 9329000 | 1135.9 |
| 1.58E+02 | 1589400 | 5260 | 152700 | 489090 | 851660 | 5110200 | 1135.9 |
| 2.51E+02 | 890070 | 5260 | 76888 | 436230 | 462170 | 2700400 | 1135.9 |
| 3.98E+02 | 585780 | 5259 | 40688 | 383740 | 289410 | 1461800 | 1135.8 |
| 6.31E+02 | 440940 | 5259 | 21575 | 321940 | 199860 | 803540 | 1135.7 |
| 1.00E+03 | 352850 | 5259 | 11228 | 252050 | 141510 | 434930 | 1135.6 |
| 1.58E+03 | 280860 | 5258 | 5797.7 | 183070 | 97700 | 231160 | 1135.4 |
| 2.51E+03 | 213770 | 5257 | 3035 | 124820 | 64862 | 123590 | 1135.2 |
| 3.98E+03 | 153690 | 5255 | 1639.3 | 81752 | 41850 | 68552 | 1134.8 |
| 6.31E+03 | 105290 | 5252 | 922.86 | 52691 | 26731 | 40496 | 1134.3 |
| 1.00E+04 | 70054 | 5248 | 543.13 | 34044 | 17174 | 25909 | 1133.6 |
| 1.58E+04 | 46157 | 5241 | 333.78 | 22305 | 11212 | 18055 | 1132.4 |
| 2.51E+04 | 30566 | 5230 | 213.6 | 14912 | 7478.4 | 13634 | 1130.8 |
| 3.98E+04 | 20534 | 5212 | 142.07 | 10202 | 5110.1 | 11009 | 1128.4 |
| 6.31E+04 | 14064 | 5179 | 98.18 | 7153.5 | 3582.8 | 9324.4 | 1124.7 |
| 1.00E+05 | 9845.8 | 5120 | 70.61 | 5145.3 | 2581.3 | 8089.2 | 1119.2 |
| 1.58E+05 | 7048.7 | 5012 | 52.951 | 3793.8 | 1914 | 6973.4 | 1110.7 |
| 2.51E+05 | 5147.6 | 4811 | 41.418 | 2855 | 1461.5 | 5749.1 | 1097.5 |

| Frequency (Hz) | Heart | Blood | Breast fat | Lung deflated | Lung inflated | Muscle | Dry skin |
|---|---|---|---|---|---|---|---|
| 3.98E+05 | 3799.9 | 4450 | 33.657 | 2166.9 | 1146.7 | 4354.1 | 1076.6 |
| 6.31E+05 | 2780.4 | 3857 | 28.106 | 1622.9 | 916.75 | 2962.4 | 1043.3 |
| 1.00E+06 | 1967.3 | 3026 | 23.656 | 1170.5 | 733.18 | 1836.4 | 990.76 |
| 1.58E+06 | 1335.4 | 2106 | 19.57 | 806.15 | 569.73 | 1082.7 | 910.86 |
| 2.51E+06 | 888.12 | 1319 | 15.627 | 539.91 | 417.52 | 636.43 | 797.78 |
| 3.98E+06 | 596.28 | 777.8 | 12.156 | 362.71 | 286.16 | 386.74 | 655.39 |
| 6.31E+06 | 411.45 | 456.9 | 9.5653 | 250.57 | 188.08 | 248.48 | 501.75 |
| 1.00E+07 | 293.47 | 280 | 7.8933 | 180.32 | 123.66 | 170.73 | 361.66 |
| 1.58E+07 | 216.56 | 184.6 | 6.9027 | 135.81 | 84.238 | 125.8 | 251.88 |
| 2.51E+07 | 165.38 | 132.7 | 6.3334 | 107.07 | 60.584 | 99.06 | 175.02 |
| 3.98E+07 | 130.77 | 103.6 | 6.0044 | 88.183 | 46.232 | 82.708 | 124.76 |
| 6.31E+07 | 107.11 | 86.84 | 5.8097 | 75.594 | 37.318 | 72.482 | 92.935 |
| 1.00E+08 | 90.816 | 76.82 | 5.6903 | 67.108 | 31.64 | 65.972 | 72.929 |

The relative permittivity is given by $\varepsilon/\varepsilon_0$ where $\varepsilon_0$ is the permittivity of vacuum and it is equal to $8.854\times10^{-12}$ F/m.

# Appendix 4

## A4.1 The LABWINDOWS/CVI computer application software code

```
/*-------------------------------------------------------------------------------------------------------
TITLE: Single channel system GUI
CREATED BY: Georgios Panagi
PURPOSE: To communicate with the single channel system in the FPGA through RS232 port
FEATURES:
1. Controls the RS232 port - set the baud rate, parity, stop bits, data bits
2. Read the data recorded by the system
3. Calculates the phase difference between the detection channel and the excitation channel
4. Time stamps and stores the calculated phase value into a predefined text file
-------------------------------------------------------------------------------------------------------*/
#include <rs232.h>
#include <utility.h>
#include <formatio.h>
#include <cvirte.h>
#include <userint.h>
#include "single_channel_gui.h"
static int panelHandle;

int     Time_measur1,byte_read1,byte_read2,byte_read3,byte_read4,
        byte1,byte2,byte3,byte4,RS232err,Sample_Freq,fpgafreq,
        file_handle,xor_pulse_val,dirselectstatus,filenamestatus,
        pathstatus, comport;

char    totstring1[100], result [150],endresult[200],prj_dir[260],FileNameToWrite[60],
        WriteFileName[60],PathName[260];
```

```
double  phase1;
//---------------------------------------------------------------------------------------------------------
// MAIN FUNCTION
int main (int argc, char *argv[]) {
        if (InitCVIRTE (0, argv, 0) == 0)
                return -1;    /* out of memory */
        if ((panelHandle = LoadPanel (0, "single_channel_gui.uir", PANEL)) < 0)
                return -1;
        DisplayPanel (panelHandle);
        RunUserInterface ();
        DiscardPanel (panelHandle);
        return 0; }
//---------------------------------------------------------------------------------------------------------
// CLOCK PERIOD FUNCTION - Function for calculating the clock pulse from frequency
double xclock() {
        double tclock;
        GetCtrlVal (panelHandle, PANEL_FPGAFREQ, &fpgafreq);
        tclock = (1.0/fpgafreq);
        return (tclock); }
//---------------------------------------------------------------------------------------------------------
// PHASE CALCULATION FUNCTION - Function for calculating the phase
double phasecalc (int M, int N) {
        double calc1,ttclock;
        char tclockstr [30];
        ttclock = xclock();
        GetCtrlVal (panelHandle, PANEL_DOWNCONVFREQ, &Sample_Freq);
        calc1= M*ttclock*360*Sample_Freq/N;
        return (calc1); }
//---------------------------------------------------------------------------------------------------------
// SET THE DIRECTORY
int CVICALLBACK SETDIRBUTTONCallBack (int panel, int control, int event, void
*callbackData, int eventData1, int eventData2) {
        switch (event)     {
                case EVENT_COMMIT:
```

```
                    // Select the directory to save your work
                    dirselectstatus = DirSelectPopup ("c:\\", "Select Directory", 1, 1, prj_dir);
                    Delay (0.5);

                    // Name the file
                    filenamestatus = PromptPopup ("FILE NAME","Enter data file name
                    (No extensions)", FileNameToWrite, 50);

                    //Add the extension
                    Fmt(WriteFileName, "%s<%s.txt",FileNameToWrite);

                    // Make the path to follow
                    pathstatus = MakePathname (prj_dir, WriteFileName, PathName);

                    // Write the path to the textbox
                    ResetTextBox (panelHandle, PANEL_TEXTBOX1, "");
                    InsertTextBoxLine (panelHandle,PANEL_TEXTBOX1,-1,PathName);
                    break;}
        return 0; }
//---------------------------------------------------------------------------------------------------------
// DATA ACQUISITION, PROCESSING AND CALCULATION FUNCTION
int dataproc (int byte1,int byte2,int byte3,int byte4) {
        // turn the bytes into a string
        Fmt(totstring1,"%s<x[w2p0]%x[w2p0]%x[w2p0]%x[w2p0]",
        byte4,byte3,byte2,byte1);

        // Turn the string into integer
        Scan(totstring1,"%s>%x", &Time_measur1);

        // Calculate the phase for each channel
        phase1 = phasecalc(Time_measur1,xor_pulse_val);

        // Turn the results of the phase calculations into one string
        Fmt(result, "%s<%f[p3] ", phase1);
        Fmt(endresult,"%s<%s   %s",TimeStr(),result);

        // write the string of the phase calculation results to the txt file
        WriteLine (file_handle, endresult, -1);
```

```
        return 0;}
//---------------------------------------------------------------------------------------------------
// CONSTANT CHECK ON THE COM PORT
/* This function is initiated by InstallComCallback in the STARTBUTTONCallback. The
InstallComCallback constantly monitors the COM port and waits for the data to appear at
the port. When the data appears then it raises the flag LWRS_RECEIVE and it executes
the function ComCallBack. */

void ComCallback(int COMport, int eventMask, void *callbackdata){
        if (LWRS_RECEIVE) {
                // Read the bytes from the comport
                byte_read1 = ComRdByte (comport);
                byte_read2 = ComRdByte (comport);
                byte_read3 = ComRdByte (comport);
                byte_read4 = ComRdByte (comport);

                // Call the data acquisition, processing and calculation function
                dataproc (byte_read1,byte_read2,byte_read3,byte_read4); }}
//---------------------------------------------------------------------------------------------------
int CVICALLBACK STARTBUTTONCallBack (int panel, int control, int event,  void
*callbackData, int eventData1, int eventData2) {
        switch (event)     {
                case EVENT_COMMIT:
                        // Read the value of the XOR pulses from the GUI
                        GetCtrlVal (panelHandle, PANEL_XORPULSEVAL, &xor_pulse_val);

                        // open the txt file
                        file_handle                                                    =
OpenFile(PathName,VAL_WRITE_ONLY,VAL_APPEND,
                        VAL_ASCII);

                        //Open the comport
                        RS232err = OpenComConfig (1, devicename, 115200, 0, 8, 1, 3000,
                        3000);

                        // COMCALLBACK
```

```
                InstallComCallback (1, LWRS_RECEIVE, 4, 0, ComCallback, NULL);

                break;}
        return 0;}

//---------------------------------------------------------------------------------------------------
int CVICALLBACK QuitCallback (int panel, int control, int event, void *callbackData, int
eventData1, int eventData2) {
        switch (event) {
                case EVENT_COMMIT:
                CloseCom (1);
                QuitUserInterface (0);
                break;}
        return 0; }
```

# Appendix 5

## A5.1 Air circular coil inductance calculation

The inductance of an air circular coil can be calculated by the Wheeler formula which is

$$L = \frac{N^2 D^2}{18\mathrm{D} + 40\mathrm{H}} \qquad \text{(A5.1)}$$

where L is the coil inductance, D is the coil diameter and H is the coil height.

However the Wheeler formula does not take into account the diameter of the wire and it is assumed that there is no space between the coil windings.

## A5.2 Air circular coil self resonance frequency calculation

The self resonance frequency of the an air circular coil can be calculated by

$$\omega = \frac{1}{\sqrt{LC}} \qquad \text{(A5.2)}$$

where L is the coil inductance and C is the coil capacitance.

## A5.3 Air rectangular coil inductance calculation

The inductance of an air rectangular coil can be calculated by [152]

$$L_{rect} = N^2 \frac{\mu_0 \mu_r}{\pi} \left[ -2(w+h) + 2\sqrt{h^2+w^2} - h \ln\left(\frac{h+\sqrt{h^2+w^2}}{w}\right) - w \ln\left(\frac{w+\sqrt{h^2+w^2}}{h}\right) + h \ln\left(\frac{2h}{a}\right) + w \ln\left(\frac{2w}{a}\right) \right] \qquad \text{(A5.3)}$$

# Appendix 6

## A6.1 The MATLAB code

### A6.1.1 Function for loading the files

```
function [MITData, ECGData]=load_signals(DataPath)
old_dir=pwd;            % Save old directory
%    Get MIT File names
eval (['cd ', DataPath, 'MIT\']);   % Change to directory
eval('MITnames=dir');               % get Names
eval(['cd ', old_dir]);             % change back to old directory
 eval (['cd ', DataPath, 'ECG\']);   % Change to directory
eval('ECGnames=dir');               % get Names
eval(['cd ', old_dir]);             % change back to old directory

 if (length(MITnames)==length(ECGnames))  % check if equal number of files
        for k=3:length(MITnames)        % Loop through the file name list
                MITFile=MITnames(k).name    % start with index 3 as 1 & 2 are '.' & '..'
                ECGFile=ECGnames(k).name
                MITData = load([DataPath, 'MIT\', MITFile],'-ASCII'); %Loads in MIT data
                ECGData = load([DataPath, 'ECG\', ECGFile],'-ASCII'); %Loads in ECG data
                ind=find(MITFile == '_');   % Find separater
                Name=MITFile(1:ind-1);      % extract file name
                figure
                FFT_heartlung (MITData, ECGData, Name) % FFT the data
        end
else
        disp('Unequal number of signal files!!')
end
```

### A6.1.2 Function for heart signal extraction from MIT signal

```
function [y,df]= ExtractHeart (MITHeartData)
FirstWindowSize=80;    % Extract Movement
SecondWindowSize=15;   % Smooth extracted movement
ThirdWindowSize=30;     % Smooth Time-Domain Signal
offset=0;

Start=1;
d=MITHeartData;
df=filter(ones(1,FirstWindowSize)/FirstWindowSize, 1, d);   % Extract
dff=filter(ones(1,SecondWindowSize)/SecondWindowSize, 1, df); % Smooth
len=length(d);
new_len=(FirstWindowSize+SecondWindowSize); % Length of startup values
x=1:(len-(FirstWindowSize+SecondWindowSize-1))-offset; % x-axis adjusted to remove
startup values

d_adj=d(new_len:len-offset);
df_adj=df(new_len:len-offset);
dff_adj=dff((new_len+offset):len);

length (df_adj)
length (dff_adj)

length(x)
length(d_adj)

sub=d_adj-dff_adj;
L=length(sub);
tsub= (1:L)/19.6;

subplot (3,1,1);
plot(tsub,sub)
xlim([0 60])
xlabel('Time (s)')
ylabel('Phase (degrees)')

subplot (3,1,2);
```

```
plot(tsub,sub)
xlim([140 200])
xlabel('Time (s)')
ylabel('Phase (degrees)')

subplot (3,1,3);
plot(tsub,sub)
xlim([280 340])
xlabel('Time (s)')
ylabel('Phase (degrees)')

y=sub;
```

### A6.1.3 Function for breathing signal extraction from MIT signal

```
function [y]= ExtractBreath (MITData)
 FirstWindowSize=200;    % Extract Movement
SecondWindowSize=50;   % Smooth extracted movement
ThirdWindowSize=10;     % Smooth Time-Domain Signal

d=MITData;
df=filter(ones(1,FirstWindowSize)/FirstWindowSize, 1, d);   % Extract
dff=filter(ones(1,SecondWindowSize)/SecondWindowSize, 1, df); % Smooth
len=length(d);
new_len=(FirstWindowSize+SecondWindowSize); % Length of startup values
x=1:len-(FirstWindowSize+SecondWindowSize-1); % x-axis adjusted to remove startup
                                                % values
d_adj=d(new_len:len);
df_adj=df(new_len:len);
dff_adj=dff(new_len:len);

length(x)
length(d)

sub=d_adj-dff_adj;
length(sub)

y=filter(ones(1,ThirdWindowSize)/ThirdWindowSize, 1, sub); % Smooth TD
```

### A6.1.4 Function for FFT

```
function FFT_heartlung (MITData, ECGData, Name)

% Extract the Breathing and Heart signals from the MIT trace
MITBreathData=ExtractBreath (MITData);
MITHeartData=ExtractHeart (MITData);

FR = 19.6; %The frame rate used for the measurement - frames per second
fSamplingMIT = FR;%Calculate the sampling frequency
tSamplingMIT = 1/fSamplingMIT;%Calculate the sampling time

%Prepare the MIT Breath signal variables
NBreathsamps = length(MITBreathData);%Measure the length of the data set
tBreathMIT = (1:NBreathsamps)/ fSamplingMIT;%Prepare time data for plot
%Prepare freq data for plot
fBreathMIT = fSamplingMIT*(0:NBreathsamps/2-1)/NBreathsamps;

%Prepare the MIT signal Heart variables
NHeartsamps = length(MITHeartData);  % Measure the length of the data set
tHeartMIT = (1:NHeartsamps)/ fSamplingMIT;  %Prepare time data for plot
%Prepare freq data for plot
fHeartMIT = fSamplingMIT*(0:NHeartsamps/2-1)/NHeartsamps;

%Prepare the time domain variables
Nsamps = length(MITData);  % Measure the length of the data set
tMIT = (1:Nsamps)/ fSamplingMIT;  %Prepare time data for plot

% ECG
fSamplingECG = 100;%Sampling Frequency
tSamplingECG = 1/fSamplingECG;%Sampling Time
ECGNsamps = length(ECGData);  % Measure the length of the data set
tECG = (1:ECGNsamps)/ fSamplingECG;  %Prepare time data for plot
%Prepare freq data for plot
fECG = fSamplingECG*(0:ECGNsamps/2-1)/ECGNsamps;

%MIT Breath signal FFT
MITBreathData_fft = abs(fft(MITBreathData)); %Retain Magnitude
```

```
%Discard Half of Points
MITBreathData_fft = MITBreathData_fft(1:NBreathsamps/2);

%MIT Heart signal FFT
MITHeartData_fft = abs(fft(MITHeartData)); %Retain Magnitude
%Discard Half of Points
MITHeartData_fft = MITHeartData_fft(1:NHeartsamps/2);

%ECG FFT
ECGData_fft = abs(fft(ECGData)); %Retain Magnitude
ECGData_fft = ECGData_fft(1:ECGNsamps/2);%Discard Half of Points

% Plot STFT
Plot_BPM(MITHeartData, ['Heart Rate (bpm) - ', Name],FR)

% Plot the MIT Breath signal Frequency Domain
% subplot(3,1,1)
% plot(fBreathMIT, MITBreathData_fft)
% %plot(fshift, abs(MIT_Data_fft))
% xlim([0.05 1])
% xlabel('Frequency (Hz)')
% ylabel('Amplitude')
% title('MIT Frequency Response - Respiration')

% Plot the MIT Heart signal Frequency Domain
% subplot(3,1,2)
% plot(fHeartMIT, MITHeartData_fft)
% %plot(fshift, abs(MIT_Data_fft))
% xlim([0.5 4])
% xlabel('Frequency (Hz)')
% ylabel('Amplitude')
% title('MIT Frequency Response - Heart')

% Plot the ECG Frequency Domain
% subplot(3,1,3)
% plot(fECG, ECGData_fft)
% xlim([0.5 4])
```

```
% xlabel('Frequency (Hz)')
% ylabel('Amplitude')
% title('Frequency Response - ECG')

% Plot the Time Domain ECG signal
% subplot(4,1,1)
% plot(tECG, ECGData)
% xlabel('Time (s)')
% ylabel('Amplitude (microVolts)')
% title('Time domain - ECG')

% Plot the Time Domain MIT plot
% subplot(4,1,2)
% plot(tMIT, MITData)
% xlabel('Time (s)')
% ylabel('Phase (degrees)')
% title(['Time domain - MIT ', Name])
```

### A6.1.5 Function for STFT

```
function Plot_BPM(y, Name, FR)
%This function requires the following inputs,
% y - input signal
% Name - Name of the signal trace
% FR - Frame Rate

figure
F=0.5:0.05:4;   % in 3 bpm steps
[Y,F,T,P]=spectrogram(y,192, 128, F,FR,'yaxis');
surf(T,F*60,10*log10(abs(P)), 'EdgeColor','none');
axis xy; axis tight; colormap(jet); view(0,90);
xlabel('Time');
ylabel('bpm');
title(['Heart Beat - ', Name]);
```

# Bibliography

[1] Merriam-Webster Online Dictionary."Tomography." Internet: http://www.merriam-webster.com/dictionary/tomography, [27 Apr., 2011]

[2] Merriam-Webster Online Dictionary."Graphy." Internet: http://www.merriam-webster.com/dictionary/graphy, [27 Apr., 2011]

[3] Compact Oxford English Dictionary."Tomography." Internet: http://www.askoxford.com/concise_oed/tomography?view=uk, [27 Apr., 2011]

[4] University of Leeds."What is Tomography?." Internet: http:// www.leeds.ac.uk/olil/tomography/WhatIsTomography.php, [24 Jun., 2011]

[5] R. Shroy, M. VanLysel, M. Yaffe, I. Cunningham, P. Judy, S. Conolly, A. Macovski, J. Pauly, J. Schenck, K. Kwong, D. Chesler, X. Hu, W. Chen, M. Patel, K. Ugurbil, B. Croft, B. Tsui, R. Goldberg, S. Smith, J. Mottley, K. Ferrara, X. Zhou, G. Johnson, T. Budinger, H. VanBrocklin, D. Barber, W. Greenleaf and T. Piantanida. "Section 7: Imaging," in *The Biomedical Engineering Handbook*, 2nd ed., vol. 1. Joseph D. Bronzino (Ed.) (Ed.). Ed Boca Raton: CRC Press LLC, 2000,

[6] University of Manchester."Industrial Process Tomography at Manchester." Internet: http://www.tomography.manchester.ac.uk, [27 Apr., 2011]

[7] H. Griffiths. "Magnetic Induction Tomography." *Measurement Science Technology*, vol. 12, pp. 1126-1131, 2001.

[8] A. Korzhenevskii and V. Cherepenin. "Magnetic Induction Tomography." *Journal of Communications and Electronics*, vol. 42, no. 4, pp. 506-512, 1997.

[9] Oxford Dictionaries."Mutual Induction." Internet: http://oxforddictionaries.com/definition/mutual%2Binduction?q=mutual+induction, [19 Jun., 2012]

[10] K. Saladin. Human anatomy.: The McGraw-Hill Companies, Inc., 2008, .

[11] S. Watson. "Instrumentation for low-conductivity Magnetic Induction Tomography." PhD Thesis, University of Glamorgan, 2009.

[12] H. Griffiths, W.R. Stewart and W. Gough. "Magnetic induction tomography. A measuring system for biological tissues." *Ann N Y Acad Sci*, vol. 873, pp. 335-345, Apr. 1999.

[13] S. Watson, R.J. Williams, H. Griffiths, W. Gough and A. Morris. "Magnetic induction tomography: phase versus vector-voltmeter measurement techniques." *Physiol Meas*, vol. 24, no. 2, pp. 555-564, May. 2003.

[14] X. Ma, A. Peyton, R. Binns and S. Higson. "Electromagnetic techniques for imaging the cross-section distribution of molten steel flow in the continuous casting nozzle." *IEEE Sensors Journal*, vol. 5, no. 2, pp. 224-232, 2005.

[15] X. Ma, A. Peyton, S. Higson, A. Lyons and S. Dickinson. "Hardware and software design for an Electromagnetic Induction Tomography (EMT) system for high contrast metal process applications." *Measurement Science and Technology*, vol. 17, no. 1, pp. 111-118, 2006.

[16] E. Hammer, E. Abro and E. Cimpan. "A high frequency magnetic field probe for determination of interface levels in separation tanks," in *Process Imaging for Automatic Control*, 1993, pp. 294-299.

[17] J. Netz, E. Forner and S. Haagemann. "Contactless impedance measurement by Magnetic Induction Tomography - a possible method for investigation of brain impedance." *Physiological Measurements*, no. 14, pp. 463-471, 1993.

[18] R. Merwa, K. Hollaus, B. Oszkar and H. Scharfetter. "Detection of brain oedema using magnetic induction tomography: a feasibility study of the likely sensitivity and detectability." *Physiol Meas*, vol. 25, no. 1, pp. 347-354, Feb. 2004.

[19] H. Griffiths. "Magnetic Induction Tomography," in *Electrical Impedance Tomography: methods, history and applications*, 1st, David Holder (Ed.). Ed : CRC Press, 2005, pp. 213-238

[20] R. Guardo, G. Charron, Y. Goussard and P. Savard. "Contactless measurement of thoracic conductivity changes by Magnetic Induction Tomography," in *Proceedings of the 19th International Conference IEEE/EMBS*, 1997, pp. 2450-2453.

[21] S. Watson, R. Williams, W. Cough, A. Morris and H. Griffiths. "Phase measurements in biomedical Magnetic Induction Tomography". *2nd World Congress on Industrial Process Tomography*, 2001.

[22] H. Scharfetter, H.K. Lackner and J. Rosell. "Magnetic induction tomography: hardware for multi-frequency measurements in biological tissues." *Physiol Meas*, vol. 22, no. 1, pp. 131-146, Feb. 2001.

[23] H. Scharfetter, A. Kostinger and S. Issa. "Spectroscopic 16 channel Magnetic Induction Tomography: the new Graz MIT system," in *IFMBE Proceedings*, 2007, pp. 452-455.

[24] M. Steffen and S. Leonhardt. "Development of the multichannel simultaneous Magnetic Induction Tomography measurement system Musimitos," in *IFMBE Proceedings*, 2007, pp. 448-451.

[25] H. Scharfetter, R. Casanas and J. Rosell. "Biological tissue characterization by Magnetic Induction Spectroscopy (MIS): Requirements and limitations." *IEEE Transactions on Biomedical Engineering*, vol. 50, no. 7, pp. 870-880, Jul. 2003.

[26] T. Glisson Jr. "Current, Voltage and resistance," in *Introduction to circuit analysis and design*, 1st. ed., Ed : Springer, 2011, pp. 19-42

[27] S. Watson, A. Morris, R.J. Williams, H. Griffiths and W. Gough. "A primary field compensation scheme for planar array magnetic induction tomography." *Physiol Meas*, vol. 25, no. 1, pp. 271-279, Feb. 2004.

[28] A. Peyton, M. Beck, J. deOliveira, G. Lyon, Z. Yu, M. Brown and J. Ferrera. "Development of Electromagnetic Tomography (EMT) for industrial Applications. Part 1: Sensor Design and Instrumentation," in *1st World Congress on Industrial Process Tomography*, 1999.

[29] S. Watson, R.J. Williams, W. Gough and H. Griffiths. "A magnetic induction tomography system for samples with conductivities below 10 S m−1." *Meas. Sci. Technol.*, vol. 19, no. 4, 2008.

[30] H.C. Wee. "Development of Digital Signal Processing measurement platform for Biomedical Magnetic Induction Tomography and Spectroscopy system." PhD Thesis, University of Glamorgan, 2011.

[31] S. Watson, R. Williams, A. Morris, W. Cough and H. Griffiths. "The Cardiff Magnetic Induction Tomography system," in *Proceedings of the International Federation for Medical and Biological Engineering EMBE*, 2002, pp. 116-117.

[32] A. Korjenevsky, V. Cherepenin and S. Sapetsky. "Magnetic induction tomography: experimental realization." *Physiol Meas*, vol. 21, no. 1, pp. 89-94, Feb. 2000.

[33] C. Igney, S. Watson, R. Williams, H. Griffiths and O. Dossel. "Design and performance of a planar-array MIT system with normal sensor alignment." *Physiological Measurements*, vol. 26, no. 2, 2005.

[34] D. Gürsoy and H. Scharfetter. "Magnetic Induction pneumography: a planar coil system for continuous monitoring of lung function via contactless measurements." *J Electr Bioimp*, vol. 1, no. , pp. 56-62, . 2010.

[35] H. Griffiths, M. Zolgharni, P. Ledger and S. Watson. "The Cardiff Mk2b MIT head array: optimising the coil configuration." *Journal of Physics: Conference Series*, vol. 224, no. 1, 2010.

[36] A. Peyton, S. Watson, R. Williams, H. Griffiths and W. Gough. "Characterising the effects of the external electromagnetic shield on a Magnetic Induction Tomography sensor," in *Proceedings of the 3rd World Congress on Industrial Process Tomography*, 2003, pp. 352-357.

[37] H.C. Wee, S. Watson, R. Patz, H. Griffiths and R.J. Williams. "A Magnetic Induction Tomography system with sub-millidegree phase noise and high long-term phase stability," in *4th European Conference of the International Federation for Medical and Biological Engineering IFMBE Proceedings*, 2009, pp. 744-747.

[38] A. Hajimiri and T.H. Lee. "A general theory of phase noise in electrical oscillators." *IEEE Journal of Solid-State circuits*, vol. 33, no. 2, pp. 179-194, . 1998.

[39] J. Watson. "Noise," in *Analog and switching circuit design*, 1st ed., Ed Bristol:

Adam Hilger Ltd, 1984, pp. 142-168

[40] W. van Etten. "Noise in networks and systems," in *Introduction to random signals and noise*, 1st ed., Ed Sussex: John Wiley & Sons Inc., 2005, pp. 129-152

[41] H. Scharfetter, A. Köstinger and S. Issa. "Hardware for quasi-single-shot multifrequency magnetic induction tomography (MIT): the Graz Mk2 system." *Physiol Meas*, vol. 29, no. 6, pp. S431-43, Jun. 2008.

[42] F. Liebold, M. Hamsch and C.H. Igney. "Contact-less human vital sign monitoring with a 12 channel synchronous parallel processing magnetic impedance measurement system," in *4th European Conference of the International Federation for Medical and Biological Engineering IFMBE Proceedings*, 2009, pp. 1070-1073.

[43] G. Panayi, R. Patz, S. Watson, S. Kalogirou and R. Williams. "A high frequency phase reference," in *Proceedings of 5th International Research and Education Colloquium*, 2004, pp. 47-53.

[44] Report in support from Mphil to PhD, G. Panayi. "Magnetic Induction Tomography for biomedical and industrial applications requiring fast measurements," University of Glamorgan, 2009.

[45] A. Soliman and M. Ismail. "Active compensation of opamps." *IEEE Transactions on Circuits and Systems*, vol. 26, no. 2, pp. 112-117, . 1979.

[46] T. Glisson Jr. "Sinusoids, Phasors and Impedance," in *Introduction to circuit analysis and design*, 1st ed., Ed : Springer, 2011, pp. 383-477

[47] A. Lance, W. Seal and F. Labaar. "Phase noise and AM noise measurements in the frequency domain," in *Infrared and millimeter waves*, 1st ed., vol. 11. Kenneth J. Button (Ed.). Ed New York: Academic Press, 1984, pp. 239-289

[48] G. Ballou. "Fundamentals and units of measurement," in *Handbook for sound engineers The new audio cyclopedia*, 2nd., Glen Ballou (Ed.). Ed Indiana: SAMS, 1991, pp. 1417-1459

[49] M. Wagdy and M. Lucas. "A phase measurement offset compensation technique suitable for automation." *IEEE Transactions on Instrumentation and Measurement*, vol. IM-36, no. 3, pp. 712-724, 1987.

[50] K. Ibrahim and M. Abduk-Karim. "A novel digital phase meter." *IEEE Transactions on Instrumentation and Measurements*, vol. IM-36, no. 3, pp. 711-716, 1987.

[51] S. Mahmud. "Error analysis of digital phase measurements of distorted waves." *IEEE Transactions on Instrumentation and Measurements*, vol. IM-38, no. 1, pp. 6-9, 1989.

[52] S. Mahmud, N. Mahmud and S. Vishnubhotla. "Hardware implementation of a new phase measurement algorithm." *IEEE Transactions on Instrumentation and Measurements*, vol. 39, no. 2, pp. 331-334, 1990.

[53] S. Mahmud. "High precision phase measurement using adaptive sampling." *IEEE*

*Transaction on Instrumentation and Measurement*, vol. 38, no. 5, pp. 954-960, 1989.

[54] S. Mahmud. "High precision phase measurement using reduced sine and cosine tables." *IEEE Transactions on Instrumentation and Measurement*, vol. 39, no. 39, pp. 56-60, 1990.

[55] S. Watson, R.J. Williams, H. Griffiths, W. Gough and A. Morris. "A transceiver for direct phase measurement magnetic induction tomography," in *Proceedings of the 23rd Annual International Conference of the IEEE Engineering in Medicine and Biology Society*, 2001, pp. 3182-3184.

[56] S. Watson, R. Williams, H. Griffiths, W. Gough and A. Morris. "Frequency downconversion and phase noise in MIT." *Physiological Measurements*, no. 23, pp. 189-194, 2002.

[57] J. Scofield. "A frequency domain description of a lock-in amplifier." *American Journal of Physics*, vol. 2, no. 62, pp. 129-133, 1994.

[58] Technical Note TN1000, "What is a lock-in amplifier?," Signal Recovery Ltd, 2000.

[59] E. Ifeachor and B. Jevris. Digital signal processing: a practical approach. Essex UK: Addison-Wesley, 1993.

[60] R. Patz, S. Watson, C. Ktistis, M. Hamsch and A.J. Peyton. "Performance of a FPGA-based Direct Digitising Signal measurement module for MIT." *Journal of Physics: Conference Series*, vol. 224, no. 1, 2010.

[61] H. Wei and M. Soleimani. "Hardware and software design for a National Instrument-based magnetic induction tomography system for prospective biomedical applications." *Physiological Measurements*, no. 33, pp. 863-879, . 2012.

[62] S.M. Huang, A.B. Plaskowski, C.G. Xie and M.S. Beck. "Tomographic imaging of two-component flow using capacitance sensors." *Journal of Physics E: Scientific Instruments*, vol. 22, pp. 173-177, 1989.

[63] Data sheet, . "PXI/DAQ/DAQe-2200 Series," ADLINK Technologies Ltd, 2012.

[64] W. Yin, C. Guang, J. Jiang and Z. Cui. "The design of a FPGA-based Digital Magnetic Induction Tomography (MIT) system for metallic object imaging". *International Instrumentation and Measurement Technology Conference*, Austin, USA, 2010.

[65] W. Yin, G. Chen, L. Chen and B. Wang. "The design of a digital Magnetic Induction Tomography (MIT) system for metallic object imaging based on half cycle demodulation ." *IEEE Sensors Journal*, vol. 11, no. 10, pp. 2233-2240, 2011.

[66] M. Hamsch, C. Igney and M. Vauhkonen. "16 channel Magnetic Induction Tomography system featuring parallel readout," in *IFMBE proceedings*, 2007, pp. 484-487.

[67] M. Vauhkonen, M. Hamsch and C.H. Igney. "A measurement system and image reconstruction in magnetic induction tomography." *Physiol Meas*, vol. 29, no. 6, pp.

S445-54, Jun. 2008.

[68] M. Steffen and S. Leonhardt. "Non contact monitoring of heart and lung activity by Magnetic Induction measurement." *Acta Polytechnica*, vol. 48, no. 3, pp. 71-78, . 2008.

[69] N. Terzija, W. Yin, G. Gerbeth, F. Stefani, K. Timmel, T. Wondrak and A. Peyton. "Electromagnetic inspection of a two-phase flow of GaInSn and argon." *Flow Measurement and Instrumentation*, no. 22, pp. 10-16, 2011.

[70] N. Terzija, W. Yin, G. Gerbeth, F. Stefani, K. Timmel, T. Wondrak and A.J. Peyton. "Use of electromagnetic induction tomography for monitoring liquid metal/gas flow regimes on a model of an industrial steel caster." *Meas. Sci. Technol.*, no. 22, 2011.

[71] I. Ismail, J.C. Gamio, S.F.A. Bukhari and W.Q. Yang. "Tomography for multi-phase flow measurement in the oil industry." *Flow Measurement and Instrumentation*, no. 16, pp. 145-155, 2005.

[72] I. Babelli. "In search of an ideal multiphase flow meter for the oil industry." *Arabian Journal of Science and Engineering*, vol. 27, no. 2B, pp. 113-126, 2002.

[73] Handbook, S. Corneliussen, J.P. Couput, E. Dahl, E. Dykesteen, K.E. Froysa, E. Malde, H. Moestue, P.O. Moksnes, L. Scheers and H. Tunheim. "Handbook of Multiphase Flow Metering," The Norwegian Society for Oil and Gas Measurement & The Norwegian Society of Chartered Technical and Scientific Professionals, 2005.

[74] Questions and answers Bulletin, T. Patten. "Considering multiphase flow," Micro Motion Inc., 2007.

[75] G. Falcone, G.F. Hewitt, C. Alimonti and B. Harrison. "Multiphase flow metering: current trends and future developments," in *SPE 71474 Annual Technical Conference and Exhibition*, 2001, pp. 1-13.

[76] R. Thorn, G.A. Johansen and E.A. Hammer. "Three phase flow measurement in the offshore oil industry is there a place for process tomography?," in *1st World Congress on Industrial Process Tomography*, 1999, pp. 228-235.

[77] University of Leeds."Industrial Process Tomography." Internet: http://www.leeds.ac.uk/olil/processTomography.php, [11 Sep., 2011]

[78] T. Dyakowski, F.C. Laurent and A. Jaworski. "Applications of electrical tomography for gas-solids and liquid-solids flows - a review." *Powder Technology*, vol. 112, pp. 174-192, 2000.

[79] H. Jin, Y. Han, S. Yang and G. He. "Electrical resistance tomography coupled with differential pressure measurement to determine phase hold-ups in gas–liquid–solid outer loop bubble column." *Flow Measurement and Instrumentation*, vol. 21, no. 3, pp. 228-232, 2010.

[80] R.A. Albrechtsen, Z.Z. Yu and A.J. Peyton. "Preliminary experiments on the investigation of the inductive technique for measuring water content in multiphase

flow". Bergen, 1995.

[81] E.A. Hammer and G. Fossdal. "A new water in oil monitor based on high frequency magnetic field excitation". Wroclaw, 2002.

[82] C. Gabriel, S. Gabriel and E. Corthout. "The dielectric properties of biological tissues: I. Literature review." *Phys. Med. Biol.*, vol. 41, pp. 2231-2249, 1996.

[83] S. Grimnes and O.G. Martinsen. Bioimpedance and bioelectricity basics. London: Academic Press, 2000, pp. 375.

[84] R. Pethig and D.B. Kell. "The passive electrical properties of biological systems: their significance in physiology, biophysics and biotechnology." *Phys. Med. Biol.*, vol. 32, no. 8, pp. 933-970, 1987.

[85] K.S. Cole and C.R. Cole. "Dispersion and absorption in dielectrics; I. Alternating current characteristics." *Journal of Chemical Physics*, no. 9, pp. 341-351, 1941.

[86] K.R. Foster and H.P. Schwan. "Dielectric properties of tissues and biological materials: A critical review." *CRC Critical reviews in Biomedical Engineering*, vol. 17, no. 1, pp. 25-104, 1989.

[87] H.P. Schwan. "Electrical properties of tissue and cell suspensions." *Adv Biol Med Phys*, no. 5, pp. 147-209, 1957.

[88] H.P. Schwan. "Electrical properties of tissues and cell suspensions: mechanisms and models," in *Proceedings of 16th Annual International Conference of the IEEE Engineering in Medicine and Biology Society*, 1994.

[89] H.P. Schwan and S. Takashima. "Electrical conduction and dielectric behavior in biological systems," in *Encyclopedia of applied physics (Vol. Biophysics and Medical Physics)*, G. L. Trigg. (Ed.). Ed : Wiley VCH, 1993.

[90] Institute of Applied Physics Italian National Research Council."Dielectric properties of body tissues." Internet: http://niremf.ifac.cnr.it/tissprop/, [15 Sep., 2011]

[91] S. Gabriel, R.W. Lau and C. Gabriel. "The dielectric properties of biological tissues: II. Measurements in the frequency range 10 Hz to 20 GHz." *Phys. Med. Biol.*, vol. 41, pp. 2251-2269, 1996.

[92] S. Gabriel, R.W. Lau and C. Gabriel. "The dielectric properties of biological tissues: III. Parametric models for the dielectric spectrum of tissues." *Phys. Med. Biol.*, vol. 41, pp. 2271-2293, 1996.

[93] Report, C. Gabriel. "Compilation of the dielectric properties of body tissues at RF and microwave frequencies," Occupational and environmental health directorate, Radiofrequency Radiation Division, Brooks Air Force Base, 1996.

[94] M.T. La Povere, G.D. Pinna, R. Maestri, A. Mortara, S. Capomolla, O. Febo, R. Ferrari, M. Franchini, M. Gnemmi, C. Opasish, P.G. Riccardi, E. Traversi and F. Cobelli. "Short-term heart rate variability strongly predicts sudden cardiac death in chronic heart failure patients." *Circulation*, vol. , no. 107, pp. 565-570, 2003.

[95] A. Murray. Arrhythmia monitoring. Denmark: S&W Medico Teknik A/S, 1984.

[96] H. Tsuji, M.G. Larson, F. Venditti, E. Manders, J.C. Evans, C.L. Feldman and D. Levy. "Impact of reduced heart rate variability on risk for cardiac events: the Framingham heart study." *Circulation*, no. 94, pp. 2850-2855, 1996.

[97] W.B. Kannel, G. Kannel, R.S. Paffenbarger and L.A. Cupples. "Heart rate and cardiovascular mortality: The Framingham study." *American Heart Journal*, vol. 113, no. 6, pp. 1489-1494, 1987.

[98] The cardiovascular system. New York: Britannica Educational Publishing, 2011, pp. 250.

[99] A. Aleksandrowicz and S. Leonhardt. "Wireless and non contact ECG measurement system - the "Aachen SmartChair"." *Acta Polytechnica*, vol. 47, no. 4-5, pp. 68-71, 2007.

[100] K.M. Lee, S.M. Lee and K.S. Park. "Belt type wireless and non contact electrocardiogram monitoring system using flexible active electrodes." *International Journal of Bioelectromagnetism*, vol. 12, no. 4, pp. 153-157, 2010.

[101] R. Paradiso, G. Loriga and N. Taccini. "A wearable health care system based on knitted integrated sensors." *IEEE Transactions on Information Technology and Biomedicine*, vol. 9, no. 3, pp. 337-344, 2005.

[102] F.P. Wieringa, F. Mastik and A.F.W. Van der Steen. "Contactless multiple wavelength photoplethysmographic imaging: a first step toward "SpO2 camera" technology." *Annals of Biomedical Engineering*, vol. 33, no. 8, pp. 1034-1041, 2005.

[103] J. Hao, M. Jayachandran, P.L. Kng, S.F. Foo, P.W. Aung Aung and Z. Cai. "FBG based smart bed system for healthcare applications." *Optoelectron. China*, vol. 3, no. 1, pp. 78-83, 2010.

[104] K. Tavakolian, F.M. Zadeh, Y. Chuo, A. Vaseghi and B. Kaminska. "Development of a novel contactless mechanocardiograph device." *International Journal of Telemedecine and Applications*, 2008.

[105] M. Zakrzewski, A. Kolinummi and J. Vanhala. "Contactless and unobtrusive measurement of heart rate in home environment," in *Engineering in Medicine and Biology Society, 2006*, 2006, pp. 2060 - 2063.

[106] R. Fletcher and J. Han. "Low cost differential front-end for Doppler radar vital sign monitoring", Boston, Massachusets, 2009.

[107] J.J. Carr and J.M. Brown. "The human respiratory system and its measurement," in *Introduction to biomedical technology*, 4th ed., Ed Ohio: Prentice Hall, 2001, pp. 305-329

[108] R. Mason, V. Broaddus, T.E. King, D.E. Schraufnagel, J.F. Murray and J.A. Nadel. Textbook of respiratory medicine. Philadelfia, PA: Elsevier, 2010.

[109] A.T. Johnson, C.G. Lausted and J.D. Bronzino. "Respiratory system," in *The*

*biomedical engineering handbook*, 2nd ed., vol. 1. Joseph D. Bronzino (Ed.). Ed Boca Raton: CRC Press, 2000.

[110] M. Folke, L. Cernerud, M. Ekstrom and B. Hok. "Critical review of non-invasive respiratory monitoring in medical care." *Med. Biol. Eng. Comput.*, vol. 41, pp. 377-383, 2003.

[111] J. Malmivuo and R. Plonsey. "Impedance Plethysmography," in *Bioelectromagnetism - Principles and applications of bioelectric and biomagnetic fields*, 1st ed., Ed Oxford UK: Oxford University Press, 1995.

[112] K. Cohen, D. Panescu, J. Booske, J. Webster and W. Tompkins. "Design of an inductive plethysmograph for ventilation measurement." *Physiological Measurement*, vol. 15, no. 2, pp. 217-232, 1994.

[113] G.K. Wolf and J.H. Arnold. "Non invasive assessment of lung volume: Respiratory inductance plethysmography and electrical impedance tomography." *Critical Care Medicine*, vol. 33, no. 3, pp. 163-169, 2005.

[114] J. Malmivuo and R. Plonsey. "Impedance Tomography," in *Bioelectromagnetism - Principles and applications of bioelectric and biomagnetic fields*, 1st ed., Ed Oxford UK: Oxford University Press, 1995.

[115] T. Muders, H. Luepschen and C. Putensen. "Impedance tomography as a new monitoring technique." *Curr. Opin. Crit. Care*, vol. 16, no. 3, pp. 269-275, 2010.

[116] D.C. Barber and B.H. Brown. "Applied potential tomography." *J. Phys. E: Sci. Instrum.*, vol. 17, no. 9, pp. 723-733, 1984.

[117] I. Frerichs. "Electrical Impedance Tomography (EIT) in applications related to lung and ventilation: a review of experimental and clinical activities." *Physiological Measurement*, vol. 21, no. 2, 2000.

[118] I. Frerichs, J. Hinz, P. Herrmann, G. Weisser, G. Hahn, T. Dudykevych, M. Quintel and G. Hellige. "Detection of local lung air content by electrical impedance tomography compared with electron beam CT." *Journal of Applied Physiology*, vol. 93, no. 2, pp. 660-666, 2002.

[119] Maltron International Ltd."Maltron Sheffield MK 3.5." Internet: http://www.maltronint.com/eit/msmk35.php, [01 Oct., 2013]

[120] Draeger Ltd."Pulmovista 500." Internet: http://campaigns.draeger.com/pulmovista500/en/ , [01 Oct., 2013]

[121] P.P. Tarjan and R. McFee. "Electrodeless measurements of the effective resistivity of the human torso and head by Magnetic Induction." *IEEE Trans. Biomed. Eng.*, vol. BME-15, pp. 276-278, 1968.

[122] J.J. Carr and J.M. Brown. "Physiological pressure and other cardiovascular measurements and devices," in *Introduction to Biomedical Technology*, 4th ed., Ed Ohio: Prentice Hall, 2001, pp. 234-303

[123] A. Cordes, J. Foussier and S. Leonhardt. "Breathing detection with a portable

impedance measurement system: First measurements," in *Annual International Conference of the IEEE EMBS*, 2009, pp. 2767-2770.

[124] B. Razani. "Phase locked loops," in *RF microelectronics*, 2nd ed., Ed: Prentice Hall, 2011, pp. 597-654

[125] W. Egan. "Phase detectors," in *Frequency synthesis by phase lock*, 2nd ed., Ed New York: John Wiley & Sons Inc., 1999, pp. 175-245

[126] Application note 200-3, "Fundamentals of Time Interval Measurements," Hewlett-Packard Company, 1997.

[127] J. Kalisz. "Review of methods for Time Interval Measurements with picosecond resolution." *Metrologia*, vol. 41, no. , pp. 17-32, 2004.

[128] Application note 162-1, "Time Interval Averaging," Hewlett-Packard Company, 1970.

[129] Data sheet, "Spartan-3 FPGA family: complete data sheet," Xilinx Inc., 2006.

[130] Digilent Inc.."Spartan-3 Board." Internet: http://www.digilentinc.com/Products/Detail.cfm?Prod=S3BOARD, [Jul., 2013]

[131] Tutorial note, "Analog multipliers," Analog Devices Inc., 2009.

[132] Data sheet, "AD835: 250 MHz, Voltage Output 4-Quadrant Multiplier," Analog Devices Inc., 2010.

[133] Data sheet, "AD8056: Low Cost, Dual, 300 MHz Voltage Feedback Amplifier rev. J," Analog Devices Inc., 2006.

[134] R. Mancini. "Development of the ideal op amp equations," in *Opamps for everyone*, 1st ed., Ron Mancini (Ed.). Ed : Texas Instruments Inc., 2002, pp. 3.1-3.12

[135] Data sheet, "LT1016 UltraFast 10ns comparator," Linear Technology Corporation, 1991.

[136] Application report SCEA021A, N. Sultana and C. Cockrill. "Texas Instruments voltage-level translation devices," Texas Instruments, 2002.

[137] Data sheet, "74LVC245 Octal bus transceiver with direction pin; 3-state," Philips Semiconductors Ltd, 1994.

[138] Xilinx Inc.."ISE WebPACK Design Software." Internet: http://www.xilinx.com/products/design-tools/ise-design-suite/ise-webpack.htm, [Jul., 2013]

[139] Mentor Graphics Inc.."ModelSim ASIC and FPGA design." Internet: http://www.mentor.com/products/fv/modelsim/, [Jul., 2013]

[140] Application note, "Metastability considerations," Xilinx Inc., 1997.

[141] White paper WP-01082-1.2, J. Stephenson, D. Chen, R. Fung and J. Chromczak.

"Understanding metastability in FPGAs," Altera, 2009.

[142] R. Ginosar. "Metastability and synchronisers: a tutorial." *Design & Test of Computers, IEEE*, vol. 28, no. 5, pp. 23-35, 2011.

[143] Data sheet, "Max3232 3-V to 5-V multichannel RS-232 line driver/receiver with 15-kV ESD protection ," Texas Instruments Inc., 2004.

[144] M. Munteanu."UART ." Internet: http://www.hp-h.com/p/munte, [24 Apr., 2010]

[145] National Instruments Inc."NI Labwindows/CVI." Internet: http://www.ni.com/lwcvi/, [Jul., 2013]

[146] Data sheet, "DS-1000 5-tap silicon delay line," Maxim Inc.

[147] Data sheet, "Coaxial amplifier ZHL-3A," Mini-Circuits Inc.

[148] Application note, "Relay technical notes," American Zettler Inc.

[149] Application note 13C3311, "The application of relay coil suppression with DC relays," Tyco Electronics Corporation, 1998.

[150] Application note 13C3264, "Coil suppression can reduce relay life," Tyco Electronics Corporation, 2000.

[151] L. Sherwood. Fundamentals of physiology: A human perspective.: Thomson Brooks/Cole, 2006, pp. 380.

[152] Electromagnetic Combatibility Laboratory Missouri University of Science and Technology."Rectangular loop inductance calculator." Internet: http://emclab.mst.edu/inductance/rectgl/, [30 Jul., 2013]

[153] Data sheet, "ADA4899-1: Unity-Gain Stable, Ultralow Distortion, 1 nV/√Hz Voltage Noise, High Speed Op Amp rev. B," Analog Devices Inc., 2007.

[154] H. Mahdavi and J. Rosell Ferrer. "Simulation of a Magnetic Induction method for determining passive electrical property changes of human trunk due to vital activities," in *Proceedings of the 2012 COMSOL Conference*, 2012.

[155] G. Matheou, E. Kyriacou, P. Chimonidou, C. Pattichis, E. Lambrinou, V. Barberis and G. Georghiou. "A post cardiac surgery home-monitoring system," in *12th International Conference on computer systems and technologies - ComSysTech'11*, 2011, pp. 341-347.

[156] "Dyna Vision units." Internet: http://www.dyna-vision.com/index.php?option=com_content&view=article&id=7%3Adyna-vision-units&catid=3%3Aproduct&Itemid=9&lang=en, [12 Aug., 2013]

[157] J. Semmlow. "Time-Frequency Analysis," in *Biosignal and Biomedical Image Processing*, 1st ed., Ed : Marcel Dekker Inc., 2004, pp. 149-180

[158] P. Horowitz and W. Hill. "High frequency and high speed techniques," in *The Art of Electronics*, 2nd ed., Ed New York: Cambridge University Press, 1989, pp. 863-915

[159] W. Yang. "Hardware design of electrical capacitance tomography systems." *Meas. Sci. Technol.*, vol. 7, no. 3, pp. 225-232, 1996.

[160] M. Cheney, D. Isaacson and J.C. Newel. "Electrical Impedance Tomography." *SIAM Review*, vol. 41, no. 1, pp. 85-101, 1999.

[161] L. Borcea. "Electrical Impedance Tomography." *Inverse Problems*, vol. 18, no. 6, pp. 99-136, 2002.